THE UNIVERSITY OF CHICAGO

IDENTIFICATION AND CHARACTERIZATION OF THE MOLECULE RESPONSIBLE FOR LYSOSOMAL CA2+/H+ EXCHANGE IN HUMANS

A DISSERTATION SUBMITTED TO

THE FACULTY OF THE DIVISION OF THE PHYSICAL SCIENCES

IN CANDIDACY FOR THE DEGREE OF

DOCTOR OF PHILOSOPHY

DEPARTMENT OF CHEMISTRY

BY

MATTHEW ZAJAC

CHICAGO, ILLINOIS

AUGUST 2022

Dedication

To Mom and Dad:

For always being proud of me,

And allowing me to be proud of myself,

This is for you.

Table of Contents

List of Figures

List of Tables

List of Publications

1) **M. Zajac**, P. Anees, S. Mukherjee, K. Henn D. Oettinger, J. Srikumar, J. Zou, A. Saminathan, Y. Krishnan. (2022). Molecular Identification of the Long-Sought Human Lysosomal Ca2+/H+ Exchanger. *Science*. In Review.
2) A. Saminathan*, **M. Zajac***, P. Anees, Y. Krishnan. (2021) Organelle-level precision with next-generation targeting technologies. *Nat Rev Mater.* doi: 10.1038/s41578-021-00396-8.
3) B. Suresh, A. Saminathan, K. Chakraborty, C. Cui, **M. Zajac**, L. Becker, Y. Krishnan. (2021) Tubular lysosomes harbor active ion gradients and poise macrophages for phagocytosis. *Proc Natl Acad Sci USA*. doi: 10.1073/pnas.2113174118.
4) P. Anees, **M. Zajac**, Y. Krishnan. (2020) Quantifying phagosomal HOCl at single immune-cell resolution. *Methods Cell Biol.* doi:10.1016/bs.mcb.2020.10.006.
5) **M. Zajac**, K. Chakraborty, S. Saha, V. Mahadevan, D.T. Infield, A. Accardi, Z. Qiu, Y. Krishnan. (2020) What biologists want from their chloride reporters – a conversation between chemists and biologists. *J. Cell Sci.* **133** doi:10.1242/jcs.240390.
6) **M. Zajac**. (2019) Reproduction, rethought. *Nature* **575**, 55-56.
7) S. Sharma, **M. Zajac**, Y. Krishnan. (2019). A DNA Aptamer for Cyclic Adenosine Monophosphate that Shows Adaptive Recognition. *ChemBioChem* **20**, 1-7.

*Equal contribution

Acknowledgments

This work would not be a fraction of what it is without the scientific and personal support of many people. First, I owe so much gratitude to Professor Yamuna Krishnan, my doctoral advisor. Thank you, sincerely, for the all of the ATP you have spent getting me to this point. You gave me space to ideate and explore science that fascinated me, while steering my questions and curiosities in fruitful directions. Your passion for knowledge is contagious, and has molded me into a skeptical and meticulous scientist. You taught me to take pride in my craft, and that quality science requires an attention to detail beyond what I knew was possible. You were patient while you dragged me up a steep learning curve many years ago, after which you never took your foot off the gas. The work in the thesis is a direct result of what we explored and learned together, but the skills I take away from this experience go far beyond this document. Above all, I am thankful for the friendship and mutual respect we have shared since the beginning. Neither of us is the same scientist or person we were 5 years ago, and I am honored to have grown by your side.

I must also thank the graduate students and postdocs who were in the Krishnan lab when I first joined: Dr. Kasturi Chakraborty, Dr. Anand Saminathan, Dr. Bhavyashree Suresh, Dr. Maulik Jani, Dr. Shareefa Thekkan, Junyi Zou, Dr. Aneesh Tazhe Veetil, Dr. KaHo Leung, and Dr. Krishna Dan. I joined the lab largely because of a culture you worked hard to maintain – one of openness, mentorship, and collegiality. In my early days in the lab, I discussed my experimental plans by one of you first, and you patiently gave me valuable suggestions. I owe my experimental design and data interpretation skills to your guidance. By example, you all showed me how to troubleshoot failed experiments, and how to maintain a positive attitude in the face of adversity. I would also like to thank current members of the Krishnan lab: Dr. Anees Palapuravan, Dr. Koushambi Mitra, Dr. Sourajit Mukherjee, JoAnn Tinker, Daphne Oettinger, Dr. Madhanagopal Barathraj, Dr. Priyanka Dutta Gupta, Dr. Sandip Chakraborty, and Dr. Pravin Hivare. I have learned so much from your expertise and your own projects, and the questions you have asked me about my own work.

One of the things I am most proud of from my thesis work is its level of collaboration. Science is better as a team, and I have been so lucky to have a team of persistent collaborators who pushed me to be a better scientist and mentor. Specifically, I thank Anand for his unparalleled knack for experimental planning and ideation. I thank both Anand and Sourajit for their persistence with our electrophysiological experiments, when giving up seemed like a very real option. I thank Anees, Daphne, and Jainaha Srikumar for their significant contributions to all of our worm experiments. I thank Kate Henn for continually learning new things in the lab, which have elevated our work in many ways. I always felt like we were all on the same page, and working with you helped keep experiments fun every single day. Thank you so much for the ways you have improved this thesis.

Finally, this work would not be possible without the support of other faculty, staff, and students around UChicago. We are so lucky to have experts in microscopy core and sequencing core facilities, who helped me troubleshoot many failed experiments. The Krishnan lab is also lucky to have gracious neighbors in the He and Dickinson labs, and I thank them for the reagents, protocols, and instruments they have so willingly shared. In addition, the administrative staff in the Chemistry Department, specifically Vera Dragisich and Melinda Moore, keep this department moving forward in ways that few of us can even appreciate. I also thank Professors Bryan Dickinson and Eduardo Perozo, for their scientific support and professional guidance as members of my thesis committee.

I would also like to thank my friends, from graduate school and other parts of my life. There are too many to name here, but you know who you are and how much I value you. Whether we shared food and drinks together, danced like goofballs, played softball together, went to sports games and shows, watched reality TV, planned department events, or just chatted/cried about life, I have cherished every moment we have spent together. When I think of my time in Chicago, I will remember it fondly because of you all. I truly do not know how I would have gotten through graduate school without your love and support.

To my best friend and partner, Mason, I thank you for making my life whole. We always say that our meeting each other was luck, but that our love is built on intentionality. You have taught me that great

things take time, that the words we use matter, and that passions make life vibrant. You have given me the final push I needed to finish graduate school, and have made me a better partner, friend, and companion. Merging our livelihoods has been one of the most thrilling experiences I have ever had. Now a whole new chapter of our lives begins when this thesis finishes, and our paths synchronize even more. In this world, it's just us… and Gio. I love you, from M to M.

Finally, this thesis is dedicated to my parents. Your unconditional love and support are the foundation for the rest of my life. You have supported me in everything I do, from attending all my baseball games and concert band performances, to supporting my PhD journey from hundreds of miles away. I am grateful every day and consider myself so lucky to have you as my biggest fans. Your encouragements to travel, try new things, and always push myself have made me the curious scientist I am. I have watched you both spend your lives learning new things, improving yourselves, rebuilding after losses, and celebrating after wins. I do my best every day to follow your example and make you proud. I love you both so much.

Abstract

The release of Ca^{2+} stored in lysosomes is critical to cell signaling through removal of degraded cargo and transcriptional reprogramming. While lysosomal Ca^{2+} release can be accounted for by known Ca^{2+} channels, the process by which Ca^{2+} is refilled into lysosomes remains poorly understood. Current hypotheses for lysosomal Ca^{2+} import include a H^+ exchange process and direct refilling from the endoplasmic reticulum (ER). Here, using an RNA interference screen in *C. elegans,* we identify an evolutionarily conserved gene, denoted *lcax-1*, that facilitates lysosomal Ca^{2+} import. Lysosomal Ca^{2+} measurements and functional assays in *C. elegans* and mammalian cells reveal that the human homolog, LCAX-1, imports Ca^{2+} pH-dependently into lysosomes. While electrophysiological characteristics of LCAX-1 are consistent with the long sought human lysosomal Ca^{2+}/H^+ exchanger, there are notable differences in its sequence and predicted structure compared to classical CAX transporters, none of which are electrogenic. Future work on LCAX-1 should explore these differences, especially its quaternary structure and its stoichiometry of exchange. Defects in many lysosomal Ca^{2+} channels lead to different neurodegenerative diseases, and knowledge of new Ca^{2+} importers may provide new avenues to explore the physiology of Ca^{2+} channels.

I. Introduction

I.A: Importance of lysosomal Ca^{2+} homeostasis

The lysosome plays a fundamental role in shaping cellular calcium (Ca^{2+}) levels and mediating intracellular Ca^{2+} signaling events. The Ca^{2+} concentration in lysosomes is ~500μM, which is about 5000-fold higher than the cytosolic Ca^{2+} concentration (*1*). For this reason, lysosomes are often thought of as the "acidic" or "small" calcium stores of the cell. Along with other intracellular stores, such as the endoplasmic reticulum (ER) and mitochondria, lysosomes dynamically release and refill Ca^{2+} in response to environmental cues. For example, lysosomal Ca^{2+} channels respond to stimuli such as pH and nutrients, as well as ATP and other small molecules. This suggests that differential regulation of lysosomal Ca^{2+} dynamics may serve to facilitate distinct lysosomal functions, tailored to specific cellular needs.

Lysosomal Ca^{2+} is a key second messenger that mediates various cellular functions (*2*). First, Ca^{2+} release is a necessary trigger for lysosomal fusion with other organelles. Each fusion process occurs through different Ca^{2+}-dependent proteins and mechanisms. For endocytic trafficking, lysosomes must enlarge and fuse with other endosomes, with requires the Ca^{2+}-dependent recruitment of calmodulin (**Fig. 1.1A**) (*3*). For autophagy, lysosomes must fuse with autophagosomes, which depends on the Ca^{2+}-dependent interaction of lysosomes with apoptosis-linked gene 2 (ALG-2). This mediates movement of lysosomes towards the perinuclear region, where autophagosomes accumulate (**Fig. 1.1B**) (*4*). Indeed, lysosomal Ca^{2+} release is involved in other steps of autophagy, including autophagosome formation and proteolytic degradation within autolysosomes (**Fig. 1.1B**) (*5*, *6*). For phagocytosis and exocytosis, lysosome must fuse with phagosomes and the plasma membrane, respectively. Both processes occur through the Ca^{2+} binding protein synaptotagmin 7 (Syt VII), which may induce physical changes between the SNARE complex and lipid bilayers to induce membrane fusion (**Fig. 1.1C,D**) (*7*–*9*). Ca^{2+} release is also critical for endolysosomal acidification, likely by keeping K^+ and Cl^- channels open for charge compensation (*10*). In each of these situations, lysosomal Ca^{2+} release may only occur from a subset of lysosomes at any given time, and may not be synchronized to trigger global changes in cytosolic Ca^{2+}

levels. Instead, localized Ca^{2+} release likely regulates local membrane trafficking events based on the lumenal cargo and chemistry of individual endosomes (*11*).

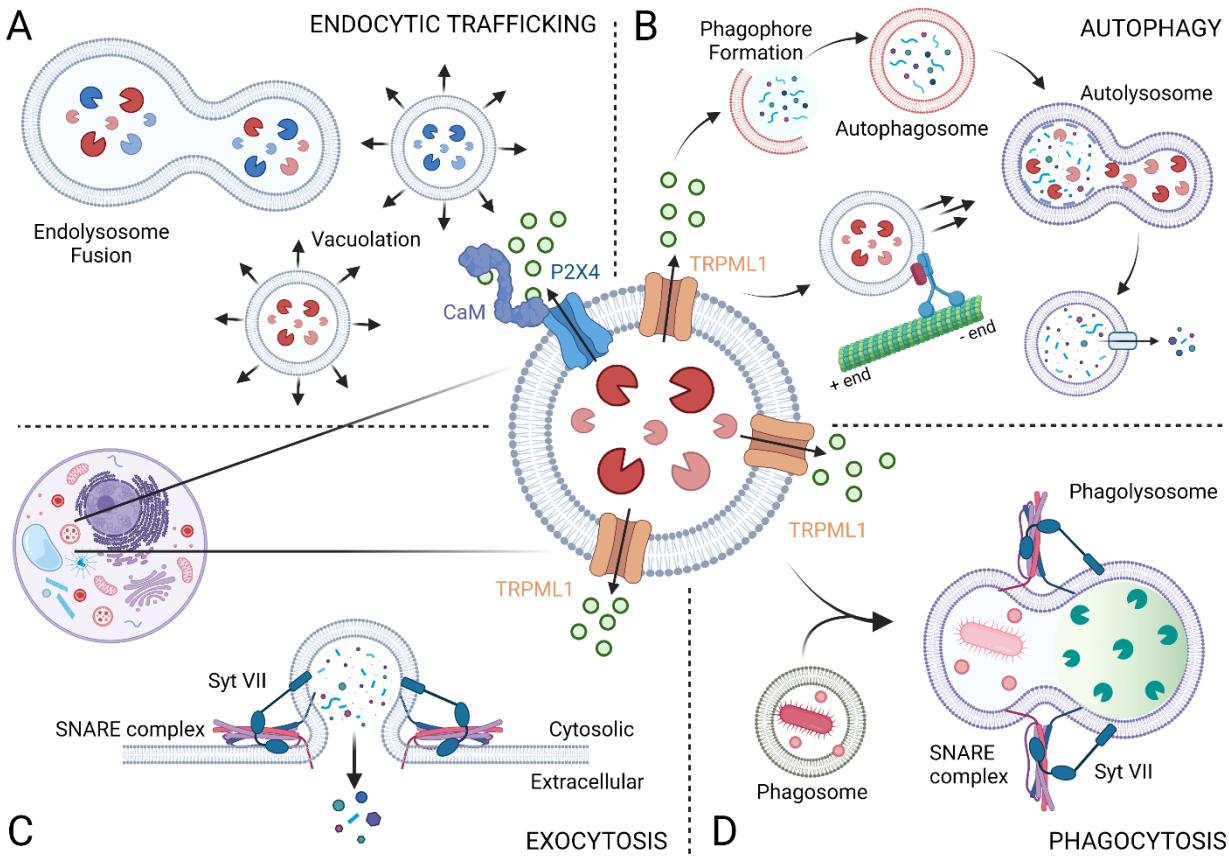

Figure 1.1: Lysosome functions mediated by Ca^{2+} release. (A) Release of lysosomal Ca^{2+} via the purinergic receptor X4 (P2X4) recruits calmodulin (CaM), promoting fusion and vacuolation (enlargement) of endolysosomes, regulating endocytic maturation. (B) Release of lysosomal Ca^{2+} via transient receptor potential cation channels of the mucolipin family 1 (TRPML1) facilitates autophagy by inducing phagophore formation and facilitating inward movement to the perinuclear region where autophagosomes accumulate. (C) Lysosomal exocytosis and plasma membrane repair occur Ca^{2+}-dependently via the Ca^{2+} sensor synaptotagmin VII (Syt VII), to facilitate membrane fusion by altering the interaction between SNARE complexes and lipid bilayers. (D) Syt VII regulates the fusion of phagosomes with lysosomes to form phagolysosomes in a Ca^{2+}-dependent manner.

However, synchronized lysosomal Ca^{2+} release can be amplified by release of Ca^{2+} from the endoplasmic reticulum (ER) by a process similar to Ca^{2+}-induced Ca^{2+} release. This leads to extracellular Ca^{2+} entering the cytosol because of ER store depletion, which evokes global Ca^{2+} signals that can modulate overall transcriptional programs, governing catabolism and cellular clearance (**Fig. 1.2A**) (*12*). Depletion of lysosomal Ca^{2+} store may also trigger the ER to directly transport Ca^{2+} into lysosomes, as

discussed in **Section I.C**. This complex Ca^{2+} signaling between lysosomes and the ER is supported by the observation of ER-lysosome contact sites, which perform a variety of structural and transfer functions, including the formation of ER-lysosome Ca^{2+} microdomains (*2*, *13*, *14*). Global Ca^{2+} signals modulate transcriptional programs via the Ca^{2+}-dependent activation of the cytosolic phosphatase calcineurin. Calcineurin dephosphorylates its substrate, transcription factor EB (TFEB). This causes TFEB to localize in the nucleus, where it activates target genes that upregulate lysosome biogenesis and autophagy (**Fig. 1.2B**) (*15*, *16*). TFEB activation increases the density of periplasmic lysosomes, promoting their fusion with the plasma membrane, bringing about exocytosis (*17*). Thus, lysosomal Ca^{2+} release is intimately linked to the induction of cellular clearance through transcriptional reprogramming.

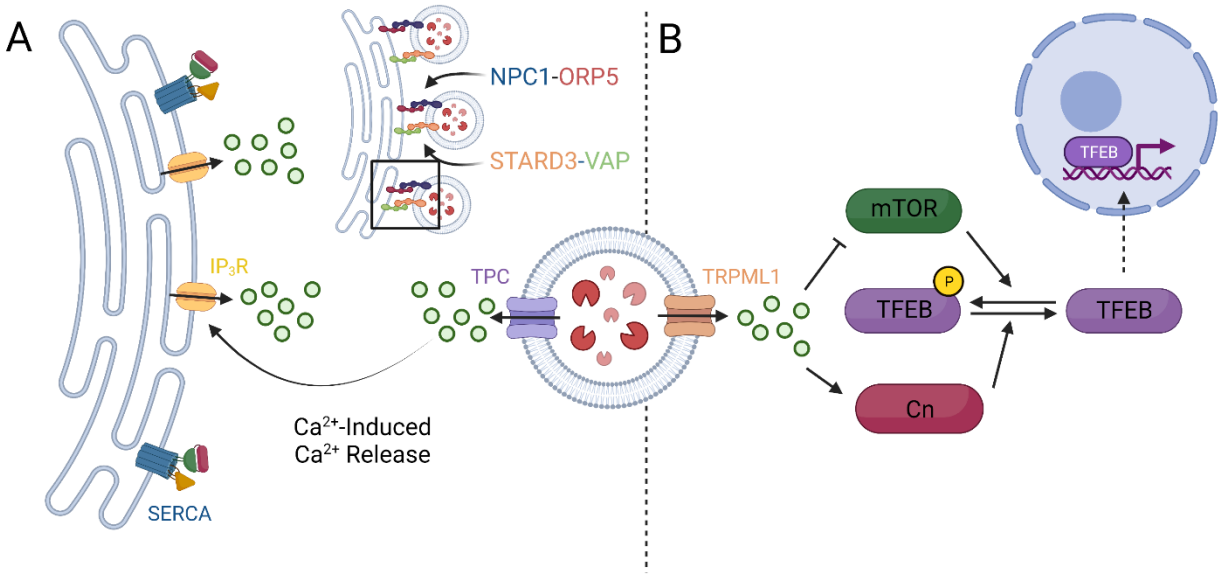

Figure 1.2: Global signaling by lysosomal Ca^{2+} release. (A) Release of lysosomal Ca^{2+} stores through two-pore channels (TPCs) leads to global cytosolic Ca^{2+} waves via amplification by the ER. Increased Ca^{2+} at the lysosome-ER contact site (which is mediated by various molecular tethers) sensitizes inositol 1,4,5-trisphosphate receptors (IP_3Rs) on the ER, leading to substantial mobilization of intracellular Ca^{2+}. (B) Lysosomal Ca^{2+} release through TRPML1 leads to local calcineurin (Cn) activation, which dephosphortylates TFEB. Dephosphorylated TFEB is no longer sequestered in the cytosol and can translocate to the nucleus where it activates transcription of lysosomal/autophagic genes. Simultaneously, mammalian target of rapamycin complex 1 (mTORC1) falls off the lysosomal membrane and can no longer phosphorylate TFEB. NPC1: Niemann-Pick type C1; ORP5: oxysterol-binding protei-related protein 5; STARD3: StAR-related lipid transfer domain protein 3; VAP: vesicle-associated membrane protein associated protein.

As intracellular Ca^{2+} stores, lysosomes also function as cytoprotective sponges that quickly mop up Ca^{2+} ions from the cytosol immediately after a cytosolic Ca^{2+} spike. Lysosomes can also release Ca^{2+}

in a controlled manner to activate cellular responses to such stress. Uptake of Ca^{2+} into acidic organelles suppresses Ca^{2+} signals in the cytosol, in response to release from intracellular stores (*18*). Intimate contacts between the ER and lysosome facilitate the lysosome to sequester Ca^{2+} released by the ER, thereby shaping overall intracellular Ca^{2+} signals (*19*). Thus, a picture of lysosomes as cytosolic Ca^{2+} buffers has emerged, where lysosomes play a cytoprotective role by preventing Ca^{2+} cytotoxicity. For example, the Ca^{2+} buffering capacity of lysosomes has a neuroprotective effect in experimental models of Parkinson's disease (*20*).

Table 1.1: Lysosome storage disorders and neurodegenerative diseases associated with dysregulated lysosomal Ca^{2+} homeostasis.

Disorder/Disease	Risk Gene	Protein Function	Lysosomal Phenotypes	Reference
Mucolipidosis type IV	TRPML1	Ca^{2+} channel	Enlarged size, trafficking and storage defects, impaired biogenesis	*(30)*
Niemann-Pick, type C	NPC1	Cholesterol efflux, other unknown roles	Low Ca^{2+} levels, lipid storage defects	*(21)*
Familial Alzheimer's disease	PSEN1	Core protein of gamma secretase complex, other unknown roles	Ca^{2+} storage and release defects, impaired fusion and autophagy	*(22,23)*
Kufor-Rakeb Syndrome	ATP13A2/ PARK9	Divalent cation and polyamine transporter	Impaired degradation, low Ca^{2+} levels	*(67-69)*
Parkinson's disease / Gaucher's disease	GBA1	Hydrolysis of glucosylceramide	Autophagic defects, impaired Ca^{2+} homeostasis	*(25,70)*
Familial Parkinson's disease	LRRK2/ PARK8	Multifunctional kinase	Morphology defects, Ca^{2+}-dependent trafficking	*(24)*
Episodic ataxia type 2, Familial hemiplegic migraine 1, spinocerebellar ataxia 6	CACNA1	Voltage-gated Ca^{2+} channel	Impaired lysosome fusion, low Ca^{2+}	*(26)*

Defective maintenance of lysosomal Ca^{2+} stores has direct implications for lysosome storage diseases (LSDs) and other pathologies resulting from cellular Ca^{2+} imbalance (**Table 1.1**). Lysosomal Ca^{2+} release or storage is impacted in mucolipidosis type IV (ML-IV) and Niemann-Pick, type C (NPC) (*21*, *22*). Lysosomal Ca^{2+} storage and release are also impaired in cells lacking presenilin (PSEN),

implying a γ-secretase-independent role for PSEN in autophagy through lysosome fusion (*23*). This may be relevant to the pathophysiology of familial Alzheimer's disease (FAD) caused by PSEN1 mutations (*24*). Parkinson's disease patients with certain risk factor mutations, such as the G2019S mutation in LRRK2, also show abnormal lysosomal Ca^{2+} homeostasis (*25*, *26*). Mutations in molecules responsible for shaping lysosomal Ca^{2+} fluxes are associated with neurological diseases such as episodic ataxia type 2, familial hemiplegic migraine-1, and spinocerebellar ataxia type 6 (*27*, *28*). A range of other rare neurodegenerative diseases are associated with alterations in autophagy, through Ca^{2+} dysregulation and other mechanisms (*29*). Finally, increasing evidence implicates lysosomal Ca^{2+} signaling in tumor development and progression through the regulation of autophagy pathways (*30*, *31*).

I.B: The molecular players involved in Ca^{2+} release

Three main types of Ca^{2+} channels are involved in release of stored lysosomal Ca^{2+} into the cytosol: transient receptor potential cation channels of the mucolipin family (TRPML), two-pore channels (TPC), and purinergic receptor X4 (P2X4) (*2*). Release channels and their activating cellular cues are now well-defined, thanks to lysosome-targeted genetically encoded calcium indicators (GECIs) and whole-lysosome electrophysiology (*1*).

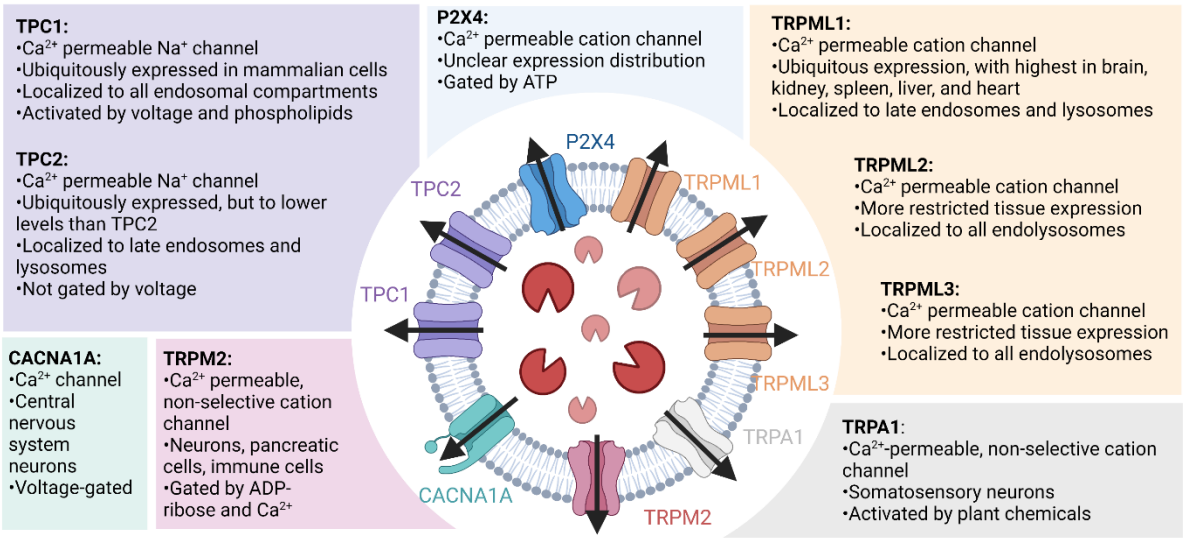

Figure 1.3: Endolysosomal channels that facilitate Ca^{2+} release, along with their tissue distribution and activating cues.

The TRPML family, consisting of TRPML1-3, is a group of Ca^{2+}-permeable cation channels present on the membranes of endolysosomes across most cell types (**Fig. 1.3**). The most characterized member of this group is TRPML1. TRPML1 is also known as mucolipin-1 (MCOLN1) and is mutated in ML-IV (*32*). Lysosomes in ML-IV patients show enlarged size, defects in trafficking, and their biogenesis is impaired (*33*). TRPML1 is activated by stimuli such as nutrient deprivation, reactive oxygen species, and phosphatidylinositol 3,5-bisphosphate ($PI(3,5)P_2$) (*34–36*). The ensuing TRPML1-mediated Ca^{2+} release has been implicated in fusion with other organelles, making it central to endocytic trafficking, lysosomal exocytosis, and autophagy (*4*, *5*, *36–38*). It also regulates lysosome size by promoting fission through a calmodulin-dependent mechanism (*39*). TRPML1 mediates direct transfer of Ca^{2+} into mitochondria, and in ML-IV patient cells, mitochondria-lysosome contact dynamics are disrupted along with Ca^{2+} transfer across both organelles (*40*). Additionally, TRPML1-mediated Ca^{2+} release activates autophagy under starvation, by regulating the desphosphorylation and subsequent nuclear translocation of TFEB (*15*). Importantly, TRPML1 is a target gene of TFEB and is upregulated under starvation, leading to a feedback loop (*15*, *35*). Concurrently, starvation inhibits the mammalian target of rapamycin complex I (mTORC1), further preventing TFEB phosphorylation and promoting its nuclear translocation. Combined, these functions are critical for lysosomes to adapt to nutritional needs in a coordinated manner (*41*, *42*). Finally, TRPML1 activity regulates key immune cell processes. It facilitates phagocytosis of large particles in macrophages through lysosomal exocytosis, dependent on Ca^{2+}-activated K^+ channels (*43*). In dendritic cells, it activates myosin II to control cell migration induced by bacterial sensing and suppressed micropinocytosis (*44*).

The TPC family consists of TPC1 and TPC2, which are present on endolysosomal membranes and ubiquitously expressed in mammalian cells (**Fig. 1.3**). TPCs are Na^+-selective channels that show limited permeability for Ca^{2+} (*1*, *45*). However, their relatively low Ca^{2+} permeability is physiologically relevant given that TPC overexpression leads to lysosomal Ca^{2+} release (*46*, *47*). In fact, TPCs appear to be the primary agent responsible for lysosomal Ca^{2+} released by nicotinic acid adenine dinucleotide phosphate (NAADP), which is how non-ER Ca^{2+} stores were first discovered (*46*, *48*, *49*).

P2X4 is an ATP-gated cation channel that is present on both the plasma membrane and lysosome membrane in certain mammalian cell types (**Fig. 1.3**). It is activated by luminal ATP and alkalinization, and is involved in lysosomal membrane fusion (*3*, *50*). Other lysosomal Ca^{2+} channels are expressed restrictively in certain cell types. These include the transient receptor potential ankyrin1 (TRPA1) in somatosensory neurons); transient receptor potential subfamily M member 2 (TRPM2) in neurons, pancreatic cells, and immune cells; and P/Q-type voltage-gated Ca^{2+} channels (VGCCs) such as CACNA1A in central nervous system neurons (**Fig. 1.3**) (*1*).

I.C: The Ca^{2+} refilling enigma in lysosomes

Unlike the mechanisms by which lysosomes empty their Ca^{2+} stores, how they replenish and maintain their high lumenal Ca^{2+} levels is unknown. In other intracellular Ca^{2+} stores, the importers responsible for Ca^{2+} influx are better defined. For example, we know that sarco/endoplasmic reticulum Ca^{2+}-ATPase (SERCA) performs this role for the ER, and mitochondrial calcium uniporter (MCU) does so for the mitochondria (*51*, *52*). There are several hypotheses for general mechanisms of lysosomal Ca^{2+} refilling, but no molecular players have been identified. This is largely because of the difficulty of measuring lumenal Ca^{2+} levels in the acidic lysosome, as discussed in **Section I.F**. Identifying such players is of great fundamental and therapeutic interest, as modulating lysosomal Ca^{2+} is critical to sculpt lysosomal functions in human physiology, as discussed in **Section I.A**.

One predominant hypothesis is that the lysosomal H^+ gradient is critical for lysosomal Ca^{2+} refilling and maintenance. Dissipating the pH gradient across mammalian lysosome membranes leads to Ca^{2+} release from the lysosome, while restoring the gradient allows the store to replenish (**Fig. 1.4A**) (*19*, *53–58*). Some evidence has shown that import of Ca^{2+} into mammalian lysosomes also increases lumenal pH (*19*, *20*). Combined, these reports indicate that a Ca^{2+}/H^+ exchange mechanism may drive Ca^{2+} uptake into lysosomes using the pH gradient. This may be carried out by a single Ca^{2+}/H^+ exchanger (CAX), or by multiple exchangers that, in tandem, lead to net Ca^{2+} import and H^+ export (**Fig. 1.4A**). However, many of the experiments that claimed to show evidence of H^+-driven Ca^{2+} import may have been subject to misinterpretation, as discussed below.

First, cytosolic Ca^{2+} probes are also sensitive to pH, and all small molecules used to release lysosomal Ca^{2+} also cause H^+ release. So it is possible that the observed Ca^{2+} signals were actually fluctuating H^+ levels. Second, increasing lysosomal pH may reduce free lysosomal Ca^{2+} by increasing its chelation with endogenous Ca^{2+} buffers in the lysosome lumen (*31*). Thus, deacidification may simply lower the free Ca^{2+} without releasing it. Third, treatments that deacidify lysosomes may also alter vesicle fission and fusion rates, and thereby indirectly affect lysosomal Ca^{2+} levels (*59*). Finally, treatments that deacidify lysosomes also affect the activity of Ca^{2+}-permeable release channels, such that alterations in lysosomal Ca^{2+} homeostasis may not be the result of Ca^{2+}/H^+ exchange mediated by a transmembrane protein. For example, low pH activates TRPML1, sensitizes TPC1 for activation by NAADP, and inhibits P2X4 (*2*). Low pH also inhibits RECS1, the newly identified Ca^{2+} and Na^+ channel, called "responsive to centrifugation and shear stress 1" (*60*).

Because of these potential contradictions, other mechanisms have been hypothesized for lysosomal Ca^{2+} entry. One alternative is that the ER directly drives lysosomal Ca^{2+} refilling (**Fig. 1.4B**). A physiological assay to monitor lysosomal Ca^{2+} refilling showed that the ER is the primary source of Ca^{2+} for the lysosome and not the transmembrane lysosomal pH gradient (*61*). In this assay, the extent of refilling is determined from the amount of Ca^{2+} released upon pharmacological activation of TRPML1 after an initial release and refilling, measured using GCaMP3 on the cytosolic surface of lysosomes (*61*). Dissipating the lysosomal pH gradient with V-ATPase inhibitors did not affect the refilling process, but emptying the ER store with SERCA inhibitors and other means completely abolished Ca^{2+} refilling in lysosomes. Blocking the ER release channel, IP3 receptor (IP3R), reduced refilling, and led to lysosomal storage phenotypes (*61*). In this model, after lysosome Ca^{2+} depletion, the lysosome first establishes contact with the ER by stabilizing or tethering their membranes. Ca^{2+} sensor proteins, such as extended synaptotagmin-like proteins, may be involved in the regulation of ER-lysosome membrane tethering, which involves several other proteins, including oxysterol-binding protein-related protein 1L (ORP1L), protrudin, and oxysterol-binding protein-related protein 5 (ORP5)/Niemann-Pick C1 protein (NPC1) (**Fig. 1.2A**) (*62*). After depletion and docking, passive Ca^{2+} transport can occur from the ER to lysosome down

the large transmembrane gradient present in Ca^{2+} deficient lysosomes. In this model, it is possible for any low-affinity Ca^{2+} channel, exchanger, or transporters to conduct this uptake (*1*). These transporters may interact directly with IP3Rs to receive Ca^{2+} from the ER. However, the molecular players involved in this ER-lysosome transport process have not been identified.

Another possibility is that lysosomes have unidentified Ca^{2+}-ATPases, which could be involved in import of Ca^{2+} from the ER or cytosol (**Fig. 1.4C**). The search for these has focused on pumps that would act similarly to SERCA, the ER Ca^{2+}-ATPase. However, lysosomal Ca^{2+} stores seem to be insensitive to SERCA inhibitors, such as thapsigargin (*63–66*). Thus, any SERCA-like Ca^{2+} pumps that maintain lysosomal stores must be thapsigargin-insensitive. The use of other inhibitors, vanadate and tBHQ, has led some to postulate the presence of a P-type Ca^{2+}-ATPase on acidic Ca^{2+} stores (*67*, *68*). Recently, the Krishnan group used a pH-correctable lysosomal Ca^{2+} probe, *CalipHluor*, and phenotypic assays in worms to identify the P5 ATPase ATP13A2 as facilitating lysosomal Ca^{2+} import in humans (*69*). Mutations in ATP13A2 lead to Kufor-Rakeb syndrome, a severe and early-onset form of Parkinson's disease, which is strongly connected to Ca^{2+} dysregulation (*70–72*). However, the transport function of ATP13A2 is controversial, with other reports suggesting that it transports multiple cations and polyamines, but not Ca^{2+} (*73–75*).

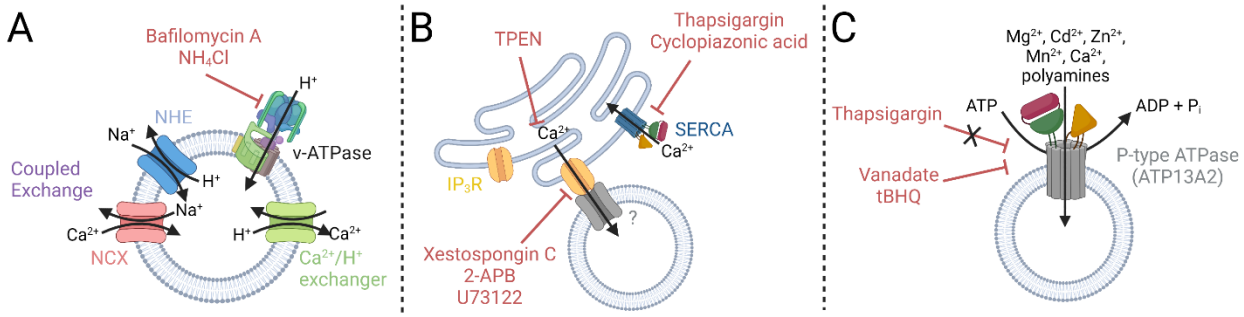

Figure 1.4: Reported mechanisms of lysosomal Ca^{2+} uptake. (A) The Ca^{2+}/H^+ hypothesis: A single protein or multiple proteins facilitate Ca^{2+} influx at the expense of H^+ efflux. Inhibition of the lysosomal v-ATPase blocks Ca^{2+} import by this mechanism. (B) The ER refilling hypothesis: Inositol 1,4,5-trisphosphate receptors (IP_3Rs) on the ER directly fill lysosomal Ca^{2+} via an unknown lysosomal transporter or channel. Inhibition of sarco/endoplasmic reticulum Ca^{2+}-ATPase (SERCA) or IP_3R, or chelating ER Ca^{2+} blocks Ca^{2+} filling by this mechanism. (C) The P-type ATPase hypothesis: A SERCA-like Ca^{2+} pump, such as ATP13A2, imports Ca^{2+} into the lysosome. SERCA inhibitors do not affect this pump, while other ATPase inhibitors do. NH_4Cl: ammonium chloride; NHE: Na^+/H^+ exchanger; NCX: Na^+/Ca^{2+} exchanger; TPEN: *N*,*N*,*N*′,*N*′-tetrakis(2-pyridinylmethyl)-1,2-ethanediamine; 2-APB: 2-Aminoethoxydiphenyl borate;

tBHQ: *tert*-Butylhydroquinone; ATP: adenosine triphosphate; ADP: adenosine diphosphate; P_i: inorganic phosphate.

Thus, the mechanisms by which lysosomes refill and maintain their Ca^{2+} store are far from understood, except in yeast and plants, which is discussed in **Section I.D**. Importantly, the various hypotheses are not mutually exclusive. On one hand, it is likely that individual mammalian lysosomes have multiple mechanisms to maintain their Ca^{2+} store, which play different roles under different physiological triggers. This is borne out at the plasma membrane, where a Ca^{2+}-ATPase and a Na^+/Ca^{2+} exchanger cooperate to perform low-capacity and high-capacity Ca^{2+} transport, respectively (*76*). Similarly, the mitochondrial membrane possesses a mitochondrial Ca^{2+} uniporter (MCU) and a Na^+/Ca^{2+} exchanger (NCLX) to conduct complementary Ca^{2+} transport (*77*). Organellar membranes of lower organisms also possess this pump/exchanger duo, as discussed in **Section I.D**. Hence, it is feasible that mammalian lysosomes harbor these complementary import mechanisms. On the other hand, different lysosome subpopulations, cell types, and tissues all have unique metabolic and catabolic demands, and could regulate lysosomal Ca^{2+} in tailored ways to maintain appropriate levels of autophagic and degradative flux. So, it would not be surprising for lysosomes to display different import mechanisms, depending on the experimental systems and conditions. Indirectly, a unifying trigger for Ca^{2+} refilling in all cases may be membrane potential. Lysosome membrane potential changes activate voltage-dependent K^+ conductance, which may facilitate Ca^{2+} flux, and can influence interactions with other organelles, including the ER (*78*, *79*).

I.D: Ca^{2+}/H^+ exchangers in lysosomes of lower organisms

The pH gradient hypothesis is especially attractive because lower organisms such as fungi and plants possess well-defined Ca^{2+}/H^+ exchange mechanisms on their vacuoles. Vacuoles in yeast and plants are analogous to lysosomes in mammalian cells. Vacuoles harbor two mechanisms for Ca^{2+} uptake: a high affinity Ca^{2+} ATPase that efficiently mediates transport triggered by small changes in cytosolic Ca^{2+}, and low affinity Ca^{2+} exchangers that transports Ca^{2+} at a high capacity in response to large bursts of cytosolic Ca^{2+} (*80*). The Ca^{2+}/H^+ exchangers (CAXs) transport substantial amounts of Ca^{2+} into the vacuolar lumen

with a stoichiometry of $1Ca^{2+}$ to 2 or $3H^{+}$, and have 11 transmembrane domains separated into two half-proteins by an acidic motif (*81*, *82*). CAXs are the major pathway for Ca^{2+} loading into the vacuole in plants and yeast, as indicated by their low affinity and high capacity (**Table 1.2**) (*83–87*). Regulatory mechanisms and structural information have now revealed the complexities of vacuolar Ca^{2+} loading in yeast and plants, as discussed in **Section I.E**.

Table 1.2: Affinities and kinetics of vacuolar Ca^{2+} importers in yeast and plants.

Organism	Protein	Protein Function	K_m (µM)	V_{max} (nmol Ca^{2+} min^{-1} mg^{-1})	References
S. cerevisiae	PMC1	Ca^{2+} ATPase	4.3	0.0288	*(80)*
	VCX1	Ca^{2+}/H^{+} exchanger	25	35.5	*(81,82)*
A. thaliana	ACA4	Ca^{2+} ATPase	0.6	0.0052	*(83)*
	CAX1	Ca^{2+}/H^{+} exchanger	15	12.5	*(84)*

CAX genes are one family of the Ca^{2+}/cation antiporter (CaCA) superfamily, which also contains the Na^{+}/Ca^{2+} (NCX) exchanger family, the $Na^{+}/Ca^{2+}/K^{+}$ (NCKX) exchanger family, the Ca^{2+}/cation (CCX) family, and the YRBG family (named after the bacterial gene *yrbG*) (*88*). CAX genes are present in the genomes of other plants, fungi, and protists. Putative CAX genes across the animal kingdom have also been identified, based on the plant and yeast CAX genes (**Table 1.3**). This includes mollusks, sea urchins, pufferfish, lizards, junglefowl, and even mammals such as the platypus and Tasmanian devil (*18*). These animal CAXs localize to acidic organelles and have unique physiological roles *in vivo.* For example, CAXs may regulate cell migration in frogs (*18*). In zebrafish, CAXs are expressed in neural crest cells and are involved in neural crest development (*89*). However, CAX genes are notably absent from the genomes of nematodes, fruit flies, mice, and humans (*90*).

Table 1.3: List of CAX family genes in diverse prokaryotes and eukaryotes.

Organism	Common Name	Protein	Ref	Organism (cont.)	Common Name	Protein	Ref
Saccharomyces cerevisiae	Brewer's yeast	VCX1	*(82)*	*Danio rerio*	Zebra fish	DrCAX1	*(88)*
Saccharomyces cerevisiae	Brewer's yeast	VNX1	*(79)*	*Xenopus laevis*	African clawed frog	XlaCAX	*(18)*

Table 1.3 (continued)

Escherichia coli	Bacteria	EcchaA	*(87)*	*Capitella teleta*	Annelid worm	CteCAX	*(18)*
Arabidopsis thaliana	Thale cress	CAX1	*(86)*	*Aplysia californica*	California sea hare	AcaCAX	*(18)*
Arabidopsis thaliana	Thale cress	CAX2	*(79)*	*Stronglylo-centrotus purpuratus*	Sea urchin	SpuCAX	*(18)*
Chlamydo-monas reinhardtii	Green algae	CrCAX1	*(79)*	*Branchio-stoma floridae*	Florida lancelet	BflCAX	*(18)*
Oryza sativa	Rice	OsCAX1	*(79)*	*Takifugu rubripes*	Japanese puffer fish	TruCAXa	*(18)*
Oryza sativa	Rice	OsCAX2	*(79)*	*Takifugu rubripes*	Japanese puffer fish	TruCAXb	*(18)*
Aspergillus nidulans	Fungus	VCXA	*(79)*	*Latimeria chalumna*	West Indian Ocean coelacanth	LcaCAX	*(18)*
Schizosaccharo-myces pombe	Fission yeast	SpCAX1	*(79)*	*Xenopus tropicalis*	Western clawed frog	XtrCAX	*(18)*
Cryptococcus neoformans	Fungus	CnVCX1	*(79)*	*Anolis carolinensis*	Green anole	AcarCAX	*(18)*
Toxoplasma gondii	Parasite	TgCAX	*(79)*	*Gallus gallus*	Red junglefowl	GgaCAX	*(18)*
Dictyostelium discoideum	Amoeba	DdCAX	*(79)*	*Ornitho-rhynchus anatinus*	Platypus	OanCAX	*(18)*
				Sarcophilus harrisii	Tasmanian Devil	ShaCAX	*(18)*

I.E: A case study on CAX characterization: the story of VCX1

The best understood CAX mechanism in nature is that of VCX1, which acts in yeast vacuoles. To better appreciate the identification and characterization of a human lysosomal Ca^{2+}/H^{+} exchanger, it is worth discussing how this was done for VCX1. In fact, the trajectory of how VCX1 was characterized is remarkably similar to the uncovering of a human lysosomal Ca^{2+}/H^{+} exchanger (LCAX-1) presented in this thesis (**Fig. 1.5**).

A Ca^{2+} transport mechanism driven by a proton motive force in yeast vacuoles was first described in 1983 (*91*). In isolated vacuoles, radiolabeled $^{45}Ca^{2+}$ uptake was impaired by inhibition of H-ATPase, implying a pH-dependent import mechanism. In addition, the lumenal pH increases when Ca^{2+} is added to the buffer outside the vacuole. It was not until 1996 that VCX1 was finally identified as the molecule responsible for the Ca^{2+}/H^{+} exchange that explains this observation (*85*). It had been previously known that yeast devoid of PMC1 grows poorly in high Ca^{2+} conditions. In such a strain, the Ca^{2+}-dependent phosphatase calcineurin inhibits an independent factor required for Ca^{2+} tolerance, since inactivating calcineurin restored Ca^{2+} tolerance (*83*). Cunningham and Fink identified the calcineurin target as VCX1, by isolating genes that restore growth to yeast devoid of PMC1 in high Ca^{2+} conditions (*85*). Radiolabeled $^{45}Ca^{2+}$ uptake assays then confirmed the impaired vacuolar import of Ca^{2+} in yeast devoid of VCX1. Determination of the concentration of Ca^{2+} that causes a 50 percent decrease in growth in a wide range of genetic backgrounds revealed the complex regulation of PMC1 and VCX1 by cytosolic Ca^{2+} via calmodulin and calcineurin. Elevation of cytosolic Ca^{2+} activates calmodulin, which activates calcineurin. Calcineurin then inactivates VCX1, yet activates PMC1, likely by posttranslational modifications, to tightly control cytosolic Ca^{2+} concentration and prevent over-loading of Ca^{2+} into the vacuole.

Identification of the molecule responsible for pH-dependent vacuolar Ca^{2+} import opened up the door to understanding its physiological function and regulation. It turns out that VCX1 and the vacuolar pH gradient are critical for proper clearance of cytosolic Ca^{2+} after elevation, whereas PMC1 does not seem to play a role (*84*, *92*). This is consistent with the idea of VCX1 as the high-capacity importer responsive to large changes in cytosolic Ca^{2+}, and PMC1 as the fine-tuner. Around the same time, details about the calcineurin regulation mechanism were uncovered by identifying VCX1 mutants that disrupt its inhibition by calcineurin (*93*). These hyperactive variants often transport Mn^{2+} in addition to Ca^{2+}. But the exact mechanism by which calcineurin inhibits VCX1 is still not yet known, and could be indirect, e.g., through inhibition of H-ATPase.

Finally, in 2013, the structure of VCX1 was determined and used to develop a model to describe the mechanism by which it conducts Ca^{2+} current using a pH gradient (*94*). Like other members of the

CAX family, VCX1 has 11 transmembrane helices, with the first helix having a targeting or signaling role. The remaining 10 transmembrane helices perform transport, and are composed of two symmetric halves connected through a negatively charged loop, called the acidic loop or acidic helix. Each symmetric half possesses one conserved GNXXE sequence required for Ca^{2+} binding and transport. The crystal structure shows a central four-helix core kinked at their midpoints to create an hourglass shape. At the central part of the hourglass, the two conserved GNXXE sequences come into close proximity to create a central Ca^{2+} binding site. The acidic loop sits parallel to the membrane and lies underneath this Ca^{2+} binding site on the cytosolic side. Molecular dynamics simulations suggest that this acidic loop maintains a helical formation in presence of two Ca^{2+} ions but becomes more flexible in their absence, indicating a regulatory mechanism that augments conductance in the presence of increased cytosolic Ca^{2+}. A cycle follows where a H^+ gradient drives a conformational change to the cytosol-open conformation, where active site glutamate residues maintain their negative charge and bind Ca^{2+} coordinated by the proximal acidic loop. Coordination of Ca^{2+} displaces water to initiate straightening of the internal hourglass and expose the active site glutamate residues to the vacuole. Exposure to the acidic vacuole lowers the affinity of glutamates for Ca^{2+}, leading to release of Ca^{2+} into the vacuole.

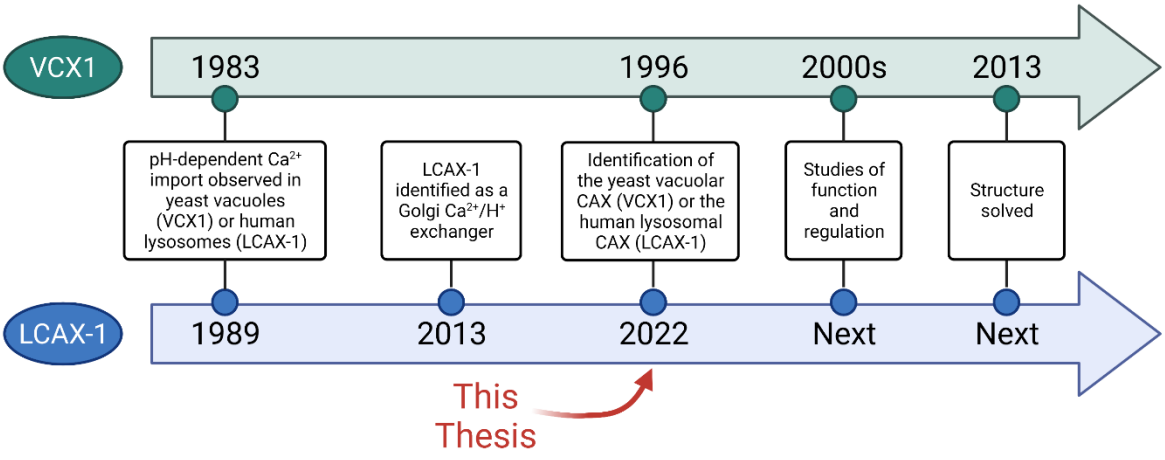

Figure 1.5: Trajectories of the identification and characterization of the proteins responsible for vacuolar Ca^{2+}/H^+ exchange in yeast (top) and lysosomal Ca^{2+}/H^+ exchange in humans (bottom).

I.F: Methods to evaluate lysosomal Ca^{2+} import

A range of techniques have been used to visualize and analyze lysosomal Ca^{2+} dynamics. These tools have been used to understand how lysosomes contribute to cellular Ca^{2+} signals, measure the Ca^{2+} concentration in lysosomes under certain situations, and explain the effect of lysosomal Ca^{2+} on lysosome functions. But only recently have tools been developed that can directly interrogate lysosomal Ca^{2+} by correcting for effects of pH. These pH-correctable tools, combined with electrophysiological techniques, have enabled us to better quantify lysosomal Ca^{2+} levels and fluxes.

I.F.1: Cytosolic Ca^{2+} indicators

The first, and perhaps the simplest, technique is to obtain information from cytosolic Ca^{2+} signals. Cytosolic Ca^{2+} is relatively straightforward to measure because of the availability of fluorescent reporters, such as fura-2 and fluo-4 (*95*, *96*). A suite of these reporters has been developed with variable affinities, spectral characteristics, cell permeabilities, and ratiometric capabilities (**Table 1.4**) (*97*, *98*). In general, all of these chemical indicators consist of a fluorophore moiety and an Ca^{2+}-complexing moiety (such as BAPTA), often joined by a molecular linker. Ca^{2+}-binding modifies the fluorescence based on photoinduced electron transfer (PET) or photoinduced charge transfer (PCT) (*99*). In PET-based sensors, which are the vast majority of Ca^{2+} indicators, an electron-donating group on the Ca^{2+}-complexing moiety is connected to the conjugated aromatic system of the fluorescent dye through a bridge. This donor group quenches fluorescence due to electron transfer, unless Ca^{2+} binding reduces the energy of the donor HOMO to prevent electron transfer (**Fig. 1.6A**). In PCT-based sensors, an electron-donor (or electron-acceptor) is conjugated directly in the aromatic system (without a bridge). Upon excitation, a full charge transfer occurs, making the excited state more polar. Interaction of Ca^{2+} with the donor (or acceptor) alters the energy of both states, but more severely for the excited state. This causes a spectral shift that can be used to quantify Ca^{2+} levels (**Fig. 1.6B**).

Table 1.4: Properties of available small molecule Ca^{2+} indicators.

Indicator	K_d for Ca^{2+} (μM)	Excitation (nm)	Emission (nm)	Quantitation method	References
Rhodamines					

Table 1.4 (continued)

Rhod-1	2.3	556	578	Single wavelength	(*99*)
Rhod-2	0.52	549	581	Single wavelength	(*99*)
Rhod-3	0.38	555	580	Single wavelength	(*99*)
Rhod-4	0.53	530	555	Single wavelength	(*99*)
Rhod-FF	19	552	580	Single wavelength	(*100*, *101*)
Rhod-5N	320	551	576	Single wavelength	(*99*)
Rhod-5F	1.1	560	580	Single wavelength	(*69*)
Extended Rhodamines (X-Rhods)					
X-Rhod-1	0.0007	580	602	Single wavelength	(*102*)
X-Rhod-5F	1.6	581	603	Single wavelength	(*102*)
X-Rhod-FF	17	580	603	Single wavelength	(*103*)
X-Rhod-5N	350	580	602	Single wavelength	(*99*)
Calcium Crimson	0.185	590	615	Single wavelength	(*104*)
CaSiR-1	0.58	647	664	Single wavelength	(*99*)
Calcium Rubies (functionalized X-Rhods)					
CaRuby-Me	3.4	586	604	Single wavelength	(*99*)
CaRuby-F-N3	6.2	586	604	Single wavelength	(*99*)
CaRuby-Cl-N	21.6	586	604	Single wavelength	(*99*)
CaRuby-Nano	0.2	586	604	Single wavelength	(*99*)
Calcium Orange	0.185	549	576	Single wavelength	(*99*)
Fura dyes					
Fura-2	0.145	363/335	512	Ratiometric excitation	(*95*)
Fura-4F	0.00077	336/366	511	Ratiometric excitation	(*105*)
Fura-5F	0.0004	336/363	512	Ratiometric excitation	(*106*)
Fura-2-ff	35	335/360	505	Ratiometric excitation	(*107*, *108*)
Fura-FF	5.5	335/364	510	Ratiometric excitation	(*105*)
Fura-6F	5.3	336/364	512	Ratiometric excitation	(*105*)
Fura Red	0.14	458/488	597	Ratiometric excitation	(*99*)
Mag-Fura-2	25	329/369	511	Ratiometric excitation	(*109*)
Mag-Fura-5	28	369	505	Single wavelength	(*110*)
Mag-Fura-Red	17	488	630	Single wavelength	(*111*)
Fluo dyes					
Fluo-3	0.325	506	526	Single wavelength	(*112*)

Table 1.4 (continued)

Fluo-4	0.345	494	516	Single wavelength	(*96*)
Fluo 4FF	9.7	491	516	Single wavelength	(*103*)
Fluo 5F	2.3	491	518	Single wavelength	(*103*)
Fluo-5N	90	491	516	Single wavelength	(*113*)
Mag-Fluo-4	22	490	517	Single wavelength	(*114*)
Calcium Green-1	0.19	490	531	Single wavelength	(*104*)
Oregon Green BAPTA conjugates					
Oregon Green BAPTA-1	0.17	488	520	Single wavelength	(*115*)
Oregon Green BAPTA-5N	20	494	521	Single wavelength	(*116*)
Oregon Green BAPTA-6F	3	494	524	Single wavelength	(*117*)
Indo dyes					
Indo-1	0.23	488	405/485	Ratiometric emission	(*95*)
Mag-Indo-1	35	349	480/390	Ratiometric emission	(*118*)

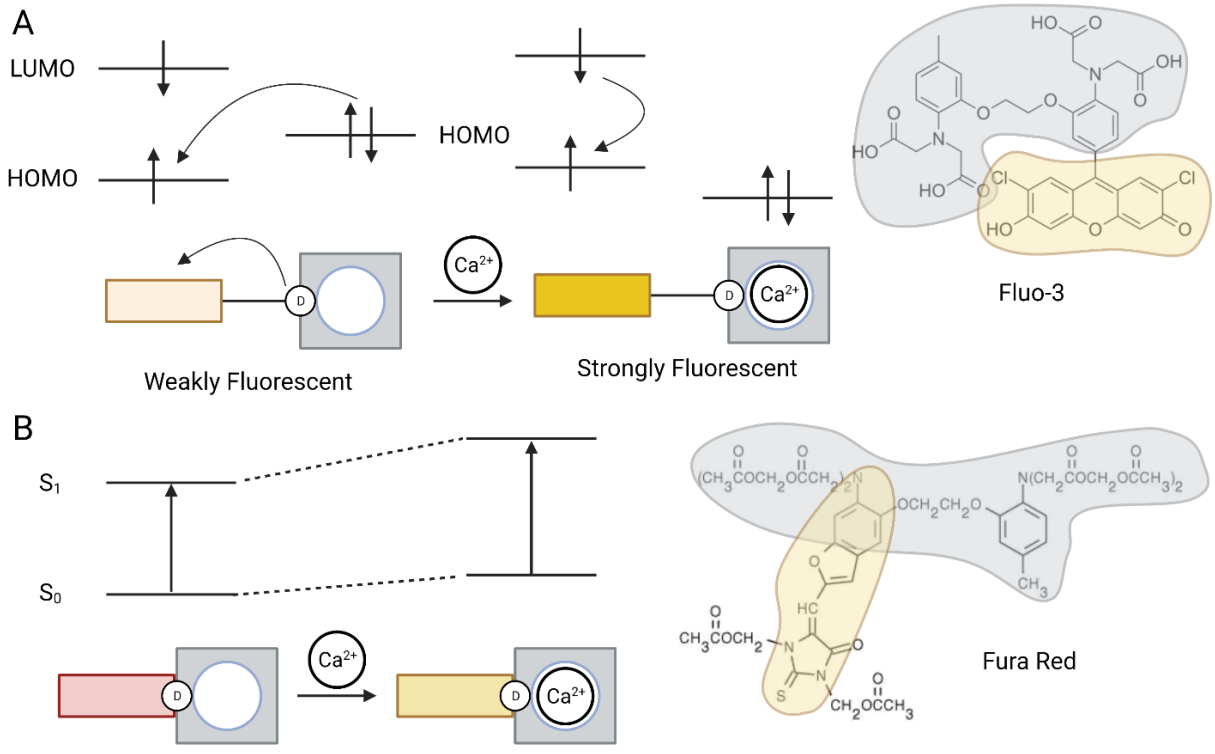

Figure 1.6: Mechanisms of Ca^{2+} sensing by small molecule indicators. (A) PET-based sensors, such as Fluo-3, have an electron-donating group on the Ca^{2+}-complexing moiety (BAPTA in the case of Fluo-3) connected to the fluorescent dye through a bridge. This donor group quenches fluorescence, unless Ca^{2+}

binding reduces the energy of the donor HOMO to prevent electron transfer. (B) PCT-based sensors, such as Fura Red, have an electron-donor conjugated directly in the aromatic system without a bridge. Interaction of Ca^{2+} with the donor alters the energy more severely for the excited state.

These PET and PCT probes have made it simple to quantify cytosolic Ca^{2+} or record its dynamics, as the neutral and constant cytosolic pH does not interfere with measurements. However, interpreting these results can be complex, because multiple Ca^{2+} sources contribute to signals and make it difficult to isolate any individual factor. However, this technique has still been used to understand the contribution of lysosomal Ca^{2+} stores to overall Ca^{2+} signaling. One strategy is to empty a given Ca^{2+} store pharmacologically and use the cytosolic Ca^{2+} spike as a proxy for the size of the Ca^{2+} store or evaluate the contribution of a given store or release channel. For example, thapsigargin and ATP are often used to empty the ER store. On the other hand, NAADP or ML-SA-1 are often used to empty the lysosomal store (**Table 1.5**). The converse strategy is to use the recovery of the cytosolic Ca^{2+} spike to evaluate the contribution of a given Ca^{2+} reuptake mechanism. Such techniques have been used to show the importance of lysosomal Ca^{2+} uptake and exchange with the ER for global Ca^{2+} signaling (*20*, *58*, *119*). However, these methods do suffer from caveats, such as the likelihood that triggering one Ca^{2+} store may indirectly affect another one.

Table 1.5: Agents that target endolysosomal Ca^{2+} stores. GPN: glycyl-L-phenylalanine 2-napthylamide; BafA: bafilomycin A1; ConA: concanamycin A; NAADP: nicotinic acid adenine dinucleotide phosphate; ML-SA1: mucolipin synthetic agonist 1.

Agent	Mechanism	Advantages	Disadvantages	Reference
GPN	Cleavage by Cathepsin C in the lysosome, resulting in swelling and permeabilization that releases Ca^{2+} (and other small solutes)	• Directly and selective releases lysosomal Ca^{2+} • Rapid and reversible	• Crude approach to breach lysosomal membrane	(*120*, *121*)
BafA/ ConA	Inhibition of lysosome acidification by v-ATPase to collapse pH gradient and inhibit Ca^{2+} uptake	• Potent and highly selective for endolysosomes	• Indirect effect on Ca^{2+} • May be slow depending on cell type	(*122*, *123*)
Nigericin/ Monensin	Ionophores that translocate H^+ across membranes to collapse pH gradient and inhibit Ca^{2+} uptake	• Rapid and robust effect on pH and Ca^{2+}	• Indirect effect on Ca^{2+} • Not selective for endolysosomes	(*124*)

Table 1.5 (continued)

NAADP	Activator of TPC Ca^{2+} release channels	•	Highly selective for endolysosomes	•	Sluggish because of delay in membrane permeability	(*59*)
ML-SA1	Activator of TRPML1 Ca^{2+} release channels	•	Highly selective for endolysosomes	•	Sensitivity of TRPML1 to lysosomal pH	(*125*)

I.F.2: Perilysosomal genetically encoded Ca^{2+} indicators

One way to improve this technique is monitor local cytosolic Ca^{2+} around the lysosome, instead of global cytosolic Ca^{2+}. This still avoids the problems of measuring lumenal Ca^{2+}. It also has the added advantage of recording Ca^{2+} signals that may be specific to lysosomes and not detectable in global cytosolic signals. To record such signals, genetically encoded Ca^{2+} indicators (GECIs) can be tethered to the cytosolic face of lysosomes as fusion proteins with membrane proteins. GECIs employing fluorescence and chemiluminescence resonance energy transfer (FRET and CRET) mechanisms have been engineered (**Table 1.6**) (*126–128*). However, the most common types of GECIs are those where a Ca^{2+}-dependent conformational change of GFP leads to fluorescence changes. These GFP-based Ca^{2+} probes are named GCaMP and consist of a fusion of calmodulin (CaM) binding peptide M13, circularly permuted GFP, and CaM (*129*). When Ca^{2+} binds to CaM, conformational changes due to the CaM-M13 interaction induce a conformational change in GFP to change its fluorescence intensity. Improved versions of GCaMP have been engineered to optimize brightness, pH sensitivity, affinity, and Ca^{2+} specificity (**Fig. 1.7A**) (*130–135*). A GCaMP-TRPML1 fusion was used to understand lysosomal Ca^{2+} refilling mechanisms (*1*, *125*). The probe showed a robust spike following an initial ML-SA treatment, a proxy for lysosomal store depletion. Upon second application, the size of the perilysosomal GCaMP spike depends on how much lysosomal Ca^{2+} was refilled between applications. This technique has been used to show that multiple factors are important for Ca^{2+} refilling, such as the ER and the lysosomal K^+ gradient (*61*, *78*). However, this method has some potential limitations. First, GECIs usually have higher affinities (sub-micromolar range), which may not be ideal for monitoring higher perilysosomal Ca^{2+}. Second, these reporters are still pH-sensitive, and we do not know whether pH fluctuates in the perilysosomal area.

Finally, measurements with these probes are still indirect, even though they are more specific than global cytosolic recordings.

Table 1.6: Properties of commonly used genetically-encoded Ca^{2+} indicators (GECIs). GECO: genetically encoded calcium indicator for calcium imaging; YC: yellow cameleon; EGFP: enhanced green fluorescent profiles; EYFP: enhanced yellow fluorescent protein; OFP: orange fluorescent protein.

Indicator	K_d for Ca^{2+} (µM)	Excitation (nm)	Emission (nm)	Fluorophore(s)	Reference
Single fluorophore					
GCaMP1.3	0.24	480	510	EGFP	(*136*, *137*)
GCaMP1.6	0.15	480	510	EGFP	(*136*, *137*)
GCaMP2	0.15	480	511	EGFP	(*136*, *137*)
GCaMP3	0.33	480	513	EGFP	(*136*, *137*)
GCaMP5A	0.31	480	510	EGFP	(*136*, *137*)
GCaMP6f	0.38	480	510	EGFP	(*136*, *137*)
G-GECO1	0.75	480	512	EGFP	(*137*, *138*)
B-GECO1	0.16	380	446	EGFP Y66H	(*137*, *138*)
R-GECO1	0.48	561	600/589	mApple	(*137*, *138*)
GEX-GECO1	0.32	400/488	512/506	EGFP	(*137*, *138*)
Flash-Pericam	0.7	400	514	EYFP	(*136*, *137*, *139*)
Inverse-Pericam	0.2	500	515/517	EYFP	(*136*, *137*, *139*)
Ratiometric-Pericam	1.7	415/494	511/517	EYFP	(*136*, *137*, *139*)
Camgaroo-1	7.0	480	513	EYFP	(*136*, *137*, *140*)
Camgaroo-2	5.3	480	535	Citrine	(*136*, *137*, *140*)
R-CaMP1.7	0.15	562	584	mRuby	(*99*, *141*)
Two fluorophores					
YC2.1	0.1/4.3	430	476/528	ECFP/YFP	(*136*, *137*, *142*)
YC2.6	0.09/0.95	430	480/530	ECFP/EYFP	(*136*, *137*, *142*)
YC3.1	1.5	430	476/528	ECFP/YFP	(*136*, *137*, *142*)
YC4.6	0.06/14.4	430	480/530	ECFP/YFP	(*136*, *137*, *142*)

Table 1.6 (continued)

YC-Nano140	0.14	430	480/530	ECFP/Venus	(*137*, *143*)
YC-Nano15	0.015	430	480/530	ECFP/Venus	(*137*, *143*)
D4cpV	64	420	480/535	ECFP/Venus	(*136*, *137*, *144*)
TN-L15	1.2	432	480/535	ECFP/Citrine	(*136*, *137*, *145*)
D1GO-Cam	1.53	477	510/560	OFP/EGFP	(*137*, *146*)

I.F.3: Lumenal Ca^{2+} reporters

Thus, the ideal method to directly assess lysosomal Ca^{2+} levels is to use reporters within the organelle itself. Unfortunately, such measurements are complicated several factors. First, the majority of lumenal Ca^{2+} is buffered and bound, such that most methods only measure the portion of Ca^{2+} that is free. However, this issue is not usually addressed, as the free Ca^{2+} is in equilibrium with the bound Ca^{2+}, such that a fall in the total store would lead to a parallel fall in the free Ca^{2+}. Second, the reporter must be passively trapped in or actively targeted to the lysosomal lumen. Third, the probe must have an affinity suitable for the high concentration of Ca^{2+} in lysosomes. This is especially difficult in such a highly acidic environment, which may reduce the affinity of the Ca^{2+}-binding motif significantly. Finally, the probe should have normalizing factors to eliminate artifacts due to uptake as well as pH changes. This last factor is especially critical because lumenal pH dynamically fluctuates in parallel with Ca^{2+} release, such that it is nearly impossible to alter one without altering the other.

Reporters that satisfy all of these criteria are rare, and have not been developed until recently. One example of this is the use of two dextran conjugates to simultaneously measure lysosomal pH and Ca^{2+}. For example, Fura Dextran (furaDx) and Oregon Green Dextran (OGDx) have been used to show pH-dependent mechanisms of lysosomal Ca^{2+} import (**Fig. 1.7B**) (*53*, *60*). However, differential uptake of the separate dextran conjugates and lack of control over stoichiometry makes this method difficult to provide single-lysosome resolution. To improve upon this, the Krishnan lab developed a pH-correctable, DNA-based reporter for lysosomal calcium (*69*). This probe, called *CalipHluor*, consists of a DNA duplex scaffold whose negative backbone enables scavenger receptor-mediated endocytic uptake of the

sensor into endolysosomes. On the DNA duplex, the sensor contains a pH-sensitive module, a Ca^{2+}-sensitive fluorophore with appropriate affinity, and an internal ion-independent reference dye in 1:1:1 stoichiometry (**Fig. 1.7C**). This probe was used to accurately measure Ca^{2+} levels in distinct endolysosomal, identify the P-type ATPase ATP13A2 as a facilitator of lysosomal Ca^{2+} accumulation, and visualize Ca^{2+} gradients in tubular lysosomes (*69*, *147*).

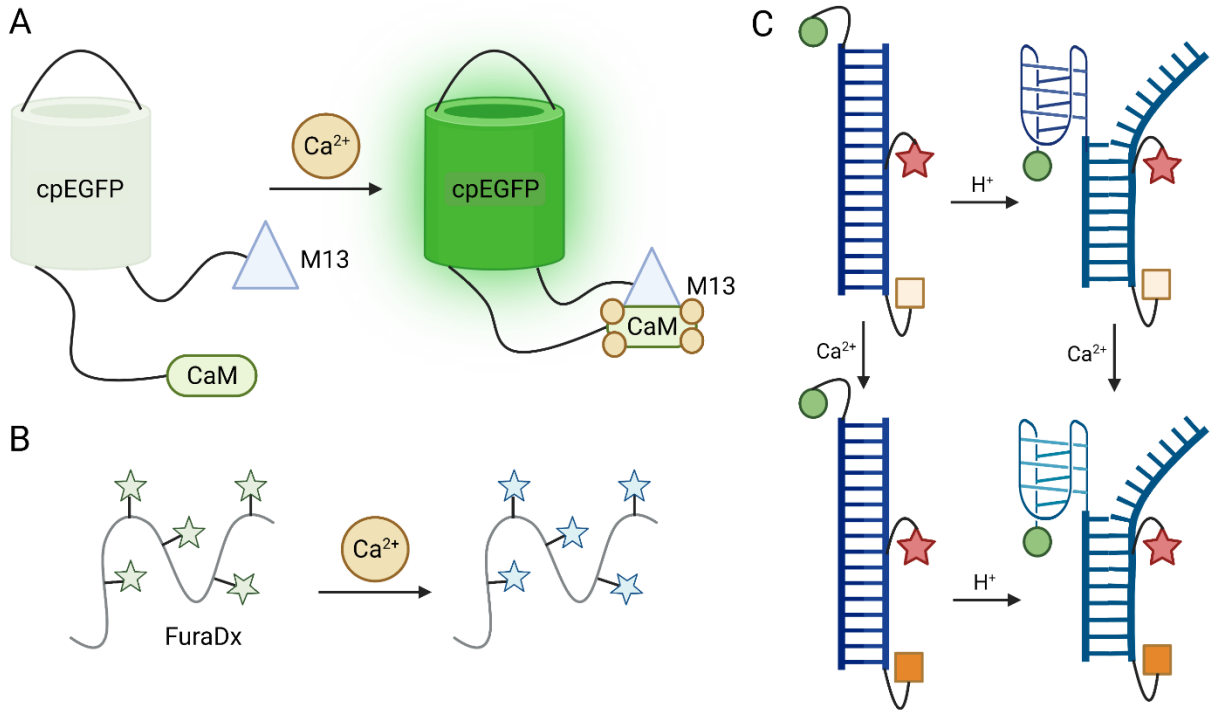

Figure 1.7: Mechanism of Ca^{2+} sensing by common Ca^{2+} indicators. (A) GCaMP family indicators contain a circularly permutated EGFP (cpEGFP), calmodulin (CaM), and a peptide from myosin light-chain kinase (M13). Upon Ca^{2+} binding, the CaM domain undergoes a conformational change that causes it to bind to the M13 domain. This prevents water from accessing the chromophore, leading to deprotonation and EGFP fluorescence. (B) Fura dextran (FuraDx) is a conjugate of the ratiometric Ca^{2+} indicator fura-2 (stars) and water-soluble dextran, which facilitates cellular loading by endocytosis. (C) *CalipHluor* is a DNA-based probe that reports Ca^{2+} using a pH correction. pH-induced FRET between Alexa488 (green circle) and Alexa647 (red star) reports on pH ratiometrically. A Ca^{2+} sensitive reporter (Rhod-5F, orange square), reports Ca^{2+} ratiometrically when normalized by Alexa647 fluorescence.

I.F.4: Electrophysiological techniques

Alternatively, non-fluorescent techniques can also provide information about lysosomal Ca^{2+} dynamics. The most pertinent one for this study is lysosomal electrophysiology. Biological membranes control the osmolarity of fluids on either side, producing large differences in the concentration gradients of specific ions, especially Na^+, K^+, Cl^- and Ca^{2+} (*148*). They essentially serve as capacitors that store and

separate charge between two conductive solutions. The equilibrium potential of each ion results in an electrical potential across the membrane that can be measured as voltage (*149*). Charged particles traverse the membrane through ion channels and transporters, and their movement is measured as current. As such, the electrical potential and current flow can be measured by a variety of electrophysiological methods.

Standard methods to analyze plasma membrane ion channels, such as the patch-clamp technique, can directly measure the current passing through the cell membrane at a fixed voltage (voltage clamp) (*150*). In this electrophysiological technique, a glass electrode (micropipette) is used to make a tight seal on the surface of the cell (*150*). Different patch-clamp configurations can study all ion channels in the cell membrane (whole-cell mode), or individual ion channels in intact cell membrane (cell-attached mode) or excised membrane patches (outside-out and inside-out modes) (*148*). All of these experiments start with the patch pipette forming a high-resistance (gigaohm) seal with the membrane, after which pressure can be applied to break in to the cell and obtain whole-cell recordings. Following break in, a voltage clamp program (such as steps or a ramp) can be applied to study the current through the cell membrane. In this technique, current is injected that is opposite and equal to the current flowing through the ion channels, and the amount of current required to keep the membrane potential at the desired value gives a direct measure of the current flowing across the membrane (*148*). Importantly, the buffer solution in the pipette becomes interchangeable with the solution inside the membrane upon break-in, giving us control over internal ionic conditions. Similarly, the availability of the bath solution gives us control over the external ionic conditions.

These methods are not readily applicable to intracellular ion channels because of the inability to access intracellular membranes with patch pipettes. In addition, the small size of endosomes and lysosomes prevents the use of standard patch-clamp electrodes. To solve this issue, endolysosomal ion channels have been expressed or reconstituted in artificial membranes or lipid bilayers. These techniques have been used to identify molecules responsible for NAADP-sensitive endolysosomal Ca^{2+} release (*49*, *151–153*). The drawback of these methods is that the ion channel is studied outside of its physiological

environment, risking the loss of important modulatory factors. To overcome these challenges, a newer method uses conventional patch-clamping on pharmacologically enlarged and isolated endolysosomal vesicles (*154*). Late endosomes and lysosomes can be enlarged with the PIKfyve inhibitor PM201636 or vacuolin-1, or by transient transfection with mutated Rab5 marker proteins (*154–156*). Then, a glass electrode is used to dissect the cell and release an enlarged lysosome. Finally, the dissection electrode is exchanged for a recording electrode to measure current, as in conventional patch-clamp methods. This method allows for direct measurements of endolysosomal ion channels in their quasi-native environment with robust control over the same ionic and electric parameters as in conventional patch-clamp (*154*). However, endolysosome enlargement may change the lipid environment, especially since the mechanism by which vacuolin-1 enlarges endolysosomes is not fully understood. Further, the method is technically challenging; it requires additional steps to excise the cell, extrude the lysosome, and exchange the pipette. However, these methods have been used to show the current profiles of various endolysosomal ion channels, and to explore physiological regulators of their activity (*78*, *79*, *157–163*).

The subcellular expression of the protein discussed in this thesis (LCAX-1) allows us to study it on both the plasma membrane with conventional techniques and the lysosome membrane using swollen endolysosome excision. This offers us the opportunity to study it in its more native context (the lysosome membrane) as well as to use the simpler cell surface techniques to characterize it in more detail. Thus, we use a combination of these techniques to characterize the current conducted by LCAX-1.

I.G: Thesis outline

Thus, over the course of 30 years, the yeast pH-dependent vacuolar Ca^{2+} import mechanism has become remarkably well-characterized. And it has opened up our structural and functional understanding of the broader CAX family and CaCA superfamilies. Here, I identify the functional human equivalent of VCX1, although it appears to be sequentially and structurally distinct. We know that in various systems, human lysosomes have a pH-dependent Ca^{2+} import mechanism, as discussed in **Section I.C**. But the lack of a CAX gene in humans has prevented us from characterizing the role of this import mechanism. Thus, we must look outside the CaCA family to find the molecule(s) responsible in order to fully describe the

critical role of lysosomes in shaping cytosolic Ca^{2+} dynamics. In this thesis, I describe the identification of TMEM165, a member of the UPF0016 family and a Golgi cation exchanger, as responsible for the elusive human lysosomal Ca^{2+}/H^{+} exchange. As such, we hereby call TMEM165, lysosomal Ca^{2+}/H^{+} exchanger 1 (LCAX-1).

Chapter 2 outlines the experiments done to identify the worm homolog of LCAX-1 as a facilitator of lysosomal Ca^{2+} import. It explores the phenotypes that result from impaired lysosomal Ca^{2+} homeostasis. This chapter also discusses the literature basis for hypothesizing that LCAX-1 imports lysosomal Ca^{2+} via H^{+} exchange.

Chapter 3 describes the validation of human LCAX-1 as a lysosomal Ca^{2+} importer in multiple systems. This chapter first focuses on experiments that show lysosomal localization of LCAX-1. It then explores experiments using LCAX-1 mutants that regulate its subcellular localization and thereby affect its Ca^{2+} import role at the lysosome. Finally, this chapter uses a fluorescent probe for calcium and electrophysiological characterization to show its direct conductance of Ca^{2+}.

Chapter 4 explores the H^{+} conductance and pH dependence of LCAX-1. It first presents data showing that Ca^{2+} import by LCAX-1 is associated with lysosome deacidification. This chapter then discusses that the converse is also true, that lysosome deacidification is critical for Ca^{2+} import by LCAX-1. Finally, it explores electrophysiological data to directly show the dependence of LCAX-1 current on lysosomal pH.

Chapter 5 outlines the identification of putative Ca^{2+} binding sites in LCAX-1. It first presents bioinformatic studies to identify cation binding regions, based on homology to the yeast exchanger VCX1. It then validates that mutations in these regions impair the ability of LCAX-1 to transport Ca^{2+}, using experiments in yeast, worms, and mammalian cells.

Chapter 6 concludes this thesis with discussions related to the outstanding questions concerning LCAX-1. Specifically, it explores how LCAX-1 fits in to the expanding discussion of lysosomal Ca^{2+} import. It also poses questions about the structure, stoichiometry, and expression of LCAX-1. Finally, it

presents a case for continuing to study LCAX-1, because of its fundamental biological interest and its potential disease relevance.

1.H: References

1. J. Yang, Z. Zhao, M. Gu, X. Feng, H. Xu, Release and uptake mechanisms of vesicular Ca2+ stores. *Protein Cell*. **10**, 8–19 (2019).

2. A. Ballabio, J. S. Bonifacino, Lysosomes as dynamic regulators of cell and organismal homeostasis. *Nat. Rev. Mol. Cell Biol.* **21**, 101–118 (2020).

3. Q. Cao, X. Z. Zhong, Y. Zou, R. Murrell-Lagnado, M. X. Zhu, X.-P. Dong, Calcium release through P2X4 activates calmodulin to promote endolysosomal membrane fusion. *J. Cell Biol.* **209**, 879–894 (2015).

4. X. Li, N. Rydzewski, A. Hider, X. Zhang, J. Yang, W. Wang, Q. Gao, X. Cheng, H. Xu, A molecular mechanism to regulate lysosome motility for lysosome positioning and tubulation. *Nat. Cell Biol.* **18**, 404–417 (2016).

5. A. Scotto Rosato, S. Montefusco, C. Soldati, S. Di Paola, A. Capuozzo, J. Monfregola, E. Polishchuk, A. Amabile, C. Grimm, A. Lombardo, M. A. De Matteis, A. Ballabio, D. L. Medina, TRPML1 links lysosomal calcium to autophagosome biogenesis through the activation of the CaMKKβ/VPS34 pathway. *Nat. Commun.* **10**, 5630 (2019).

6. T. Sun, X. Wang, Q. Lu, H. Ren, H. Zhang, CUP-5, the C. elegans ortholog of the mammalian lysosomal channel protein MLN1/TRPML1, is required for proteolytic degradation in autolysosomes. *Autophagy*. **7**, 1308–1315 (2011).

7. Y. Lai, X. Lou, C. Wang, T. Xia, J. Tong, Synaptotagmin 1 and Ca2+ drive trans SNARE zippering. *Sci. Rep.* **4**, 4575 (2014).

8. A. Reddy, E. V. Caler, N. W. Andrews, Plasma membrane repair is mediated by Ca(2+)-regulated exocytosis of lysosomes. *Cell*. **106**, 157–169 (2001).

9. C. Czibener, N. M. Sherer, S. M. Becker, M. Pypaert, E. Hui, E. R. Chapman, W. Mothes, N. W. Andrews, Ca2+ and synaptotagmin VII-dependent delivery of lysosomal membrane to nascent phagosomes. *J. Cell Biol.* **174**, 997–1007 (2006).

10. B. Lelouvier, R. Puertollano, Mucolipin-3 regulates luminal calcium, acidification, and membrane fusion in the endosomal pathway. *J. Biol. Chem.* **286**, 9826–9832 (2011).

11. H. Xu, D. Ren, Lysosomal physiology. *Annu. Rev. Physiol.* **77**, 57–80 (2015).

12. B. S. Kilpatrick, E. R. Eden, A. H. Schapira, C. E. Futter, S. Patel, Direct mobilisation of lysosomal Ca2+ triggers complex Ca2+ signals. *J. Cell Sci.* **126**, 60–66 (2013).

13. C. J. Penny, B. S. Kilpatrick, J. M. Han, J. Sneyd, S. Patel, A computational model of lysosome-ER Ca2+ microdomains. *J. Cell Sci.* **127**, 2934–2943 (2014).

14. C. J. Penny, B. S. Kilpatrick, E. R. Eden, S. Patel, Coupling acidic organelles with the ER through Ca^{2+} microdomains at membrane contact sites. *Cell Calcium*. **58**, 387–396 (2015).

15. D. L. Medina, S. Di Paola, I. Peluso, A. Armani, D. De Stefani, R. Venditti, S. Montefusco, A. Scotto-Rosato, C. Prezioso, A. Forrester, C. Settembre, W. Wang, Q. Gao, H. Xu, M. Sandri, R. Rizzuto, M. A. De Matteis, A. Ballabio, Lysosomal calcium signalling regulates autophagy through calcineurin and TFEB. *Nat. Cell Biol.* **17**, 288–299 (2015).

16. M. Sardiello, M. Palmieri, A. di Ronza, D. L. Medina, M. Valenza, V. A. Gennarino, C. Di Malta, F. Donaudy, V. Embrione, R. S. Polishchuk, S. Banfi, G. Parenti, E. Cattaneo, A. Ballabio, A gene network regulating lysosomal biogenesis and function. *Science*. **325**, 473–477 (2009).

17. D. L. Medina, A. Fraldi, V. Bouche, F. Annunziata, G. Mansueto, C. Spampanato, C. Puri, A. Pignata, J. A. Martina, M. Sardiello, M. Palmieri, R. Polishchuk, R. Puertollano, A. Ballabio, Transcriptional activation of lysosomal exocytosis promotes cellular clearance. *Dev. Cell*. **21**, 421–430 (2011).

18. M. Melchionda, J. K. Pittman, R. Mayor, S. Patel, Ca2+/H+ exchange by acidic organelles regulates cell migration in vivo. *J. Cell Biol.* **212**, 803–813 (2016).

19. C. I. López-Sanjurjo, S. C. Tovey, D. L. Prole, C. W. Taylor, Lysosomes shape Ins(1,4,5)P3-evoked Ca2+ signals by selectively sequestering Ca2+ released from the endoplasmic reticulum. *J. Cell Sci.* **126**, 289–300 (2013).

20. S. Jung, Y. Chung, Y. Lee, Y. Lee, J. W. Cho, E.-J. Shin, H.-C. Kim, Y. J. Oh, Buffering of cytosolic calcium plays a neuroprotective role by preserving the autophagy-lysosome pathway during MPP+-induced neuronal death. *Cell Death Discov.* **5**, 130 (2019).

21. K. Kiselyov, S. Yamaguchi, C. W. Lyons, S. Muallem, Aberrant Ca2+ handling in lysosomal storage disorders. *Cell Calcium*. **47**, 103–111 (2010).

22. E. Lloyd-Evans, A. J. Morgan, X. He, D. A. Smith, E. Elliot-Smith, D. J. Sillence, G. C. Churchill, E. H. Schuchman, A. Galione, F. M. Platt, Niemann-Pick disease type C1 is a sphingosine storage disease that causes deregulation of lysosomal calcium. *Nat. Med.* **14**, 1247–1255 (2008).

23. K. Coen, R. S. Flannagan, S. Baron, L. R. Carraro-Lacroix, D. Wang, W. Vermeire, C. Michiels, S. Munck, V. Baert, S. Sugita, F. Wuytack, P. R. Hiesinger, S. Grinstein, W. Annaert, Lysosomal calcium homeostasis defects, not proton pump defects, cause endo-lysosomal dysfunction in PSEN-deficient cells. *J. Cell Biol.* **198**, 23–35 (2012).

24. J.-H. Lee, W. H. Yu, A. Kumar, S. Lee, P. S. Mohan, C. M. Peterhoff, D. M. Wolfe, M. Martinez-Vicente, A. C. Massey, G. Sovak, Y. Uchiyama, D. Westaway, A. M. Cuervo, R. A. Nixon, Lysosomal proteolysis and autophagy require presenilin 1 and are disrupted by Alzheimer-related PS1 mutations. *Cell*. **141**, 1146–1158 (2010).

25. L. N. Hockey, B. S. Kilpatrick, E. R. Eden, Y. Lin-Moshier, G. C. Brailoiu, E. Brailoiu, C. E. Futter, A. H. Schapira, J. S. Marchant, S. Patel, Dysregulation of lysosomal morphology by pathogenic LRRK2 is corrected by TPC2 inhibition. *J. Cell Sci.* **128**, 232–238 (2015).

26. B. S. Kilpatrick, J. Magalhaes, M. S. Beavan, A. McNeill, M. E. Gegg, M. W. J. Cleeter, D. Bloor-Young, G. C. Churchill, M. R. Duchen, A. H. Schapira, S. Patel, Endoplasmic reticulum and lysosomal Ca^{2+} stores are remodelled in GBA1-linked Parkinson disease patient fibroblasts. *Cell Calcium*. **59**, 12–20 (2016).

27. S. Rajakulendran, D. Kaski, M. G. Hanna, Neuronal P/Q-type calcium channel dysfunction in inherited disorders of the CNS. *Nat. Rev. Neurol.* **8**, 86–96 (2012).

28. X. Feng, J. Yang, Lysosomal calcium in neurodegeneration. *Messenger (Los Angel)*. **5**, 56–66 (2016).

29. F. Darios, G. Stevanin, Impairment of lysosome function and autophagy in rare neurodegenerative diseases. *J. Mol. Biol.* **432**, 2714–2734 (2020).

30. A. Kondratskyi, M. Yassine, K. Kondratska, R. Skryma, C. Slomianny, N. Prevarskaya, Calcium-permeable ion channels in control of autophagy and cancer. *Front. Physiol.* **4**, 272 (2013).

31. Y. Wu, P. Huang, X.-P. Dong, Lysosomal calcium channels in autophagy and cancer. *Cancers (Basel)*. **13** (2021), doi:10.3390/cancers13061299.

32. M. Sun, E. Goldin, S. Stahl, J. L. Falardeau, J. C. Kennedy, J. S. Acierno, C. Bove, C. R. Kaneski, J. Nagle, M. C. Bromley, M. Colman, R. Schiffmann, S. A. Slaugenhaupt, Mucolipidosis type IV is caused by mutations in a gene encoding a novel transient receptor potential channel. *Hum. Mol. Genet.* **9**, 2471–2478 (2000).

33. A. Miller, J. Schafer, C. Upchurch, E. Spooner, J. Huynh, S. Hernandez, B. McLaughlin, L. Oden, H. Fares, Mucolipidosis type IV protein TRPML1-dependent lysosome formation. *Traffic*. **16**, 284–297 (2015).

34. X. Zhang, X. Cheng, L. Yu, J. Yang, R. Calvo, S. Patnaik, X. Hu, Q. Gao, M. Yang, M. Lawas, M. Delling, J. Marugan, M. Ferrer, H. Xu, MCOLN1 is a ROS sensor in lysosomes that regulates autophagy. *Nat. Commun.* **7**, 12109 (2016).

35. W. Wang, Q. Gao, M. Yang, X. Zhang, L. Yu, M. Lawas, X. Li, M. Bryant-Genevier, N. T. Southall, J. Marugan, M. Ferrer, H. Xu, Up-regulation of lysosomal TRPML1 channels is essential for lysosomal adaptation to nutrient starvation. *Proc Natl Acad Sci USA*. **112**, E1373-81 (2015).

36. X. Dong, D. Shen, X. Wang, T. Dawson, X. Li, Q. Zhang, X. Cheng, Y. Zhang, L. S. Weisman, M. Delling, H. Xu, PI(3,5)P(2) controls membrane trafficking by direct activation of mucolipin Ca(2+) release channels in the endolysosome. *Nat. Commun.* **1**, 38 (2010).

37. M. S. Kim, S. Muallem, S. H. Kim, K. B. Kwon, M. S. Kim, Exosomal release through TRPML1-mediated lysosomal exocytosis is required for adipogenesis. *Biochem. Biophys. Res. Commun.* **510**, 409–415 (2019).

38. T. Tsunemi, T. Perez-Rosello, Y. Ishiguro, A. Yoroisaka, S. Jeon, K. Hamada, M. Rammonhan, Y. C. Wong, Z. Xie, W. Akamatsu, J. R. Mazzulli, D. J. Surmeier, N. Hattori, D. Krainc, Increased Lysosomal Exocytosis Induced by Lysosomal Ca2+ Channel Agonists Protects Human Dopaminergic Neurons from α-Synuclein Toxicity. *J. Neurosci.* **39**, 5760–5772 (2019).

39. Q. Cao, Y. Yang, X. Z. Zhong, X.-P. Dong, The lysosomal Ca2+ release channel TRPML1 regulates lysosome size by activating calmodulin. *J. Biol. Chem.* **292**, 8424–8435 (2017).

40. W. Peng, Y. C. Wong, D. Krainc, Mitochondria-lysosome contacts regulate mitochondrial Ca2+ dynamics via lysosomal TRPML1. *Proc Natl Acad Sci USA*. **117**, 19266–19275 (2020).

41. C. Settembre, R. Zoncu, D. L. Medina, F. Vetrini, S. Erdin, S. Erdin, T. Huynh, M. Ferron, G. Karsenty, M. C. Vellard, V. Facchinetti, D. M. Sabatini, A. Ballabio, A lysosome-to-nucleus signalling mechanism senses and regulates the lysosome via mTOR and TFEB. *EMBO J.* **31**, 1095–1108 (2012).

42. C.-Y. Lim, R. Zoncu, The lysosome as a command-and-control center for cellular metabolism. *J. Cell Biol.* **214**, 653–664 (2016).

43. X. Sun, M. Xu, Q. Cao, P. Huang, X. Zhu, X.-P. Dong, A lysosomal K+ channel regulates large particle phagocytosis by facilitating lysosome Ca2+ release. *Sci. Rep.* **10**, 1038 (2020).

44. M. Bretou, P. J. Sáez, D. Sanséau, M. Maurin, D. Lankar, M. Chabaud, C. Spampanato, O. Malbec, L. Barbier, S. Muallem, P. Maiuri, A. Ballabio, J. Helft, M. Piel, P. Vargas, A.-M. Lennon-Duménil, Lysosome signaling controls the migration of dendritic cells. *Sci. Immunol.* **2** (2017), doi:10.1126/sciimmunol.aak9573.

45. X. Wang, X. Zhang, X.-P. Dong, M. Samie, X. Li, X. Cheng, A. Goschka, D. Shen, Y. Zhou, J. Harlow, M. X. Zhu, D. E. Clapham, D. Ren, H. Xu, TPC proteins are phosphoinositide- activated sodium-selective ion channels in endosomes and lysosomes. *Cell*. **151**, 372–383 (2012).

46. E. Brailoiu, D. Churamani, X. Cai, M. G. Schrlau, G. C. Brailoiu, X. Gao, R. Hooper, M. J. Boulware, N. J. Dun, J. S. Marchant, S. Patel, Essential requirement for two-pore channel 1 in NAADP-mediated calcium signaling. *J. Cell Biol.* **186**, 201–209 (2009).

47. P. J. Calcraft, M. Ruas, Z. Pan, X. Cheng, A. Arredouani, X. Hao, J. Tang, K. Rietdorf, L. Teboul, K.-T. Chuang, P. Lin, R. Xiao, C. Wang, Y. Zhu, Y. Lin, C. N. Wyatt, J. Parrington, J. Ma, A. M. Evans, A. Galione, M. X. Zhu, NAADP mobilizes calcium from acidic organelles through two-pore channels. *Nature*. **459**, 596–600 (2009).

48. H. C. Lee, R. Aarhus, A derivative of NADP mobilizes calcium stores insensitive to inositol trisphosphate and cyclic ADP-ribose. *J. Biol. Chem.* **270**, 2152–2157 (1995).

49. S. J. Pitt, T. M. Funnell, M. Sitsapesan, E. Venturi, K. Rietdorf, M. Ruas, A. Ganesan, R. Gosain, G. C. Churchill, M. X. Zhu, J. Parrington, A. Galione, R. Sitsapesan, TPC2 is a novel NAADP-sensitive Ca2+ release channel, operating as a dual sensor of luminal pH and Ca2+. *J. Biol. Chem.* **285**, 35039–35046 (2010).

50. P. Huang, Y. Zou, X. Z. Zhong, Q. Cao, K. Zhao, M. X. Zhu, R. Murrell-Lagnado, X.-P. Dong, P2X4 forms functional ATP-activated cation channels on lysosomal membranes regulated by luminal pH. *J. Biol. Chem.* **289**, 17658–17667 (2014).

51. J. M. Baughman, F. Perocchi, H. S. Girgis, M. Plovanich, C. A. Belcher-Timme, Y. Sancak, X. R. Bao, L. Strittmatter, O. Goldberger, R. L. Bogorad, V. Koteliansky, V. K. Mootha, Integrative genomics identifies MCU as an essential component of the mitochondrial calcium uniporter. *Nature*. **476**, 341–345 (2011).

52. A. Raffaello, C. Mammucari, G. Gherardi, R. Rizzuto, Calcium at the Center of Cell Signaling: Interplay between Endoplasmic Reticulum, Mitochondria, and Lysosomes. *Trends Biochem. Sci.* **41**, 1035–1049 (2016).

53. K. A. Christensen, J. T. Myers, J. A. Swanson, pH-dependent regulation of lysosomal calcium in macrophages. *J. Cell Sci.* **115**, 599–607 (2002).

54. E. J. Dickson, J. G. Duman, M. W. Moody, L. Chen, B. Hille, Orai-STIM-mediated Ca2+ release from secretory granules revealed by a targeted Ca2+ and pH probe. *Proc Natl Acad Sci USA*. **109**, E3539-48 (2012).

55. R. Salceda, G. Sánchez-Chávez, Calcium uptake, release and ryanodine binding in melanosomes from retinal pigment epithelium. *Cell Calcium*. **27**, 223–229 (2000).

56. P. P. Gonçalves, S. M. Meireles, P. Neves, M. G. Vale, Distinction between Ca(2+) pump and Ca(2+)/H(+) antiport activities in synaptic vesicles of sheep brain cortex. *Neurochem. Int.* **37**, 387–396 (2000).

57. S. A. Hilden, N. E. Madias, H+/Ca2+ exchange in rabbit renal cortical endosomes. *J. Membr. Biol.* **112**, 131–138 (1989).

58. C. I. López Sanjurjo, S. C. Tovey, C. W. Taylor, Rapid recycling of Ca2+ between IP3-sensitive stores and lysosomes. *PLoS ONE*. **9**, e111275 (2014).

59. A. J. Morgan, F. M. Platt, E. Lloyd-Evans, A. Galione, Molecular mechanisms of endolysosomal Ca2+ signalling in health and disease. *Biochem. J.* **439**, 349–374 (2011).

60. P. Pihán, F. Lisbona, J. Borgonovo, S. Edwards-Jorquera, P. Nunes-Hasler, K. Castillo, O. Kepp, H. Urra, S. Saarnio, H. Vihinen, A. Carreras-Sureda, S. Forveille, A. Sauvat, D. De Giorgis, A. Pupo, D. A. Rodríguez, G. Quarato, A. Sagredo, F. Lourido, A. Letai, C. Hetz, Control of lysosomal-mediated cell death by the pH-dependent calcium channel RECS1. *Sci. Adv.* **7**, eabe5469 (2021).

61. A. G. Garrity, W. Wang, C. M. Collier, S. A. Levey, Q. Gao, H. Xu, The endoplasmic reticulum, not the pH gradient, drives calcium refilling of lysosomes. *eLife*. **5** (2016), doi:10.7554/eLife.15887.

62. M. J. Phillips, G. K. Voeltz, Structure and function of ER membrane contact sites with other organelles. *Nat. Rev. Mol. Cell Biol.* **17**, 69–82 (2016).

63. K. J. Mitchell, F. A. Lai, G. A. Rutter, Ryanodine receptor type I and nicotinic acid adenine dinucleotide phosphate receptors mediate Ca2+ release from insulin-containing vesicles in living pancreatic beta-cells (MIN6). *J. Biol. Chem.* **278**, 11057–11064 (2003).

64. X. Zong, M. Schieder, H. Cuny, S. Fenske, C. Gruner, K. Rötzer, O. Griesbeck, H. Harz, M. Biel, C. Wahl-Schott, The two-pore channel TPCN2 mediates NAADP-dependent Ca(2+)-release from lysosomal stores. *Pflugers Arch.* **458**, 891–899 (2009).

65. E. K. Rooney, J. D. Gross, M. Satre, Characterisation of an intracellular Ca2+ pump in Dictyostelium. *Cell Calcium*. **16**, 509–522 (1994).

66. A. A. Genazzani, A. Galione, Nicotinic acid-adenine dinucleotide phosphate mobilizes Ca2+ from a thapsigargin-insensitive pool. *Biochem. J.* **315 (Pt 3)**, 721–725 (1996).

67. J. Ezaki, M. Himeno, K. Kato, Purification and characterization of (Ca2+-Mg2+)-ATPase in rat liver lysosomal membranes. *J. Biochem.* **112**, 33–39 (1992).

68. J. J. López, C. Camello-Almaraz, J. A. Pariente, G. M. Salido, J. A. Rosado, Ca2+ accumulation into acidic organelles mediated by Ca2+- and vacuolar H+-ATPases in human platelets. *Biochem. J.* **390**, 243–252 (2005).

69. N. Narayanaswamy, K. Chakraborty, A. Saminathan, E. Zeichner, K. Leung, J. Devany, Y. Krishnan, A pH-correctable, DNA-based fluorescent reporter for organellar calcium. *Nat. Methods*. **16**, 95–102 (2019).

70. S. van Veen, D. M. Sørensen, T. Holemans, H. W. Holen, M. G. Palmgren, P. Vangheluwe, Cellular function and pathological role of ATP13A2 and related P-type transport ATPases in Parkinson's disease and other neurological disorders. *Front. Mol. Neurosci.* **7**, 48 (2014).

71. B. Dehay, A. Ramirez, M. Martinez-Vicente, C. Perier, M.-H. Canron, E. Doudnikoff, A. Vital, M. Vila, C. Klein, E. Bezard, Loss of P-type ATPase ATP13A2/PARK9 function induces general lysosomal deficiency and leads to Parkinson disease neurodegeneration. *Proc Natl Acad Sci USA*. **109**, 9611–9616 (2012).

72. D. C. Schöndorf, M. Aureli, F. E. McAllister, C. J. Hindley, F. Mayer, B. Schmid, S. P. Sardi, M. Valsecchi, S. Hoffmann, L. K. Schwarz, U. Hedrich, D. Berg, L. S. Shihabuddin, J. Hu, J. Pruszak, S. P. Gygi, S. Sonnino, T. Gasser, M. Deleidi, iPSC-derived neurons from GBA1-associated Parkinson's disease patients show autophagic defects and impaired calcium homeostasis. *Nat. Commun.* **5**, 4028 (2014).

73. S. van Veen, S. Martin, C. Van den Haute, V. Benoy, J. Lyons, R. Vanhoutte, J. P. Kahler, J.-P. Decuypere, G. Gelders, E. Lambie, J. Zielich, J. V. Swinnen, W. Annaert, P. Agostinis, B. Ghesquière, S. Verhelst, V. Baekelandt, J. Eggermont, P. Vangheluwe, ATP13A2 deficiency disrupts lysosomal polyamine export. *Nature*. **578**, 419–424 (2020).

74. K. Schmidt, D. M. Wolfe, B. Stiller, D. A. Pearce, Cd2+, Mn2+, Ni2+ and Se2+ toxicity to Saccharomyces cerevisiae lacking YPK9p the orthologue of human ATP13A2. *Biochem. Biophys. Res. Commun.* **383**, 198–202 (2009).

75. J. Tan, T. Zhang, L. Jiang, J. Chi, D. Hu, Q. Pan, D. Wang, Z. Zhang, Regulation of intracellular manganese homeostasis by Kufor-Rakeb syndrome-associated ATP13A2 protein. *J. Biol. Chem.* **286**, 29654–29662 (2011).

76. M. Brini, E. Carafoli, The plasma membrane Ca^{2}+ ATPase and the plasma membrane sodium calcium exchanger cooperate in the regulation of cell calcium. *Cold Spring Harb. Perspect. Biol.* **3** (2011), doi:10.1101/cshperspect.a004168.

77. L. Boyman, G. S. B. Williams, D. Khananshvili, I. Sekler, W. J. Lederer, NCLX: the mitochondrial sodium calcium exchanger. *J. Mol. Cell. Cardiol.* **59**, 205–213 (2013).

78. W. Wang, X. Zhang, Q. Gao, M. Lawas, L. Yu, X. Cheng, M. Gu, N. Sahoo, X. Li, P. Li, S. Ireland, A. Meredith, H. Xu, A voltage-dependent K+ channel in the lysosome is required for refilling lysosomal Ca2+ stores. *J. Cell Biol.* **216**, 1715–1730 (2017).

79. Q. Cao, X. Z. Zhong, Y. Zou, Z. Zhang, L. Toro, X.-P. Dong, BK channels alleviate lysosomal storage diseases by providing positive feedback regulation of lysosomal ca2+ release. *Dev. Cell*. **33**, 427–441 (2015).

80. J. K. Pittman, Vacuolar Ca(2+) uptake. *Cell Calcium*. **50**, 139–146 (2011).

81. S. Patel, R. Docampo, Acidic calcium stores open for business: expanding the potential for intracellular Ca2+ signaling. *Trends Cell Biol.* **20**, 277–286 (2010).

82. S. Blackford, P. A. Rea, D. Sanders, Voltage sensitivity of H+/Ca2+ antiport in higher plant tonoplast suggests a role in vacuolar calcium accumulation. *J. Biol. Chem.* **265**, 9617–9620 (1990).

83. K. W. Cunningham, G. R. Fink, Calcineurin-dependent growth control in Saccharomyces cerevisiae mutants lacking PMC1, a homolog of plasma membrane Ca2+ ATPases. *J. Cell Biol.* **124**, 351–363 (1994).

84. A. Miseta, R. Kellermayer, D. P. Aiello, L. Fu, D. M. Bedwell, The vacuolar Ca^{2+} /H^{+} exchanger Vcx1p/Hum1p tightly controls cytosolic Ca^{2+} levels in *S. cerevisiae*. *FEBS Lett.* **451**, 132–136 (1999).

85. K. W. Cunningham, G. R. Fink, Calcineurin inhibits VCX1-dependent H+/Ca2+ exchange and induces Ca2+ ATPases in Saccharomyces cerevisiae. *Mol. Cell. Biol.* **16**, 2226–2237 (1996).

86. M. Geisler, N. Frangne, E. Gomès, E. Martinoia, M. G. Palmgren, The*aca4* gene of arabidopsis encodes a vacuolar membrane calcium pump that improves salt tolerance in yeast. *Plant Physiol.* **124**, 1814–1827 (2000).

87. K. D. Hirschi, R. G. Zhen, K. W. Cunningham, P. A. Rea, G. R. Fink, CAX1, an H+/Ca2+ antiporter from Arabidopsis. *Proc Natl Acad Sci USA*. **93**, 8782–8786 (1996).

88. L. Emery, S. Whelan, K. D. Hirschi, J. K. Pittman, Protein Phylogenetic Analysis of Ca(2+)/cation Antiporters and Insights into their Evolution in Plants. *Front. Plant Sci.* **3**, 1 (2012).

89. M. Manohar, H. Mei, A. J. Franklin, E. M. Sweet, T. Shigaki, B. B. Riley, C. W. Macdiarmid, K. Hirschi, Zebrafish (Danio rerio) endomembrane antiporter similar to a yeast cation/H(+) transporter is required for neural crest development. *Biochemistry*. **49**, 6557–6566 (2010).

90. T. Shigaki, K. D. Hirschi, Diverse functions and molecular properties emerging for CAX cation/H+ exchangers in plants. *Plant Biol (Stuttg)*. **8**, 419–429 (2006).

91. Y. Ohsumi, Y. Anraku, Calcium transport driven by a proton motive force in vacuolar membrane vesicles of Saccharomyces cerevisiae. *J. Biol. Chem.* **258**, 5614–5617 (1983).

92. R. Kellermayer, R. Szigeti, M. Kellermayer, A. Miseta, The intracellular dissipation of cytosolic calcium following glucose re-addition to carbohydrate depleted Saccharomyces cerevisiae. *FEBS Lett.* **571**, 55–60 (2004).

93. J. K. Pittman, N.-H. Cheng, T. Shigaki, M. Kunta, K. D. Hirschi, Functional dependence on calcineurin by variants of the Saccharomyces cerevisiae vacuolar Ca2+/H+ exchanger Vcx1p. *Mol. Microbiol.* **54**, 1104–1116 (2004).

94. A. B. Waight, B. P. Pedersen, A. Schlessinger, M. Bonomi, B. H. Chau, Z. Roe-Zurz, A. J. Risenmay, A. Sali, R. M. Stroud, Structural basis for alternating access of a eukaryotic calcium/proton exchanger. *Nature*. **499**, 107–110 (2013).

95. G. Grynkiewicz, M. Poenie, R. Y. Tsien, A new generation of Ca2+ indicators with greatly improved fluorescence properties. *J. Biol. Chem.* **260**, 3440–3450 (1985).

96. K. R. Gee, K. A. Brown, W. N. Chen, J. Bishop-Stewart, D. Gray, I. Johnson, Chemical and physiological characterization of fluo-4 Ca(2+)-indicator dyes. *Cell Calcium*. **27**, 97–106 (2000).

97. M. Collot, C. D. Wilms, A. Bentkhayet, P. Marcaggi, K. Couchman, S. Charpak, S. Dieudonné, M. Häusser, A. Feltz, J.-M. Mallet, CaRuby-Nano: a novel high affinity calcium probe for dual color imaging. *eLife*. **4** (2015), doi:10.7554/eLife.05808.

98. M. Collot, C. Loukou, A. V. Yakovlev, C. D. Wilms, D. Li, A. Evrard, A. Zamaleeva, L. Bourdieu, J.-F. Léger, N. Ropert, J. Eilers, M. Oheim, A. Feltz, J.-M. Mallet, Calcium rubies: a family of red-emitting functionalizable indicators suitable for two-photon Ca2+ imaging. *J. Am. Chem. Soc.* **134**, 14923–14931 (2012).

99. M. Oheim, M. van 't Hoff, A. Feltz, A. Zamaleeva, J.-M. Mallet, M. Collot, New red-fluorescent calcium indicators for optogenetics, photoactivation and multi-color imaging. *Biochim. Biophys. Acta*. **1843**, 2284–2306 (2014).

100. J. I. E. Bruce, D. R. Giovannucci, G. Blinder, T. J. Shuttleworth, D. I. Yule, Modulation of [Ca2+]i signaling dynamics and metabolism by perinuclear mitochondria in mouse parotid acinar cells. *J. Biol. Chem.* **279**, 12909–12917 (2004).

101. P. Fernyhough, N. A. Calcutt, Abnormal calcium homeostasis in peripheral neuropathies. *Cell Calcium*. **47**, 130–139 (2010).

102. L. E. García-Chacón, K. T. Nguyen, G. David, E. F. Barrett, Extrusion of Ca2+ from mouse motor terminal mitochondria via a Na+-Ca2+ exchanger increases post-tetanic evoked release. *J Physiol (Lond)*. **574**, 663–675 (2006).

103. R. M. Paredes, J. C. Etzler, L. T. Watts, W. Zheng, J. D. Lechleiter, Chemical calcium indicators. *Methods*. **46**, 143–151 (2008).

104. M. Eberhard, P. Erne, Calcium binding to fluorescent calcium indicators: calcium green, calcium orange and calcium crimson. *Biochem. Biophys. Res. Commun.* **180**, 209–215 (1991).

105. D. L. Wokosin, C. M. Loughrey, G. L. Smith, Characterization of a range of fura dyes with two-photon excitation. *Biophys. J.* **86**, 1726–1738 (2004).

106. J. C. Mercer, W. I. Dehaven, J. T. Smyth, B. Wedel, R. R. Boyles, G. S. Bird, J. W. Putney, Large store-operated calcium selective currents due to co-expression of Orai1 or Orai2 with the intracellular calcium sensor, Stim1. *J. Biol. Chem.* **281**, 24979–24990 (2006).

107. V. A. Golovina, M. P. Blaustein, Spatially and functionally distinct Ca2+ stores in sarcoplasmic and endoplasmic reticulum. *Science*. **275**, 1643–1648 (1997).

108. M. J. Devinney, I. J. Reynolds, K. E. Dineley, Simultaneous detection of intracellular free calcium and zinc using fura-2FF and FluoZin-3. *Cell Calcium*. **37**, 225–232 (2005).

109. A. M. Hofer, I. Schulz, Quantification of intraluminal free [Ca] in the agonist-sensitive internal calcium store using compartmentalized fluorescent indicators: some considerations. *Cell Calcium*. **20**, 235–242 (1996).

110. J. Palecek, M. B. Lips, B. U. Keller, Calcium dynamics and buffering in motoneurones of the mouse spinal cord. *J Physiol (Lond)*. **520 Pt 2**, 485–502 (1999).

111. K. Ukhanov, S. J. Mills, B. V. Potter, B. Walz, InsP(3)-induced Ca(2+) release in permeabilized invertebrate photoreceptors: a link between phototransduction and Ca(2+) stores. *Cell Calcium*. **29**, 335–345 (2001).

112. J. P. Kao, A. T. Harootunian, R. Y. Tsien, Photochemically generated cytosolic calcium pulses and their detection by fluo-3. *J. Biol. Chem.* **264**, 8179–8184 (1989).

113. D. X. P. Brochet, D. Yang, A. Di Maio, W. J. Lederer, C. Franzini-Armstrong, H. Cheng, Ca2+ blinks: rapid nanoscopic store calcium signaling. *Proc Natl Acad Sci USA*. **102**, 3099–3104 (2005).

114. M. K. Park, O. H. Petersen, A. V. Tepikin, The endoplasmic reticulum as one continuous Ca(2+) pool: visualization of rapid Ca(2+) movements and equilibration. *EMBO J.* **19**, 5729–5739 (2000).

115. K. L. Brain, M. R. Bennett, Calcium in sympathetic varicosities of mouse vas deferens during facilitation, augmentation and autoinhibition. *J Physiol (Lond)*. **502 (Pt 3)**, 521–536 (1997).

116. C. White, G. McGeown, Imaging of changes in sarcoplasmic reticulum [Ca(2+)] using Oregon Green BAPTA 5N and confocal laser scanning microscopy. *Cell Calcium*. **31**, 151–159 (2002).

117. K. Tanaka, L. Khiroug, F. Santamaria, T. Doi, H. Ogasawara, G. C. R. Ellis-Davies, M. Kawato, G. J. Augustine, Ca2+ requirements for cerebellar long-term synaptic depression: role for a postsynaptic leaky integrator. *Neuron*. **54**, 787–800 (2007).

118. B. S. Launikonis, J. Zhou, L. Royer, T. R. Shannon, G. Brum, E. Ríos, Confocal imaging of [Ca2+] in cellular organelles by SEER, shifted excitation and emission ratioing of fluorescence. *J Physiol (Lond)*. **567**, 523–543 (2005).

119. A. Bandyopadhyay, D. W. Shin, D. H. Kim, Regulation of ATP-induced calcium release in COS-7 cells by calcineurin. *Biochem. J.* **348 Pt 1**, 173–181 (2000).

120. M. Jadot, C. Colmant, S. Wattiaux-De Coninck, R. Wattiaux, Intralysosomal hydrolysis of glycyl-L-phenylalanine 2-naphthylamide. *Biochem. J.* **219**, 965–970 (1984).

121. T. Haller, P. Dietl, P. Deetjen, H. Völkl, The lysosomal compartment as intracellular calcium store in MDCK cells: a possible involvement in InsP3-mediated Ca2+ release. *Cell Calcium*. **19**, 157–165 (1996).

122. M. Huss, G. Ingenhorst, S. König, M. Gassel, S. Dröse, A. Zeeck, K. Altendorf, H. Wieczorek, Concanamycin A, the specific inhibitor of V-ATPases, binds to the V(o) subunit c. *J. Biol. Chem.* **277**, 40544–40548 (2002).

123. E. J. Bowman, A. Siebers, K. Altendorf, Bafilomycins: a class of inhibitors of membrane ATPases from microorganisms, animal cells, and plant cells. *Proc Natl Acad Sci USA*. **85**, 7972–7976 (1988).

124. A. J. Morgan, L. C. Davis, A. Galione, Imaging approaches to measuring lysosomal calcium. *Methods Cell Biol.* **126**, 159–195 (2015).

125. D. Shen, X. Wang, X. Li, X. Zhang, Z. Yao, S. Dibble, X. Dong, T. Yu, A. P. Lieberman, H. D. Showalter, H. Xu, Lipid storage disorders block lysosomal trafficking by inhibiting a TRP channel and lysosomal calcium release. *Nat. Commun.* **3**, 731 (2012).

126. A. Miyawaki, J. Llopis, R. Heim, J. M. McCaffery, J. A. Adams, M. Ikura, R. Y. Tsien, Fluorescent indicators for Ca2+ based on green fluorescent proteins and calmodulin. *Nature*. **388**, 882–887 (1997).

127. A. Persechini, J. A. Lynch, V. A. Romoser, Novel fluorescent indicator proteins for monitoring free intracellular Ca2+. *Cell Calcium*. **22**, 209–216 (1997).

128. V. Baubet, H. Le Mouellic, A. K. Campbell, E. Lucas-Meunier, P. Fossier, P. Brúlet, Chimeric green fluorescent protein-aequorin as bioluminescent Ca2+ reporters at the single-cell level. *Proc Natl Acad Sci USA*. **97**, 7260–7265 (2000).

129. J. Nakai, M. Ohkura, K. Imoto, A high signal-to-noise Ca(2+) probe composed of a single green fluorescent protein. *Nat. Biotechnol.* **19**, 137–141 (2001).

130. M. Ohkura, M. Matsuzaki, H. Kasai, K. Imoto, J. Nakai, Genetically encoded bright Ca2+ probe applicable for dynamic Ca2+ imaging of dendritic spines. *Anal. Chem.* **77**, 5861–5869 (2005).

131. Y. N. Tallini, M. Ohkura, B.-R. Choi, G. Ji, K. Imoto, R. Doran, J. Lee, P. Plan, J. Wilson, H.-B. Xin, A. Sanbe, J. Gulick, J. Mathai, J. Robbins, G. Salama, J. Nakai, M. I. Kotlikoff, Imaging cellular signals in the heart in vivo: Cardiac expression of the high-signal Ca2+ indicator GCaMP2. *Proc Natl Acad Sci USA*. **103**, 4753–4758 (2006).

132. L. Tian, S. A. Hires, T. Mao, D. Huber, M. E. Chiappe, S. H. Chalasani, L. Petreanu, J. Akerboom, S. A. McKinney, E. R. Schreiter, C. I. Bargmann, V. Jayaraman, K. Svoboda, L. L. Looger, Imaging neural activity in worms, flies and mice with improved GCaMP calcium indicators. *Nat. Methods*. **6**, 875–881 (2009).

133. J. Akerboom, T.-W. Chen, T. J. Wardill, L. Tian, J. S. Marvin, S. Mutlu, N. C. Calderón, F. Esposti, B. G. Borghuis, X. R. Sun, A. Gordus, M. B. Orger, R. Portugues, F. Engert, J. J. Macklin, A. Filosa, A. Aggarwal, R. A. Kerr, R. Takagi, S. Kracun, L. L. Looger, Optimization of a GCaMP calcium indicator for neural activity imaging. *J. Neurosci.* **32**, 13819–13840 (2012).

134. T.-W. Chen, T. J. Wardill, Y. Sun, S. R. Pulver, S. L. Renninger, A. Baohan, E. R. Schreiter, R. A. Kerr, M. B. Orger, V. Jayaraman, L. L. Looger, K. Svoboda, D. S. Kim, Ultrasensitive fluorescent proteins for imaging neuronal activity. *Nature*. **499**, 295–300 (2013).

135. Y. Yang, N. Liu, Y. He, Y. Liu, L. Ge, L. Zou, S. Song, W. Xiong, X. Liu, Improved calcium sensor GCaMP-X overcomes the calcium channel perturbations induced by the calmodulin in GCaMP. *Nat. Commun.* **9**, 1504 (2018).

136. M. Mank, O. Griesbeck, Genetically encoded calcium indicators. *Chem. Rev.* **108**, 1550–1564 (2008).

137. J. Oh, C. Lee, B.-K. Kaang, Imaging and analysis of genetically encoded calcium indicators linking neural circuits and behaviors. *Korean J. Physiol. Pharmacol.* **23**, 237–249 (2019).

138. Y. Zhao, S. Araki, J. Wu, T. Teramoto, Y.-F. Chang, M. Nakano, A. S. Abdelfattah, M. Fujiwara, T. Ishihara, T. Nagai, R. E. Campbell, An expanded palette of genetically encoded Ca^{2+} indicators. *Science*. **333**, 1888–1891 (2011).

139. T. Nagai, A. Sawano, E. S. Park, A. Miyawaki, Circularly permuted green fluorescent proteins engineered to sense Ca2+. *Proc Natl Acad Sci USA*. **98**, 3197–3202 (2001).

140. G. S. Baird, D. A. Zacharias, R. Y. Tsien, Circular permutation and receptor insertion within green fluorescent proteins. *Proc Natl Acad Sci USA*. **96**, 11241–11246 (1999).

141. J. Akerboom, N. Carreras Calderón, L. Tian, S. Wabnig, M. Prigge, J. Tolö, A. Gordus, M. B. Orger, K. E. Severi, J. J. Macklin, R. Patel, S. R. Pulver, T. J. Wardill, E. Fischer, C. Schüler, T.-W. Chen, K. S. Sarkisyan, J. S. Marvin, C. I. Bargmann, D. S. Kim, L. L. Looger, Genetically encoded calcium indicators for multi-color neural activity imaging and combination with optogenetics. *Front. Mol. Neurosci.* **6**, 2 (2013).

142. A. Miyawaki, O. Griesbeck, R. Heim, R. Y. Tsien, Dynamic and quantitative Ca2+ measurements using improved cameleons. *Proc Natl Acad Sci USA*. **96**, 2135–2140 (1999).

143. K. Horikawa, Y. Yamada, T. Matsuda, K. Kobayashi, M. Hashimoto, T. Matsu-ura, A. Miyawaki, T. Michikawa, K. Mikoshiba, T. Nagai, Spontaneous network activity visualized by ultrasensitive Ca(2+) indicators, yellow Cameleon-Nano. *Nat. Methods*. **7**, 729–732 (2010).

144. A. E. Palmer, M. Giacomello, T. Kortemme, S. A. Hires, V. Lev-Ram, D. Baker, R. Y. Tsien, Ca2+ indicators based on computationally redesigned calmodulin-peptide pairs. *Chem. Biol.* **13**, 521–530 (2006).

145. N. Heim, O. Griesbeck, Genetically encoded indicators of cellular calcium dynamics based on troponin C and green fluorescent protein. *J. Biol. Chem.* **279**, 14280–14286 (2004).

146. M. Waldeck-Weiermair, M. R. Alam, M. J. Khan, A. T. Deak, N. Vishnu, F. Karsten, H. Imamura, W. F. Graier, R. Malli, Spatiotemporal correlations between cytosolic and mitochondrial Ca(2+) signals using a novel red-shifted mitochondrial targeted cameleon. *PLoS ONE*. **7**, e45917 (2012).

147. B. Suresh, A. Saminathan, K. Chakraborty, C. Cui, L. Becker, Y. Krishnan, Tubular lysosomes harbor active ion gradients and poise macrophages for phagocytosis. *BioRxiv* (2020), doi:10.1101/2020.12.05.413229.

148. C. L. Hill, G. J. Stephens, An introduction to patch clamp recording. *Methods Mol. Biol.* **2188**, 1–19 (2021).

149. A. L. Hodgkin, A. F. Huxley, A quantitative description of membrane current and its application to conduction and excitation in nerve. *J Physiol (Lond)*. **117**, 500–544 (1952).

150. E. Neher, B. Sakmann, J. H. Steinbach, The extracellular patch clamp: a method for resolving currents through individual open channels in biological membranes. *Pflugers Arch.* **375**, 219–228 (1978).

151. S. J. Pitt, A. K. M. Lam, K. Rietdorf, A. Galione, R. Sitsapesan, Reconstituted human TPC1 is a proton-permeable ion channel and is activated by NAADP or Ca2+. *Sci. Signal.* **7**, ra46 (2014).

152. F. Zhang, S. Jin, F. Yi, P.-L. Li, TRP-ML1 functions as a lysosomal NAADP-sensitive Ca2+ release channel in coronary arterial myocytes. *J. Cell. Mol. Med.* **13**, 3174–3185 (2009).

153. F. Zhang, P.-L. Li, Reconstitution and characterization of a nicotinic acid adenine dinucleotide phosphate (NAADP)-sensitive Ca2+ release channel from liver lysosomes of rats. *J. Biol. Chem.* **282**, 25259–25269 (2007).

154. C.-C. Chen, C. Cang, S. Fenske, E. Butz, Y.-K. Chao, M. Biel, D. Ren, C. Wahl-Schott, C. Grimm, Patch-clamp technique to characterize ion channels in enlarged individual endolysosomes. *Nat. Protoc.* **12**, 1639–1658 (2017).

155. X.-P. Dong, X. Cheng, E. Mills, M. Delling, F. Wang, T. Kurz, H. Xu, The type IV mucolipidosis-associated protein TRPML1 is an endolysosomal iron release channel. *Nature*. **455**, 992–996 (2008).

156. C.-C. Chen, M. Keller, M. Hess, R. Schiffmann, N. Urban, A. Wolfgardt, M. Schaefer, F. Bracher, M. Biel, C. Wahl-Schott, C. Grimm, A small molecule restores function to TRPML1 mutant isoforms responsible for mucolipidosis type IV. *Nat. Commun.* **5**, 4681 (2014).

157. A. Jha, M. Ahuja, S. Patel, E. Brailoiu, S. Muallem, Convergent regulation of the lysosomal two-pore channel-2 by Mg^{2+}, NAADP, $PI(3,5)P_2$ and multiple protein kinases. *EMBO J.* **33**, 501–511 (2014).

158. Y. Sakurai, A. A. Kolokoltsov, C.-C. Chen, M. W. Tidwell, W. E. Bauta, N. Klugbauer, C. Grimm, C. Wahl-Schott, M. Biel, R. A. Davey, Ebola virus. Two-pore channels control Ebola virus host cell entry and are drug targets for disease treatment. *Science*. **347**, 995–998 (2015).

159. C. Cang, Y. Zhou, B. Navarro, Y.-J. Seo, K. Aranda, L. Shi, S. Battaglia-Hsu, I. Nissim, D. E. Clapham, D. Ren, mTOR regulates lysosomal ATP-sensitive two-pore Na(+) channels to adapt to metabolic state. *Cell*. **152**, 778–790 (2013).

160. A. Saminathan, J. Devany, K. S. Pillai, A. T. Veetil, M. Schwake, Y. Krishnan, A DNA-based voltmeter for organelles: Supplementary information. *BioRxiv* (2019), doi:10.1101/523019.

161. C.-C. Chen, E. Krogsaeter, C. Grimm, Two-pore and TRP cation channels in endolysosomal osmo-/mechanosensation and volume regulation. *Biochim. Biophys. Acta Mol. Cell Res.* **1868**, 118921 (2021).

162. X.-P. Dong, X. Wang, H. Xu, TRP channels of intracellular membranes. *J. Neurochem.* **113**, 313–328 (2010).

163. T. J. Jentsch, M. Pusch, CLC chloride channels and transporters: structure, function, physiology, and disease. *Physiol. Rev.* **98**, 1493–1590 (2018).

II. Identification of a Potential Lysosomal Ca^{2+}/H^{+} Exchanger in Worms

II.A: Introduction

II.A.1: A screen to identify lysosomal Ca^{2+} importers

To identify potential human lysosomal human Ca^{2+}/H^{+} exchangers, we looked first to another organism with no known CAX genes, *Caenorhabditis elegans.* In *C. elegans*, well-defined organismal, cellular, and organellar phenotypes result from lysosomal Ca^{2+} imbalance. Adult worms have 6 coelomocytes that continuously and nonspecifically endocytose fluid from the body cavity (the pseudocoelom) (*1*). These scavenger cells contain membrane-bound endolysosomes that can be visualized by light microscopy, such as by green fluorescent protein (GFP) secreted into the pseudocoelom from muscle cells and endocytosed by coelomocytes (*2*). For example, the coelomocyte endolysosomes are easy to observe in a transgenic worm strain called *arIs37[pmyo-3::ssGFP]*, which display bright fluorescent vesicles in coelomocytes (*2*). Importantly, uptake into coelomocytes is fairly nonspecific, enabling loading with dextran conjugates and DNA nanodevices, among other macromolecules (*2*–*4*). In a screen for new mutants defective in endocytosis by coelomocytes, the *arIs37[pmyo-3::ssGFP]* worms were mutagenized with ethyl methanesulfonate (EMS). They found genes known to be involved in receptor-mediated endocytosis, as well as new genes in a family they named *cup* (coelomocyte uptake).

Among this family of genes was *cup-5*, the worm homolog of the human lysosomal Ca^{2+} release channel TRPML1. Loss of TRPML1 leads to ML-IV, a lysosomal storage disorder characterized by severe developmental neuropathology (*5*, *6*). Cells from patients with ML-IV have normal lysosomal hydrolases, unlike in other lysosomal storage disorders (*7*). Instead, they exhibit abnormal endocytosis of lipids and large endocytic vesicles (*8*, *9*). Thus, striking parallels have emerged between *cup-5* mutant worms and cells from patients with ML-IV. In *cup-5* mutant worms, called *arIs37*;*cup-5(ar465)* because of the *ar465* hypomorph that possesses a G401E mutation, GFP accumulates excessively in coelomocytes, suggesting enhanced uptake and/or decreased degradation by coelomocytes (*10*). This leads to accumulation of large vacuoles. Given the role of TRPML1 in Ca^{2+} release-mediated fusion and cellular clearance, it is likely that *cup-5* mutations lead to defective endocytic trafficking, autophagy, and

exocytosis. Indeed, pH-corrected lysosomal Ca^{2+} measurements with the DNA device, *CalipHluor*, revealed that heterozygous knockout of *cup-5* leads to ~4-fold higher Ca^{2+} levels in coelomocyte lysosomes, consistent with *cup-5* being a Ca^{2+} release channel (*11*). Because of these Ca^{2+}-mediated defects in endocytosis, *cup-5* inactivation leads to embryonic lethality and low brood size (*12*). This occurs because embryonic cells endocytose yolk and degrade it to provide energy and basic metabolites for development (*13*). Embryos lacking *cup-5* do not process yolk appropriately, which leads to a decrease in nutrient availability and the activation of autophagy (*12*). But because cells in *cup-5* mutant worms also have defective autophagy, starvation leads to apoptosis and embryonic lethality.

For our purposes, these findings provide a tiered screen that can evaluate genes affecting lysosomal Ca^{2+} homeostasis by measuring worm survival, lysosome size, and lysosomal calcium (**Fig. 2.1**). Because these phenotypes result from the lysosomal Ca^{2+} release activity of *cup-5*, inactivating a Ca^{2+} import mechanism compensates for defects. In a sense, this balances out lysosomal Ca^{2+} levels, thereby restoring endocytic defects and rescuing embryonic lethality. This compensation has already been shown with the *C. elegans* homolog of ATP13A2, called *catp-6*. Knockdown of *catp-6* in *cup-5* mutant worms normalized lysosomal Ca^{2+} levels, restored lysosome size, and reversed lethality (*11*). This knockdown assay suits us well to screen for lysosomal Ca^{2+}/H^{+} exchangers because: (i) RNA interference (RNAi) by feeding is simple, potent, and specific in worms; (ii) worm survival provides a quick readout of lysosomal Ca^{2+} modulation; and (iii) lysosome size and Ca^{2+} measurements confirm that rescuing lethality occurs through restoration of lysosome function (*11*, *14*). Thus, we proceeded with this three-tiered screen to identify human lysosomal Ca^{2+}/H^{+} exchangers by their worm homologs.

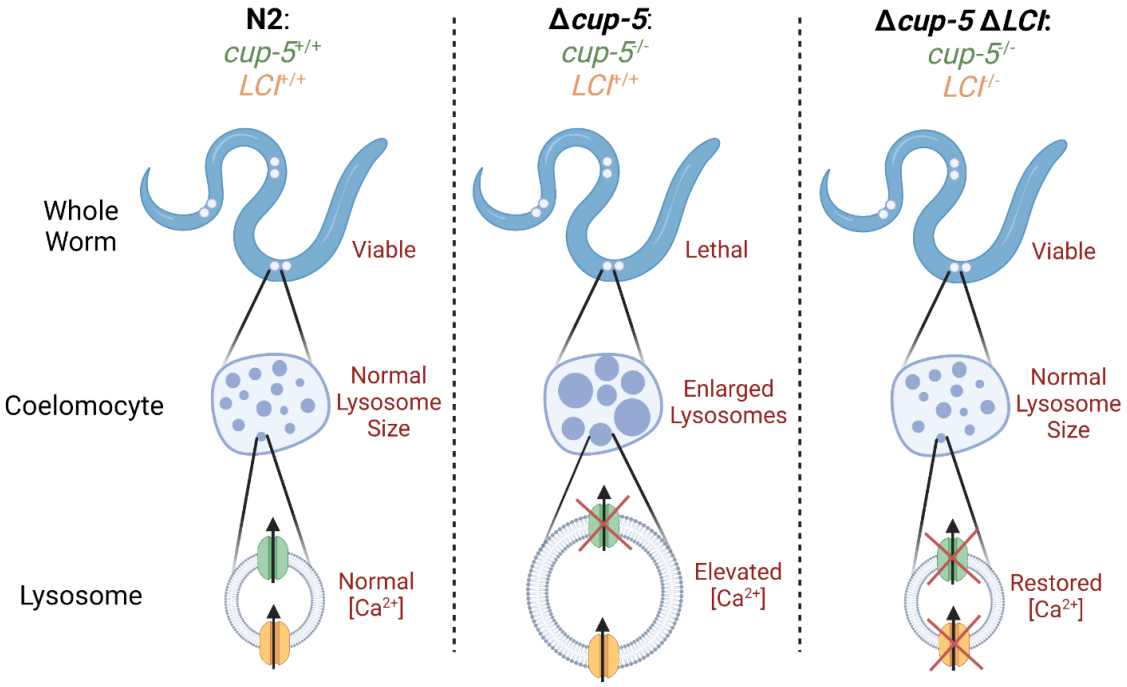

Figure 2.1: **Three-tiered screen to identify lysosomal Ca^{2+} importers (LCIs)**. Deletion of the Ca^{2+} release channel *cup-5* causes elevated lysosomal Ca^{2+} levels, which leads to lysosome enlargement due to storage defects and worm lethality. In this background, deletion of an LCI would compensate for this defect by restoring lysosomal Ca^{2+} levels and rescuing lysosome size and worm survival.

II.A.2: Rationale for the candidate genes

The assays described in **Section II.A.1** identify genes that facilitate Ca^{2+} import into lysosomes. They indicate nothing about H^+ conductance or pH gradient sensitivity. They also do not even imply that the identified genes transport Ca^{2+} themselves. Thus, we selected genes for this screen that have literature basis for cation exchange activity, and then validate direct Ca^{2+}/H^+ exchanger in later chapters. We first selected a subset of Na^+/Ca^{2+} exchangers (NCXs). Under normal conditions, these transporters facilitate the influx of three Na^+ ions and extrusion of one Ca^{2+} ion across the plasma membrane (*15*). Although their activity alone would not explain the observed pH gradient-sensitive Ca^{2+} import mechanism observed on lysosomes, it is possible that they could collaborate with Na^+/H^+ exchangers (NHEs) to enable the net import of Ca^{2+} and export of H^+ (*16*). The *C. elegans* genome has 10 Na^+/Ca^{2+} exchanger genes (*ncx1-ncx10*). The first three (*ncx1-ncx3*) belong to the NCX family of exchangers, with *ncx-1* being the closest relative to the human orthologs (NCX1-NCX3) (*17*). The next two (*ncx4-ncx5*) belong

to the NCKX branch and are closely related to two of the human NCKX orthologs (NCKX1-NCKX2) (*17*). The last five (*ncx6-ncx10*) belong to the CCX branch, and are closely related to the human NCKX-6 (*17*). These genes are expressed in different tissues of the worm, including muscles, neuronal cells, and renal tissue. We chose a subset of these exchangers (*ncx1-ncx4*) to test whether this family of genes facilitates Ca^{2+} import into coelomocyte lysosomes. There is some evidence of NCX and NCKX activity on acidic organelles, and endocytosis of plasma membrane populations could recruit them to lysosomes (*18–21*).

Next, we selected the *C. elegans* gene *Y54F10AL.1* for the screen because of evidence that its human homolog, TMEM165, is a Ca^{2+}/H^{+} exchanger in the Golgi. Defects in TMEM165 cause a subtype of congenital disorders of glycosylation (CDG) that leads to growth retardation, psychomotor retardation, muscular weakness, and death during infancy or childhood (*22*, *23*). There are about 50 different types of CDG, which mostly result from mutations in genes encoding proteins involved glycosylation (glycosyltransferases, glycosidases, and nucleotide-sugar transporters) (*24*). However, TMEM165 mutations seem to cause CDG phenotypes by altering Golgi pH and cation homeostasis (*25*). The mutations were identified during clinical analysis of five children who were diagnosed with CDG Type II based on symptoms and glycosylation status (*22*). Three patients had a homozygous mutation (c.792+182G>A) in TMEM165 that led to a truncated and nonfunction protein. One patient had a homozygous missense mutation (c.377G>A) in TMEM165 that led to the protein mutation R126H. The last patient had a heterozygous missense compound mutation (c.376C>T and c.911G>A) that led to the double mutant protein R126C and G304R. Importantly, these single or double nucleotide mutations seem to alter the intracellular distribution of TMEM165 to favor lysosomes over the Golgi, but do not affect the protein's transport function (*26*). Separately, a patient with CDG phenotypes was identified with a mutation in TMEM165 (c.323A>G) that led to the mutation E108G (*27*). TMEM165 has putative orthologs in all eukaryotes and in many bacteria, indicating high conservation and ancient function (*22*). It has seven transmembrane domains, with the N-terminal transmembrane domain serving as a signal peptide that may get removed. Orthologs of TMEM165 belong to the UPF0016 family of membrane

proteins of unknown function (*28*). This family contains two copies of an EΦGD(KR)(ST) motif flanked by two hydrophobic regions, suggestive of a cation transporter regulated by proton pumping. Interestingly, the E108 mutated in a patient with CDG is located in one of these motifs, suggesting that its transport function may be relevant to disease phenotypes (*27*). The UPF0016 family members also contain two homologous domains that adopt opposite orientations in the membrane separated by a central loop. Thus, the UPF0016 family members exhibit striking similarities to the CaCA superfamily, although they do not share notable sequence homology (*28*). Indeed, the yeast ortholog Gdt1 localizes to the cis- and medial-Golgi apparatus, where it controls intracellular Ca^{2+} (and Mn^{2+}) stores by acting as a cation-proton antiporter to facilitate tolerance to high Ca^{2+} (*29*, *30*). The absence of Gdt1 confers growth defects to yeast grown in high levels of Ca^{2+}, which can be rescued by expression of human TMEM165, suggesting a conserved role in Ca^{2+} and Mn^{2+} transport (*25*). However, expression of the disease mutant E108G fails to rescue Ca^{2+} toxicity (but not Mn^{2+} toxicity), further supporting the function of TMEM165 as a Ca^{2+} transporter (*31*). Additionally, electrophysiology experiments in mammalian cells suggest it transports Ca^{2+}, and the absence of TMEM165 leads to hyperacidic lysosomes and Golgi (*25*, *32*). TMEM165 stability is linked to the Golgi P-type ATPase SPCA1, which transports Ca^{2+} and Mn^{2+} into the Golgi lumen and is mutated in a severe skin disease called Hailey-Hailey disease (*33*–*35*). TMEM165 has unique cell-specific effects that further support its role in Ca^{2+} homeostasis, such as its role in lactating breast tissues to support proper lactose synthetase function during milk production (*36*, *37*). Finally, in addition to its extensively described role in glycosylation, TMEM165 plays a role in certain cancers, where its overexpression leads to more invasiveness (*36*, *38*). Combined, these results indicate that TMEM165 could be part of a unique family of Golgi-localized Ca^{2+}/H^{+} exchangers, which upon deletion or mislocalization, can lead to glycosylation defects and developmental issues. As such, we wondered whether it may have additional physiological relevance as a potential lysosomal Ca^{2+}/H^{+} exchanger.

Finally, we selected two lysosomal membrane proteins to serve as negative and positive controls to show the specificity of our initial screen. One of these is *clh-6*, whose human homolog CLCN7 is a

lysosomal Cl^-/H^+ antiporter (*39*). We would expect that knocking down such an exchanger in this set of assays would not rescue the worm survival, lysosome size, or lysosomal Ca^{2+} levels of *cup-5* mutants, because it has shown no effect on lysosomal Ca^{2+} levels (*11*). Thus, we selected *clh-6* as a negative control for this screen. The other is *catp-6*, whose human homolog ATP13A2 is a P5 ATPase reported to transport cations such as Mn^{2+}, Zn^{2+}, Mg^{2+}, and Cd^{2+}, as well as polyamines, in lysosomes (*40*, *41*). Importantly, knocking down *catp-6* in *cup-5* mutant worms rescues worm survival, lysosome size, and lysosomal Ca^{2+} levels, implying that it also facilitates Ca^{2+} accumulation (*11*). Thus, we selected *catp-6* as a positive control for this screen.

II.B: Materials and Methods

II.B.1: Chemicals and reagents

Modified oligonucleotides (Supplementary Table S1) were purchased from IDT (USA), subjected to ethanol precipitation and quantified using UV absorbance. Carbenicillin and NGM plate ingredients were purchased from Sigma.

II.B.2: *C. elegans* strains

Standard methods were used to maintain *C. elegans* (*42*). The wild-type strain was the *C. elegans* isolate from Bristol, strain N2. Three strains used in the study were provided by the Caenorhabditis Genetics Center: *+/mT1 II; cup-5(ok1698)/mT1 [dpy-10(e128)] III*, a heterozygous knockout of *cup-5* balanced by *dpy-10* marked translocation; *arIs37[myo-3p::ssGFP+dpy-20(+)]I*, a transgenics strain expressing soluble GFP (ssGFP) in the body muscles which is secreted into the pseudocoelom and endocytosed by coelomocytes; and *arIs37[myo-3p::ssGFP+dpy-20(+)]Icup5(ar465)*, a transgenic strain with enlarged GFP-containing vesicles in coelomocytes due to a point mutation in *cup-5*. The strain with a heterozygous knockout of *lcax-1* was generated and provided by D. Moerman (University of British Columbia) using CRISPR/Cas9 technology and verified by sequencing (*43*). Heterozygous *lcax-1*$^{+/-}$ worms are marked by pharyngeal GFP, homozygous *lcax-1*$^{+/+}$ progeny are functionally wild-type but lack GFP, and homozygous *lcax-1*$^{-/-}$ progeny are embryonic lethal. The genotype of this worm is

Y54F10AL.1(gk5484[loxP + Pmyo-2::GFP::unc-54 3' UTR + Prps-27::neoR::unc-54 3' UTR + loxP])/+ III.

II.B.3: Gene knockdown in *C. elegans*

Gene knockdown was performed using Ahringer Library-based RNAi methods (*44*). The RNAi clones used were L4440 empty vector control, *catp-6* (W08D2.5, Ahringer Library), *cup-5* (R13A5.1, Ahringer Library), *lcax-1* (Y54F10AL.1, Ahringer Library), *ncx-1* (Y113G7A.4, Ahringer Library), *ncx-2* (C10G8.5, Ahringer Library), *ncx-3* (ZC168.1), *ncx-4* (F35C12.2), and *clh-6* (R07B7.1, Ahringer Library). RNA knockdown and genetic background were confirmed by probing messenger RNA levels of the candidate gene, assayed by RT-PCR. Briefly, total RNA was isolated using the Trizol-chloroform method and 1 ug total RNA was converted to complementary DNA using oligo-dT primers and SuperScriptIV RT according to manufacturer protocols. Then, 5 µL of cDNA product was used to setup up a PCR using gene-specific primers for *Y54F10AL.1* (F: ATTCCACCGATTTCCACCCC, R: CTTCTTGGCCCTCATTCGGT, 527 bp) *ncx-1* (F: ACAACTACAAATGCGATGACCA, R: ATTGTCGATGGTCCCAGCTC, 515bp), *ncx-2* (F: TTCGCTACCATCCCACCAAC, R: CAGTAGGCTTCCAATGCGGA, 539bp) , *ncx-3* (F: CGGTTTGGTGACTGCTGTTG, R: CGTAGACAATCCAGAGGCCC, 449bp), *ncx-4* (F: GTCTACCGATTCCGTGGCTT, R: CCGTTGATGCAGACCGTTTT, 359bp), *clh-6* (F: ACGACTGCAGGGTGTATGTG, R: CGAGACCTGTCCATGAGAGC, 574bp), *catp-6* (F: ATTGTTGGTGCAGTCAACGC, R: GGGGGAATGTTATGCAAGTCG, 503bp), *cup-5* (F: GCGGTTAGAGCAAATTCCCC, R: TGAGCGCCAAGATTTCCAGA, 561bp), and *act-1* (F: TGCAGAAGGAAATCACCGCT, R: AGAAAGCTGGTGGTGACGAT, 251 bp) where indicated. PCR products were separated on a 0.8% agarose-Tris base, acetic acid, and EDTA (TAE) gel.

II.B.4: Survival assay in *C. elegans*

The *N2*, *+/mT1 II; cup-5(ok1698)/mT1 [dpy-10(e128)] III*, and *Y54F10AL.1(gk5484[loxP + Pmyo-2::GFP::unc-54 3' UTR + Prps-27::neoR::unc-54 3' UTR + loxP])/+ III* nematode strains were used for this assay, which was performed as previously described (*11*). Five L4 worms of the indicated

strain were placed on plates containing RNAi bacterial strains for L4440 empty vector, *ncx-1, ncx-1, ncx-3, ncx-4, clh-6, lcax-1, catp-6,* or *cup-5*. The worms were allowed to grow for 24 hours and lay eggs, after which the adult worms were removed from the plates. Eggs were allowed to hatch and grow into adults for 3 days. The worm plates were imaged under an Olympus SZX-Zb12 Research Stereomicroscope (Olympus Corporation of the Americas) with a Zeiss Axiocam color CCD camera (Carl Zeiss Microscopy). Images were then analyzed using ImageJ to count the number of adult worms per plate.

II.B.5: Lysosome size assay in *C. elegans*

The *N2, arIs37[myo-3p::ssGFP+dpy-20(+)]I , arIs37[myo-3p::ssGFP+dpy-20(+)]Icup5(ar465),* and *Y54F10AL.1(gk5484[loxP + Pmyo-2::GFP::unc-54 3' UTR + Prps-27::neoR::unc-54 3' UTR + loxP])/+ III* nematode strains were used for this assay, which was performed as previously described (*11*). Briefly, five L4 worms were placed on plates containing the indicated RNAi bacterial strains. After 24 hours of laying eggs, the adult worms were removed from plates. After 3 days, the adult worms are imaged to check for lysosome size differences. Worms were imaged on a confocal microscope for either ssGFP-labeled coelomocyte lysosomes or a DNA duplex with Alexa647 (**Table 2.1**). Lysosome areas were measured using ImageJ, and enlarged lysosomes were defined as those whose diameter is ≥33% of the diameter of the largest lysosomes in N2 worms. Lysosome size data were plotted as the percentage of area occupied by large lysosomes relative to the total lysosomal area.

Table 2.1: **Sequences of DNA oligos used in this study.** D1 and D2 were used for labeling of coelomocyte lysosomes for lysosome size assay.

Sequence Name	DNA sequence information
D1	5'-DBCO-ATC AAC ACT GCA CAC CAG ACA GCA AGA TCC TAT ATA TA-3'
D2	5'-Alexa 647-TA TAT ATA GGA TCT TGC TGT CTG GTG TGC AGT GTT GAT-3'

II.B.6: Image acquisition

Confocal images were captured with a Leica TCS SP5 II STED laser confocal microscope (Leica Microsystems, Buffalo Grove, IL, USA) equipped with a 63X, 1.4 NA, oil immersion objective. GFP was excited using an argon laser with wavelength of 488nm, and Alexa647 was excited using an He-Ne laser

with wavelength of 633nm. All emissions were filtered using an acousto-optical beam splitter (AOBS) with settings suitable for each fluorophore and recorded using hybrid detector.

II.B.7: Statistics

For statistical analysis between two samples, a two-sample two-tailed test assuming unequal variance was conducted. For comparison of multiple samples, one-way ANOVA with a post hoc Tukey test was conducted. All statistical analysis was performed in Origin.

II.C: Results and Discussion

II.C.1: Survival assay in *cup-5*$^{+/-}$ worms

We performed the screen described in **Section II.A.1** with RNAi for the genes outlined in **Section II.A.2**. As expected, *cup-5*$^{+/-}$ worms have reduced survival compared to wild-type (N2) worms (**Fig. 2.2A,B)**. In addition, knocking down *clh-6* and *catp-6* led to the expected results, as the former failed to rescue survival while the latter rescued survival. Thus, with our negative and positive controls indicating that reversing lethality of *cup-5*$^{+/-}$ worms provides info specifically about lysosomal Ca^{2+} import mechanisms, we proceeded to test our potential lysosomal Ca^{2+}/cation exchangers. Knocking down any of the NCX genes (*ncx1-4*) failed to rescue survival of these worms, implying that their Na^{+}/Ca^{2+} exchange function does not facilitate Ca^{2+} import in lysosomes. However, knocking down the uncharacterized gene *Y54F10AL.1* (hereby denoted *lcax-1*) rescued lethality. Indeed, all knockdowns showed significant reduction in mRNA levels of the gene of interest (**Fig. 2.2C**). Thus, we proceeded to test lysosome-specific phenotypes of *lcax-1* depletion.

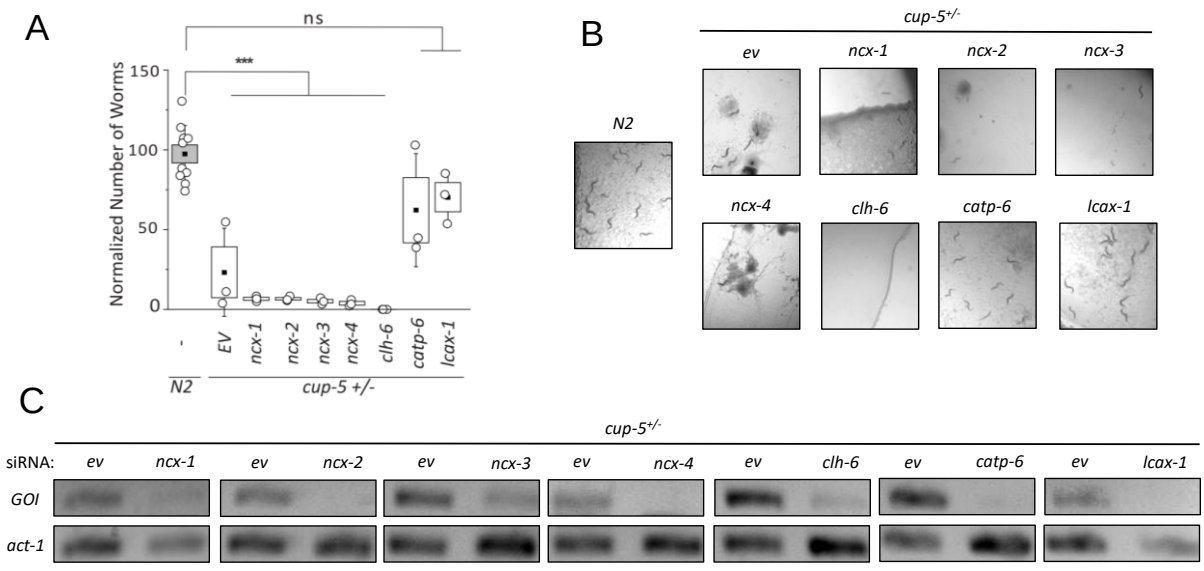

Figure 2.2: Survival assay in cup-5$^{+/-}$ worms. (A) Number of *cup-5*$^{+/-}$ progeny following RNAi knockdown of indicated proteins. (B) Representative images showing the number of progeny of N2 worms or *cup-5*$^{+/-}$ worms on plates containing indicated RNAi bacteria. (C) RT-PCR analysis of total RNA isolated from *cup-5*$^{+/-}$ worms for the indicated gene of interest (GOI) following knockdown of the indicated gene, compared to treatment with empty vector. *ev*, empty vector; *ncx*, Na^+/Ca^{2+} exchanger; *clh-6*, Cl^- channel protein; *catp-6*, Ca^{2+}-transporting ATPase; *lcax-1*, lysosomal Ca^{2+}/H^+ exchanger. All experiments performed in triplicate. Boxes and bars represent the s.e.m. and standard deviation, respectively. ns: $p>0.05$; ***$p<0.001$ (one-way ANOVA with Tukey post hoc test).

II.C.2: Lysosome size assay in *cup-5* mutant worms

We then analyzed lysosome size in *arIs37;cup-5(ar465)* worms, whose point mutation in *cup-5* leads to swollen lysosomes but not lethality. In addition, lysosomes can be visualized in these worms by GFP secreted into the pseudocoelom and endocytosed by coelomocytes. As expected, these mutant worms display larger lysosomes than wild-type worms (*arIs37*), with about double the area of coelomocytes taken up by large lysosomes (**Fig. 2.3A,B)**. Furthermore, depletion of *lcax-1* in this background restored lysosome size back down to normal. These results imply that *lcax-1* fulfills a role complementary to that of *cup-5*, such that it rescues endocytic abnormalities and the resulting storage defects.

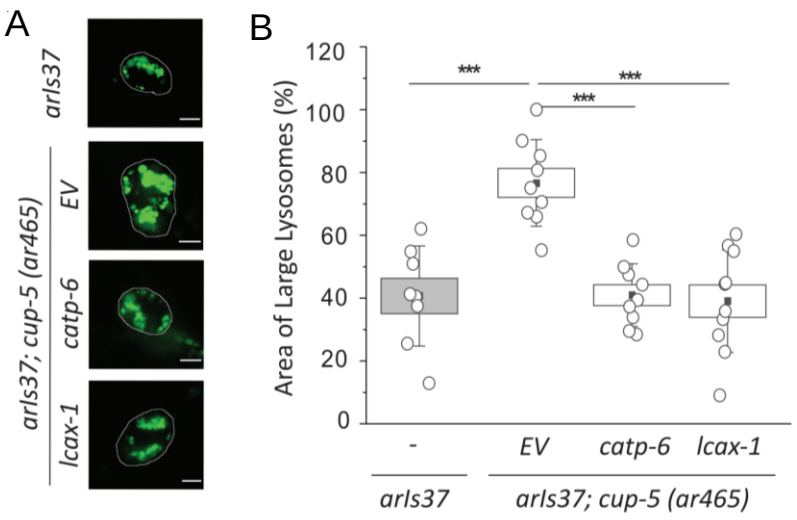

Figure 2.3: Lysosome size assay in *cup-5* mutant worms. (A) Representative fluorescence images of lysosomes in coelomocytes of *arIs37* and *arIs37; cup-5(ar465)* worms following on RNAi knockdown of indicated proteins. (B) Percentage area occupied by enlarged lysosomes in the indicated genetic background (n>10 cells, >75 lysosomes). Scale bar, 5 μm. All experiments performed in triplicate. Boxes and bars represent the s.e.m. and standard deviation, respectively. ***p<0.001 (one-way ANOVA with Tukey post hoc test).

II.C.3: Survival assay in *lcax-1*$^{+/-}$ worms

We then wondered whether the relationship between *lcax-1* and *cup-5* is commutative by studying phenotypes in worms lacking *lcax-1*. Interestingly, homozygous knockout of *lcax-1* caused embryonic lethality, so we generated heterozygous knockout worms to study their phenotypes. Indeed, these worms show reduced expression of *lcax-1* compared to N2 worms (**Fig. 2.4A**). This led us to reason that we may be able to carry out the analogous survival and lysosome size assays in *lcax-1*$^{+/-}$ worms. Specifically, if *lcax-1* indeed facilitates import of Ca^{2+} into lysosomes, its depletion would lead to low lysosomal Ca^{2+} levels, which would similarly lead to lysosome storage phenotypes of swollen lysosomes and lethality, and knockdown of lysosomal Ca^{2+} release channels would rescue such phenotypes (**Fig. 2.4B**). Indeed, *lcax-1*$^{+/-}$ worms show reduced survival compared to N2 worms, and knockdown of *cup-5* restored worm survival (**Fig. 2.4C,D)**. Knockdown of *cup-5* showed significant reduction in mRNA levels (**Fig. 2.4E)**. Combined, these results indicate that *lcax-1* plays a complementary role to *cup-5*, and that this role is critical for worm survival, as would be expected for a lysosomal Ca^{2+} importer.

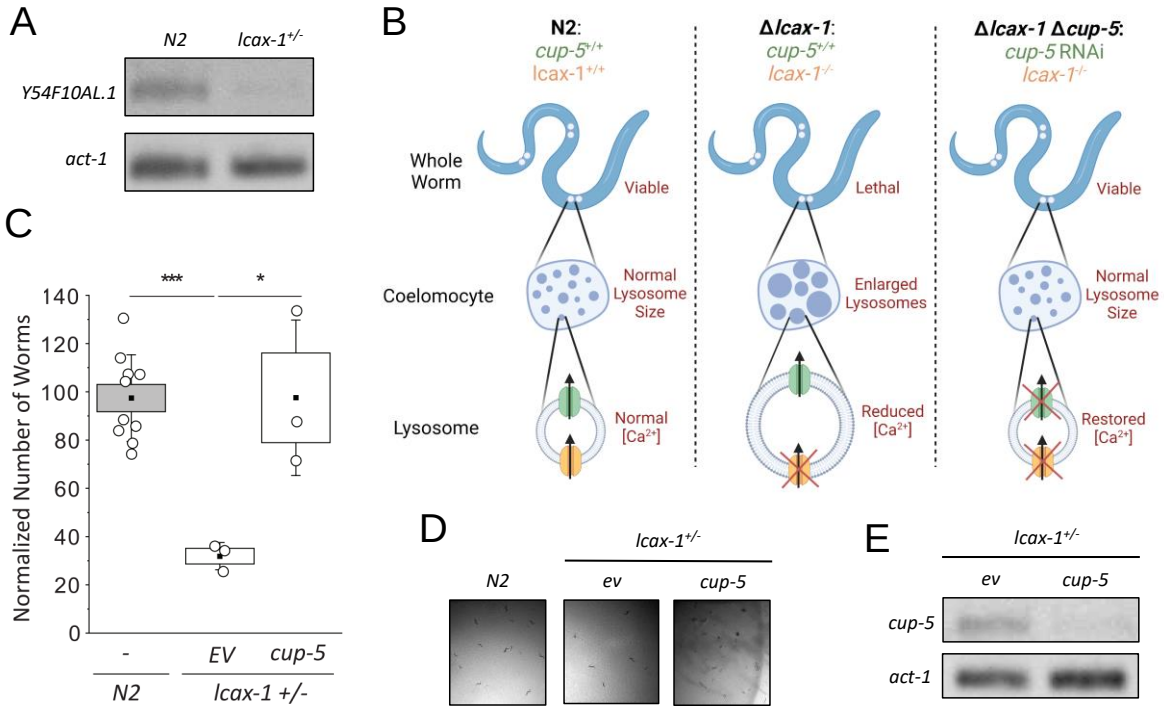

Figure 2.4: Characterization of and survival assay in *lcax-1*$^{+/-}$ worms. (A) RT-PCR analysis of total RNA isolated from N2 or *lcax-1*$^{+/-}$ worms for the *lcax-1* (*Y54F10AL.1*) gene, with actin (*act-1*) used as a control. (B) Conceptual basis for phenotypes observed in *lcax-1*$^{+/-}$ worms. (C) Number of *lcax-1*$^{+/-}$ progeny following RNAi knockdown of *cup-5*. (D) Representative images showing the number of progeny of N2 worms or *lcax-1*$^{+/-}$ worms in plates containing RNAi bacteria of empty vector (*ev*, control) or *cup-5*. (E) RT-PCR analysis of total RNA isolated from *lcax-1*$^{+/-}$ worms for the *cup-5* gene following knockdown of *cup-5*, compared to treatment with empty vector. All experiments performed in triplicate. Boxes and bars represent the s.e.m. and standard deviation, respectively. *p<0.05; ***p<0.001 (one-way ANOVA with Tukey post hoc test).

II.C.4: Lysosome size assay in *lcax-1*$^{+/-}$ worms

To confirm that the lethality of *lcax-1* depletion is due to lysosome dysfunction, we also analyzed lysosome size in these worms by marking coelomocyte lysosomes with Alexa647-labeled duplex DNA. As with GFP secreted into the pseudocoelom, such DNA devices are endocytosed by these scavenger cells and trafficked to lysosomes upon injection into the pseudocoelom. Heterozygous *lcax-1* knockout worms show larger lysosomes than N2 worms, and knockdown of *cup-5* partially rescues lysosome size (**Fig. 2.5A,B**). These results further substantiate that *lcax-1* facilitates Ca^{2+} import into lysosomes, and its loss leads to lysosome storage phenotypes.

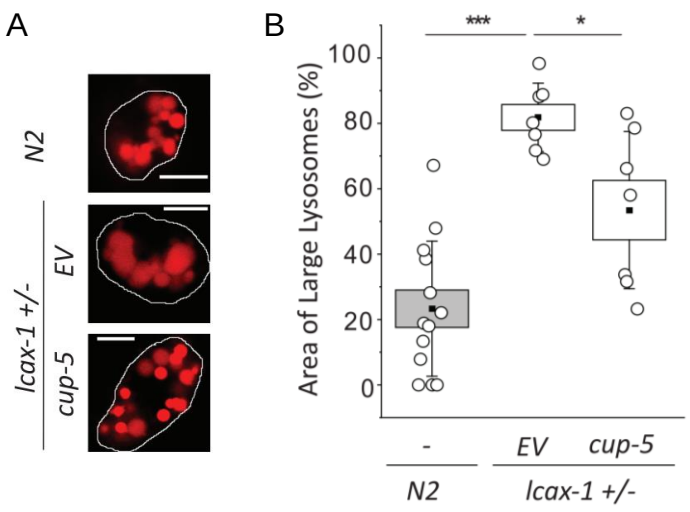

Figure 2.5: Lysosome size assay in lcax-1$^{+/-}$ worms. (A) Representative fluorescence images of lysosomes in coelomocytes of N2 and *lcax-1*$^{+/-}$ worms in the indicated genetic background. Lysosomes are labeled with Alexa647 duplex DNA. (B) Percentage area occupied by enlarged lysosomes in the indicated genetic background (n>5 cells, >50 lysosomes). Scale bar, 5 μm. All experiments performed in triplicate. Boxes and bars represent the s.e.m. and standard deviation, respectively. *p<0.05; ***p<0.001 (one-way ANOVA with Tukey post hoc test).

II.D: Conclusion

By analyzing worm and lysosome phenotypes that result from lysosomal Ca^{2+} imbalance, we have identified the worm homolog of TMEM165 as a potential facilitator of lysosomal Ca^{2+} import. Importantly, these results say nothing about its specific role as a transporter, let alone as an exchanger. This will be the subject of electrophysiological and uptake assays in future chapters. However, evidence in literature suggests that this highly conserved protein acts as a Ca^{2+}/H^{+} exchanger, with physiological relevance in Golgi processes, such as N-glycosylation. Our data here suggest that it may play an additional exchange role in lysosomes, where its dysfunction leads to lysosome storage phenotypes. Of course, it is possible for its effect on lysosome phenotypes to be an indirect result of Golgi dysfunction and defective lysosome-Golgi communication, resulting in global Ca^{2+} dysregulation. This seems unlikely given that *lcax-1* depletion phenocopies *cup-5* depletion, but will be experimentally ruled out by comparing wild-type human LCAX-1 with Golgi-localized LCAX-1 in future chapters.

II.E: References

1. B. G. Chitwood, M. B. Chitwood, An introduction to nematology. *An introduction to nematology*. (1937).

2. H. Fares, I. Greenwald, Genetic analysis of endocytosis in Caenorhabditis elegans: coelomocyte uptake defective mutants. *Genetics*. **159**, 133–145 (2001).

3. S. Surana, J. M. Bhat, S. P. Koushika, Y. Krishnan, An autonomous DNA nanomachine maps spatiotemporal pH changes in a multicellular living organism. *Nat. Commun.* **2**, 340 (2011).

4. K. Chakraborty, P. Anees, S. Surana, S. Martin, J. Aburas, S. Moutel, F. Perez, S. P. Koushika, P. Kratsios, Y. Krishnan, Tissue-specific targeting of DNA nanodevices in a multicellular living organism. *eLife*. **10** (2021), doi:10.7554/eLife.67830.

5. R. Bargal, N. Avidan, E. Ben-Asher, Z. Olender, M. Zeigler, A. Frumkin, A. Raas-Rothschild, G. Glusman, D. Lancet, G. Bach, Identification of the gene causing mucolipidosis type IV. *Nat. Genet.* **26**, 118–123 (2000).

6. M. Sun, E. Goldin, S. Stahl, J. L. Falardeau, J. C. Kennedy, J. S. Acierno, C. Bove, C. R. Kaneski, J. Nagle, M. C. Bromley, M. Colman, R. Schiffmann, S. A. Slaugenhaupt, Mucolipidosis type IV is caused by mutations in a gene encoding a novel transient receptor potential channel. *Hum. Mol. Genet.* **9**, 2471–2478 (2000).

7. S. Merin, N. Livni, E. R. Berman, S. Yatziv, Mucolipidosis IV: ocular, systemic, and ultrastructural findings. *Invest. Ophthalmol.* **14**, 437–448 (1975).

8. C. S. Chen, G. Bach, R. E. Pagano, Abnormal transport along the lysosomal pathway in mucolipidosis, type IV disease. *Proc Natl Acad Sci USA*. **95**, 6373–6378 (1998).

9. R. Bargal, G. Bach, Mucolipidosis type IV: abnormal transport of lipids to lysosomes. *J. Inherit. Metab. Dis.* **20**, 625–632 (1997).

10. H. Fares, I. Greenwald, Regulation of endocytosis by CUP-5, the Caenorhabditis elegans mucolipin-1 homolog. *Nat. Genet.* **28**, 64–68 (2001).

11. N. Narayanaswamy, K. Chakraborty, A. Saminathan, E. Zeichner, K. Leung, J. Devany, Y. Krishnan, A pH-correctable, DNA-based fluorescent reporter for organellar calcium. *Nat. Methods*. **16**, 95–102 (2019).

12. L. Schaheen, H. Dang, H. Fares, Basis of lethality in C. elegans lacking CUP-5, the Mucolipidosis Type IV orthologue. *Dev. Biol.* **293**, 382–391 (2006).

13. B. Grant, D. Hirsh, Receptor-mediated endocytosis in the Caenorhabditis elegans oocyte. *Mol. Biol. Cell*. **10**, 4311–4326 (1999).

14. D. Conte, L. T. MacNeil, A. J. M. Walhout, C. C. Mello, *Curr. Protoc. Mol. Biol.*, in press, doi:10.1002/0471142727.mb2603s109.

15. M. Ottolia, K. D. Philipson, NCX1: mechanism of transport. *Adv. Exp. Med. Biol.* **961**, 49–54 (2013).

16. A. J. Morgan, F. M. Platt, E. Lloyd-Evans, A. Galione, Molecular mechanisms of endolysosomal Ca2+ signalling in health and disease. *Biochem. J.* **439**, 349–374 (2011).

17. V. Sharma, C. He, J. Sacca-Schaeffer, E. Brzozowski, D. E. Martin-Herranz, Z. Mendelowitz, D. A. Fitzpatrick, D. M. O'Halloran, Insight into the family of Na+/Ca2+ exchangers of Caenorhabditis elegans. *Genetics*. **195**, 611–619 (2013).

18. R. L. Lamason, M.-A. P. K. Mohideen, J. R. Mest, A. C. Wong, H. L. Norton, M. C. Aros, M. J. Jurynec, X. Mao, V. R. Humphreville, J. E. Humbert, S. Sinha, J. L. Moore, P. Jagadeeswaran, W. Zhao, G. Ning, I. Makalowska, P. M. McKeigue, D. O'donnell, R. Kittles, E. J. Parra, K. C.

Cheng, SLC24A5, a putative cation exchanger, affects pigmentation in zebrafish and humans. *Science*. **310**, 1782–1786 (2005).

19. C.-Y. Pan, L.-L. Tsai, J.-H. Jiang, L.-W. Chen, L.-S. Kao, The co-presence of Na+/Ca2+-K+ exchanger and Na+/Ca2+ exchanger in bovine adrenal chromaffin cells. *J. Neurochem.* **107**, 658–667 (2008).

20. N. R. Mahapatra, M. Mahata, P. P. Hazra, P. M. McDonough, D. T. O'Connor, S. K. Mahata, A dynamic pool of calcium in catecholamine storage vesicles. Exploration in living cells by a novel vesicle-targeted chromogranin A-aequorin chimeric photoprotein. *J. Biol. Chem.* **279**, 51107–51121 (2004).

21. T. López-Hernández, D. Puchkov, E. Krause, T. Maritzen, V. Haucke, Endocytic regulation of cellular ion homeostasis controls lysosome biogenesis. *Nat. Cell Biol.* **22**, 815–827 (2020).

22. F. Foulquier, M. Amyere, J. Jaeken, R. Zeevaert, E. Schollen, V. Race, R. Bammens, W. Morelle, C. Rosnoblet, D. Legrand, D. Demaegd, N. Buist, D. Cheillan, N. Guffon, P. Morsomme, W. Annaert, H. H. Freeze, E. Van Schaftingen, M. Vikkula, G. Matthijs, TMEM165 deficiency causes a congenital disorder of glycosylation. *Am. J. Hum. Genet.* **91**, 15–26 (2012).

23. R. Zeevaert, F. de Zegher, L. Sturiale, D. Garozzo, M. Smet, M. Moens, G. Matthijs, J. Jaeken, Bone Dysplasia as a Key Feature in Three Patients with a Novel Congenital Disorder of Glycosylation (CDG) Type II Due to a Deep Intronic Splice Mutation in TMEM165. *JIMD Rep.* **8**, 145–152 (2013).

24. J. Jaeken, G. Matthijs, Congenital disorders of glycosylation: a rapidly expanding disease family. *Annu. Rev. Genomics Hum. Genet.* **8**, 261–278 (2007).

25. D. Demaegd, F. Foulquier, A.-S. Colinet, L. Gremillon, D. Legrand, P. Mariot, E. Peiter, E. Van Schaftingen, G. Matthijs, P. Morsomme, Newly characterized Golgi-localized family of proteins is involved in calcium and pH homeostasis in yeast and human cells. *Proc Natl Acad Sci USA*. **110**, 6859–6864 (2013).

26. C. Rosnoblet, D. Legrand, D. Demaegd, H. Hacine-Gherbi, G. de Bettignies, R. Bammens, C. Borrego, S. Duvet, P. Morsomme, G. Matthijs, F. Foulquier, Impact of disease-causing mutations on TMEM165 subcellular localization, a recently identified protein involved in CDG-II. *Hum. Mol. Genet.* **22**, 2914–2928 (2013).

27. S. Schulte Althoff, M. Grüneberg, J. Reunert, J. H. Park, S. Rust, C. Mühlhausen, Y. Wada, R. Santer, T. Marquardt, TMEM165 deficiency: postnatal changes in glycosylation. *JIMD Rep.* **26**, 21–29 (2016).

28. D. Demaegd, A.-S. Colinet, A. Deschamps, P. Morsomme, Molecular evolution of a novel family of putative calcium transporters. *PLoS ONE*. **9**, e100851 (2014).

29. A. M. Dudley, D. M. Janse, A. Tanay, R. Shamir, G. M. Church, *Mol. Syst. Biol.*, in press, doi:10.1038/msb4100004.

30. A.-S. Colinet, P. Sengottaiyan, A. Deschamps, M.-L. Colsoul, L. Thines, D. Demaegd, M.-C. Duchêne, F. Foulquier, P. Hols, P. Morsomme, Yeast Gdt1 is a Golgi-localized calcium transporter required for stress-induced calcium signaling and protein glycosylation. *Sci. Rep.* **6**, 24282 (2016).

31. J. Stribny, L. Thines, A. Deschamps, P. Goffin, P. Morsomme, The human Golgi protein TMEM165 transports calcium and manganese in yeast and bacterial cells. *J. Biol. Chem.* **295**, 3865–3874 (2020).

32. H. Wang, Y. Yang, F. Huang, Z. He, P. Li, W. Zhang, W. Zhang, B. Tang, In situ fluorescent and photoacoustic imaging of golgi ph to elucidate the function of transmembrane protein 165. *Anal. Chem.* **92**, 3103–3110 (2020).

33. A.-S. Roy, S. Miskinyte, A. Garat, A. Hovnanian, M.-A. Krzewinski-Recchi, F. Foulquier, SPCA1 governs the stability of TMEM165 in Hailey-Hailey disease. *Biochimie*. **174**, 159–170 (2020).

34. E. Lebredonchel, M. Houdou, H.-H. Hoffmann, K. Kondratska, M.-A. Krzewinski, D. Vicogne, C. M. Rice, A. Klein, F. Foulquier, Investigating the functional link between TMEM165 and SPCA1. *Biochem. J.* **476**, 3281–3293 (2019).

35. T. A. Reinhardt, J. D. Lippolis, R. E. Sacco, The Ca(2+)/H(+) antiporter TMEM165 expression, localization in the developing, lactating and involuting mammary gland parallels the secretory pathway Ca(2+) ATPase (SPCA1). *Biochem. Biophys. Res. Commun.* **445**, 417–421 (2014).

36. P. Murali, B. P. Johnson, Z. Lu, L. Climer, D. A. Scott, F. Foulquier, G. Oprea-Ilies, V. Lupashin, R. R. Drake, K. L. Abbott, Novel role for the Golgi membrane protein TMEM165 in control of migration and invasion for breast carcinoma. *Oncotarget*. **11**, 2747–2762 (2020).

37. N. A. Snyder, M. V. Palmer, T. A. Reinhardt, K. W. Cunningham, Milk biosynthesis requires the Golgi cation exchanger TMEM165. *J. Biol. Chem.* **294**, 3181–3191 (2019).

38. J.-S. Lee, M.-Y. Kim, E.-R. Park, Y. N. Shen, J.-Y. Jeon, E.-H. Cho, S.-H. Park, C. J. Han, D. W. Choi, J. J. Jang, K.-S. Suh, J. Hong, S. B. Kim, K.-H. Lee, TMEM165, a Golgi transmembrane protein, is a novel marker for hepatocellular carcinoma and its depletion impairs invasion activity. *Oncol. Rep.* **40**, 1297–1306 (2018).

39. K. Chakraborty, K. Leung, Y. Krishnan, High lumenal chloride in the lysosome is critical for lysosome function. *eLife*. **6**, e28862 (2017).

40. K. Schmidt, D. M. Wolfe, B. Stiller, D. A. Pearce, Cd2+, Mn2+, Ni2+ and Se2+ toxicity to Saccharomyces cerevisiae lacking YPK9p the orthologue of human ATP13A2. *Biochem. Biophys. Res. Commun.* **383**, 198–202 (2009).

41. S. van Veen, S. Martin, C. Van den Haute, V. Benoy, J. Lyons, R. Vanhoutte, J. P. Kahler, J.-P. Decuypere, G. Gelders, E. Lambie, J. Zielich, J. V. Swinnen, W. Annaert, P. Agostinis, B. Ghesquière, S. Verhelst, V. Baekelandt, J. Eggermont, P. Vangheluwe, ATP13A2 deficiency disrupts lysosomal polyamine export. *Nature*. **578**, 419–424 (2020).

42. S. Brenner, The genetics of Caenorhabditis elegans. *Genetics*. **77**, 71–94 (1974).

43. V. Au, E. Li-Leger, G. Raymant, S. Flibotte, G. Chen, K. Martin, L. Fernando, C. Doell, F. I. Rosell, S. Wang, M. L. Edgley, A. E. Rougvie, H. Hutter, D. G. Moerman, CRISPR/Cas9 Methodology for the Generation of Knockout Deletions in Caenorhabditis elegans. *G3 (Bethesda)*. **9**, 135–144 (2019).

44. R. S. Kamath, J. Ahringer, Genome-wide RNAi screening in Caenorhabditis elegans. *Methods*. **30**, 313–321 (2003).

III. Validation That Human TMEM165 Imports Ca^{2+} Into Lysosomes

III.A: Introduction

Mutations in TMEM165/LCAX-1 lead to a type of congenital disorder of glycosylation (CDG) characterized by growth and psychomotor retardation, muscular weakness, and skeletal abnormalities (*1*). The mechanism by which these mutations lead to these phenotypes is not completely known. However, patients with CDG caused by LCAX-1 mutations have abnormal protein N-glycosylation and intracellular Ca^{2+} homeostasis, implying that LCAX-1 may have a transport role that necessary for Golgi function (*1*). Four different CDG-causing mutations have been found in LCAX-1: (i) a homozygous mutation in three patients that led to a truncated and non-functional protein; (ii) a homozygous mutation in one patient that led to the missense mutation R126H; (iii) a heterozygous mutation in one patient that led to the compound missense mutations R126C and G304R; and (iv) a homozygous mutation in two patients that led to the missense mutation E108G (**Fig. 3.1**) (*2*, *3*). The R126C, R126H, and G304R mutations do not seem to affect the transport function of LCAX-1, while the E108G mutations reduces Ca^{2+} transport by LCAX-1 (*4*). Thus, the former mutations must affect some other aspect of LCAX-1 that leads to Golgi ionic imbalance and abnormal N-glycosylation.

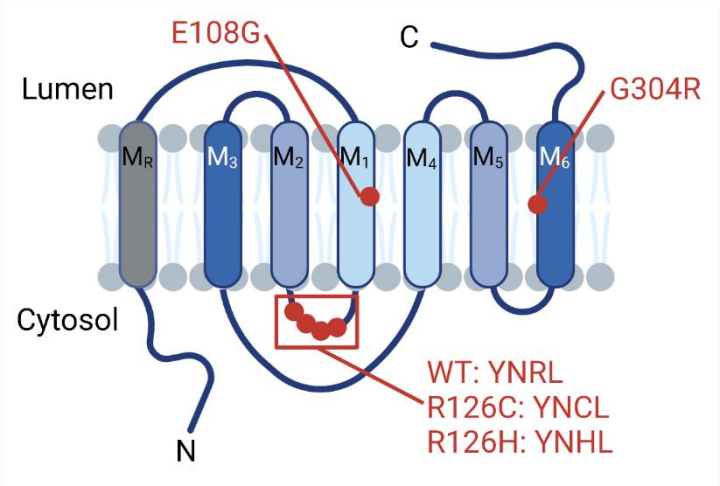

Figure 3.1. LCAX-1 topology and disease mutations. CDG-causing mutations are indicated in red, and transmembrane domain colors indicate internal symmetry. M_R: regulatory membrane domain; M_1-M_6: membrane domains 1-6.

Interestingly, R126 is present within a putative lysosomal targeting signal in LCAX-1 (**Fig. 3.1**) (*2*). Lysosome-targeted membrane proteins possess sorting signals in their cytosolic domains. All of these lysosome targeting signals appear close (6-13 residues) to a transmembrane domain, and are sensitive to

the exact amino acid composition (*5*, *6*). These signals include dileucine-based motifs, such as DXXLL, and tyrosine-based motifs, such as YXXΦ (where Φ represents a bulky hydrophobic residue) (*7*, *8*). For example, the mannose 6-phosphate receptor (MPR) contains a cluster of acidic residues followed by a double leucine (DDS**D**ED**LL**) referred to as an "acidic-cluster-dileucine" (AC-LL) signal (*9*). This allows it to mediate the sorting of newly synthesized M6P-containing lysosomal lumenal proteins from the secretory pathway by trafficking between endosomes and the TGN. On the other hand, lysosomal associated membrane protein 1 (LAMP-1) contains the sequence G**Y**QT**I**, which mediates its direct transport from the TGN to endosomes, to be eventually delivered to late endosomes and lysosomes (*6*). The putative lysosome targeting signal in LCAX-1 is the tyrosine-based **Y**NR**L**, where the arginine (R126) is mutated in multiple patients with CDG (**Fig. 3.1**). Interestingly, while wild-type LCAX-1 localizes to both the lysosome and the Golgi, a single R126H or R126C mutation favors lysosomal localization (*2*). On the other hand, the compound R126C and G304R mutation favors Golgi localization (*2*). Thus, altering the subcellular balance of LCAX-1 to favor either lysosomes or the Golgi seems to lead to CDG phenotypes.

Canonical lysosomal targeting motifs interact with heterotetrametric adaptor protein (AP) complexes, such as AP-1, AP-2, AP-3, and AP-4 (**Fig. 3.2**) (*6*). AP-1 localizes to the TGN and endosomes and contains four subunits: γ, β1, μ1, and σ1 (*10*). These assemble into a globular core composed of the N-terminal domains of γ and β1, and the entire μ1 and σ1 subunits. From this globular core, the C-terminal parts of γ and β1 extend as long, unstructured hinge domains that end in folded "ear" domains. The dileucine-based and tyrosine-based motifs bind to the μ1 and γ-σ1 subunits of AP-1, respectively (**Fig. 3.2**) (*11*, *12*). The hinge domains then bind clathrin and the ear domains bind accessory proteins, contributing to recruitment to the TGN and endosomes via clathrin-coated vesicle intermediates (*13–15*). The other AP complexes exhibit similar quaternary structures, but with slightly different individual subunits (*6*, *10*). All complexes recognize tyrosine-based motifs through their version of the μ subunit (*12*, *16*).

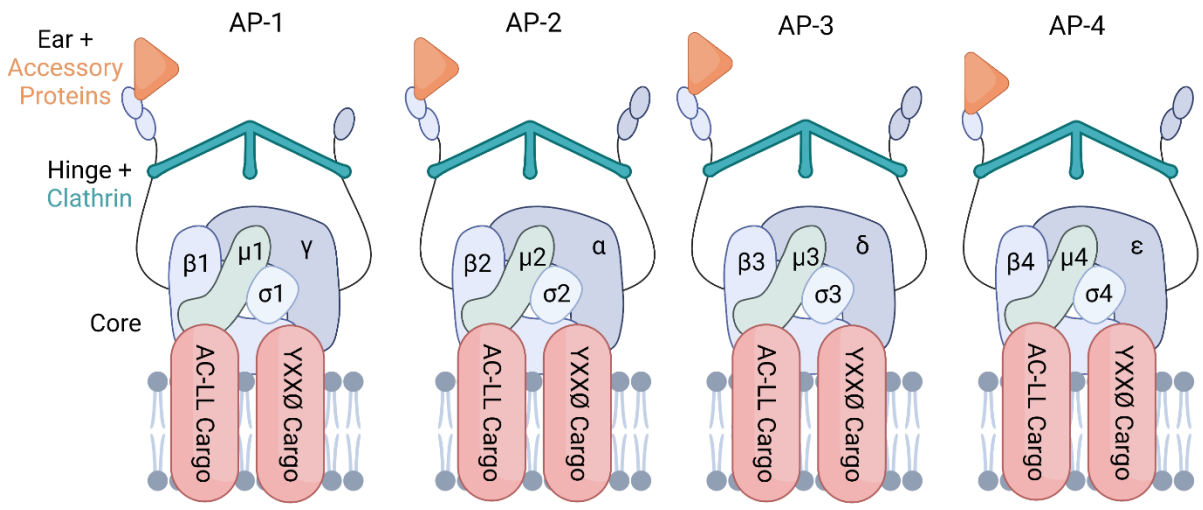

Figure 3.2: Adaptor protein (AP) complexes binding lysosomal membrane protein cargo. AP complexes display similar quaternary structure, but with different individual subunits. Lysosomal membrane proteins with tyrosine-based motifs (YXXΦ) bind the γ/α/δ/ε-σ subunit interface, while those with acidic-cluster-dileucine (AC-LL) motifs bind the μ subunit. The hinge domains bind clathrin and the ear domains bind accessory proteins to transport cargo via clathrin-coated vesicles.

Lysosomal membrane proteins reach lysosomes either directly or indirectly. In the direct pathway, proteins traffic intracellularly from the TGN to early or late endosomes (and then to lysosomes) without travelling to the cell surface (**Fig. 3.3**) (*17*). In the indirect pathway, proteins traffic from the TGN to the plasma membrane, followed by internalization via endocytosis to late endosomes and lysosomes (**Fig. 3.3**) (*17*). The participation of different AP complexes in each pathway is not completely known, and seems to vary for specific membrane protein cargo. However, AP-2 seems to be the predominant complex involved in mediating internalization mechanisms at the cell surface (*18*, *19*). LCAX-1 appears to reach lysosomes via the indirect pathway, through the cell surface (**Fig. 3.3**) (*2*). As expected, the compound R126C and G304R mutations reduce cell surface localization of LCAX-1, and the single R126C or R126H mutations increase cell surface localization of LCAX-1 (*2*). Thus, R126 seems to mediate subcellular localization by regulating protein internalization from the plasma membrane. Indeed, mutating R126 delays internalization of LCAX-1. Interestingly, interaction between the tyrosine-based motif and AP-2 is favored with an arginine at the second X position and a leucine for the Φ residue (as in wild-type LCAX-1) (*20*). Mutating that arginine could impair this interaction and lead to a delay in internalization. On the other hand, mutating that arginine increases localization in acidic

compartments by promoting exit from the TGN and increasing AP-dependent vesicle budding. Thus, it is unclear exactly how R126 mutations alter subcellular distributions, and which AP complexes may be involved.

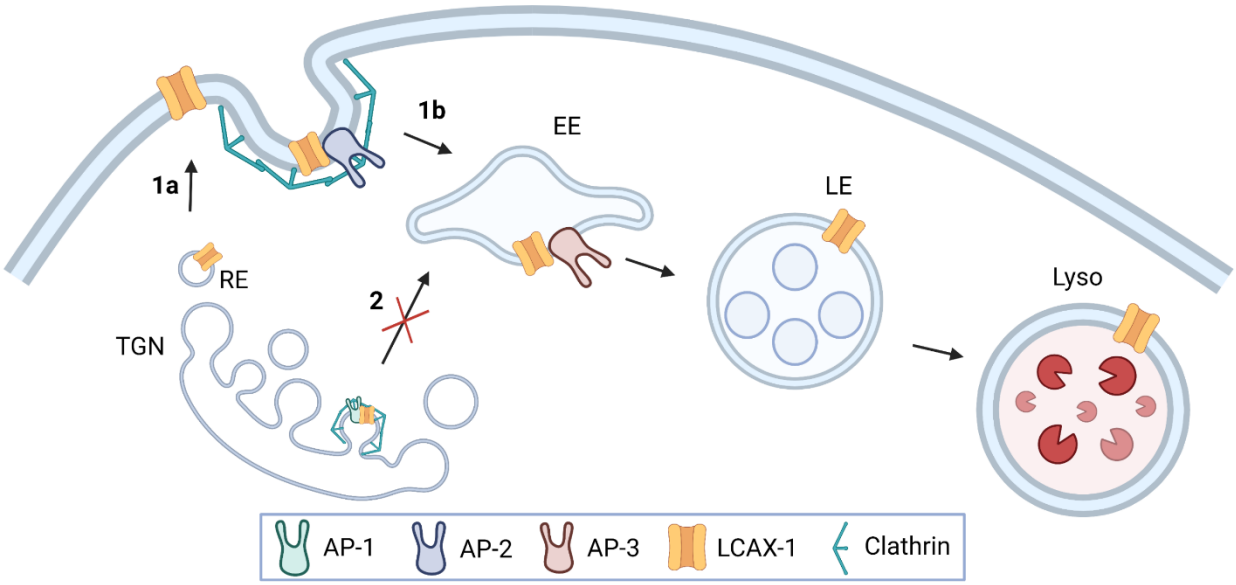

Figure 3.3: Indirect pathway of LCAX-1 transport from the trans-Golgi network (TGN) to lysosomes (Lyso). LCAX-1 is trafficked from the TGN through recycling endosomes (REs) to the cell surface (**1a**), after which it is internalized via clathrin-mediated endocytosis via AP-2 (**1b**). It then traffics through early endosomes (EEs) and late endosomes (LEs) to reach lysosomes. LCAX-1 does not seem to traffic directly from the TGN to EEs via AP-1 (**2**).

The subcellular distribution of these disease mutations implies multiple things that are relevant to our study. First, wild-type LCAX-1 is present on mammalian lysosomes, the TGN, and the plasma membrane. Second, reducing either the Golgi population or the lysosomal population of LCAX-1 leads to disease phenotypes. Third, we can isolate lysosome-specific roles of LCAX-1 by comparing the effects of these mutants. Combined, these disease mutants allow us to study physiologically relevant Ca^{2+} import function of LCAX-1 on lysosomes.

III.B: Materials and Methods

III.B.1: Chemicals and reagents

Modified oligonucleotides were purchased from IDT (USA), subjected to ethanol precipitation and quantified using UV absorbance. Chemicals used for the previously synthesized Rhod-5F-azide were

purchased from Sigma and Alfa Aesar as previously described (*21*). DCF used for previously described conjugation was purchased from Fisher Scientific (*22*). Vacuolin-1 was purchased from Cayman Chemical. EGTA, ampicillin, kanamycin, carbenicillin, adenosine triphosphate, Triton X-100, bovine serum albumin, glyoxal, methane sulfonic acid, HEPES, calcium hydroxide, magnesium chloride, and N-methyl-D-glucamine were purchased from Sigma. Monodisperse silica microspheres were obtained from Cospheric. TMR-dextran (10 kDa) and Fura Red were purchased from Thermo Fisher Scientific. Rabbit anti-TMEM165 was purchased from ProteinTech. Mouse anti-GM130 was purchased from Santa Cruz Biotechnology. Alexa488 Goat anti-Rabbit, Alexa647 Goat anti-Mouse, and GFP Polyclonal Antibody Alexa555 were purchased from Thermo Fisher Scientific. Paraformaldehyde and glycine were purchased from Fisher Scientific. Anti-pan cadherin antibody was purchased from Abcam.

III.B.2: Mammalian cell culture, plasmids, and transfection

HeLa cells and SK-BR-3 cells were purchased from ATCC and cultured according to recommended guidelines. LCAX-1 KO HeLa cells were purchased from Creative Biogene. Cells were cultured in Dulbecco's Modified Eagle's Medium (DMEM) (Invitrogen Corporation, USA) containing 10% heat-inactivated fetal bovine serum (FBS) (Invitrogen Corporation, USA), 100 U/mL penicillin and 100 μg/mL streptomycin (Gibco), and maintained at 37°C under 5% CO_2. Cells were passaged using 0.25% Trypsin-EDTA (Gibco) and plated at 50-60% confluency for transfection.

For mammalian expression of LCAX-1 fused to EGFP, the cDNA of TMEM165 (Harvard Medical School Plasmid Database) was cloned into the pEGFP-N1 plasmid, which was obtained from M. Fransen (KU Leuven). Cloning was done using Gibson assembly techniques. Briefly, inserts and backbones were amplified using polymerase chain reaction (PCR), using LongAmp Taq DNA Polymerase (NEB) and primers with 5' overhangs enabling 15-20bp overlap of the insert and backbone. Amplification was verified on 0.8% Agarose gel before digestion of starting templates with DpnI (NEB) and purification of PCR products (DNA Clean and Concentrator, Zymo Research). At least 2-fold molar excess of insert was added to the backbone for Gibson reaction using the Gibson Assembly Master Mix (NEB). The assembly reaction was transformed into competent DH5α E. coli cells, and colonies grown in

kanamycin were inoculated in liquid LB with ampicillin. The plasmid DNA was isolated via minipreparation (GeneJET Plasmid Miniprep Kit, Thermo Scientific) and verified by sequencing, using forward and reverse primers upstream and downstream of the ligation sites. For mammalian expression of LCAX-1 fused to DsRed, the DNA for DsRed (a kind gift from B. Dickinson at the University of Chicago) was cloned into the LCAX-1-EGFP plasmid, replacing EGFP, using Gibson assembly techniques.

For mammalian expression of LCAX-1 disease mutants fused to EGFP, the above construct was subject to site-directed mutagenesis using the Q5 Site-Directed Mutagenesis Kit (NEB). The R126C mutant was generated using forward primer GCGCTATAACTGCCTGACCGT and reverse primer ATTGCCATGATGGCTGCTATAAAAAATG. The R126H mutant was generated using the forward primer CGCTATAACCACCTGACCGTG and the reverse primer CATTGCCATGATGGCTGC. The G304R mutant was generated using the forward primer GACAATCATAAGAGGCATCGTTTTTTTG and the reverse primer ACAGTTCTGACAGAGATTTTC. Resulting plasmids were verified by sequencing. The GFP-Rab7 plasmid was a kind gift from Richard Pagano (Addgene plasmid #12605).

HeLa cells were transiently transfected with the respective plasmids using Lipofectamine 3000 (Thermo Fisher) according to manufacturer protocols. After incubation for 4 hours, the transfection medium was replaced with fresh DMEM. Imaging or electrophysiology experiments were performed on cells 48h following transfection.

III.B.3: *C. elegans* strains

The strain with a heterozygous knockout of *lcax-1* was generated and provided by D. Moerman (University of British Columbia) using CRISPR/Cas9 technology and verified by sequencing (*23*). Heterozygous *lcax-1*$^{+/-}$ worms are marked by pharyngeal GFP, homozygous *lcax-1*$^{+/+}$ progeny are functionally wild-type but lack GFP, and homozygous *lcax-1*$^{-/-}$ progeny are embryonic lethal. The genotype of this worm is *Y54F10AL.1(gk5484[loxP + Pmyo-2::GFP::unc-54 3' UTR + Prps-27::neoR::unc-54 3' UTR + loxP])/+ III*. Transgenic strains expressing human LCAX-1 variants were generated by microinjecting of plasmid DNA into *lcax-1*$^{+/-}$ gonads to produce extrachromosomal arrays.

The injected plasmid contained an LCAX-1 variant with the promoter region of *lcax-1* and the 3' UTR of *unc-54*. Pharyngeal mCherry was used as an injection marker. The plasmid construction, worm injection, and verification by sequencing was performed by SunyBiotech (Fujian, China) using established protocols.

III.B.4: Survival assay in *C. elegans*

The *N2*, and *Y54F10AL.1(gk5484[loxP + Pmyo-2::GFP::unc-54 3' UTR + Prps-27::neoR::unc-54 3' UTR + loxP])/+ III* nematode strains were used for this assay, which was performed as previously described in **Section II.B.4**. Briefly, five L4 worms of the indicated strain were placed on OP50 plates. The worms were allowed to grow for 24 hours and lay eggs, after which the adult worms were removed from the plates. Eggs were allowed to hatch and grow into adults for 3 days. The worm plates were imaged under an Olympus SZX-Zb12 Research Stereomicroscope (Olympus Corporation of the Americas) with a Zeiss Axiocam color CCD camera (Carl Zeiss Microscopy). Images were then analyzed using ImageJ to count the number of adult worms per plate.

III.B.5: Lysosome size assay in *C. elegans*

The *N2*, and *Y54F10AL.1(gk5484[loxP + Pmyo-2::GFP::unc-54 3' UTR + Prps-27::neoR::unc-54 3' UTR + loxP])/+ III* nematode strains were used for this assay, which was performed as previously described in **Section II.B.5**. Briefly, five L4 worms were placed on OP50 plates. After 24 hours of laying eggs, the adult worms were removed from plates. After 3 days, the adult worms are imaged to check for lysosome size differences. Worms were imaged on a confocal microscope for a DNA duplex with Alexa647 (**Table 3.1**). Lysosome areas were measured using ImageJ, and enlarged lysosomes were defined as those whose diameter is ≥33% of the diameter of the largest lysosomes in N2 worms. Lysosome size data were plotted as the percentage of area occupied by large lysosomes relative to the total lysosomal area.

Table 3.1: **Sequences of DNA oligos used in this study.** D1 and D2 were used for labeling of coelomocyte lysosomes for lysosome size assay. C1, C2, and C3 were used for lysosomal Ca^{2+} imaging in worms. OG-C1, C2, and C3 were used for lysosomal Ca^{2+} imaging in mammalian cells.

Sequence Name	DNA sequence information
D1	5'-DBCO-ATC AAC ACT GCA CAC CAG ACA GCA AGA TCC TAT ATA TA-3'
D2	5'-Alexa 647-TA TAT ATA GGA TCT TGC TGT CTG GTG TGC AGT GTT GAT-3'
C1	5'-Amino-ATA ACA CAT AAC ACA TAA CAA AAT ATA TAT CCT AGA ACG ACA GAC AAA CAG TGA GTC-3'
C2	5'-ATTO647-TAT ATT TTG TTA TGT GTT ATG TGT TAT-3'
C3	5'-DBCO-GAC TCA CTG TTT GTC TGT CGT TCT AGG ATA-3'
OG-C1	5'-Oregon Green- ATA ACA CAT AAC ACA TAA CAA AAT ATA TAT CCT AGA ACG ACA GAC AAA CAG TGA GTC-3'

III.B.6: RT-PCR

The extrachromosomal expression of LCAX-1 was confirmed by probing messenger RNA levels of the candidate gene, assayed by RT-PCR. Briefly, total RNA was isolated using the Trizol-chloroform method and 1 ug total RNA was converted to complementary DNA using oligo-dT primers and SuperScriptIV RT according to manufacturer protocols. Then, 5 µL of cDNA product was used to setup up a PCR using gene-specific primers for *Y54F10AL.1* (F: ATTCCACCGATTTCCACCCC, R: CTTCTTGGCCCTCATTCGGT, 527 bp), TMEM165 (F: CACCAGCAGCTCCAGTTCAT, R: TGAGAGCGATCACCCCATTC, 544 bp), and *act-1* (F: TGCAGAAGGAAATCACCGCT, R: AGAAAGCTGGTGGTGACGAT, 251 bp) where indicated. PCR products were separated on a 0.8% agarose-Tris base, acetic acid, and EDTA (TAE) gel.

III.B.7: Colocalization in live cells

To evaluate the subcellular localization of LCAX-1 mutants, we analyzed colocalization with TMR-dextran or FITC-dextran in live cells. In both experiments, COS7 cells were transfected with the indicated variant of LCAX-1-EGFP or LCAX-1-DsRed with Lipofectamine 3000 according to manufacturer protocol and either imaged or fixed 48h later. In the live cell experiments, transfected COS7 cells were pulsed with 1 mg/mL TMR-dextran or 5 mg/mL FITC-dextran for 1h and chased for 16h prior to imaging. Where indicated, COS7 cells were also incubated in 5µM vacuolin-1 for 24h prior to imaging on a confocal microscope (details in **Section III.B.14**). Pearson's correlation coefficient (PCC) was

calculated using software in ImageJ, both before and after a pixel shift. No threshold PCC was used for colocalization with TMR-dextran or FITC-dextran.

III.B.8: Immunofluorescence

In anti-GM130 experiments, COS7 cells were transfected with the indicated variant of LCAX-1-EGFP. Two days later, they were washed 3x with PBS and fixed using 4% paraformaldehyde at RT for 10min. Then, cells were washed 3x with PBS and permeabilized with 0.2% Triton X-100 for 5min prior to washing again and blocking with 3% BSA for 60min. Cells were then incubated with 1:1000 anti-GM130 and 1:1000 anti-TMEM165 in 0.3% BSA overnight at 4°C. Finally, cells were washed 3x with PBS and incubated in 1:1000 goat anti-mouse Alexa647 and 1:1000 goat anti-rabbit Alexa488 in 0.3% BSA for 60min before imaging on a confocal microscope (details in **Section III.B.14**). Above threshold PCC was used for colocalization with GM130.

For immunofluorescence to check LCAX-1 expression, HeLa cells or LCAX-1 KO HeLa cells were fixed, permeabilized, and blocked as above. Cells were then incubated with 1:1000 anti-TMEM165 in 0.3% BSA in PBS overnight at 4°C. Cells were washed 3x with PBS and incubated in 1:1000 goat anti-rabbit Alexa488 in 0.3% BSA in PBS for 60min before imaging on a confocal microscope (details in **Section III.B.14**). Background-subtracted whole cell intensity was used to evaluate expression levels.

For immunofluorescence in SK-BR-3 cells, cells were fixed, permeabilized, and blocked as above. Cells were then incubated with 1:1000 anti-TMEM165 and either 1:100 anti-LAMP1 or 1:1000 anti-GM130 in 0.3% BSA in PBS overnight at 4°C. Cells were washed 3x with PBS and incubated in 1:1000 goat anti-rabbit Alexa488 and 1:1000 goat anti-mouse Alexa647 in 0.3% BSA in PBS for 60min before imaging on a confocal microscope (details in **Section III.B.14**).

For immunofluorescence in cells with swollen lysosomes, HeLa cells were pre-treated with 5μm vacuolin-1 prior to fixation. Two days later, cells were washed 3x with PBS and fixed using 1% glyoxal solution in PBS for 5 minutes. Then, cells were washed 3x with PBS and permeabilized with 0.2% Triton X-100 for 10 minutes. Then, cells were washed 3x with PBS and blocked with 3% BSA for 1 hour. Cells were then incubated in 1:100 mouse anti-LAMP1 and/or 1:200 rabbit anti-TMEM165 in 0,3% BSA

overnight at 4°C. Finally, cells were washed 3x with PBS and incubated in 1:1000 goat anti-rabbit Alexa488 and/or 1:1000 goat anti-mouse Alexa647 in 0.3% BSA for 1 hour before imaging on a confocal microscope (details in **Section III.B.14**).

For surface-only immunostaining, HeLa cells were first transfected with LCAX-1-EGFP. Two days later, cells were fixed with 2% PFA for 10 minutes on ice and washed 3x with ice-cold PBS. Cells were then blocked with 3% BSA with 0.3M glycine in PBS for 30 minutes. Cells were then incubated in 1:100 anti-GFP Alexa555 and 1:500 rabbit anti-pan cadherin in blocking buffer overnight at 4°C. After washing 3x with PBS, cells were incubated in 1:1000 goat anti-rabbit Alexa647 in blocking buffer for 1 hour before washing and imaging on a confocal microscope (details in **Section III.B.14**).

III.B.9: Lysosomal Ca^{2+} imaging in *C. elegans*

In vivo lysosomal pH and Ca^{2+} measurements were made using *CalipHluor2.0* according to protocols and calibrations established previously (*21*, *22*). The methods used are summarized briefly below.

III.B.9.a: CalipHluor 2.0 preparation

In *CalipHluor 2.0*, the Ca^{2+} indicator, Rhod-5F (O), fluoresces upon binding Ca^{2+} (*21*). The K_d of Rhod-5F for Ca^{2+} binding is pH dependent, which is why *CalipHluor 2.0* incorporates a pH sensing dye dichlorofluorescein (DCF, G) (*22*). For ratiometric quantification of Ca^{2+} and pH, we incorporate Alexa Fluor 647 (R) as a reference dye. Thus, the G/R ratio maps the pH at every pixel and is used to obtain pH-corrected values of Ca^{2+} based on the O/R ratio at single-lysosome resolution. *CalipHluor 2.0* was prepared according to previously reported procedure (*22*). Oligonucleotides used to form *CalipHluor 2.0* are listed in **Table 3.1**.

III.B.9.b: In vitro pH and calcium calibration

The calibration curve used here to make pH measurements with the DCF/Alexa647 (G/R) ratio from *CalipHluor 2.0* was prepared in ref. 64. The resulting curve was fitted to Equation 1:

$$pH = pH_{1/2} + 0.3\ln\left(\frac{K_1 - K_2}{Y - K_2} - 1\right) \qquad \text{Eq. 1}$$

where K_1, K_2, and $pH_{1/2}$ represent parameters from a Boltzmann fit of the calibration curve and Y represents the G/R ratio. An *in vitro* bead calibration of *CalipHluor 2.0* at pH 5 on the same day of measurements (see below) was used to correct for day-to-day variation in the calibration curve. The K_d curve used to correct for the effect of pH on Rhod-5F binding to Ca^{2+} was determined in ref. 45. The curve was fitted to Equation 2:

$$K_d = 1.03 + (5.14 * 10^{12} * e^{-\frac{pH}{0.189}}) + (3.108 * 10^{6} * e^{-\frac{pH}{0.412}}) \qquad \text{Eq. 2}$$

To calculate the effect of pH on the fold-change in the Rhod-5F/Alexa647 (O/R) ratio of *CalipHluor 2.0* from 0.1 µM to 1 mM free Ca^{2+}, we used the fold-change calibration curve prepared in ref. 11. The curve was fitted to Equation 3 to get the minimum O/R (O/R at 0.1 µM Ca^{2+}) as a function of pH and normalized to the maximum O/R (O/R at 1 mM Ca^{2+}):

$$O/R_{min} = \frac{1}{4.24+0.12*e^{0.5*pH}} \qquad \text{Eq. 3}$$

An *in vitro* bead calibration of *CalipHluor 2.0* was performed on the same day as measurements were made to correct for day-to-day variation in fold-change, as previously described (*21*, *22*). Briefly, 500 nM of *CalipHluor 2.0* was incubated with 0.6 um monodisperse silica beads in 20 mM sodium phosphate buffer, pH 5.1 containing 500 mM NaCl for 30mins at RT. The beads were washed 3x by spinning at 10k rpm for 10mins at RT. Beads absorbed with *CalipHluor 2.0* were incubated with clamping buffer (HEPES (10 mM), MES (10 mM), sodium acetate (10 mM), EGTA (10 mM), KCl (140 mM), NaCl (500 mM), and $MgCl_2$ (1 mM)) for 30 mins at RT containing 0.1 µM or 1 mM free calcium buffers at pH 5. Beads absorbed with *CalipHluor 2.0* were then imaged in DCF (G), Rhod-5F (O), and Alexa647 (R) on a glass slide under the same exposure settings as used for measurements later. Background-subtracted G, O, and R intensities were used to calculate G/R at pH 5.1 to correct Eq. 1 and O/R_{min} and O/R_{max} to correct Eq. 3.

III.B.9.c: In vivo pH and calcium measurements

pH and Ca^{2+} measurements in worms were carried out as previously described for *CalipHluor*$_{Ly}$, but with *CalipHluor 2.0*. *CalipHluor 2.0* is endocytosed by scavenger receptors and marks lysosomes of

coelomocytes in live worms (*21, 24–26*). Briefly, 500 nM *CalipHluor 2.0* was microinjected into the pseudocoelom of young adult worms with the indicated genetic background. After microinjections, worms were incubated for 2h for maximum labeling of coelomocyte lysosomes. Worms were then anesthetized using 40 mM sodium azide in M9 solution and imaged by wide-field microcopy (details in image acquisition section). Resulting images were background subtracted before calculating the G/R and O/R ratios for each lysosome. Equation 1 was then used to calculate the pH at every lysosome. Equation 2 was then used to calculate the K_d of *CalipHluor 2.0* for Ca^{2+} at every lysosome. Equation 3 was then used to calculate the O/R_{min} and O/R_{max} of *CalipHluor 2.0* at every lysosome. Finally, the pH-corrected free $[Ca^{2+}]$ was calculated for every lysosome using Equation 4:

$$[Ca^{2+}] = K_d * [\frac{O/R - O/R_{min}}{O/R_{max} - O/R}] \quad \text{Eq. 4}$$

Three independent experiments, each with >5 worms, were made for pH and $[Ca^{2+}]$ values for each genetic condition. Lysosomes with O/R values below O/R_{min} were designated as having a $[Ca^{2+}]$ less than 0.1 µM. Lysosomes with O/R values above O/Rmax were designated as having a $[Ca^{2+}]$ above 1 mM. To estimate a maximum $[Ca^{2+}]$ for the exchanger-dead mutant worms, lysosomes with <0.1 µM $[Ca^{2+}]$ were counted as having 0.1uM $[Ca^{2+}]$.

III.B.9.d: pH and -log[Ca^{2+}] maps

Images were acquired in three channels (DCF, Rhod-5F, and Alexa647) by widefield microscopy to quantify pH and $[Ca^{2+}]$ at single-lysosome resolution as described above. All image calculations below were done using ImageJ modules. To show representative pH and $[Ca^{2+}]$ maps, images were background-subtracted and smoothed. The Alexa647 image was then duplicated and thresholded to create a binary mask. Background-subtracted DCF, Rhod-5F, and Alexa647 images were then multiplied with the binary mask to get processed images. The processed DCF and Rhod-5F images were divided by the processed Alexa647 image to get a pseudocolor G/R and O/R image, respectively. The G/R image was then plugged into Equation 1 to get a pseudocolored pH map. The pseudocolored pH map was then used to get a pseudocolored K_d map using Equation 2 and a pseudocolored O/R_{min} map using Equation 3. The O/R

image, K_d map, and O/R_{min} map were then used to get a $[Ca^{2+}]$ map using Equation 4. Finally, to compare maps on an appropriate calibration scale, the -log$[Ca^{2+}]$ map was calculated.

III.B.10: Lysosomal Ca^{2+} imaging in cells

Lysosomal pH and Ca^{2+} measurements in live mammalian cells were made using similar methods as in live worms, but with *CalipHluor*^{mLy}, which contains pH sensor Oregon Green 488 (OG488) instead of DCF. As such, the preparation and calibration of *CalipHluor*^{mLy} were done using the sequences in **Table 3.1** and the equations above, but with the appropriate calibration curve for OG488, as previously described (*21*).

To make measurements in HeLa cells, the appropriate chase time was first determined by analyzing colocalization with endosomal markers. For colocalization with late endosomes, HeLa cells were transfected with Rab7-EGFP. Two days later, cells were treated with 500 nM Alexa647-labeled dsDNA in HBSS for 15 minutes before washing the dsDNA off with PBS and chasing in DMEM for the indicated amount of time (3 hr or 5 hr). For colocalization with lysosomes, HeLa cells were treated with 5 mg/mL FITC-dextran in DMEM for 3 hours. Cells were then washed 3x with PBS and incubated overnight in DMEM. Cells were then treated with 500 nM Alexa647-labeled dsDNA in HBSS for 15 minutes before washing the dsDNA off with PBS and chasing in DMEM for the indicated amount of time (3 hr or 5 hr). For both colocalization experiments, cells were imaged on a confocal microscope (see image acquisition section) in the relevant channels before determining colocalization using Pearson's Correlation Coefficient (PCC).

pH and Ca^{2+} measurements were then made by incubating HeLa cells in 500 nM *CalipHluor*^{mLy} in HBSS for 15 minutes, washing 3x with PBS, and then incubating cells in HBSS for 5 hr. Cells were then imaged on a widefield microscope (see image acquisition section) in the relevant channels. Resulting images were background subtracted before calculating the G/R and O/R ratios for each lysosome. The above equations were used to calculate the pH and Ca^{2+} concentration for individual lysosomes. Three independent experiments, each with >50 lysosomes each, were made for pH and $[Ca^{2+}]$ values for each genetic condition. Lysosomes with O/R values below O/R_{min} were designated as having a $[Ca^{2+}]$ less than

0.5 µM. Lysosomes with O/R values above O/Rmax were designated as having a [Ca^{2+}] above 0.5 mM. Lysosomes with pH<4 were not included in Ca^{2+} measurements. pH and -log[Ca^{2+}] maps were made as described above.

III.B.11: Cytosolic Ca^{2+} dynamics

To evaluate the effect of LCAX-1 activity on cytosolic Ca^{2+} buffering, we used the ratiometric Ca^{2+} dye Fura Red according to manufacturer protocols. First, HeLa (WT or LCAX-1 KO) or SK-BR-3 cells were mock-transfected or transfected with the indicated mutant of LCAX-1-EGFP. Two days later, cells were pulsed with 10 µM Fura Red in HBSS for 15 min, washed 3x with PBS, and then chased for 30min in HBSS. Prior to imaging in Tyrode's solution (NaCl 134 mM, KCl 2.68 mM, $CaCl_2$ 1.8 mM, $MgCl_2$ 1.05 mM, NaH_2PO_4 0.417 mM, $NaHCO_3$ 11.9 mM, d-glucose 5.56 mM), cells were washed 3x again with PBS. The imaging protocol was set up to take an LCAX-1-EGFP image at the start, and Fura Red images every 5 seconds. After 8 image acquisitions, the solution was replaced with Tyrode's solution supplemented with 100 µM ATP. Images were taken for 5 minutes. Fura Red images were then background-subtracted by the intensity of an ROI outside the cell. The 440/647 image was then duplicated and thresholded to create a binary mask. Both images were multiplied by the mask to create processed 440/647 and 488/647 images. The processed 440/647 image was then divided by the processed 488/647 image to get a 440/488 (excitation ratio) pseudocolored map. For representative images, the pseudocolored maps at indicated time points were then smoothed. The 440/488 ratio was then plotted as a function of time, normalized to 1 at t=0s. To calculate the rate of cytosolic Ca^{2+} removal, the slope of the linear fit of the decreasing portion of the 440/488 curves was calculated.

III.B.12: Whole-cell electrophysiology

Whole-cell recordings were performed with an Axopatch 200 A amplifier (Molecular Devices) and digitized using an NI-6251 DAQ (National Instruments). The amplifier and digitizer were controlled using WinWCP software (Strathclyde Electrophysiology Software). All data were sampled at 10 kHz and later filtered at 1 kHz using a 4-pole lowpass Bessel filter. The borosilicate glass capillaries (Sutter) with dimensions of 1.5 mm x 0.86 mm (OD/ID) were pulled using a Sutter P-97 micropipette puller. Patch

pipettes were then positioned using an MP325 motorized manipulator (Sutter). The buffers used for the bath and pipette solutions were designed to reduce background currents from ions other than calcium. The extracellular/bath solution contained (in mM): 140 NMDG, 10 HEPES, 1 $MgCl_2$, 5 EGTA, 5 glucose, and $Ca(OH)_2$ to get 30 nM free [Ca^{2+}], and was set to pH 7.5 with MSA. The pipette solution contained (in mM): 140 NMDG, 10 HEPES, 1 $MgCl_2$, 5 EGTA, and variable $Ca(OH_2)$ to get either 1 nM , 1 µM, or 1 mM free [Ca^{2+}], and was set to pH 7.5 with MSA. Total calcium at each pH was calculated to maintain the indicated amount of free calcium using https://somapp.ucdmc.ucdavis.edu/pharmacology/bers/maxchelator/CaMgATPEGTA-TS.htm for each experiment. Mock-transfected or LCAX-1-EGFP transfected HeLa cells were washed in PBS before incubating in the indicated extracellular solution for whole-cell clamping. Whole-cell voltage clamping was performed according to established protocols (*27*). Voltage was ramped from -100mV to +100mV. As indicated in **Figure 3.16B**, positive voltage is taken as cytosol-positive, and positive current is taken as positive current moving outward from the cytosol. Current density was calculated by normalizing the current with whole-cell capacitance, which was determined immediately after establishing the whole-cell patch to estimate cell surface area. Representative traces shown were smoothed using 24-point adjacent-averaging. Where indicated, the current or current density at +100mV was plotted for each condition.

III.B.13: Image acquisition

Widefield microscopy was carried out on an IX83 inverted microscope (Olympus Corporation of the Americas, Center Valley, PA, USA) using a 60X, 1.4 numerical aperture (NA), differential interference contract (DIC) oil immersion objective (PLAPON) and Evolve Delta 512 EMCCD camera (Photometrics, USA), and controlled using MetaMorph Premier Ver 7.8.12.0 (Molecular Devices, LLC, USA).

For *CalipHluor2.0* imaging in worms, images were acquired with an exposure of 150ms and EM gain of 150 for DCF, an exposure of 150ms and EM gain of 150 for Rhod-5F, and an exposure of 50ms and EM gain of 50 for Alexa647. DCF channel images were obtained using a 480/20 band-pass excitation filter, 520/40 band-pass emission filter, and an 89016 dichroic; Rhod-5F channel images were obtained

using a 545/25 band-pass excitation filter, 595/50 band-pass emission filter, and an 89016 dichroic; and Alexa647 channel images were obtained using a 640/30 band-pass excitation filter, 705/72 band-pass emission filter, and an 89016 dichroic.

For *CalipHluor*^{mLy} imaging in cells, images were acquired with an exposure 200ms and EM gain of 200 for OG488, an exposure of 200ms and EM gain of 200 for Rhod-5F, and an exposure of 200ms and EM gain of 200 for Alexa647. OG488 channel images were obtained using a 480/20 band-pass excitation filter, 520/40 band-pass emission filter, and an 89016 dichroic; Rhod-5F channel images were obtained using a 545/25 band-pass excitation filter, 595/50 band-pass emission filter, and an 89016 dichroic; and Alexa647 channel images were obtained using a 640/30 band-pass excitation filter, 705/72 band-pass emission filter, and an 89016 dichroic.

For cytosolic Ca^{2+} recording cells, Fura Red was recorded by excitation at 440nm or 488nm and emission at 647nm. 440/647 images were acquired using a 430/24 band-pass excitation filter, 705/72 band-pass emission filter, and an 89016 dichroic with an exposure of 150ms and EM gain of 150. 488/647 images were acquired using a 480/20 band-pass excitation filter, 705/72 band-pass emission filter, and an 89016 dichroic with an exposure of 200ms and EM gain of 200.

To check expression of LCAX-1 in the relevant experiments, EGFP images were acquired using a 480/20 band-pass excitation filter, 520/40 band-pass emission filter, and an 89016 dichroic.

Confocal images were captured with a Leica TCS SP5 II STED laser confocal microscope (Leica Microsystems, Buffalo Grove, IL, USA) equipped with a 63X, 1.4 NA, oil immersion objective. GFP and Alexa488 were excited using an argon laser with wavelength of 488nm; Alexa647 was excited using an He-Ne laser with wavelength of 633nm; and TMR, DsRed, and Alexa555 were excited using a DPSS laser at 561nm. All emissions were filtered using an acousto-optical beam splitter (AOBS) with settings suitable for each fluorophore and recorded using hybrid detector.

III.B.14: Image analysis

Images were analyzed using Fiji (NIH, USA). For lysosomal pH and Ca^{2+} measurements with *CalipHluor 2.0*, regions of coelomocytes containing single isolated lysosomes in each Alexa647 (R)

image were manually selected and the coordinates were saved in the ROI plugin. For each coelomocyte, the most focused plane was manually selected in the Alexa647 channel and used for all other channels. For background computation, a nearby region outside of the worm was manually selected and saved as an ROI. The same regions were selected in the DCF (G) and Rhod-5F (O) images by recalling the ROIs. After background subtraction, the mean intensity for each endosome (G, O, and R) was measured and exported to OriginPro (OriginLab, USA). Ratios of G to R intensities (G/R) and O to R intensities (O/R) were obtained by dividing the mean intensity of a given lysosome in the G or O image by the corresponding intensity in the R image. Representative images are shown as pseudo-colored maps, where G, O, and R images were modified by thresholding in ImageJ before dividing and undergoing the relevant image calculations in ImageJ. Analogous image analysis methods were used to make lysosomal Ca^{2+} measurements in cells with *CalipHluor*^{mLy} and cytosolic Ca^{2+} measurements in cells with Fura Red.

III.B.15: Statistics

For statistical analysis between two samples, a two-sample two-tailed test assuming unequal variance was conducted. For comparison of multiple samples, one-way ANOVA with a post hoc Tukey test was conducted. All statistical analysis was performed in Origin.

III.C: Results and Discussion

III.C.1: Subcellular localization of WT LCAX-1

As discussed in **Section II.A.1**, previous work has revealed that wild-type LCAX-1 appears to be predominantly Golgi-localized, with minor populations on the plasma membrane and lysosomes. Interestingly, its direct yeast homolog, Gdt1, is exclusively localized to the Golgi, where it functions as a Ca^{2+}/H^{+} antiporter (*28*). Separately, Vcx1 functions as a Ca^{2+}/H^{+} exchanger exclusively on the vacuole. Thus, it appears that human LCAX-1 evolved from Gdt1 and other UPF0016 family members, but acquired the functionality of Vcx1 and other CAX family members. We sought to explore the subcellular localization of wild-type LCAX-1 in more depth, in various systems. First, we overexpressed an LCAX-1-EGFP fusion in HeLa cells and found minimal colocalization with the endolysosomal marker TMR-Dextran and some colocalization with the Golgi marker GM130 (**Fig. 3.4A**). However, given that the pH

sensitivity of EGFP would lead to more quenching in lysosomes, we sought to use a fluorescent tag that is insensitive to the chemical environment. Indeed, LCAX-1-DsRed overexpressed in HeLa cells showed significant colocalization with the endolysosomal marker FITC-Dextran (**Fig. 3.4B**). Further, LCAX-1-EGFP is visible on the membranes of TMR-Dextran-positive vesicles swollen with the small molecule vacuolin-1 (**Fig. 3.4C**). Thus, overexpressed WT LCAX-1 seems to localize predominantly to the Golgi, with a minor population in lysosomes.

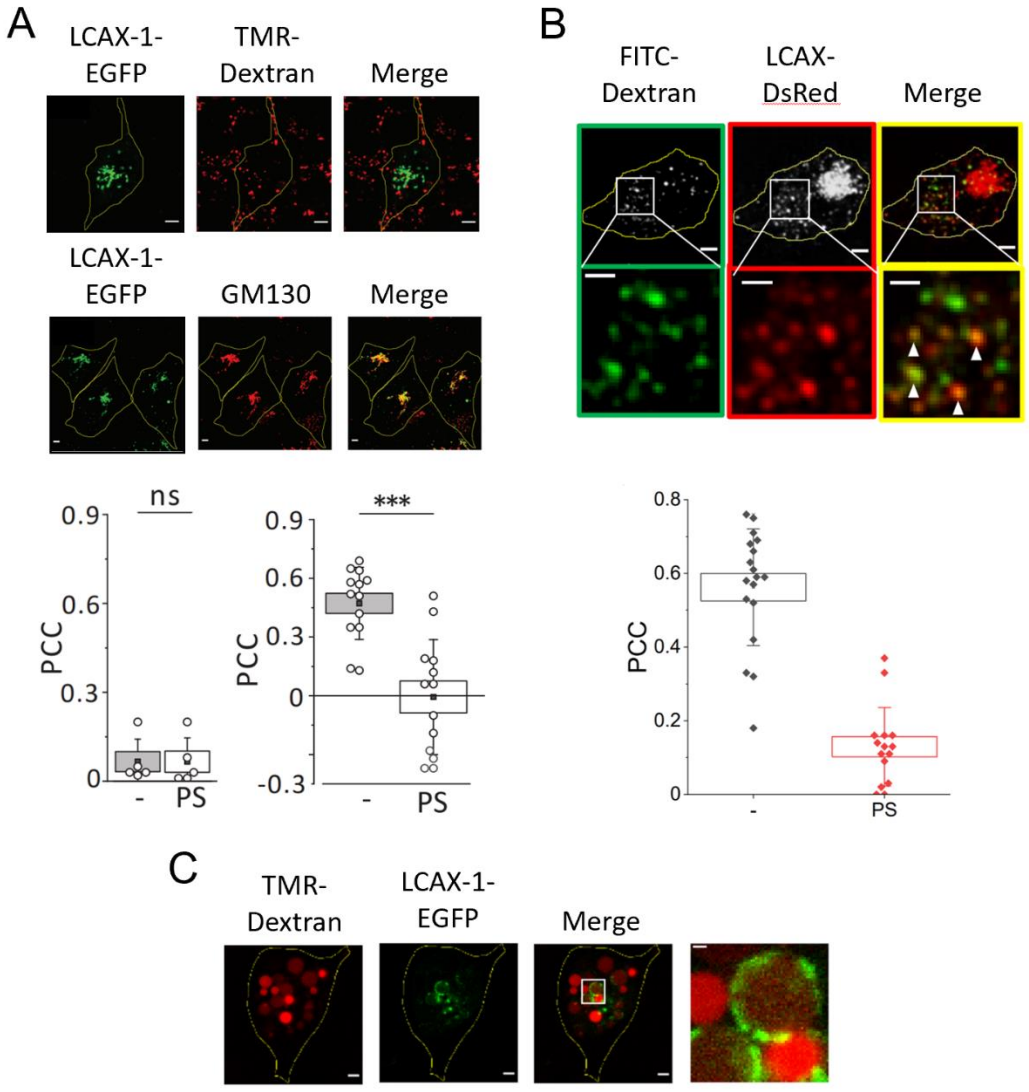

Figure 3.4: Localization of overexpressed LCAX-1 in COS7 cells. (A) Top, representative fluorescence images of cells transiently expressing LCAX-1-EGFP (green) and TMR-Dextran-labeled lysosomes (red) or immunostained for GM130 (red). Bottom, Pearson correlation coefficient (PCC) of LCAX-1 and TMR-dextran or GM130 before and after pixel shift (PS). n>10 cells. (B) Top, representative fluorescence images of cells transiently expressing LCAX-1-DsRed (red) and labeled with FITC-dextran (green). White arrows

indicate LCAX-1-positive lysosomes in inset merge image. Bottom, PCC of colocalization between LCAX-1 and FITC-dextran before and after PS. (C) Representative confocal images of cells transiently transfected with LCAX-1-EGFP (green). Lysosomes were labelled with 1 mg/mL TMR-dextran (red) and swollen with 5µM vacuolin-1 before imaging. Scale bar 5µm. ns, not significant ($p>0.05$); ***$p<0.001$ (one-way ANOVA with Tukey post hoc test).

However, overexpression systems can lead to artifacts, especially as it pertains to lysosome-localized proteins. Overexpressed proteins can end up nonspecifically in different compartments, especially the lysosome, where proteins may travel to be degraded. This is likely not the case here, as we see LCAX-1 on the membranes of swollen vesicles and not in the lumen. However, to rule out the possibility of this artifact, we tested the subcellular localization of endogenous LCAX-1 in various systems. LCAX-1 shows significant colocalization with Golgi marker GM130 in multiple cell lines (**Fig. 3.5A**). However, upon swelling lysosomes with vacuolin-1, a significant amount of LCAX-1 could be seen on the membranes of LAMP1-positive vesicles (**Fig. 3.5B**). In a breast cancer cell line with high LCAX-1 expression, SK-BR-3, endogenous LCAX-1 could be detected on LAMP1-positive vesicles, while still having significant colocalization with Golgi marker GM130 (**Fig. 3.5C**). Thus, endogenous LCAX-1 is expressed predominantly on the Golgi, with a minor population present on lysosomes that is sensitive to overall expression levels.

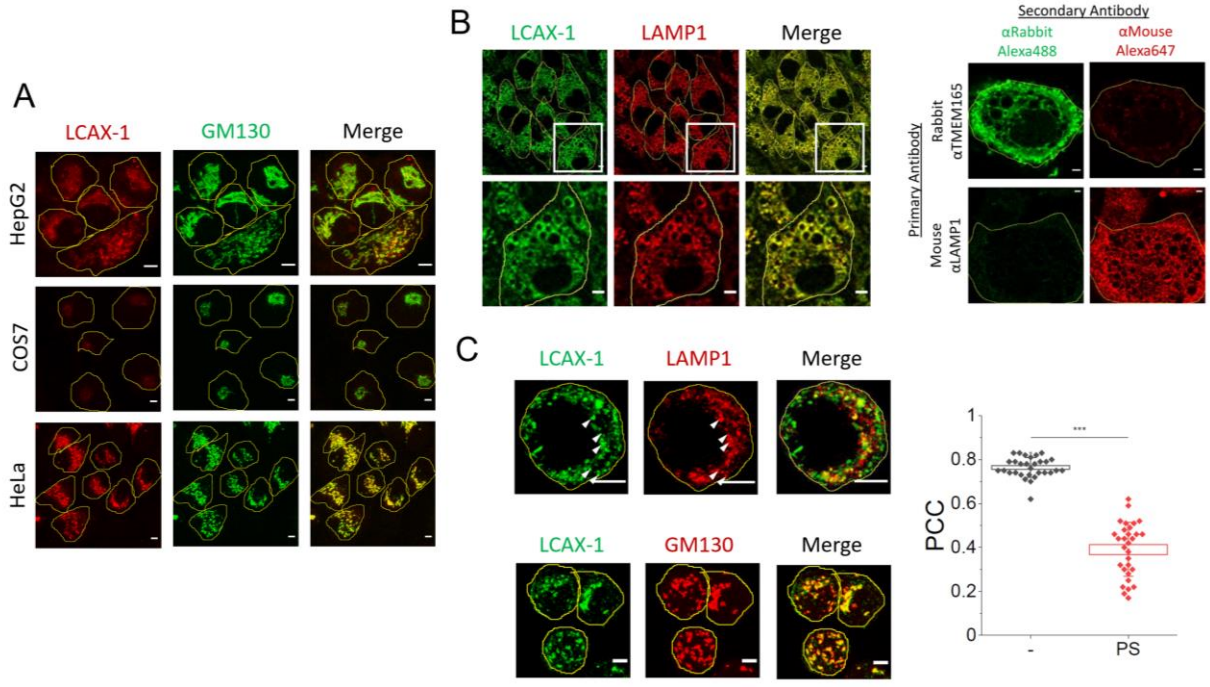

Figure 3.5: Localization of endogenous LCAX-1. (A) Representative immunofluorescence images of LCAX-1 (red) and GM130 (green) in the indicated cell lines. (B) Left, representative immunofluorescence images of LCAX-1 in HeLa cells pre-treated with vacuolin-1 to swell lysosomes. Cells were stained with antibodies to LCAX-1 (green) and LAMP1 (red) after glyoxal fixation to maintain lysosome structure. Right, representative immunofluorescence images showing specificity of secondary antibodies and spectral independence of fluorophores used. (C) Left, representative immunofluorescence images of LCAX-1 in SK-BR-3 cells. Cells were stained with antibodies to LCAX-1 (green) and LAMP1 or GM130 (red). White arrows indicate LAMP1-positive vesicles that contain LCAX-1. Right, Pearson correlation coefficient (PCC) of LCAX-1 and GM130. Scale bar 5μm. ns, not significant ($p>0.05$); ***$p<0.001$ (one-way ANOVA with Tukey post hoc test).

III.C.2: Subcellular localization of LCAX-1 mutants

As discussed in **Section III.A**, previous work has shown that mutations in LCAX-1 associated with CDG alter the subcellular distribution of LCAX-1. Specifically, the R126H mutation leads to LCAX-1 localized predominantly to lysosomes, while the compound R126C and G304R mutation leads to LCAX-1 localized predominantly to the Golgi (*2*). To confirm this, we expressed single mutants of LCAX-1 fused to EGFP in HeLa cells and evaluated colocalized with lysosomal and Golgi markers. Indeed, the single mutants R126C and R126H favor lysosome localization, while the single mutant G304R favors Golgi localization (**Fig. 3.6A-D**). These results support previous hypotheses that altering the subcellular distribution of LCAX-1 underlies CDG disease phenotypes. Combined with the results in **Section III.C.1**, this implies that LCAX-1 plays a functional role in both lysosomes and the Golgi, and that mutations that disrupt its trafficking to favor either compartment lead to cellular Ca^{2+} imbalance. In addition, given the robustness of the localization differences, we can leverage these mutants to compare the effects of LCAX-1 expressed on different intracellular membranes.

III.C.3: Effect of human LCAX-1 on phenotypes in *C. elegans*

To evaluate whether human LCAX-1 rescues phenotypes of *lcax-1*$^{+/-}$ through its function on the lysosome, we expressed WT and mutant LCAX-1 extrachromosomally in these worms (**Fig. 3.7A**). In this genetic background, we hypothesized that lysosome-localized LCAX-1 can rescue the lethality, large lysosomes, and low lysosomal Ca^{2+} caused by *lcax-1* depletion by restoring lysosomal Ca^{2+} import (**Fig. 3.7B)**. On the other hand, we hypothesized that Golgi-localized LCAX-1 would not rescue these phenotypes (**Fig. 3.7B)**. Using the differences between these mutants, we can then evaluate the lysosomal

role of WT LCAX-1. Indeed, lysosome-localized (R126C) LCAX-1 rescued the lethality of *lcax-1*$^{+/-}$ worms, while Golgi-localized (G304R) LCAX-1 did not (**Fig. 3.8A,B**). Importantly, WT LCAX-1 restored worm survival as much as R126C LCAX-1, if not more, implying a lysosome-specific role in Ca^{2+} store maintenance for human LCAX-1 (**Fig. 3.8A,B**). We then confirmed this by evaluating lysosome size. Only WT and R126C LCAX-1 restored lysosome size down to normal, while G304R LCAX-1 failed to restore the large lysosomes of *lcax-1*$^{+/-}$ worms (**Fig. 3.8C,D**).

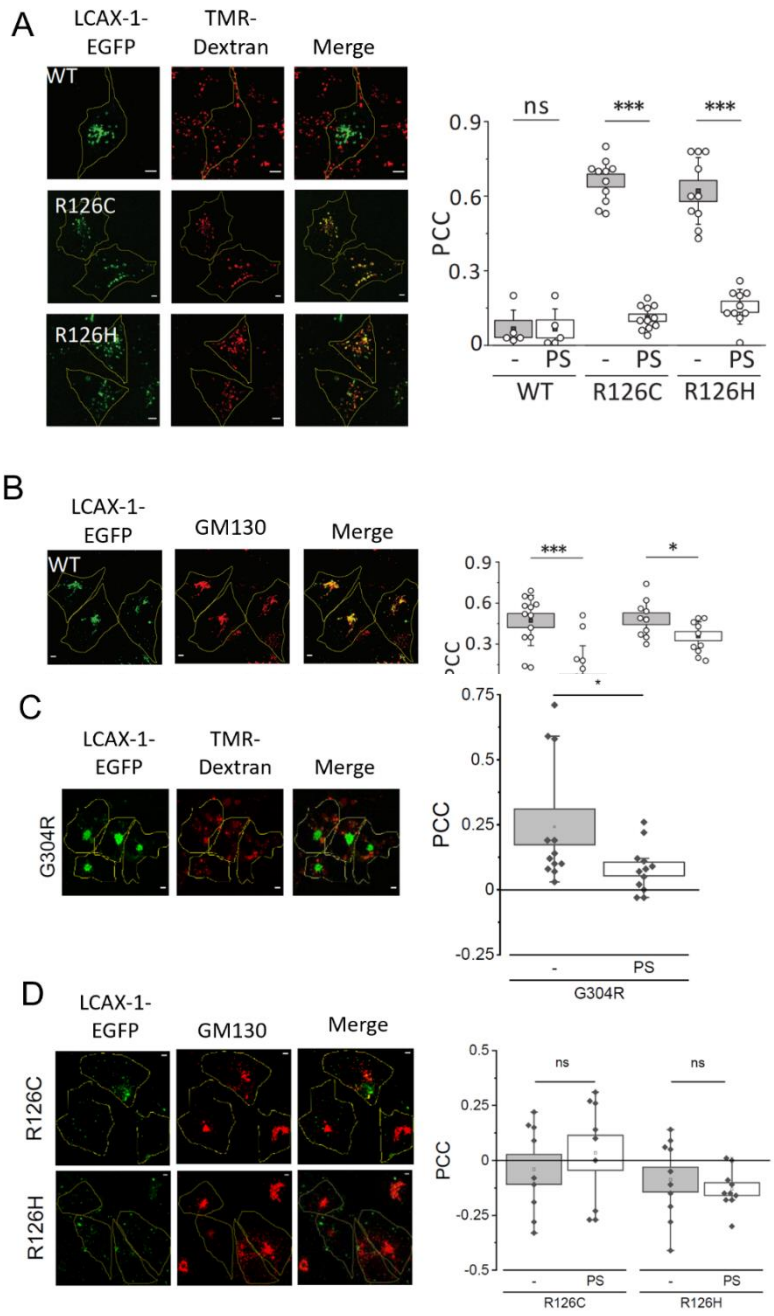

Figure 3.6: Localization of LCAX-1 mutants in COS7 cells. (A) Left, representative images of the indicated lysosome-favoring variant of LCAX-1-EGFP (green) with TMR-Dextran (red). Right, Pearson correlation coefficient (PCC) of LCAX-1 and TMR-dextran before and after pixel shift (PS). (B) Left, representative images of the indicated Golgi-favoring variant of LCAX-1-EGFP (green) with anti-GM130 (red). Right, PCC of LCAX-1 and GM130 before and after PS. (C) Left, representative images of the Golgi-favoring variant of LCAX-1-EGFP (green) with TMR-dextran (red). Right, PCC between G304R LCAX-1 and TMR-dextran before and after PS. (b) Left, representative images of the indicated lysosome-favoring variant of LCAX-1-EGFP (green) and anti-GM130 (red). Right, PCC between LCAX-1 mutants and GM130 before and after PS. Scale bar 5 µm. Boxes and bars represent the s.e.m. and outliers, respectively. ns, not significant (P>0.05); *P<0.05; ***P<0.001.

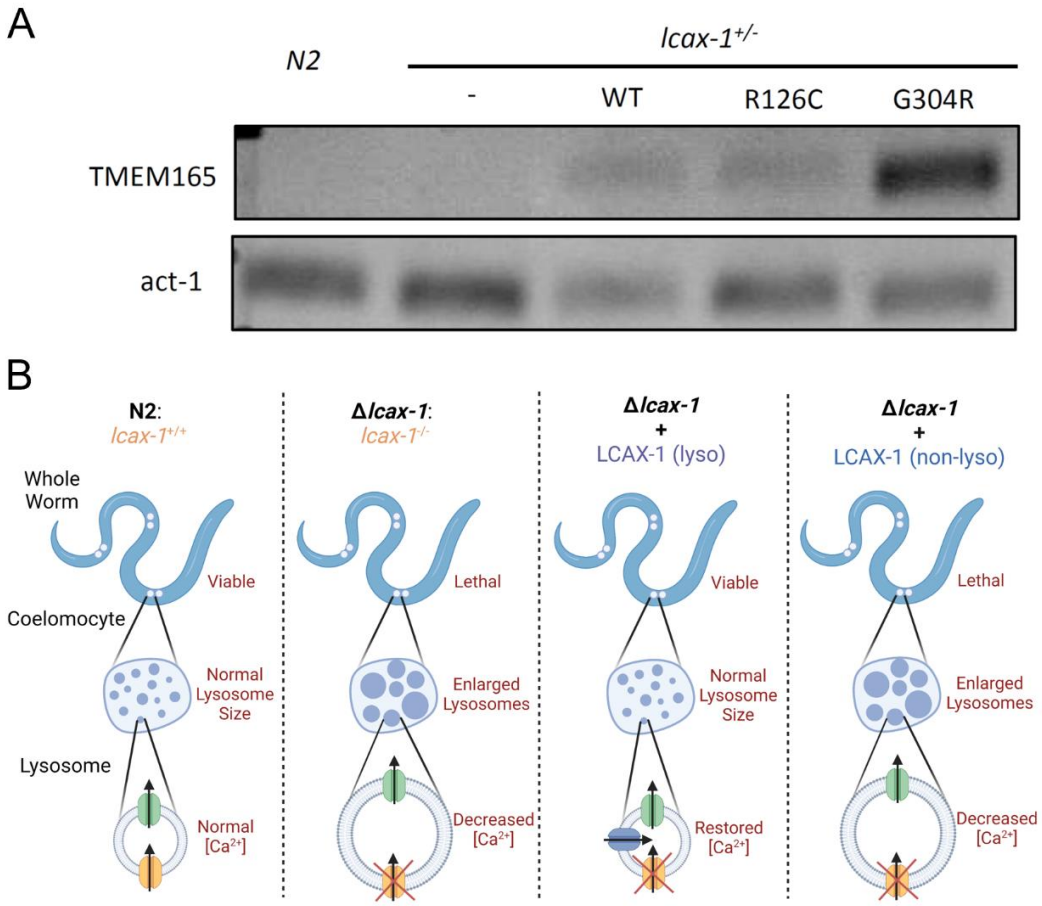

Figure 3.7: Basis of assays done in *lcax-1*$^{+/-}$ worms expressing human LCAX-1 localization mutants. (A) RT-PCR analysis of the indicated genes in N2 worms and *lcax-1*$^{+/-}$ worms with or without extrachromosomal expression of the indicated mutant of human LCAX-1. (B) Schematic of principle underlying rescue of *lcax-1*$^{+/-}$ worm phenotypes with human LCAX-1 localization variants.

Finally, we measured lysosomal Ca^{2+} levels at single-lysosome resolution using a previously described DNA-based, pH-correctable Ca^{2+} reporter, *CalipHluor 2.0* (*21*). This probe comprises 4 modules: (i) a pH-sensitive fluorophore tuned to the pH of coelomocyte lysosomes (dichlorofluorescein, DCF, G); (ii) a Ca^{2+}-sensitive fluorophore with appropriate affinity for Ca^{2+} (Rhod-5F, O); (iii) an internal reference dye to ratiometrically quantitate pH and Ca^{2+} (Alexa647, R); and (iv) a targeting domain to transport the probe to lysosomes via scavenger receptor-mediated endocytosis (negatively charged backbone) (**Fig. 3.9A**). Thus, the G/R ratio provides a readout of pH, while the O/R ratio provides a readout of Ca^{2+} (and pH due to the pH-sensitive affinity of Rhod-5F for Ca^{2+}). However, since we have lysosome-by-lysosome pH measurements, we can calculate the Ca^{2+} K_d, O/R_{min} (O/R at 0.1 µM

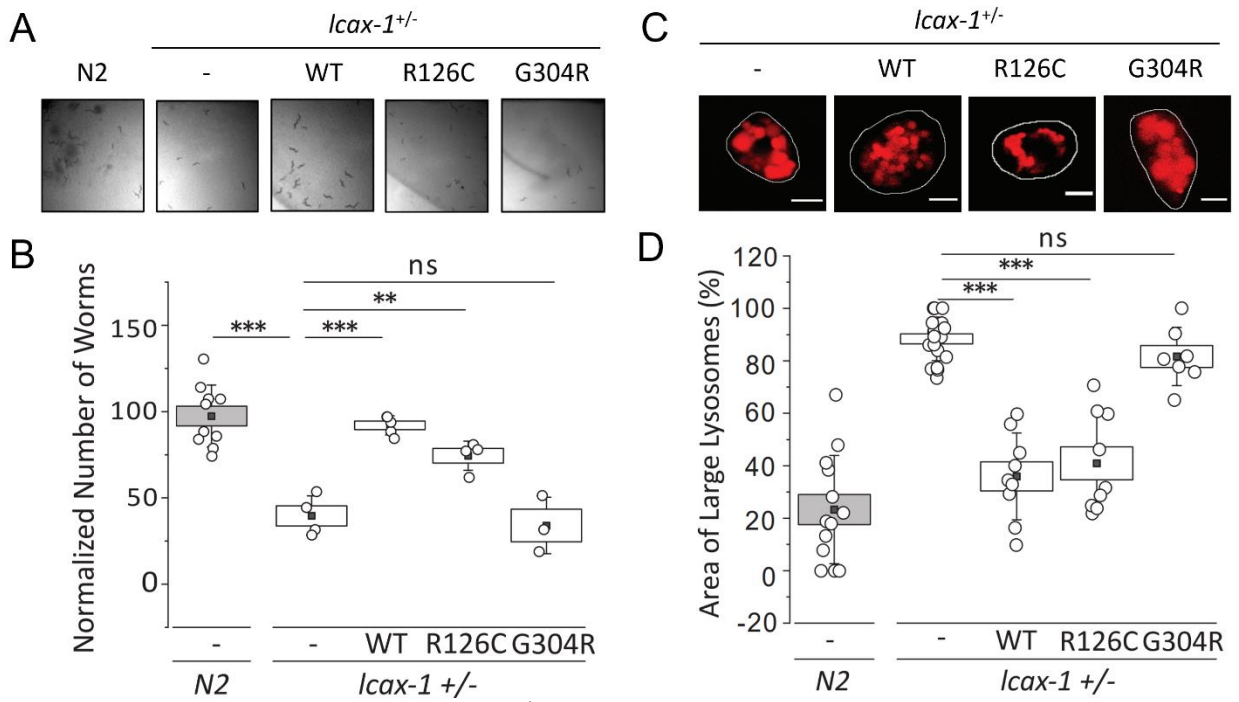

Figure 3.8: Worm phenotypes of *lcax-1*$^{+/-}$ worms expressing LCAX-1 localization mutants. (A) Representative images showing the number of progeny of N2 worms or *lcax-1*$^{+/-}$ worms without or with extrachromosomal expression of the indicated mutant of human LCAX-1. (B) Number of progeny of *lcax-1*$^{+/-}$ worms extrachromosomally expressing the indicated human LCAX-1 variant (n>3 replicates). (C) Top, representative fluorescence images of lysosomes in coelomocytes of worms in the indicated genetic background. Lysosomes are labelled with Alexa647 duplex DNA. (D) Percentage of area occupied by enlarged lysosomes in worms of the indicated genetic background. n>5 cells, >50 lysosomes. Scale bar 5 µm. Boxes and bars represent the s.e.m. and standard deviation, respectively. ns, not significant (p>0.05); **p<0.01; ***p<0.001 (one-way ANOVA with Tukey post hoc test).

Ca^{2+}), and O/R_{max} (O/R at 1 mM Ca^{2+}) at the relevant pH (**Fig. 3.9B**). In this way, we can get lysosome-level pH-corrected Ca^{2+} measurements. When injected into the pseudocoelom of worms, *CalipHluor 2.0* gets endocytosed by coelomocytes and delivered to lysosomes, as with other DNA-based nanodevices (*21*, *24–26*, *29*, *30*). Worms devoid of *lcax-1* exhibit about 50-fold lower lysosomal Ca^{2+} than N2 worms, showing the drastic effect of depleting a high-capacity lysosomal Ca^{2+} importer (**Fig. 3.9C,D**). Compared to the ~10-fold decrease in lysosomal Ca^{2+} caused by knocking out the ATP13A2 homolog *catp-6*, depletion of *lcax-1* causes a significant reduction in the lysosomal store (*21*). Thus, we hypothesize that LCAX-1 and ATP13A2 act in parallel as high-capacity and low-capacity importers, mirroring the relationship seen between exchangers and ATPases seen on other biological membranes. Importantly, the effect we see by knocking out *lcax-1* is actually an underestimate, since a significant portion of lysosomes

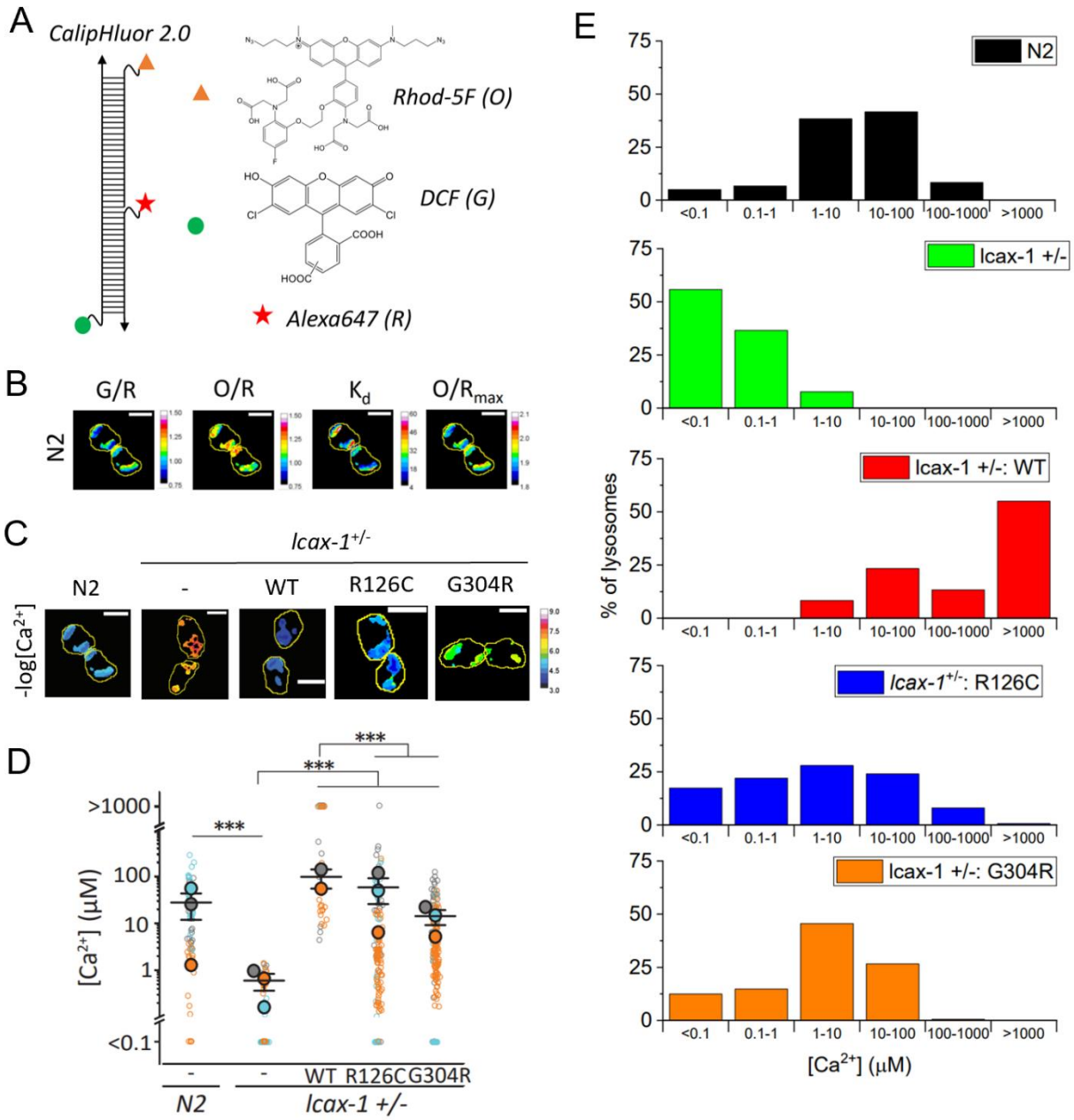

Figure 3.9: Lysosomal Ca^{2+} levels in *lcax-1*$^{+/-}$ worms expressing LCAX-1 localization mutants. (A) Structure of *CalipHluor 2.0*, which consists of Rhod-5F (orange triangle), DCF (green circle), and Alexa647 (red star) on a DNA duplex. (B) Representative pseudocolored maps of the DCF/Alexa647 ratio (G/R) and Rhod-5F/Alexa647 ratio (O/R) of *CalipHluor2.0* in N2 worms. These maps are used according to equations in the Methods section to generate K_d and O/R_{max} maps. (C) Representative $-\log([Ca^{2+}])$ maps in *CalipHluor2.0*-labeled lysosomes in coelomocytes in indicated genetic backgrounds. (D) Distribution of lysosomal Ca^{2+} in the indicated genetic backgrounds. Data represents the means (closed blue, orange, and gray circles) of 3 independent experiments (open blue, orange, and gray circles). Lysosomes with Ca^{2+} levels below O/R_{min} or above O/R_{max} of *CalipHluor2.0* are plotted as <0.1μM and >1000μM, respectively. (E) Distribution of lysosomes with the indicated Ca^{2+} concentration measured using *CalipHluor2.0* in the indicated genetic backgrounds. Scale bar 5 μm. I-shaped box represents the mean ± s.e.m. ***p<0.001 (one-way ANOVA with Tukey post hoc test).

in these worms fall below the quantifiable Ca^{2+} range of our probe and cannot contribute to the observed mean. Looking at the distribution of lysosomes with specific ranges of Ca^{2+} levels, we can see that *lcax-1*$^{+/-}$ worms have strikingly low levels of lysosomal Ca^{2+} (**Fig. 3.9E**). Expression of WT and R126C LCAX-1 fully restored lysosomal Ca^{2+} levels (**Fig. 3.9C-E)**. Surprisingly, worms expressing G304R LCAX-1 have partially restored lysosomal Ca^{2+} levels (**Fig. 3.9C-E)**. This surprising result will be discussed in detail later, but we hypothesize that it results from LCAX-1 acting as a dimer. In the heterozygous knockout background, a heterodimer of WT and G304R LCAX-1 could form and be partially localized to the lysosome. This possibility is the subject of future structural studies.

III.C.4: Lysosomal Ca^{2+} levels in LCAX-1 KO mammalian cells

To test whether the effect of LCAX-1 depletion in lysosomal Ca^{2+} levels is conserved in mammalian systems, we generated LCAX-1 KO HeLa cells. These cells show significant reduction in LCAX-1 expression, visualized by immunostaining (**Fig. 3.10A**). We used a variant of *CalipHluor 2.0* tuned to the pH of mammalian lysosomes, called *CalipHluor*^{mLy}. The only difference with this probe is the use of Oregon Green 488 (OG488) as the pH-sensitive fluorophore (**Fig. 3.10B**). Pulsing cells with this probe for 15 minutes and then incubating cells for 5 hours led to efficient lysosomal localization of *CalipHluor*^{mLy} in HeLa cells (**Fig. 3.10C**). Using this protocol, we found that LCAX-1 KO cells
We found that the loss of LCAX-1 reduces lysosomal Ca^{2+} by about 5-fold, supporting its role as a lysosomal Ca^{2+} importer (**Fig. 3.10D**). As with measurements in *C. elegans*, this effect is an underestimate because twice as many lysosomes in LCAX-1 KO worms fall below the quantifiable Ca^{2+} range of *CalipHluor*^{mLy} (**Fig. 3.10E**). In addition, lysosomes with pH under 4.0 were discarded for Ca^{2+} measurements because the Ca^{2+} affinity of Rhod-5F at such acidic conditions is too low to accurately measure Ca^{2+}. Because we expect lysosomes in LCAX-1 KO cells to be more acidic than in WT cells (due to LCAX-1 potentially facilitating H^+ export), we may be selectively eliminating lysosomes that have low pH and low Ca^{2+} from analysis. Despite these caveats, we still see a significant effect of LCAX-1 depletion on lysosomal Ca^{2+} levels.

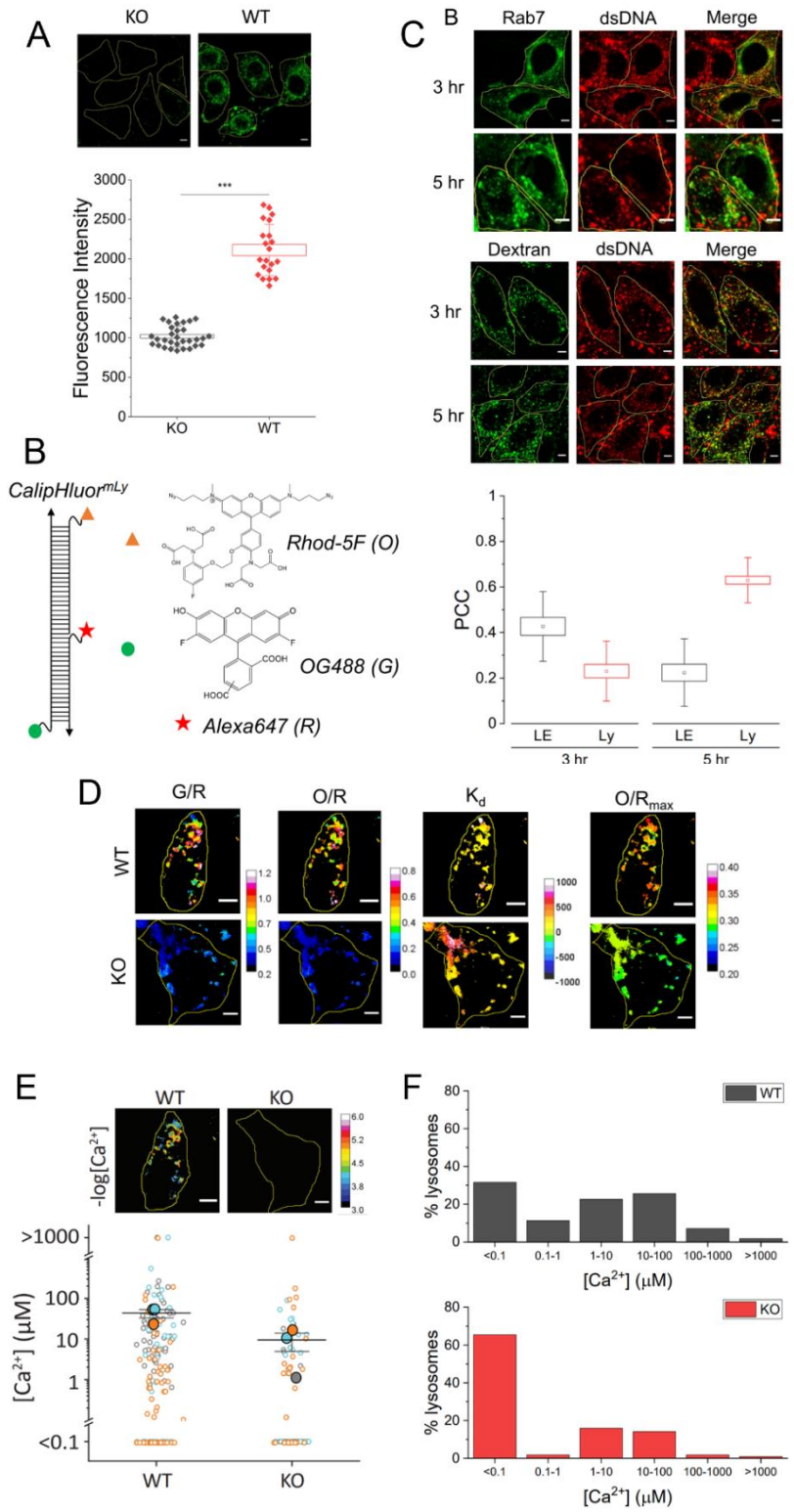

Figure 3.10: Lysosomal Ca^{2+} levels in WT and *lcax-1* KP HeLa cells. (A) Top, representative images of the endogenous expression of LCAX-1 in LCAX-1 KO cells and WT HeLa cells. Bottom, whole-cell fluorescence intensity of the Alexa488-conjugated secondary antibody to anti-LCAX-1. (B) Schematic of *CalipHluor*^{mLy}, which consists of Rhod-5F (orange triangle), Oregon Green 488 (green circle), and Alexa647 (red star) on a DNA duplex. (C) Top, representative fluorescence images of HeLa cells pulsed with Alexa647-labeled dsDNA for 15 minutes and chased for the indicated amount of time. Cells were transfected with Rab7-GFP or pulse with FITC- dextran prior to dsDNA labeling to look at late endosomal or lysosomal localization, respectively. Bottom, Pearson correlation coefficient (PCC) of dsDNA with endolysosomal markers at the indicated time points. (D) Representative pseudocolored maps of the OG488/Alexa647 ratio (G/R) and Rhod-5F/Alexa647 ratio (O/R) of *CalipHluor*^{mLy} in WT and LCAX-1 KO HeLa cells. These maps are used according to equations in the Methods section to generate K_d and O/R_{max} maps. (E) Top, representative $-\log([Ca^{2+}])$ maps of lysosomes from WT and LCAX-1 KO HeLa cells using *CalipHluor*^{mLy}. Bottom, $[Ca^{2+}]$ of individual lysosomes (open circles) from three different experiments (closed circles). Lysosomes below O/R_{min} or above O/R_{max} of *CalipHluor*^{mLy} are shown as $<0.1\mu m$ Ca^{2+} and $>1000\mu m$ Ca^{2+}, respectively. (F) Distribution of lysosomes with the indicated Ca^{2+} concentration measured using *CalipHluor2.0* in the indicated genetic backgrounds. Scale bar 5 μm. Boxes and bars represent the s.e.m. and standard deviation, respectively. I-shaped boxes show standard error of the mean. ***p<0.001 (one-way ANOVA with Tukey post hoc test).

III.C.5: Cytosolic Ca^{2+} removal by LCAX-1

Lysosomal Ca^{2+} measurements provide a static picture of the effect of LCAX-1 on the lysosomal store. However, they do not give any information on the role of LCAX-1 in the transport process from the cytosol into the lysosomal lumen. As lysosomes participate in mopping up excess cytosolic Ca^{2+} following a cytosolic Ca^{2+} spike, we wondered whether LCAX-1 was involved in this Ca^{2+} removal. We elevated cytosolic Ca^{2+} with ATP, and then tracked the speed at which cytosolic Ca^{2+} returned to normal low levels. While we are agnostic about the source of cytosolic Ca^{2+} increase, we know that ATP releases Ca^{2+} via activation of purinergic receptors on the cell surface and downstream activation of IP3R receptors on the ER. We chose to use the Ca^{2+} reporter Fura Red to track cytosolic Ca^{2+} dynamics, as its self-ratiometric readout, high photostability, and large Stokes shift are conducive to this experiment. HeLa cells devoid of LCAX-1 fail to restore the low levels of cytosolic Ca^{2+} (**Fig. 3.11A-C**). Overexpression of WT or R126C LCAX-1 rescues the ability of cells to restore low cytosolic Ca^{2+} levels faster than G304R LCAX-1 (**Fig. 3.11A-C**). This data shows that lysosome-localized LCAX-1 can better mop up cytosolic Ca^{2+} than Golgi-localized LCAX-1, which is expected given our hypothesis that LCAX-1 is a Ca^{2+}/H^{+} exchanger and lysosomes are more acidic than the Golgi. Further, it shows that WT LCAX-1 behaves more like lysosome-localized LCAX-1 in its ability to mop up cytosolic Ca^{2+}, implying that its lysosome population is functional.

We also wondered whether cells with higher endogenous expression of LCAX-1 would mop up cytosolic Ca^{2+} more efficiently. To test this hypothesis, we performed the same ATP-induced cytosolic Ca^{2+} spike assay in cells with high endogenous LCAX-1 expression: SK-BR-3 cells. To our surprise, SK-BR-3 cells displayed the same speed of cytosolic Ca^{2+} removal as HeLa cells, but a marked increase in the size of the Ca^{2+} spike triggered by ATP (**Fig. 3.12A-B**). This may indicate that SK-BR-3 cells have more dynamic overall cellular Ca^{2+} signaling than HeLa cells, such that they require high expression of LCAX-1 to mop up large amounts of Ca^{2+}. The fact that SK-BR-3 cells are derived from breast cancer tissue further supports its relevance in Ca^{2+} regulation.

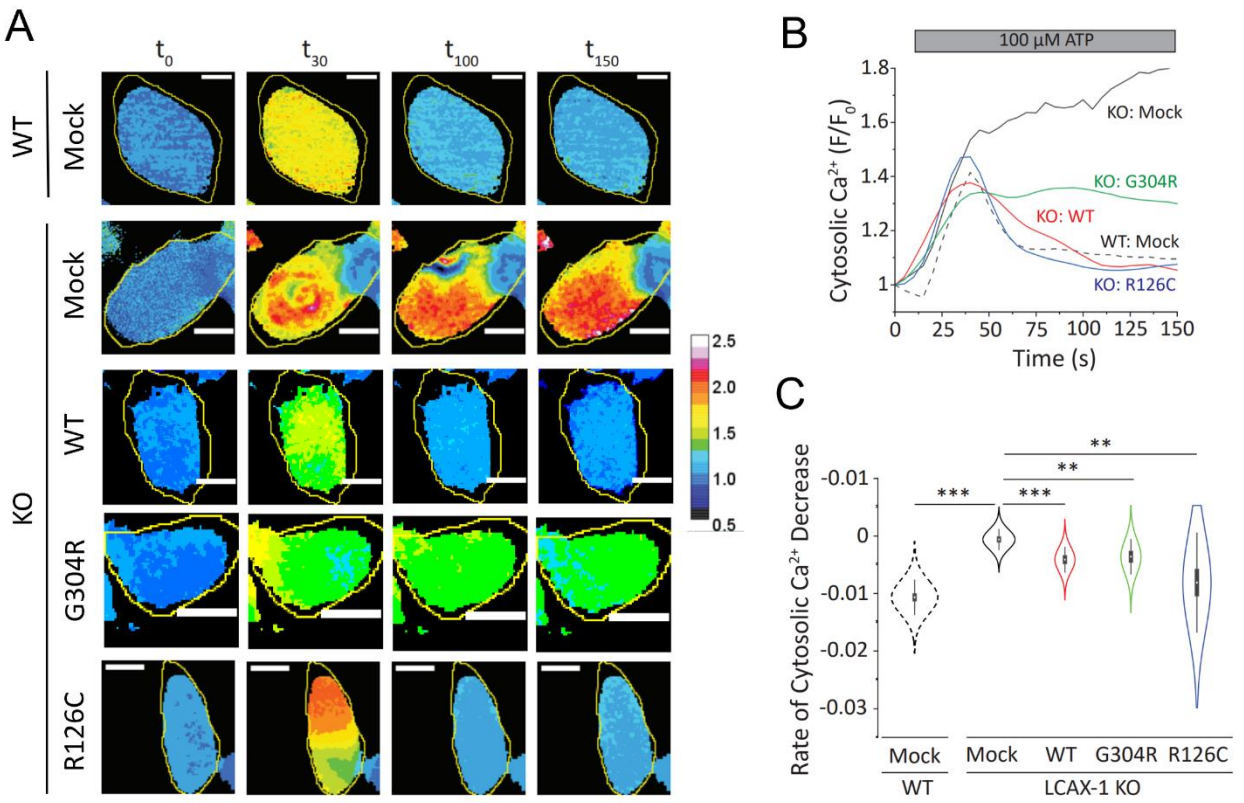

Figure 3.11: Effect of LCAX-1 on cytosolic Ca^{2+} dynamics. (A) Representative 440/488 maps of Fura Red in WT HeLa cells and LCAX-1 KO HeLa cells treated with 100 µM ATP after mock transfection or transfection with the indicated mutant of LCAX-1-EGFP. Maps shown are at t=0s (prior to ATP treatment), t=30s, t=100s, and t=150s. (B) Representative cytosolic Ca^{2+} traces given by the 440/488 ratio of Fura Red in (a). Curves are normalized to the value at t=0. (C) Slope of the linear fit of the cytosolic Ca^{2+} decrease following maximum 440/488 of Fura Red. Violin plots show normal distributions with the box showing standard error of the mean. **p<0.01; ***p<0.001 (one-way ANOVA with Tukey post hoc test).

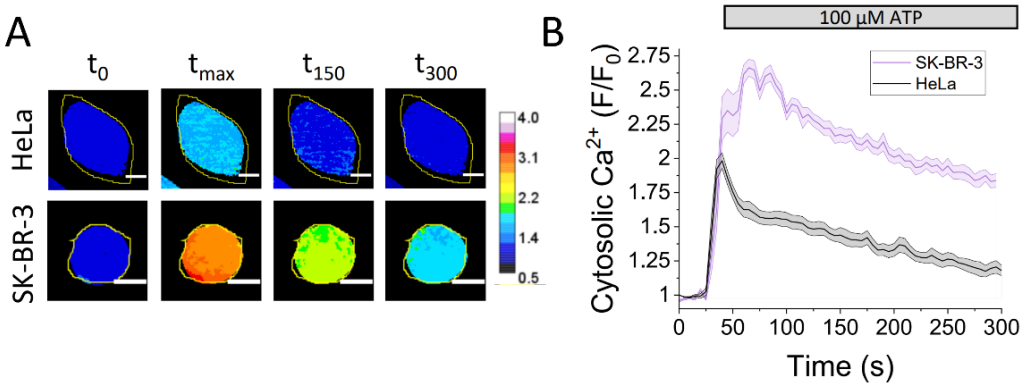

Figure 3.12: Cytosolic Ca^{2+} dynamics in SK-BR-3 cells. (A) Representative 440/488 maps of Fura Red in the indicate cells treated with 100 µM ATP. Maps shown are at t=0s (prior to ATP treatment), maximum 440/488, t=150s, and t=300s. (B) Average cytosolic Ca^{2+} levels given by 440/488 intensity of Fura Red in the indicated cell line. Shaded region represents the s.e.m.

III.C.6: Ca^{2+} currents conducted by LCAX-1

As discussed in **Section III.A.2**, fluorescence imaging methods are valuable ways to show that LCAX-1 facilitates transport of Ca^{2+} from the cytosol into lysosomes. Reporters in the cytosol and probes targeted to the lysosome lumen both support this conclusion. However, these techniques do not show that LCAX-1 is the molecule capable of directly transporting Ca^{2+}. For example, it could facilitate Ca^{2+} import by acting as an accessory unit to a greater complex or by conducting other ions to activate Ca^{2+} import. To show that LCAX-1 directly conducts Ca^{2+} current, we carried out electrophysiological experiments. In this case, we chose to perform patch-clamping on the plasma membrane to facilitate easier replication with different buffer compositions. In agreement with previous findings, we could also detect overexpressed LCAX-1 on the plasma membrane, indicating that plasma membrane patch-clamp techniques can be used to evaluate current conducted by LCAX-1 (**Fig. 3.13A**). Importantly, LCAX-1 on the plasma membrane would still export Ca^{2+} from the cytosol, but to the extracellular milieu instead of the lysosome lumen. To isolate the Ca^{2+} current component of LCAX-1, we prepared patching buffers that contain Ca^{2+} as the only transportable ion. Specifically, these buffers replace the cations K^+ and Na^+ with the large organic molecule N-methyl-D-glucamine (NMDG), and replace the anion Cl^- with methanesulfonic acid (MSA). We then dope these NMDG-MSA buffer with variable amount of $Ca(OH)_2$ and a set concentration of EGTA to precisely control the amount of free Ca^{2+} present in the buffer (**Fig. 3.13B)**. Using these buffers, we see that overexpression of LCAX-1 leads to a significantly higher outward current than mock-transfected HeLa cells (**Fig. 3.13C,D**). As outward current represents positively charged current moving from the cytosol to the extracellular milieu, we interpret this to mean that LCAX-1 transports Ca^{2+} outward (cytosol to extracellular milieu, which is equivalent to cytosol to lysosome lumen). Further, increasing the amount of Ca^{2+} in the pipette (cytosolic) buffer increased the outward current density in LCAX-1-transfected cells (**Fig. 3.13C,D**). Thus, LCAX-1 directly conducts Ca^{2+} current, especially in an outward direction (Ca^{2+} leaving the cytosol).

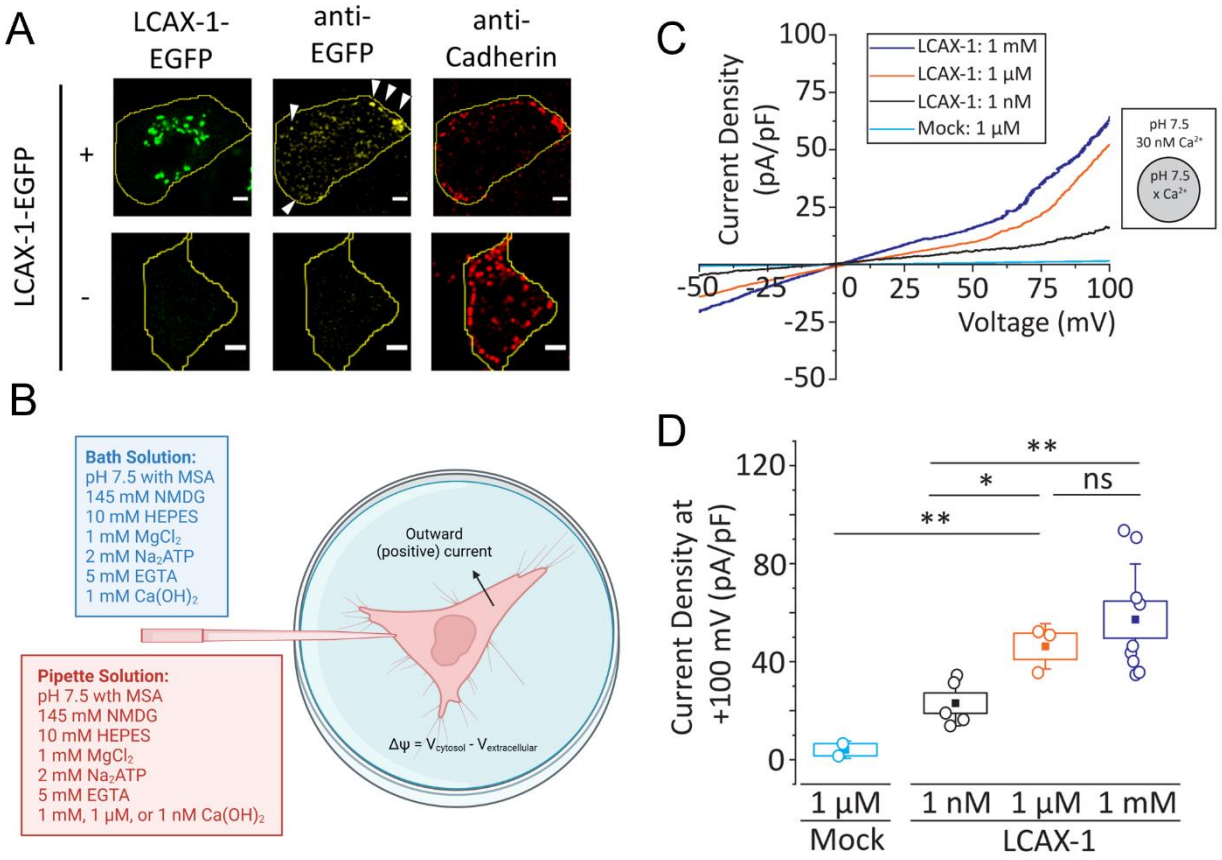

Figure 3.13: LCAX-1 currents on the plasma membrane. (A) Representative images of LCAX-1-EGFP-transfected HeLa cells and mock-transfected HeLa cells after fixation and immunostaining for EGFP (yellow) and cadherin (red), without permeabilization. (B) Buffers used for whole-cell patch-clamping, and sign conventions used for current and membrane potential. (C) Representative current density curves of mock-transfected HeLa cells (cyan) or HeLa cells expressing LCAX-1-EGFP with 1 mM (blue), 1 µM (orange) or 1 nM (black) free Ca^{2+} in the pipette/cytosolic solution. (D) Current density at +100 mV across the plasma membrane of the indicated cell types from (c).

III.D: Conclusion

The data in this chapter support the conclusion that LCAX-1 directly transports Ca^{2+} on the lysosome membrane. We have used worm phenotypes, fluorescent Ca^{2+} reporters, and electrophysiological techniques to show that it plays a direct role in maintaining the lysosomal Ca^{2+} store. It appears to be a high-capacity importer, compared to the ATPase ATP13A2, much like CAX genes from lower organisms. Thus, this chapter provides the first evidence of a molecule that imports Ca^{2+} into mammalian lysosomes seemingly via Ca^{2+}/H^{+} exchanger, which will be confirmed in the next chapter. Even though it is localized predominantly to the Golgi, it seems to be more active on the lysosome. This makes sense for a transporter whose activity depends on a steep pH gradient. A number of questions

remain that will be answered in later chapters, such as its dependence on the pH gradient and the mechanism by which it conducts Ca^{2+}. In addition, we cannot yet rule out that LCAX-1 conducts additional ions besides Ca^{2+}. More patch-clamping experiments are needed to understand if it is a nonspecific cation transporter or if it is Ca^{2+} selective. Finally, LCAX-1 is smaller compared to the known Ca^{2+} importers and exchangers. Whether such small proteins can transport ions remains to be verified, although there are example of such small proteins transporting Ca^{2+} (such as the TMBIM family) (*31*). In addition, it is possible that the active form of LCAX-1 is a dimer. Given the rescue of lysosomal Ca^{2+} by the Golgi-localized mutant of LCAX-1, this possibility seems likely.

III.E: References

1. F. Foulquier, M. Amyere, J. Jaeken, R. Zeevaert, E. Schollen, V. Race, R. Bammens, W. Morelle, C. Rosnoblet, D. Legrand, D. Demaegd, N. Buist, D. Cheillan, N. Guffon, P. Morsomme, W. Annaert, H. H. Freeze, E. Van Schaftingen, M. Vikkula, G. Matthijs, TMEM165 deficiency causes a congenital disorder of glycosylation. *Am. J. Hum. Genet.* **91**, 15–26 (2012).

2. C. Rosnoblet, D. Legrand, D. Demaegd, H. Hacine-Gherbi, G. de Bettignies, R. Bammens, C. Borrego, S. Duvet, P. Morsomme, G. Matthijs, F. Foulquier, Impact of disease-causing mutations on TMEM165 subcellular localization, a recently identified protein involved in CDG-II. *Hum. Mol. Genet.* **22**, 2914–2928 (2013).

3. S. Schulte Althoff, M. Grüneberg, J. Reunert, J. H. Park, S. Rust, C. Mühlhausen, Y. Wada, R. Santer, T. Marquardt, TMEM165 deficiency: postnatal changes in glycosylation. *JIMD Rep.* **26**, 21–29 (2016).

4. J. Stribny, L. Thines, A. Deschamps, P. Goffin, P. Morsomme, The human Golgi protein TMEM165 transports calcium and manganese in yeast and bacterial cells. *J. Biol. Chem.* **295**, 3865–3874 (2020).

5. C. Geisler, J. Dietrich, B. L. Nielsen, J. Kastrup, J. P. Lauritsen, N. Odum, M. D. Christensen, Leucine-based receptor sorting motifs are dependent on the spacing relative to the plasma membrane. *J. Biol. Chem.* **273**, 21316–21323 (1998).

6. T. Braulke, J. S. Bonifacino, Sorting of lysosomal proteins. *Biochim. Biophys. Acta*. **1793**, 605–614 (2009).

7. J. S. Bonifacino, L. M. Traub, Signals for sorting of transmembrane proteins to endosomes and lysosomes. *Annu. Rev. Biochem.* **72**, 395–447 (2003).

8. M. A. De Matteis, A. Luini, Exiting the Golgi complex. *Nat. Rev. Mol. Cell Biol.* **9**, 273–284 (2008).

9. K. F. Johnson, S. Kornfeld, The cytoplasmic tail of the mannose 6-phosphate/insulin-like growth factor-II receptor has two signals for lysosomal enzyme sorting in the Golgi. *J. Cell Biol.* **119**, 249–257 (1992).

10. M. S. Robinson, Adaptable adaptors for coated vesicles. *Trends Cell Biol.* **14**, 167–174 (2004).

11. K. Janvier, Y. Kato, M. Boehm, J. R. Rose, J. A. Martina, B.-Y. Kim, S. Venkatesan, J. S. Bonifacino, Recognition of dileucine-based sorting signals from HIV-1 Nef and LIMP-II by the AP-1 gamma-sigma1 and AP-3 delta-sigma3 hemicomplexes. *J. Cell Biol.* **163**, 1281–1290 (2003).

12. H. Ohno, J. Stewart, M. C. Fournier, H. Bosshart, I. Rhee, S. Miyatake, T. Saito, A. Gallusser, T. Kirchhausen, J. S. Bonifacino, Interaction of tyrosine-based sorting signals with clathrin-associated proteins. *Science*. **269**, 1872–1875 (1995).

13. S. Waguri, F. Dewitte, R. Le Borgne, Y. Rouillé, Y. Uchiyama, J.-F. Dubremetz, B. Hoflack, Visualization of TGN to endosome trafficking through fluorescently labeled MPR and AP-1 in living cells. *Mol. Biol. Cell*. **14**, 142–155 (2003).

14. W. W. Y. Lui, B. M. Collins, J. Hirst, A. Motley, C. Millar, P. Schu, D. J. Owen, M. S. Robinson, Binding partners for the COOH-terminal appendage domains of the GGAs and gamma-adaptin. *Mol. Biol. Cell*. **14**, 2385–2398 (2003).

15. B. Doray, S. Kornfeld, Gamma subunit of the AP-1 adaptor complex binds clathrin: implications for cooperative binding in coated vesicle assembly. *Mol. Biol. Cell*. **12**, 1925–1935 (2001).

16. J. Hirst, N. A. Bright, B. Rous, M. S. Robinson, Characterization of a fourth adaptor-related protein complex. *Mol. Biol. Cell*. **10**, 2787–2802 (1999).

17. P. Saftig, J. Klumperman, Lysosome biogenesis and lysosomal membrane proteins: trafficking meets function. *Nat. Rev. Mol. Cell Biol.* **10**, 623–635 (2009).

18. K. Janvier, J. S. Bonifacino, Role of the endocytic machinery in the sorting of lysosome-associated membrane proteins. *Mol. Biol. Cell*. **16**, 4231–4242 (2005).

19. A. Nesterov, R. E. Carter, T. Sorkina, G. N. Gill, A. Sorkin, Inhibition of the receptor-binding function of clathrin adaptor protein AP-2 by dominant-negative mutant mu2 subunit and its effects on endocytosis. *EMBO J.* **18**, 2489–2499 (1999).

20. H. Ohno, R. C. Aguilar, D. Yeh, D. Taura, T. Saito, J. S. Bonifacino, The medium subunits of adaptor complexes recognize distinct but overlapping sets of tyrosine-based sorting signals. *J. Biol. Chem.* **273**, 25915–25921 (1998).

21. N. Narayanaswamy, K. Chakraborty, A. Saminathan, E. Zeichner, K. Leung, J. Devany, Y. Krishnan, A pH-correctable, DNA-based fluorescent reporter for organellar calcium. *Nat. Methods*. **16**, 95–102 (2019).

22. B. Suresh, A. Saminathan, K. Chakraborty, C. Cui, L. Becker, Y. Krishnan, Tubular lysosomes harbor active ion gradients and poise macrophages for phagocytosis. *BioRxiv* (2020), doi:10.1101/2020.12.05.413229.

23. V. Au, E. Li-Leger, G. Raymant, S. Flibotte, G. Chen, K. Martin, L. Fernando, C. Doell, F. I. Rosell, S. Wang, M. L. Edgley, A. E. Rougvie, H. Hutter, D. G. Moerman, CRISPR/Cas9 Methodology for the Generation of Knockout Deletions in Caenorhabditis elegans. *G3 (Bethesda)*. **9**, 135–144 (2019).

24. K. Chakraborty, K. Leung, Y. Krishnan, High lumenal chloride in the lysosome is critical for lysosome function. *eLife*. **6**, e28862 (2017).

25. S. Surana, A. R. Shenoy, Y. Krishnan, Designing DNA nanodevices for compatibility with the immune system of higher organisms. *Nat. Nanotechnol.* **10**, 741–747 (2015).

26. K. Dan, A. T. Veetil, K. Chakraborty, Y. Krishnan, DNA nanodevices map enzymatic activity in organelles. *Nat. Nanotechnol.* **14**, 252–259 (2019).

27. C. Grimm, J. Vierock, P. Hegemann, J. Wietek, Whole-cell Patch-clamp Recordings for Electrophysiological Determination of Ion Selectivity in Channelrhodopsins. *J. Vis. Exp.* (2017), doi:10.3791/55497.

28. A.-S. Colinet, P. Sengottaiyan, A. Deschamps, M.-L. Colsoul, L. Thines, D. Demaegd, M.-C. Duchêne, F. Foulquier, P. Hols, P. Morsomme, Yeast Gdt1 is a Golgi-localized calcium transporter required for stress-induced calcium signaling and protein glycosylation. *Sci. Rep.* **6**, 24282 (2016).

29. S. Surana, J. M. Bhat, S. P. Koushika, Y. Krishnan, An autonomous DNA nanomachine maps spatiotemporal pH changes in a multicellular living organism. *Nat. Commun.* **2**, 340 (2011).

30. K. Chakraborty, P. Anees, S. Surana, S. Martin, J. Aburas, S. Moutel, F. Perez, S. P. Koushika, P. Kratsios, Y. Krishnan, Tissue-specific targeting of DNA nanodevices in a multicellular living organism. *eLife*. **10** (2021), doi:10.7554/eLife.67830.

31. P. Pihán, F. Lisbona, J. Borgonovo, S. Edwards-Jorquera, P. Nunes-Hasler, K. Castillo, O. Kepp, H. Urra, S. Saarnio, H. Vihinen, A. Carreras-Sureda, S. Forveille, A. Sauvat, D. De Giorgis, A. Pupo, D. A. Rodríguez, G. Quarato, A. Sagredo, F. Lourido, A. Letai, C. Hetz, Control of lysosomal-mediated cell death by the pH-dependent calcium channel RECS1. *Sci. Adv.* **7**, eabe5469 (2021).

IV: LCAX-1 Needs a Transmembrane pH Gradient to Import Calcium into Lysosomes

IV.A: Introduction

IV.A.1: Evidence of Ca^{2+}/H^{+} exchange activity by LCAX-1

Our results in previous chapters have shown that LCAX-1 mediates the import of Ca^{2+} into mammalian lysosomes. In this chapter, we present experiments showing that this import is dependent on the lysosomal pH gradient, and that LCAX-1 is a lysosomal Ca^{2+}/H^{+} exchanger. Our hypothesis that it acts like this is based on cellular and bioinformatic evidence in the literature that it appears to perform Ca^{2+}/H^{+} exchange on the Golgi. The first piece of evidence that LCAX-1 may affect organellar pH homeostasis comes from pH imaging in cells from CDG patients with LCAX-1 mutations. In patients with splicing mutants that result in nonfunctional proteins, lysosomes seem to be hyperacidic (**Fig. 4.1**) (*1*). In this study, authors used the membrane-permeable weak base, LysoSensor DND189, which has acid-dependent fluorescence. Interestingly, CDG patients with missense mutations in LCAX-1 do not seem to have hyperacidic lysosomes (*1*). In addition, knockdown of LCAX-1 with siRNA also led to an increase in LysoSensor DND189 intensity, implying increased lysosome acidity (*1*). The authors interpreted this data to mean that LCAX-1 is involved in late endosomal or lysosomal pH homeostasis, specifically that a complete loss of LCAX-1 leads to hyperacidification of lysosomes. However, we know that LysoSensor DND189 will localize to all acidic organelles, not just late endosomes and lysosomes. In addition, the probe is a turn-on sensor, with no reference dye to normalize for dye uptake and other artefacts. A more conclusive cell-based experiment used a cyanine-based Golgi-targeted fluorescent pH probe, called CPH (*2*). Interestingly, this probe localized specifically to Golgi using a phenylsulfonamide group. This probe is also self-ratiometric, providing an internal reference for better quantification. Indeed, this probe showed that LCAX-1 depletion leads to a more acidic Golgi lumen (**Fig. 4.1**) (*2*). Combined, these data show that LCAX-1 may facilitate the exit of protons from organellar lumens, such that its loss results in hyperacidification. However, this data alone does not conclusively say that LCAX-1 directly exchanges protons.

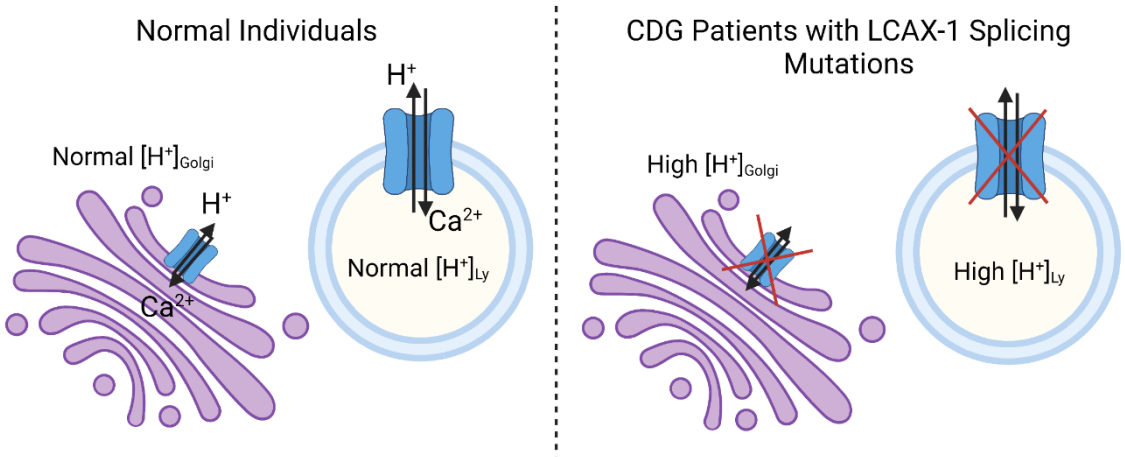

Figure 4.1: Increased Golgi and lysosomal acidity caused by loss of functional LCAX-1, due to loss of H^+ efflux.

The more convincing reasons to believe that the UPF0016 family (of which LCAX-1 is the human member) are Ca^{2+}/H^+ exchangers come from structural similarities to the CAX family, despite their much smaller size. The UPF0016 family is highly conserved, with members found in all eukaryotes and many bacteria and archaea (*3*). The human, nematode, zebrafish, and fruit fly homologs are highly similar, forming their own distinct subfamily. The most conserved portions of the UPF0016 family members are very similar to the most conserved portions of the CAX family, implying a new family of exchangers distinct from the CAX family (*3*). Similar to members of the CAX family, UPF0016 family members have two hydrophobic clusters straddling a cytosolic loop of acidic residues (**Fig. 4.2**). In CAX proteins, each hydrophobic cluster contains a highly conserved internal motif that has a conserved acidic residue (usually an aspartate or glutamate) (**Fig. 4.2B**). Similarly, UPF0016 family members contain two such symmetric glutamate-containing motifs (**E**LGDKT and **E**WGDRS in LCAX-1), one on each of its hydrophobic halves (**Fig. 4.2A**) (*1*). These EΦGD(KR)(TS) consensus patterns are the defining feature of UPF0016 family members (*3*). In the CAX family, the acidic residues neutralize the positive charges of a Ca^{2+} ion, with nearby polar residues helping to create a hydrophilic microenvironment and nonpolar residues providing conformational flexibility. The pH-sensitivity of these acidic residues allows the motif to bind and release Ca^{2+} in a way that simultaneously exports protons (*4*). Thus, these motifs in LCAX-1 may serve to facilitate Ca^{2+}/H^+ exchange via a similar mechanism. In CAX proteins, the cytosolic loop of

acidic residues serves to coordinate Ca^{2+} ions into close proximity of the central binding site (**Fig. 4.2B**) (*4*). UPF0016 family members also displays such an acidic loop (**Fig. 4.2A**). Thus, these structural similarities imply that LCAX-1 and other members of the UPF0016 family could be a unique group of Ca^{2+}/H^{+} exchangers.

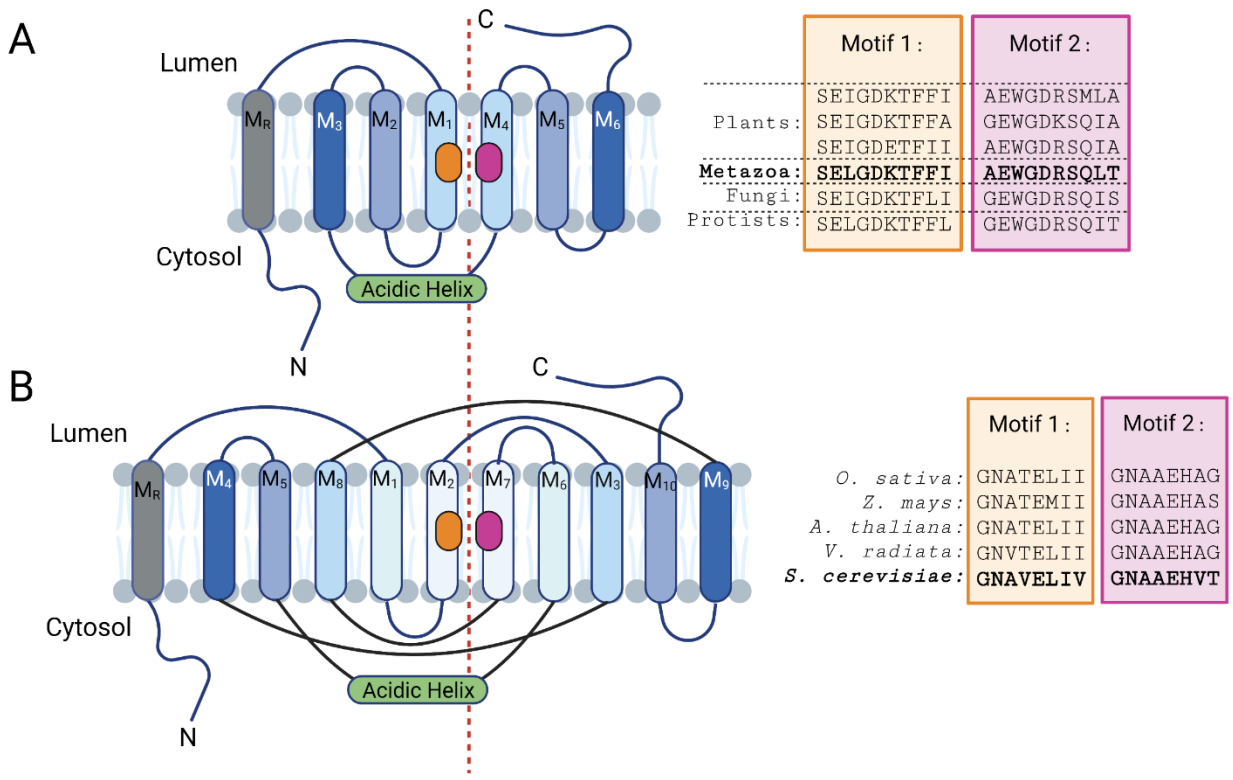

Figure 4.2: Similarities between UPF0016 and CAX family proteins. (A) Topology of LCAX-1 (the human member of the UPF0016 family), with consensus Ca^{2+} binding motifs of UPF0016 family members across different organisms. (B) Topology of VCX1 (the yeast member of the CAX family), with consensus Ca^{2+} binding motifs of CAX family members across different organisms. Transmembrane segment color indicates internal symmetry (across dotted red line).

IV.A.2: Prior art establishing H^{+} exchange in proteins

A range of tools and strategies exist to show that an ion transport mechanism is correlated to proton transport. An exchange mechanism requires reciprocity in its transport behavior. As such, three things that must be true for a transporter to be proton exchanger: (i) its activity must alter the local pH on either side of the membrane; (ii) efficiency of proton transport must affect the transport of other ions; and (iii) multiple ion transport processes must occur in synchrony. A combination of strategies has been used

to show this for mammalian Cl^-/H^+ (CLCs) and Na^+/H^+ exchangers (NHEs), as well as Ca^{2+}/H^+ exchangers (CAXs) in lower organisms. We will use a number of these strategies in this chapter, and will introduce them in this section through a discussion of the *E. coli* CLC protein, EcCLC-1.

A common approach to showing that a protein cotransports H^+ ions is to measure the pH on one side of the membrane, using a pH meter or fluorescent pH reporter. The breakthrough discovery that EcCLC-1 is not a Cl^- channel, but rather a Cl^-/H^+ exchanger, employed such techniques. A cotransport or antiport system had been previously suspected, as the reversal potential of CLC transporters did not match the Nernst equilibrium potential expected for Cl^- transport alone (*5*). When a Cl^- gradient was established across EcCLC-1-reconstituted liposomes and counterion movement was initiated with the K+ ionophore valinomycin, the pH of the external solution increased (*5*). This implied that H^+ enters the vesicle as Cl^- exits. Another way to show an ion/H^+ exchange mechanism is to show that H^+ transport affects transport of other ions. In the study identifying EcCLC-1 as an exchanger, the authors imposed a proton gradient across the liposome membrane and followed Cl^- efflux using the fluorescent Cl^- reporter 6-methyoxy-N-(3-sulphopropyl)-quinolinium (SPQ) inside liposomes. Indeed, uphill Cl^- flux was observed, through SPQ de-quenching and increased fluorescence (*5*). Collapsing the proton gradient with the proton uncoupler carbonyl cyanide-p-trifluoromethoxyphenylhydrazone (FCCP) reversed this increase in SPQ fluorescence. Finally, electrophysiological strategies can be used to demonstrate H^+ exchange mechanisms. As described in **Section I.F.4**, ion channels can be interrogated on various membranes using patch-clamp techniques. Using carefully designed buffers, the exact ions transported can be identified. In the study identifying EcCLC-1 as an exchanger, the authors performed patch-clamping on EcCLC-1-reconstititued liposomes. They used buffers with varying pH gradients at fixed Cl^- concentrations to show that the reversal potential shifts in a manner that implies stoichiometric exchange, rather than individual diffusion of ions (*5*). Further, they showed that the reversal potential measured in the presence of both Cl^- and pH gradients is the simple sum of those measured with each individual gradient alone (*5*).

This startling discovery changed how all CLC proteins were viewed. Now, we know that all intracellular mammalian CLCs (CLC-3 through CLC-7) and several plant CLCs are actually Cl^-/H^+

exchangers (*6–11*). Importantly, the three techniques mentioned here (pH measurements, Cl^- measurements, and electrophysiology) were used in all cases to illustrate exchange. This understanding has allowed us to explore the physiological relevance of CLC exchangers in acidification of various intracellular compartments, and their relevance in disease states (*6*). Further, the mechanism of ion coupling has been explored in detail, allowing to engineer "uncoupling" variants of CLC exchangers that convert exchange into pure Cl^- channels (*12–14*). Thus, our deep understanding of the CLC family escalated dramatically following the discovery that it uses a H^+ exchange mechanism.

Indeed, the identification of Ca^{2+}/H^+ exchange mechanisms has followed similar trajectories. For example, the experiments showing the yeast protein VCX1 is a vacuolar Ca^{2+}/H^+ exchanger employ many of the same fluorescent and electrophysiological techniques, as discussed in **Section I.E.** In addition, the potential mammalian Ca^{2+}/H^+ exchange mechanism has been illustrated using these techniques, as discussed in **Section I.C**. Thus, to illustrate that LCAX-1 functions as a Ca^{2+}/H^+ exchanger on mammalian lysosomes, we employed the analogous set of fluorescence-based and electrophysiological techniques to show that: (i) LCAX-1 activity alters lysosomal pH; (b) the lysosomal pH gradient affects the ability of LCAX-1 to transport Ca^{2+}; and (c) Ca^{2+} and H^+ countertransport occurs simultaneously.

IV.B: Materials and Methods

IV.B.1: Chemicals and reagents

Modified oligonucleotides were purchased from IDT (USA), subjected to ethanol precipitation and quantified using UV absorbance. Chemicals used for the previously synthesized Rhod-5F-azide were purchased from Sigma and Alfa Aesar as previously described (*15*). DCF used for previously described conjugation was purchased from Fisher Scientific (*16*). Bafilomycin A and vacuolin-1 were purchased from Cayman Chemical. EGTA, ampicillin, kanamycin, carbenicillin, ammonium chloride, adenosine triphosphate, methane sulfonic acid, HEPES, calcium hydroxide, magnesium chloride, and N-methyl-D-glucamine were purchased from Sigma. Monodisperse silica microspheres were obtained from Cospheric. Fura Red, DQ Red BSA, Alexa Fluor 488 NHS Ester, and RNase A were purchased from Thermo Fisher Scientific.

IV.B.2: Mammalian cell culture, plasmids, and transfection

HeLa cells and COS7 cells were purchased from ATCC and cultured according to recommended guidelines. LCAX-1 KO HeLa cells were purchased from Creative Biogene. Cells were cultured in Dulbecco's Modified Eagle's Medium (DMEM) (Invitrogen Corporation, USA) containing 10% heat-inactivated fetal bovine serum (FBS) (Invitrogen Corporation, USA), 100 U/mL penicillin and 100 μg/mL streptomycin (Gibco), and maintained at 37°C under 5% CO_2. Cells were passaged using 0.25% Trypsin-EDTA (Gibco) and plated at 50-60% confluency for transfection.

Mammalian expression of LCAX-1 fused to EGFP was carried out as described in **Section III.B.2**. For mammalian expression of LCAX-1 fused to mCherry (a kind gift from M. Glotzer at the University of Chicago) was coned into the LCAX-1-EGFP plasmid, replacing EGFP, using Gibson assembly techniques. Mammalian expression of LCAX-1 disease mutants fused to EGFP was carried out as described in **Section III.B.2**.

HeLa and COS7 cells were transiently transfected with the respective plasmids using Lipofectamine 3000 (Thermo Fisher) according to manufacturer protocols. After incubation for 4 hours, the transfection medium was replaced with fresh DMEM. Imaging or electrophysiology experiments were performed on cells 48h following transfection.

IV.B.3: *C. elegans* strains

The strains used in this chapter are exactly as described in **Section III.B.3**.

IV.B.4: Lysosomal pH imaging in worms

In vivo lysosomal pH measurements were made using *CalipHluor2.0* according to protocols and calibrations established previously and described in **Section III.B.9**.

IV.B.5: Lysosomal pH imaging in cells

Lysosomal pH measurements in live mammalian cells were made using *CalipHluor*^{mLy}, as described in **Section III.B.10.**

IV.B.6: Lysosomal pH dynamics

To evaluate the effect of LCAX-1 activity on lysosomal pH dynamics, we used the ratiometric lysosomal pH indicator FITC-dextran according to manufacturing protocols. Briefly, 48h following mock-transfection or transfection with the indicated mutant of LCAX-1-mCherry, HeLa (WT or LCAX-1 KO) cells were pulsed with 5 mg/mL FITC-dextran for 3 hours in DMEM before washing 3x with PBS and incubating for 16 hours in DMEM. Prior to imaging in Tyrode's solution, cells were washed 3x again with PBS. The imaging protocol was set up to take an LCAX-1-mCherry at the start, and FITC-dextran images every 5 seconds. After 8 image acquisitions, the solution was replaced with Tyrode's solution supplemented with 100 µM ATP. Images were taken for 5 minutes. FITC-dextran images were then background-subtracted by the intensity of an ROI outside the cell. The 440/514 image was then duplicated and thresholded to create a binary mask. Both images were multiplied by the mask to create processed 440/514 and 488/514 images. The processed 488/514 image was then divided by the processed 440/514 image to get a 488/440 (excitation ratio) pseudocolored map. For representative images, the pseudocolored maps at indicated time points were then smoothed. The 488/440 ratio was then plotted as a function of time, normalized to 1 at t=0s. To calculate the change in lysosomal pH, the fold change of pH from baseline to maximum was calculated.

The effect of bafilomycin A on lysosomal pH was verified, using FITC-dextran. Briefly, COS7 cells were pulsed with 5 mg/mL FITC-dextran for 3 hours before washing 3x with PBS and incubating for 16 hours in DMEM. Cells were then incubated with 500 nM Bafilomycin A or DMSO control (untreated, UT) for 30min in HBSS prior to imaging by widefield microscopy. Cells were imaged in the 488/514 and 440/514 channels described below in the image acquisition section. Images were then background-subtracted using the intensity of an ROI outside of the cells. The 488/514 image was then thresholded to create a binary mask. Both the 488/514 and 440/514 images were multiplied by the mask to generate processed images. The processed 488/514 image was divided by the processed 440/514 image to get a 488/440 (excitation ratio) pseudocolored map. For the representative images, the pseudocolored maps were then smoothed. The 488/440 ratio was then determined for individual endosomes and plotted for each treatment condition.

IV.B.7: Cytosolic Ca^{2+} dynamics

To evaluate the effect of LCAX-1 activity on cytosolic Ca^{2+} buffering, we used the ratiometric Ca^{2+} dye Fura Red according to manufacturer protocols. First, COS7 cells were mock-transfected or transfected with the indicated mutant of LCAX-1-EGFP. Two days later, cells were pulsed with 10 µM Fura Red in HBSS for 15 min, washed 3x with PBS, and then chased for 30min in HBSS. Where indicated, 500 nM Bafilomycin A was included in the chase step and in every buffer afterwards. Prior to imaging in Tyrode's solution (NaCl 134 mM, KCl 2.68 mM, $CaCl_2$ 1.8 mM, $MgCl_2$ 1.05 mM, NaH_2PO_4 0.417 mM, $NaHCO_3$ 11.9 mM, d-glucose 5.56 mM), cells were washed 3x again with PBS. The imaging protocol was set up to take an LCAX-1-EGFP image at the start, and Fura Red images every 2 seconds. After 8 image acquisitions, the solution was replaced with Tyrode's solution supplemented with 100 µM ATP. Images were taken for 2 minutes. Fura Red images were then processed and analyzed as described in **Section III.B.11.**

IV.B.8: Lysosomal proteolysis

Lysosomal proteolysis was estimated as previously described (*16*). Briefly, HeLa cells (WT or LCAX-1 KO) were pulsed with 5 mg/mL Alexa488-dextran for 1 hour before washing 3x with PBS and incubating for 16 hours in DMEM. Then, cells were incubated with 10 µg/mL DQ Red BSA in HBSS for 15 minutes, washed 3x with PBS, and chased for 30 minutes in HBSS. Cells were then imaged with a confocal microscope (see image acquisition section for details). Lysosomal proteolysis levels were estimated using the whole-cell ratio of DQ Red BSA to Alexa488-dextran (R/G). To calculate this, individual DQ Red BSA and Alexa488-dextran images were background-subtracted, and an ROI was drawn around each cell to measure whole-cell fluorescence intensity. Representative R/G maps were generated by thresholding the Alexa488-dextran image to create a binary mask. Both the R and G images were multiplied by the mask to generate processed images. The processed R image was divided by the processed G image to get an R/G.

IV.B.9: Whole-cell electrophysiology

Whole-cell recordings were performed as described in **Section III.B.12**. The only difference is that, in this chapter, the buffers are slightly different. The extracellular/bath solution contained (in mM): 140 NMDG, 10 HEPES, 1 $MgCl_2$, 5 EGTA, 5 glucose, and variable $Ca(OH)_2$ to get 30 nM free [Ca^{2+}], and was set to either pH 5.5, 6.5, or 7.5 with MSA. The pipette solution contained (in mM): 140 NMDG, 10 HEPES, 1 $MgCl_2$, 5 EGTA, and $Ca(OH_2)$ to get either 1 nM free [Ca^{2+}], and was set to pH 7.5 with MSA. Total calcium at each pH was calculated to maintain the indicated amount of free calcium using https://somapp.ucdmc.ucdavis.edu/pharmacology/bers/maxchelator/CaMgATPEGTA-TS.htm for each experiment.

IV.B.10: Lysosome electrophysiology

Borosilicate glass capillaries (Sutter) with dimensions of 1.5 mm x 0.86 mm (outer diameter/inner diameter (OD/ID)) were pulled using the following program: heat, 520; pull, 0; vel, 20; time, 200; loops, 4. Pipettes were fire-polished using an MF200 microforge (World Precision Instruments). Fire-polished patch pipettes were then used in voltage-clamping experiments. The pipette and bath solutions were designed to mimic the ionic composition of the lysosome (pH 4.5) or Golgi (pH 6.2) and cytoplasm, respectively**.** The cytosolic/batch solution contained (in mM): 20 KCl, 120 K-gluconate, 2 $MgCl_2$, 2.5 $CaCl_2$, 0.2 EGTA, 10 HEPES, 2 Na_2ATP, pH 7.25. The pipette/lumenal solution contained (in mM): 145 NaCl, 20 glucose, 5 Na3Cit, 10 EGTA, 2 CaCl2, 1 MgCl2, 10 TEA, 3 KCl, pH 4.5 or 6.2. Mock-transfected or LCAX-1-EGFP-transfected COS7 cells were treated with 5 µM vacuolin-1 overnight to increase the side of lysosomes to 1-3 µm (*17*). Cells were then washed 3x with PBS before being incubated in the indicated bath solution. Enlarged lysosomes were pushed out of the ruptured cell. After giga-ohm seal formation, break-in was performed by a zap protocol (5 V: 0.5-5s) until the appearance of capacitance transients. Voltage ramping and calculation of current were performed as described above. Positive membrane potential is taken as cytosol-positive, and positive current is taken as positive current moving outward from the cytosol. Representative traces shown were smoothed using 24-point adjacent-averaging. Where indicated, the current at +100 mV was plotted for each condition.

IV.B.11: Image acquisition

Widefield microscopy of *CalipHluor2.0, CalipHluor^{mLy}*, Fura Red, and EGFP was carried out as described in **Section III.B.13.**

For lysosomal pH recording in cells, FITC-dextran was recorded by excitation at 440nm or 488nm and emission at 514nm. 440/514 images were acquired using a 430/24 band-pass excitation filter, 520/40 band-pass emission filter, and an 89007 dichroic with an exposure of 200ms and EM gain of 200. 488/514 images were acquired using a 480/20 band-pass excitation filter, 520/40 band-pass emission filter, and an 89016 dichroic with an exposure of 200ms and EM gain of 200. To check expression of LCAX-1 in the relevant experiments, mCherry images were acquired using a 545/25 band-pass excitation filter, 595/50 band-pass emission filter, and an 89016 dichroic.

Confocal images were captured with a Leica TCS SP5 II STED laser confocal microscope (Leica Microsystems, Buffalo Grove, IL, USA) equipped with a 63X, 1.4 NA, oil immersion objective. Alexa488 was excited using an argon laser with wavelength of 488nm; and DQ Red BSA was excited using a DPSS laser at 561nm. All emissions were filtered using an acousto-optical beam splitter (AOBS) with settings suitable for each fluorophore and recorded using hybrid detector.

IV.B.12: Image analysis

Images were analyzed as described in **Section III.B.14**, applying analogous methods to make lysosomal pH measurements with FITC-dextran.

IV.B.13: Statistics

For statistical analysis between two samples, a two-sample two-tailed test assuming unequal variance was conducted. For comparison of multiple samples, one-way ANOVA with a post hoc Tukey test was conducted. All statistical analysis was performed in Origin.

IV.C: Results and Discussion

IV.C.1: Steady-state lysosomal pH measurements

We first tested whether steady-state lysosomal pH is altered by LCAX-1 activity. The pH-correctable Ca^{2+} reporters *CalipHluor 2.0* and *CalipHluor^{mLy}* used in **Sections III.C.3 and III.C.4**, respectively, offer us the opportunity to simultaneously measure lysosomal pH and Ca^{2+} in worms and

cells. In *CalipHluor 2.0*, the ratio between the pH-sensitive fluorophore dichlorofluorescein (DCF, G) and Alexa647 (R) provide a ratiometric readout of pH, sensitive in the pH region of coelomocyte lysosomes. As described and shown previously, when injected into the pseudocoelom of worms, *CalipHluor 2.0* gets endocytosed by coelomocytes and delivered to lysosomes. Surprisingly, worms devoid of *lcax-1* show no difference in pH compared to N2 worms, with lysosomes of both strains showing a pH of 5.3-5.4 (**Figure 4.3A)**. Furthermore, expression of human WT LCAX-1 or any mutant LCAX-1 in the *lcax-1*$^{+/-}$ background did not significantly alter lysosomal pH (**Figure 4.3A**). Thus, it appears at first like the worm and human homologs of LCAX-1 are not acting as H^+ exchangers. However, we know that organellar pH is tightly regulated by a complex system of proton pumps, counterion transporters, and lumenal buffers. Especially in a multicellular *in vivo* system, this may prevent significant alterations in steady state lysosomal pH, even if LCAX-1 is facilitating H^+ efflux.

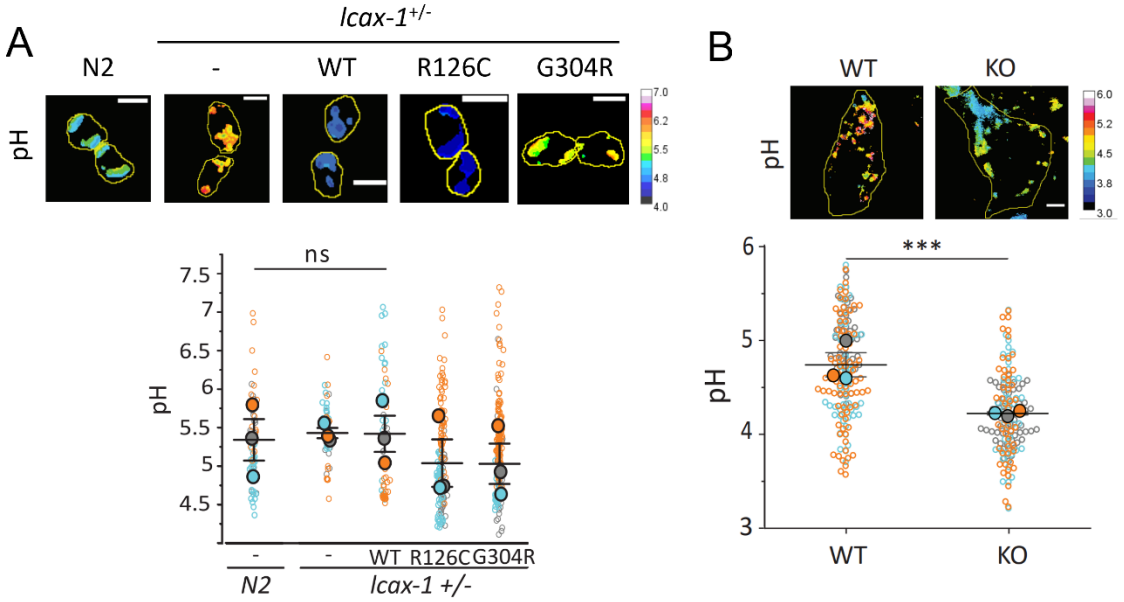

Figure 4.3: Effect of LCAX-1 expression on lysosomal pH. (A) Top, representative pH maps in *CalipHluor2.0*-labeled lysosomes in coelomocytes in indicated genetic backgrounds. Bottom, distribution of lysosomal pH in the indicated genetic backgrounds. (B) Top, representative pH maps of lysosomes from WT and LCAX-1 KO HeLa cells using *CalipHluor*^{mLy}. Bottom, pH of individual lysosomes from three different experiments. Data represents the means (closed blue, orange, and gray circles) of 3 independent experiments (open blue, orange, and gray circles). Scale bar 5 µm. I-shaped box represents the mean ± s.e.m. ns, not significant ($p>0.05$); ***$p<0.001$ (one-way ANOVA with Tukey post hoc test).

Thus, we also tested whether lysosomal pH is altered by LCAX-1 activity in a simpler system, such as mammalian cells. For this, we used *CalipHluor^{mLy}*, which substitutes Oregon Green 488 (OG488) as the pH-sensitive fluorophore, because its lower pH range matches the pH of mammalian lysosomes. Interestingly, we found that LCAX-1 KO HeLa cells have significantly lower lysosome pH than WT HeLa cells (**Fig. 4.3B**). The pH of lysosomes in WT cells is around 4.75, while the pH of lysosome in LCAX-1 KO cells is around 4.25. This decrease of about ~0.5 units corresponds to about a 3-fold increase in H^+ content, which closely resembles the estimated decrease in Ca^{2+} content of LCAX-1 KO lysosomes found in **Section III.C.4**. Thus, steady-state lysosomal pH and Ca^{2+} measurements in mammalian show that LCAX-1 facilitates Ca^{2+} import at the expense of H^+ export. Why this phenomenon is not conserved in living worms is interesting, and may reflect more robust lysosomal pH maintenance *in vivo*. Alternatively, this discrepancy could be a result of differences between heterozygous and homozygous knockout systems.

IV.C.2: Lysosomal pH dynamics following cytosolic Ca^{2+} spikes

Steady-state pH measurements offer a snapshot of lysosomal pH at any given time, but do not reflect active H^+ transport across the lysosome membrane. Alterations in steady-state lysosomal pH could occur because of any number of off-target or downstream effects other than LCAX-1 activity itself. Thus, we sought to visualize the effect of LCAX-1 activity on lysosome pH dynamics. Upon inducing a cytosolic Ca^{2+} spike with ATP, we saw in **Section III.C.5** that LCAX-1 (especially the lysosomal population) is responsible for mopping up cytosolic Ca^{2+}. If LCAX-1 acts as a lysosomal Ca^{2+}/H^+ exchanger, then its Ca^{2+} import should coincide with lysosome deacidification, as H^+ would be driven out of the lysosome. Indeed, using the self-ratiometric pH probe FITC-dextran, which localizes to endolysosomes, we see lysosomes in WT cells deacidify upon triggering a cytosolic Ca^{2+} spike with ATP (**Fig. 4.4A-C**). Thus, as previously described, lysosomes in mammalian cells appear to have a Ca^{2+}/H^+ exchange mechanism. Strikingly, lysosomes of LCAX-1 KO cells show no basification upon triggering a cytosolic Ca^{2+} spike with ATP (**Fig. 4.4A-C**). Overexpressing WT LCAX-1 or lysosome-localized LCAX-1 (but not Golgi-localized LCAX-1) restores lysosomes basification caused by cytosolic Ca^{2+}

spike (**Fig. 4.4A-C**). Thus, LCAX-1 appears to be the molecule responsible for lysosomal Ca^{2+}/H^{+} exchange. This is further illustrated by overlays of cytosolic Ca^{2+} and lysosomal pH dynamics, as measured by Fura Red and FITC-dextran in separate experiments (due to spectral overlap), but performed on the same timescales. In WT HeLa cells, we see that the decrease in cytosolic Ca^{2+} following a spike coincides with the increase in lysosomal pH (**Fig. 4.4D**). Surprisingly, we never see the lysosomal pH come back down to baseline levels, likely indicating that continuous import of Ca^{2+} by LCAX-1 (even after 5 minutes of treatment with ATP) is preventing restoration of lysosome acidity. On the other hand, LCAX-1 KO HeLa cells show no decrease in cytosolic Ca^{2+} following a spike and no lysosome deacidification (**Fig. 4.4E**). Combined, this data shows that LCAX-1 activity causes H^{+} efflux from lysosomes, which happens in synchrony with Ca^{2+} influx into lysosomes.

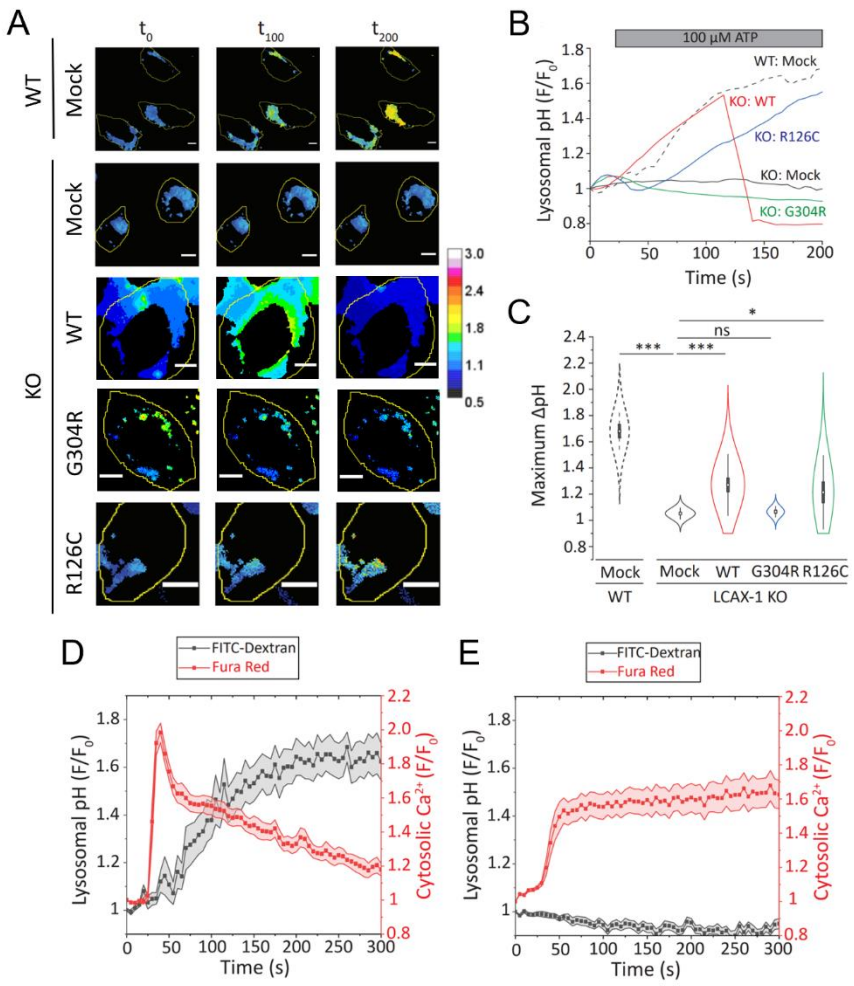

Figure 4.4: Effect of LCAX-1 on lysosomal pH dynamics after a cytosolic Ca^{2+} spike. (A) Representative 488/440 maps of FITC-dextran in WT HeLa cells and LCAX-1 KO HeLa cells treated with 100µM ATP after transfection with the indicated mutant of LCAX-1-mCherry. Maps shown are at t=0s (prior to ATP treatment), t=100s, and t=200s. (B) Representative lysosomal pH traces given by the 488/440 ratio of FITC-dextran in (a). Curves are normalized to the value at t=0. (C) Maximum change in pH, given by the maximum fold change in 488/440 over the 200-second timecourse. (D,E) Overlays of the cytosolic Ca^{2+} and lysosomal pH spike, in WT cells (D) or LCAX-1 KO cells (E). Scale bar 5 µm. Violin plots show normal distributions with the box showing standard error of the mean. ns, not significant ($p>0.05$); *$p<0.05$; ***$p<0.001$ (one-way ANOVA with Tukey post hoc test).

IV.C.3: Dependence of Ca^{2+} mopping on a pH gradient

If LCAX-1 uses the steep lysosomal pH gradient to drive Ca^{2+} up its chemical gradient, then abolishing the pH across the lysosome should prevent lysosomal Ca^{2+} uptake by LCAX-1. To directly address this question, we tested the ability of LCAX-1 to mop up cytosolic Ca^{2+} when lysosomal pH is neutralized. We achieved this by inhibiting v-ATPase with bafilomycin A, which caused a significant increase in lysosomal pH (**Fig. 4.5A**). Indeed, pretreatment with bafilomycin A reduced the efficiency by which lysosomal LCAX-1 restores cytosolic Ca^{2+} levels in HeLa cells (**Fig. 4.5B-D**). We then sought to compare these findings with a cell line showing lower endogenous expression of LCAX-1, such as COS7 cells (*18*). In these cells, low levels of LCAX-1 lead to a much slower removal of cytosolic Ca^{2+} following the cytosolic Ca^{2+} spike (**Fig. 4.5E-G**). Overexpressing either WT LCAX-1 or the lysosome-favoring mutant of LCAX-1 speeds up the restoration of low cytosolic Ca^{2+}, but not when the pH gradient across the lysosome is collapsed with the v-ATPase inhibitor, bafilomycin A (**Fig. 4.5E-G**). Thus, the pH gradient across the lysosome is necessary for LCAX-1 to drive Ca^{2+} into lysosomes in multiple systems. Combined with earlier results, this further supports the role of LCAX-1 as a Ca^{2+}/H^{+} exchanger.

IV.C.4: Effect of LCAX-1 on lysosomal function

Given the important role of lysosome acidity on lysosome function and the effect of LCAX-1 on lysosome pH dynamics, we wondered whether LCAX-1 activity affects lysosome function. To test this, we analyzed lysosomal proteolysis in WT and LCAX-1 KO cells. We used the probe DQ-Red BSA, which is endocytosed in cells and trafficked through early and late endosomes to lysosomes (*19*). The probe is a bovine serum albumin (BSA) heavily labeled with BODIPY TR-X dyes, resulting in significant self-quenching. Upon hydrolysis of the DQ-Red BSA to single dye-labeled peptides by lysosomal proteases, self-quenching is relieved. This leads to brighter red fluorescence (*19*). To make this system ratiometric, we simultaneously labeled lysosomes with Alexa488-Dextran (G) and DQ-Red BSA (R). As such, the R/G ratio provides a quasi-ratiometric readout of lysosomal proteolysis. Using this approach, we found that lysosomes in cells lacking LCAX-1 show elevated proteolysis, which may be consistent with

hyperacidic lysosomes seen in these cells (**Fig. 4.6**). Indeed, hyperacidic lysosomes are associated with abnormal lysosome phenotypes and disease states (*20*).

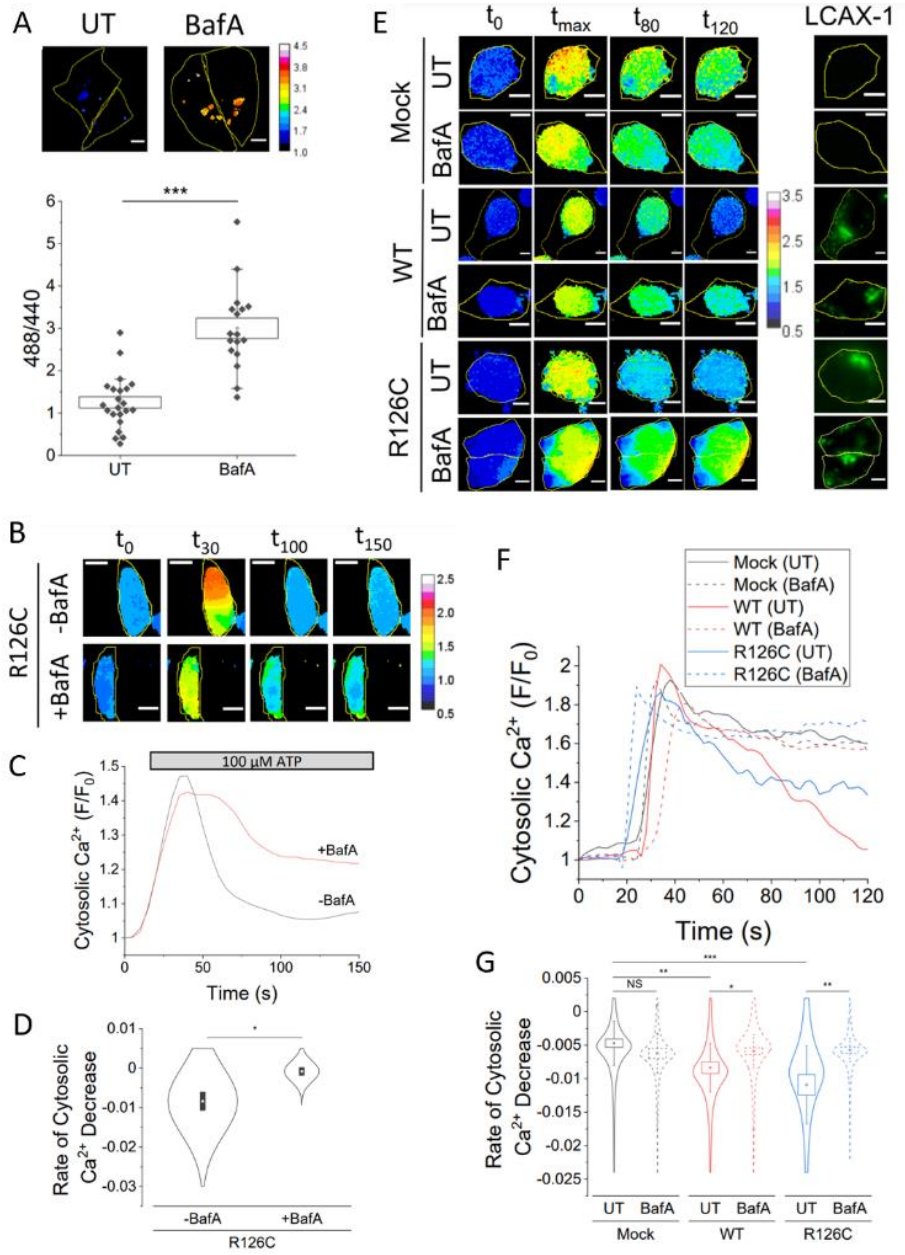

Figure 4.5: Sensitivity of LCAX-1 to the pH gradient across the lysosomal membrane. (A) Top, representative 488/440 maps of FITC-dextran in COS-7 cells either untreated or treated with 500 nM bafilomycin A for 30 min. Bottom, quantification of 488/440 ratios of individual lysosomes under the indicated conditions. (B) Representative 440/488 maps of Fura Red in LCAX-1 KO HeLa cells treated with 100 µM ATP transfected with the lysosome-favoring mutant of LCAX-1-EGFP (R126C). Where indicated, 500 nM bafilomycin A was added 30 minutes prior to and throughout the experiment. Maps shown are at t=0s (prior to ATP treatment), t=30s, t=100s, and t=150s. (C) Representative cytosolic Ca^{2+} traces given by the 440/488 ratio of Fura Red in (b). Curves are normalized to the value at t=0. (D) Slope of the linear fit of the cytosolic Ca^{2+} decrease following maximum 440/488 of Fura Red. (E) Left, representative 440/488 maps of Fura Red in COS-7 cells treated with 100 µM ATP after mock transfection or transfection with the indicated mutant of LCAX-1-EGFP. Cells were pre-labelled and treated with 500 nM bafilomycin A prior to imaging and ATP treatment, as indicated. Maps shown are at t=0s (prior to ATP treatment), maximum 440/488, t=80s, and t=120s. Right, representative GFP images showing transfection of LCAX-1-EGFP. (F) Representative cytosolic Ca^{2+} levels given by 440/488 intensity of Fura Red in (e). Curves are normalized to the value at t=0. (G) Slope of linear fit of the cytosolic Ca^{2+} decrease following maximum 440/488 of Fura Red. Scale bar 5µm. Boxes and bars indicate the s.e.m. and standard deviation, respectively. Violin plots show the normal distribution. NS, not significant (P>0.05); *P<0.05; **P<0.01; ***P<0.001 (one-way ANOVA with Tukey post hoc test).

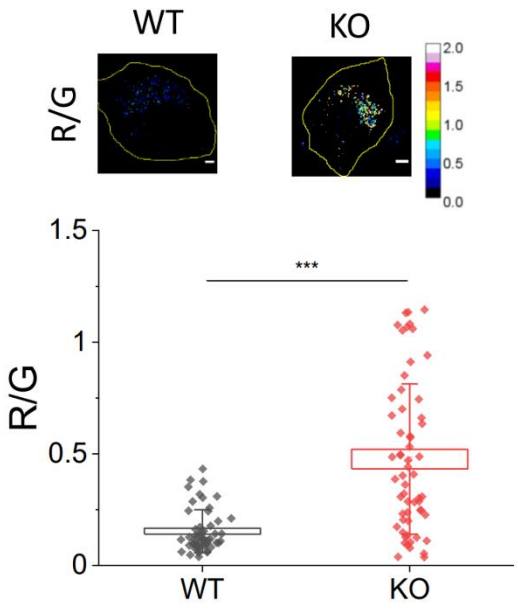

Figure 4.6: Effect of LCAX-1 on lysosomal proteolysis. Top, representative R/G maps, generated using the ratio DQ-BSA intensity to Alexa488-dextran intensity, in WT and LCAX-1 KO HeLa cells. Bottom, distribution of whole-cell R/G values. Scale bar 5µm. Boxes and bars represent the s.e.m. and standard deviation, respectively. ***p<0.001.

IV.C.5: Dependence of Ca^{2+} current on a pH gradient

The previous sets of results in this chapter show that LCAX-1 facilitates lysosomal H^+ export correlated with Ca^{2+} import, and that abolishing the lysosomal pH gradient prevents this Ca^{2+} import. These experiments imply that LCAX-1 functions as a Ca^{2+}/H^+ exchanger, but it is still possible that lysosomal pH changes are connected via other molecular players coordinated with LCAX-1. For instance, we know that Ca^{2+} export by TRPML1 and other release channels is sensitive to lysosomal pH (*21*). And we know that proper counterion movement is necessary for lysosomal pH maintenance (*22*). Thus, it could still be that LCAX-1 activity and lysosomal pH changes are connected through the dysregulation of other lysosomal transporters, rather than direct Ca^{2+}/H^+ exchange by LCAX-1. To rule out this possibility, we directly interrogated exchanger activity by patch-clamp electrophysiology. As in **Section III.C.6**, we used NMDG-MSA buffers where Ca^{2+} was the only transportable ion. We first carried out whole-cell electrophysiology in HeLa cells, and varied the transmembrane pH gradient by altering the pH of the extracellular/bath buffer (**Fig. 4.7A**). Indeed, increasing the transmembrane pH gradient increased the outward current density and shifted the reversal potential (**Fig. 4.7B-C**). Finally, we wondered whether the pH gradient dependence of LCAX-1 current is maintained in more physiological relevant contexts: on the lysosome membrane and with physiologically relevant buffer compositions. We directly interrogated LCAX-1 currents on isolated swollen lysosomes of COS7 cells, whose flatter morphology lends itself to lysosome isolation. Importantly, both WT and R126C LCAX-1-EGFP can be visualized on lysosomes of COS7 cells upon treatment with vacuolin-1, which swells lysosomes (**Fig. 4.7D-E**). We used pipette buffers to mimic the lumenal acidity and ionic concentrations

of either lysosomes (pH 4.5) or the Golgi (pH 6.2) (**Fig. 4.7F**). Interestingly, lysosomes of cells expressing LCAX-1 show a large outwardly rectifying current (positive current into the lysosome) under either condition. Importantly, at +100mV, the current at lysosomal pH was ~2.5 fold higher than at pH levels corresponding to the Golgi (**Fig. 4.7G-H**). This indicates that LCAX-1 current depends heavily on the pH gradient, and that the lysosome-localized fraction of WT LCAX-1 has significant Ca^{2+} import capacity compared to the Golgi population.

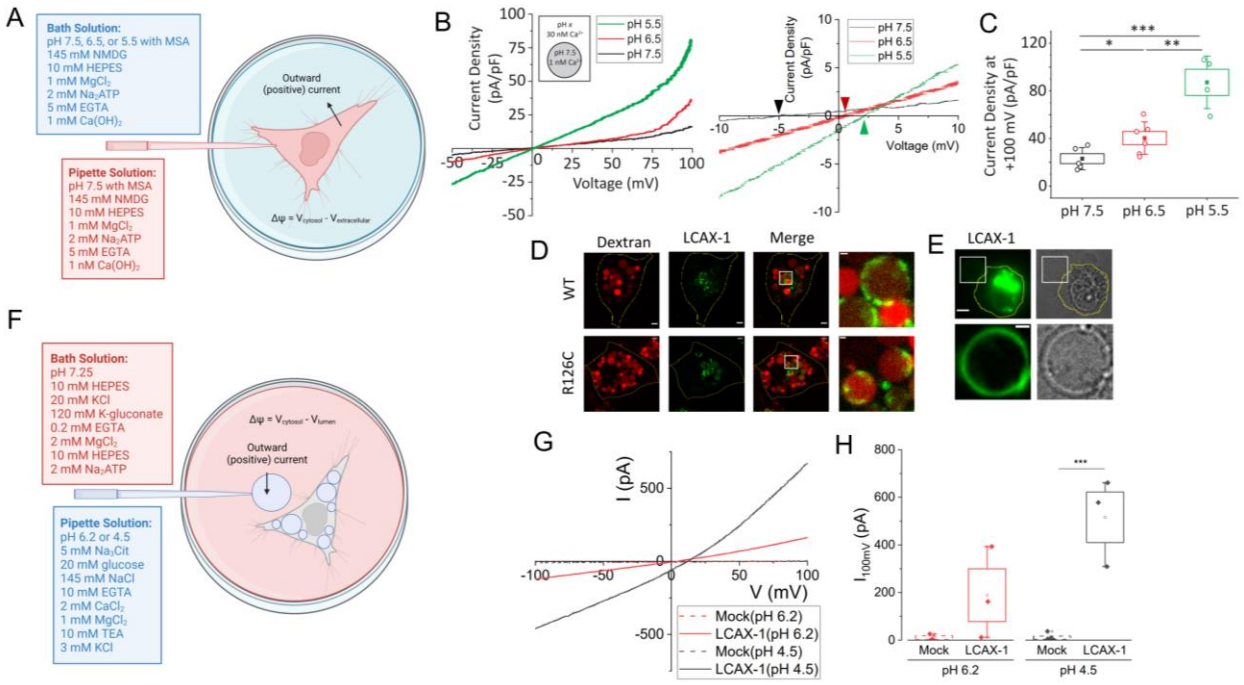

Figure 4.7: Effect of transmembrane pH gradients on LCAX-1 current. (A) Buffers used for whole-cell patch-clamping, and sign conventions used for current and membrane potential. (B) Left, representative current density curves of HeLa cells expressing LCAX-1-EGFP with 1 nM free Ca^{2+} on the pipette/cytosolic solution and an extracellular/bath pH of 7.5 (black), 6.5 (red), or 5.5 (green). Right, zoomed-in representative current density curves to show reversal potential differences. (C) Current density at +100 mV across the plasma membrane of the indicated cell types from (b). (D) Representative fluorescence images of COS-7 cells transiently transfected with WT or R126C LCAX-1-EGFP (green). Lysosomes were labelled with 1 mg/mL TMR-dextran (red) and swollen with 5µM vacuolin-1 before imaging. (E) Representative fluorescence of LCAX-1-EGFP (green) on an isolated lysosome of COS-7 cells following overnight treatment with 5 µM vacuolin-1 and cell rupture. (F) Buffers used for lysosome patch-clamping, and sign conventions used for current and membrane potential. (G) Representative IV curves of lysosome patch-clamping using a ramp from -100mV to +100mV. Lysosomes of mock-transfected HeLa cells (dashed lines) or cells transfected with LCAX-1-EGFP (solid lines) were patched with pipette solution of pH 6.2 (red) or pH 4.5 (black). (H) Current at +100mV across the lysosome membrane from indicated cells with the indicated lysosomal pH. Scale bar 5µm. Inset scale bar 2µm. Boxes and bars represent s.e.m. and outliers, respectively. *p<0.05; **p<0.01; ***p<0.001. (one-way ANOVA with Tukey post hoc test).

IV.D: Conclusion

The data in this chapter show that LCAX-1 imports Ca^{2+} up its chemical gradient into the lysosome, using the steep pH gradient. In other words, it acts as a Ca^{2+}/H^{+} exchanger. We have shown this using the same three general methods used to show that CLC proteins are H^{+} exchangers, discussed in **Section IV.A.2**. First, we showed that LCAX-1 activity alters the pH of lysosomes, using both steady-state and dynamic pH measurements. Second, we showed that a pH gradient is necessary for Ca^{2+} import by LCAX-1, using cytosolic Ca^{2+} removal assays. Third, we showed using electrophysiology that a pH gradient directly affects transport activity of LCAX-1. Combined, this data illustrates that the lysosomal population of LCAX-1 is much more active and efficient than the Golgi population of LCAX-1. Because the pH gradient across the lysosome membrane is much larger than the pH gradient across the Golgi membrane, a Ca^{2+}/H^{+} exchanger on the lysosome has a much higher Ca^{2+} transport capacity. Whether this transport capacity is enough to sustain the high Ca^{2+} store of lysosomes depends on the membrane potential and stoichiometry of exchange, and will be discussed in later chapters. But we can conclude that even though LCAX-1 is predominantly localized to the Golgi, its exchange activity on lysosomes is significant.

IV.E: References

1. D. Demaegd, F. Foulquier, A.-S. Colinet, L. Gremillon, D. Legrand, P. Mariot, E. Peiter, E. Van Schaftingen, G. Matthijs, P. Morsomme, Newly characterized Golgi-localized family of proteins is involved in calcium and pH homeostasis in yeast and human cells. *Proc Natl Acad Sci USA.* **110**, 6859–6864 (2013).

2. H. Wang, Y. Yang, F. Huang, Z. He, P. Li, W. Zhang, W. Zhang, B. Tang, In situ fluorescent and photoacoustic imaging of golgi ph to elucidate the function of transmembrane protein 165. *Anal. Chem.* **92**, 3103–3110 (2020).

3. D. Demaegd, A.-S. Colinet, A. Deschamps, P. Morsomme, Molecular evolution of a novel family of putative calcium transporters. *PLoS ONE*. **9**, e100851 (2014).

4. A. B. Waight, B. P. Pedersen, A. Schlessinger, M. Bonomi, B. H. Chau, Z. Roe-Zurz, A. J. Risenmay, A. Sali, R. M. Stroud, Structural basis for alternating access of a eukaryotic calcium/proton exchanger. *Nature*. **499**, 107–110 (2013).

5. A. Accardi, C. Miller, Secondary active transport mediated by a prokaryotic homologue of ClC Cl- channels. *Nature*. **427**, 803–807 (2004).

6. T. J. Jentsch, M. Pusch, CLC chloride channels and transporters: structure, function, physiology, and disease. *Physiol. Rev.* **98**, 1493–1590 (2018).

7. A. Picollo, M. Pusch, Chloride/proton antiporter activity of mammalian CLC proteins ClC-4 and ClC-5. *Nature*. **436**, 420–423 (2005).

8. I. Neagoe, T. Stauber, P. Fidzinski, E.-Y. Bergsdorf, T. J. Jentsch, The late endosomal ClC-6 mediates proton/chloride countertransport in heterologous plasma membrane expression. *J. Biol. Chem.* **285**, 21689–21697 (2010).

9. L. Leisle, C. F. Ludwig, F. A. Wagner, T. J. Jentsch, T. Stauber, ClC-7 is a slowly voltage-gated 2Cl(-)/1H(+)-exchanger and requires Ostm1 for transport activity. *EMBO J.* **30**, 2140–2152 (2011).

10. R. E. Guzman, M. Grieschat, C. Fahlke, A. K. Alekov, ClC-3 is an intracellular chloride/proton exchanger with large voltage-dependent nonlinear capacitance. *ACS Chem. Neurosci.* **4**, 994–1003 (2013).

11. O. Scheel, A. A. Zdebik, S. Lourdel, T. J. Jentsch, Voltage-dependent electrogenic chloride/proton exchange by endosomal CLC proteins. *Nature*. **436**, 424–427 (2005).

12. G. Novarino, S. Weinert, G. Rickheit, T. J. Jentsch, Endosomal chloride-proton exchange rather than chloride conductance is crucial for renal endocytosis. *Science*. **328**, 1398–1401 (2010).

13. S. Weinert, N. Gimber, D. Deuschel, T. Stuhlmann, D. Puchkov, Z. Farsi, C. F. Ludwig, G. Novarino, K. I. López-Cayuqueo, R. Planells-Cases, T. J. Jentsch, Uncoupling endosomal CLC chloride/proton exchange causes severe neurodegeneration. *EMBO J.* **39**, e103358 (2020).

14. S. Weinert, S. Jabs, C. Supanchart, M. Schweizer, N. Gimber, M. Richter, J. Rademann, T. Stauber, U. Kornak, T. J. Jentsch, Lysosomal pathology and osteopetrosis upon loss of H+-driven lysosomal Cl- accumulation. *Science*. **328**, 1401–1403 (2010).

15. N. Narayanaswamy, K. Chakraborty, A. Saminathan, E. Zeichner, K. Leung, J. Devany, Y. Krishnan, A pH-correctable, DNA-based fluorescent reporter for organellar calcium. *Nat. Methods*. **16**, 95–102 (2019).

16. B. Suresh, A. Saminathan, K. Chakraborty, C. Cui, L. Becker, Y. Krishnan, Tubular lysosomes harbor active ion gradients and poise macrophages for phagocytosis. *BioRxiv* (2020), doi:10.1101/2020.12.05.413229.

17. X.-P. Dong, X. Cheng, E. Mills, M. Delling, F. Wang, T. Kurz, H. Xu, The type IV mucolipidosis-associated protein TRPML1 is an endolysosomal iron release channel. *Nature*. **455**, 992–996 (2008).

18. M. Uhlén, L. Fagerberg, B. M. Hallström, C. Lindskog, P. Oksvold, A. Mardinoglu, Å. Sivertsson, C. Kampf, E. Sjöstedt, A. Asplund, I. Olsson, K. Edlund, E. Lundberg, S. Navani, C. A.-K. Szigyarto, J. Odeberg, D. Djureinovic, J. O. Takanen, S. Hober, T. Alm, F. Pontén, Proteomics. Tissue-based map of the human proteome. *Science*. **347**, 1260419 (2015).

19. R. Marwaha, M. Sharma, DQ-Red BSA Trafficking Assay in Cultured Cells to Assess Cargo Delivery to Lysosomes. *Bio Protoc.* **7** (2017), doi:10.21769/BioProtoc.2571.

20. E.-R. Nicoli, M. R. Weston, M. Hackbarth, A. Becerril, A. Larson, W. M. Zein, P. R. Baker, J. D. Burke, H. Dorward, M. Davids, Y. Huang, D. R. Adams, P. M. Zerfas, D. Chen, T. C. Markello, C. Toro, T. Wood, G. Elliott, M. Vu, Undiagnosed Diseases Network, M. C. V. Malicdan, Lysosomal storage and albinism due to effects of a de novo CLCN7 variant on lysosomal acidification. *Am. J. Hum. Genet.* **104**, 1127–1138 (2019).

21. M. Li, W. K. Zhang, N. M. Benvin, X. Zhou, D. Su, H. Li, S. Wang, I. E. Michailidis, L. Tong, X. Li, J. Yang, Structural basis of dual Ca2+/pH regulation of the endolysosomal TRPML1 channel. *Nat. Struct. Mol. Biol.* **24**, 205–213 (2017).

22. J. E. DiCiccio, B. E. Steinberg, Lysosomal pH and analysis of the counter ion pathways that support acidification. *J. Gen. Physiol.* **137**, 385–390 (2011).

V. Identification of putative Ca^{2+} binding sites in LCAX-1

V.A: Introduction

V.A.1: Studying ion channel/transporter function by mutational analyses

To unequivocally prove that a molecule is an ion channel, exchanger, or transporter, it is critical to identify putative ion binding sites. Mutating these ion binding sites should alter transport activity in terms of ion selectivity, conductivity, or coupling. Identifying such critical residues provides invaluable information about a transporter. First, it provides conclusive evidence that the target molecule is directly transporting ions, and not involved as an accessory or intermediate player. Second, it provides mechanistic information about the transporter and its regulatory triggers. Finally, these mutants offer excellent controls to show the physiological relevance of functional channels and transporters. Usually, ion binding sites are first discovered using bioinformatics or structural information, and then confirmed and characterized with mutational studies. In this chapter, we follow this trajectory to identify Ca^{2+} binding sites in LCAX-1 that upon mutation reduce activity of the exchanger. To illustrate the importance of identifying these mutants, this section will highlight examples of mutational analyses of other exchangers and transporters.

A potent example of the value of identifying ion binding sites comes from the CLC family of Cl^-/H^+ exchangers. The structures of two CLC channels (StCLC from *S. typhinmurium* and EcCLC from *E. coli*), identified a Cl^- conductance pore in the protein that contains important amino acids from four separate regions ($G_{106}SGIP_{110}$, $G_{146}KEGP_{150}$, $G_{355}XFXP_{359}$, and Y445) near the center of the membrane (*1*). These regions are highly conserved and occur at the N-termini of α-helices, creating a net positive end charge towards the ion binding site. A strong peak of electron density in the ion binding site was confirmed to be a Cl^- ion, providing evidence that this area confers anion selectivity (*1*). Indeed, the Cl^- ion is coordinated by main-chain amide nitrogen atoms that are not involved in hydrogen bonding with other residues in the protein (*1*). This observation is perhaps surprising, that Cl^- ions do not make direct contact with positively charged side chains, but rather the favorable electrostatic environment arising from partial positive charges of helix dipole interactions. This may be necessary to stabilize Cl^- ions and

permit rapid diffusion. In the conductance pore, E148 is sandwiched in between the positive ends of two α-helices, and must swing out of the way to permit Cl^- ion entry, thus acting as a gating filter (**Fig. 5.1A**) (*1*). Indeed, the E148A mutation completely opens EcCLC because it contains an uninterrupted stream of anions connecting the intracellular and extracellular solutions (*2*). Later studies that showed that EcCLC was actually a Cl^-/H^+ exchanger also revealed that the E148A mutation abolished its pH sensitivity and renders currents completely Cl^-selective (**Fig. 5.1B**) (*3*). Near this glutamate, two highly conserved phenylalanine residues form an aromatic slide that allow the protonated glutamate to move without competing with Cl^- ions in the anion-selective pathway (*4*). Gating glutamate residues have also been identified in mammalian CLC exchangers (*5–7*). Conversion of these exchangers into pure Cl^- channels with "uncoupling" mutations has revealed the physiological importance of proton-driven Cl^- accumulation in intracellular compartments (*8–12*).

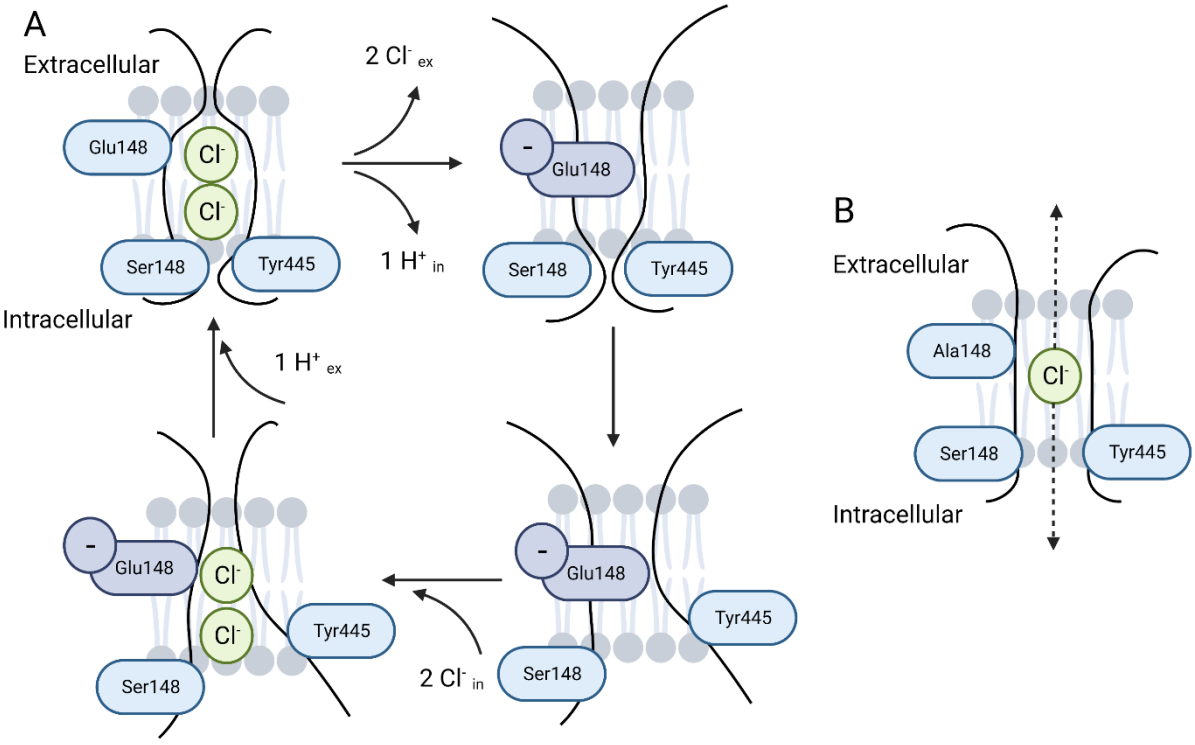

Figure 5.1: Transport cycle of CLC transporters as exchangers or channels. (A) The outward-facing occluded state (top left) undergoes a conformational change to open, which allows two Cl^- ions to leave, followed by deprotonation of Glu148 (top right). Conformational change to the inward-facing state (bottom right) then allows two Cl^- ions to enter and knocking Glu148 out of the pore (bottom left). (B) Channel-like CLC caused by a Glu148Ala mutation, which abolishes exchange activity and pH sensitivity.

Similar studies have identified gating and binding residues in Ca^{2+} transporters and exchangers. Extensive structural studies on the sarcoplasmic/endoplasmic reticulum Ca^{2+} ATPase (SERCA) have revealed cooperative binding of two Ca^{2+} ions per transport cycle. Binding of one Ca^{2+} ion to site I, buried deep in the transmembrane region, increases the affinity of site II for Ca^{2+} (*13*). After binding the second ion, ATP hydrolysis occurs and the reaction cycle proceeds. Solvent-exposed acidic residues identified through molecular dynamics and structural studies are involved in Ca^{2+} gating and recognition. These include E51, E55, E58, D59, E109, N796, and D800 (**Fig. 5.2A**) (*13–15*). Residues on cytosolic loops also bind Ca^{2+}, including D813, D815, and D818 (*16*). Allosteric signaling between Ca^{2+} binding and ATP hydrolysis has illustrated a complex picture of SERCA transport mechanisms and conformational changes. Identification of Ca^{2+} binding sites has also revealed information about other types of Ca^{2+} transporters, such as voltage-gated Ca^{2+} channels (VGCCs) and Na^{+}/Ca^{2+} exchangers (NCXs). VGCCs are highly Ca^{2+}-selective, with the pore containing four conserved glutamate residues for divalent cation binding and permeation (*17–19*). This was first determined via structures of bacterial channels and confirmed to be conserved for mammalian VGCCs (*19*, *20*). Mutating key glutamate residues seems to abrogate interactions between the pore unit and auxiliary subunits, thereby causing trafficking defects (*21*). The mechanism of NCXs, which use the Na^{+} gradient across the cell membrane to extrude Ca^{2+} from the cell, involves alternating access of its two counterions. The structure of NCX from *M. jannaschii* revealed four putative ion-binding sites (with one of them accommodating Ca^{2+} ions) and a structural mechanism for ion exchange (*22*).

Finally, structural and mutational studies have identified ion binding sites in intracellular K^{+} channels. Transmembrane protein 175 (TMEM175) is a K^{+}-selective channel on the lysosome membrane that establishes membrane potential (*23*). It is evolutionarily distinct from other K^{+} channels, displaying a unique membrane topology and lacking the typical TVGYG selectivity filter present in canonical K^{+} channels (*24*, *25*). As such, it also exhibits different electrochemical and ion permeation properties than typical K^{+} channels. The structures of bacterial and human TMEM175 have revealed unique ion-conduction pores. In bacterial TMEM175, a highly conserved layer of threonine residues confers ion

selectivity, forming a physical gate (*26*, *27*). In human TMEM175, conserved isoleucine residues in the center of the pore serve as the gating filter (**Fig. 5.2B**). In addition, its regulation by Ca^{2+} has been confirmed with the identification of Ca^{2+}-binding sites (*28*, *29*). Interestingly, mutations in TMEM175 linked to Parkinson's disease, such as M393T, also abolish channel function and ion conductance, confirming the physiological relevance of TMEM175 as a K^+ transporter (*30*, *31*). Thus, characterization of ion-binding regions of intracellular transporters reveals information about their transport mechanism and physiological relevance.

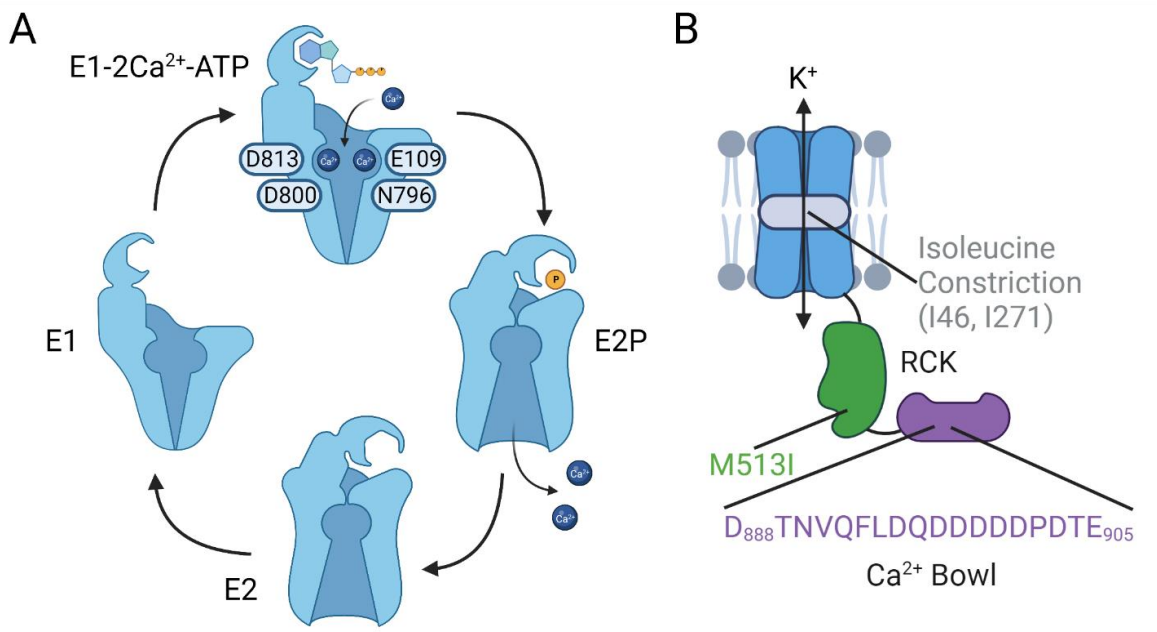

Figure 5.2: Transport mechanism and binding sites of select ion transporters. (A) Transport cycle of SERCA and some residues involved in the two Ca^{2+} binding sites. (B) Topology of TMEM175, which has an isoleucine gating filter in the pore. It also exhibits Ca^{2+} sensitivity that is lost by mutations in the RCK domain, such as D898A in the Ca^{2+} bowl, as well as M513I.

V.A.2: Previous indications of LCAX-1 binding sites

Clues about potential Ca^{2+} binding sites in LCAX-1 come from conservation analyses of its protein family (UPF0016), as well as structural information on other Ca^{2+}/H^+ exchangers. The UPF0016 family is defined by the presence of 1-2 copies of an EΦGD(KR)(ST) consensus motif (*32*). Prokaryotic members of the family are single-domain proteins with one such motif or two-domain fusions of two homologous domains and an antiparallel membrane orientation (*32*). These two-domain proteins and others likely resulted from gene duplication (*33*–*36*). The antiparallel orientation may have evolved from

a dual-topology protein that can insert in membranes in both orientation with similar likelihood (*37*, *38*). Such ancestral protein then likely associated into an antiparallel homodimer. This topology is strikingly similar to cation exchangers in general, and Ca^{2+}/H^{+} exchangers (CAXs) specifically. CAXs also consist of two homologous domains each having a highly conserved motif (which also likely arose from a gene duplication event), all separated by a conserved cytosolic acidic loop (*39–42*). In addition, the signature EΦGD(KR)(TS) motifs are strikingly similar to the signature CAX sequence necessary for Ca^{2+} binding and transport, GNXXE (*43–45*). Both have key glutamate residues, and neighboring residues that offer both flexibility and a hydrophilic environment. Thus, strictly from family conservation and similarities to CAX proteins, the key glutamates in the consensus motifs and acidic loop seem to be involved in Ca^{2+} binding.

Further suggestions of Ca^{2+} binding regions of LCAX-1 come from structural studies of CAX proteins. Around the same time, three CAX protein crystal structures were published: VCX1 from *S. cerevisiae* (*46*), YfkE from *B. subtilis* (*47*), and CAX from *A. fulgidus* (*48*). The VCX1 structure showed a central four-helix core that contains the highly conserved GNXXE repeats and forms an hourglass shape (*46*). A 20-residue acidic motif connects the duplicated halves of the protein, and contains an α-helix oriented parallel to the membrane, directly under the GNXXE repeats. The glutamates from each GNXXE repeat (E106 and E302) and neighboring residues coordinate a central Ca^{2+} ion and three ordered water molecules (*46*). The remainder of this Ca^{2+} binding site is stabilized by interactions from polar residues in neighboring transmembrane regions. The acidic cytosolic loop also coordinates two Ca^{2+} ions using key aspartate and glutamate residues (E230 and D234), causing it to maintain an α-helix formation and become more rigid (*46*). This indicates that the acidic loop may augment ion conductance in the presence of increased cytosolic Ca^{2+}. The proposed transport cycle involves a conformation change that occurs because of a proton motive force, to expose the active site glutamates to the cytosolic side, where they are deprotonated at neutral cytosolic pH (**Fig. 5.3**). Under conditions of high cytosolic Ca^{2+}, ions are coordinated by the acidic helix and brought into proximity of the active site. Active site residues partially replace the Ca^{2+} hydration shell to complete coordination, which initiates a conformation change that

opens the active site to the vacuole. The acidic pH of the vacuole lowers the Ca^{2+} affinity of the active site glutamates, leading to the release of Ca^{2+} into the vacuole.

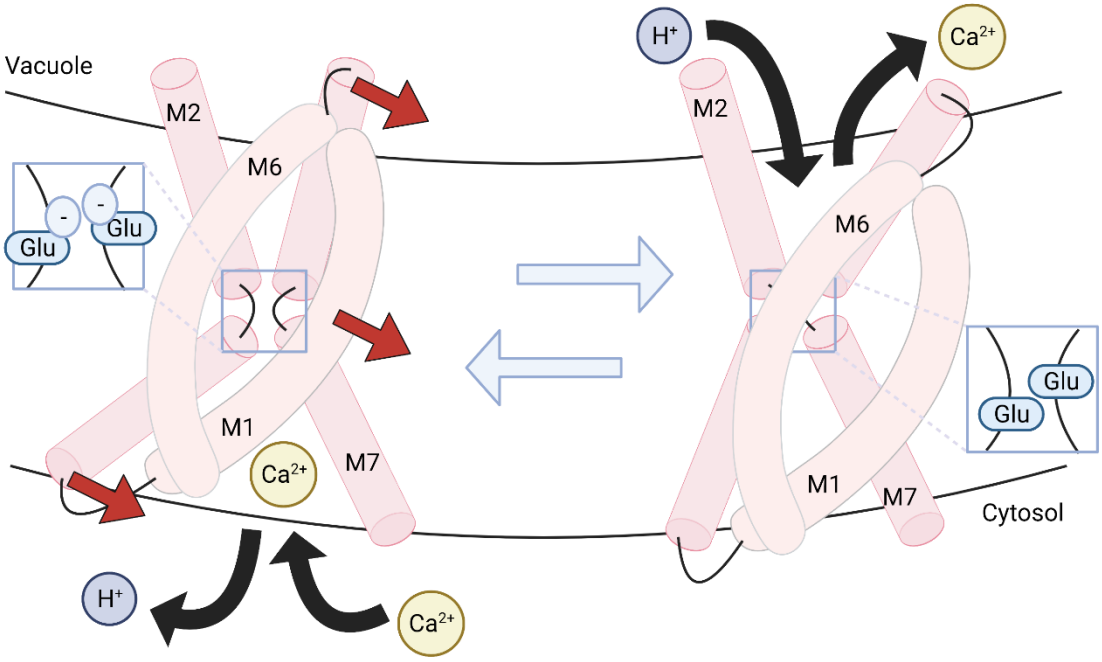

Figure 5.3: Ca^{2+}/H^{+} exchange mechanism by VCX1. In the cytosol-facing conformation (left), the active site glutamate residues (E106 and E302) maintain a negative charge. Ca^{2+} can then be coordinated by the acidic helix and reach the active site. This leads to a conformational change where M1 and M6 helices translate to close the cytosolic vestibule and open a vacuolar cleft. Now in this vacuole-facing conformation (right), the active site glutamate become protonated, lowering their Ca^{2+} affinity and leading to release of Ca^{2+} into the vacuole. The proton motive gradient across the vacuolar membrane then drives a conformational change back to the cytosol-facing conformation. This cyclical pumping of M1/M6 around the flexible M2/M7 core enables rapid exchange of Ca^{2+} and H^{+}.

Similarly, the structure of CAX from *A. fulgidus* shows a central core of helices that form the Ca^{2+} binding site with key glutamate residues (E78 and E258) (*48*). In addition, a mechanism proceeds where alternating access of the hydrophilic cavities leads to Ca^{2+} transport. Unlike VCX1, the central core consists of two hourglass kinks that bend around each other to form an octahedron, in which a pocket forms for Ca^{2+} binding (*48*). Finally, YfkE from *B. subtilis* forms a homotrimer, with each protomer containing the conserved Ca^{2+} binding site repeats with key glutamate residues (E72 and E255) (*47*). A similar mechanism of alternating access facilitates ion exchange. Thus, structural studies of these three CAX family members show highly similar Ca^{2+}/H^{+} exchange mechanisms that rely on active site

glutamates in highly conserved repeat motifs. Tertiary and quaternary structures of these CAX proteins vary, but the alternating access mechanism and Ca^{2+} binding site structure are highly conserved.

Although LCAX-1 and the UPF0016 family members show no global homology to these CAX proteins, their similarities in topology and key features are striking. Thus, they may exchange Ca^{2+} for H^{+} by a similar mechanism, with key glutamates in the EΦGD(KR)(TS) motifs and cytosolic loop involved in Ca^{2+} binding and transport. This offers clues for us to study key residues for LCAX-1 exchange activity.

V.B: Materials and Methods

V.B.1: Chemicals and reagents

Modified oligonucleotides were purchased from IDT (USA), subjected to ethanol precipitation and quantified using UV absorbance. Chemicals used for the previously synthesized Rhod-5F-azide were purchased from Sigma and Alfa Aesar as previously described (*11*). DCF used for previously described conjugation was purchased from Fisher Scientific (*49*). EGTA, ampicillin, kanamycin, carbenicillin, adenosine triphosphate, yeast synthetic drop-out media, methane sulfonic acid, HEPES, calcium hydroxide, magnesium chloride, and N-methyl-D-glucamine were purchased from Sigma. Monodisperse silica microspheres were obtained from Cospheric. Fura Red and RNase A were purchased from Thermo Fisher Scientific. YNB with ammonium sulfate was purchased from MPBio. Zymolyase was purchased from Zymo Research.

V.B.2: Mammalian cell culture, plasmids, and transfection

HeLa cells were purchased from ATCC and cultured according to recommended guidelines. LCAX-1 KO HeLa cells were purchased from Creative Biogene. Cells were cultured in Dulbecco's Modified Eagle's Medium (DMEM) (Invitrogen Corporation, USA) containing 10% heat-inactivated fetal bovine serum (FBS) (Invitrogen Corporation, USA), 100 U/mL penicillin and 100 μg/mL streptomycin (Gibco), and maintained at 37°C under 5% CO_2. Cells were passaged using 0.25% Trypsin-EDTA (Gibco) and plated at 50-60% confluency for transfection.

Mammalian expression of LCAX-1 fused to EGFP was carried out as described in **Section III.B.2**. Mammalian expression of LCAX-1 exchanger-dead mutants fused to EGFP was carried out as described in **Section III.B.2**.

HeLa cells were transiently transfected with the respective plasmids using Lipofectamine 3000 (Thermo Fisher) according to manufacturer protocols. After incubation for 4 hours, the transfection medium was replaced with fresh DMEM. Imaging or electrophysiology experiments were performed on cells 48h following transfection.

V.B.3: Bioinformatics

Topology modelling: The secondary structure of LCAX-1 was determined using JPred. 2D topology schemes of LCAX-1 and VCX1 were then prepared using TOPO2 software (outside residues, membrane residues, signature regions, and special residues off). Transmembrane segments were arranged to display the internal homology of LCAX-1 and VCX1 (**Tables 5.1, 5.2**), with putative Ca^{2+}-binding domains forming the pore in the center. Residues are colored to show homology of three critical regions between LCAX1 and VCX1: Ca^{2+} binding region #1, yellow, 36.36% identity, 54.54% similarity; Ca^{2+} binding region #2, purple, 22.22% identity, 88.88% similarity; acidic helix, green, 31.8% identity, 50.0% similarity. Percentage identity and similarities were calculated using LALIGN (BLOSUM50 matrix; -12 gap open; -2 gap extend; 10.0E() threshold). Light blue indicates the EXGDK/R motifs in LCAX-1 and the GNXXE motifs in VCX1, which are involved in Ca^{2+} binding. Red indicate the lysosome-targeting YNRL motif in LCAX-1 and the vacuole-targeting YNRV motif in VCX1.

Table 5.1: Internal symmetry of LCAX-1.

Transmembrane Domains	Identity (%)	Similarity (%)
TMD1-TMD4	28.0	76.0
TMD2-TMD5	35.0	65.0
TMD3-TMD6	21.4	64.0

Table 5.2: Internal symmetry of VCX1.

Transmembrane Domains	Identity (%)	Similarity (%)
TMD1-TMD6	31.2	75.0
TMD2-TMD7	35.0	70.0
TMD3-TMD8	31.6	57.9
TMD4-TMD9	26.7	66.7

Table 5.2 (Continued)

TMD5-TMD10	38.5	84.6

Sequence alignments: Alignments of VCX1, LCAX-1, gdt1, and Y54F10AL.1 sequences were performed using Clustal Omega (output format: ClustalW with character counts; mBed-like clustering; 0 combined iterations; guide tree iterations off; HMM iterations off). Select regions were highlighted based on homology identified above and outlined in the respective colors.

Homology modelling: Homology-based modelling of LCAX-1 was performed using MODELLER using VCX1 as a unifying template; information about other templates is provided in **Table 5.3**. The script was obtained from the MODELLER online manual provided by A. Sali using the automodel class. The resulting model was uploaded into PyMol and colored according to the previous designations.

Table 5.3: Templates used for homology-based modelling of LCAX-1.

LCAX-1 Domain	Template Protein	Organism	Identity (%)	Similarity (%)
TMD-Reg	C-C chemokine receptor type 9	Homo sapiens	71.40	78.60
TMD1	VCX1 M2b	Saccharomyces cerivisiae	36.36	54.54
TMD2	Monovalent cation-H^+ antiporter	Pyrococcus furiosus	85.70	85.70
TMD3	Two-pore calcium channel protein 2	Homo sapiens	50.00	70.00
TMD4	Calcium permeable stress-gated cation channel 1	Arabidopsis thaliana	61.50	76.90
TMD5	Calcium homeostasis modulator protein 2	Homo sapiens	44.40	55.60
TMD6	Neimann-Pick C1 protein	Homo sapiens	63.20	78.90

V.B.4: Survival assay in yeast

The yeast strain K665 (*pmc::TRP1 vcxΔ*) was a kind gift from K. Hirschi (Baylor College of Medicine). The yeast integrating plasmid YIplac128 was a kind gift from B. Glick (University of Chicago). Cloning of LCAX-1 into YIplac128 was done using Gibson assembly techniques, as described above. The K665 strain was transformed with either the YIplac128 empty vector (EV) or YIplac128

containing LCAX-1 using Frozen-EZ Yeast Transformation II Kit (Zymo Research) according to manufacturer protocols and transformed colonies were selected following growth on Synthetic Dropout Leucine (SD-Leu) agar plates overnight at 30°C. Colonies were then grown in SD-Leu liquid media while shaking at 30°C until cultures had an OD of ~0.6. For the survival assay, a series of 10-fold dilutions of each culture was prepared and dropped onto SD-Leu agar plates with the indicated amounts of added $CaCl_2$. After 48h of growth, plates were removed and visualized for growth.

V.B.5: RT-PCR in yeast

To confirm expression of LCAX-1 in the *S. cerevisiae* strain K665, RNA levels were probed using RT-PCR. gDNA was isolated using Monarch Genomic DNA Purification Kit (NEB) according to manufacturer protocols. Briefly, transformants were grown overnight in liquid SD-Leu media and cells were harvested by centrifugation for 1 minute at 12,000 x g. Cells were resuspended in lysis buffer with 10 µL zymolyase and 3 µL RNase A and incubated for 30 minutes at 37°C. Then, 10 µL Proteinase K and 100 µL Tissue Lysis Buffer were added and the mixture was vortexed thoroughly before incubating for 30 minutes at 56°C with shaking. Then, 400 µL of gDNA Binding Buffer was added, and the mixture was vortexed before transferring to a purification column in a collection tube. The column was centrifuged for 3 minutes at 1,000 x g and then 1 minute at 12,000 x g. Then, the column was washed twice with 500 µL of gDNA Wash Buffer before adding 50 µL pre-heated gDNA elution buffer. The column was incubated for 1 minute and centrifuged into a microforge tube for 1 minute at 12,000 x g. The purity and amount of DNA was determined using a NanoDrop, and 20ng of DNA was used to run a PCR using gene-specific primers for TMEM165 (same primers as above) and ACT1 (F: GAAATGCAAACCGCTGCTCA, R: GAGCCAAAGCGGTGATTTCC, 289 bp). PCR products were separated on a 0.8% agarose-Tris base, acetic acid, and EDTA (TAE) gel.

V.B.6: Localization in yeast

Cloning of LCAX-1-DsRed into YIplac128 was done using Gibson assembly techniques, as described above. The K665 strain was transformed with either the YIplac128 empty vector (EV) or YIplac128-LCAX-1-DsRed as described above, and transformed colonies were selected following growth

on SD-Leu agar plates overnight at 30°C. Colonies were then grown in SD-Leu liquid media while shaking at 30°C until cultures had an OD of ~0.6. Vacuoles were then labeled with the dye FM4-64, according to manufacturer protocols. Briefly, yeast cultures were harvested by spinning down for 1 minute at 5,000 x g for 5 minutes. The supernatant was discarded and the cell pellet was resuspended in 50 µL Yeast Extract-Peptone-Dextrose (YPD) media and 1 µL of 1.6 µM FM4-64. This mixture was incubated for 20 minutes in a 30°C water bath. Then, 1 mL YPD media was added and the mixture was centrifuged for 5 minutes at 5,000 x g. The supernatant was discarded and the cells were resuspended in 5 mL YPD media. This mixture was incubated in a shaker for 90 minutes at 30°C. The cells were centrifuged for 5 minutes at 5,000 x g before removing the supernatant and resuspending cells in 1 mL sterile water. Cells were then spun down again for 5 minutes at 5,000 x g before resuspending in 25 µL YPD media. On a coated glass slide, 7 µL of the sample was spotted and covered with a coverslip. Cells were then imaged on a widefield microscope (see image acquisition details below).

V.B.7: *C. elegans* strains

Standard methods were used to maintain *C. elegans* (*50*). The wild-type strain was the *C. elegans* isolate from Bristol, strain N2. The strain with a heterozygous knockout of *lcax-1* was generated and provided by D. Moerman (University of British Columbia) using CRISPR/Cas9 technology and verified by sequencing (*51*). Heterozygous *lcax-1*$^{+/-}$ worms are marked by pharyngeal GFP, homozygous *lcax-1*$^{+/+}$ progeny are functionally wild-type but lack GFP, and homozygous *lcax-1*$^{-/-}$ progeny are embryonic lethal. The genotype of this worm is *Y54F10AL.1(gk5484[loxP + Pmyo-2::GFP::unc-54 3' UTR + Prps-27::neoR::unc-54 3' UTR + loxP])/+ III*. Transgenic strains expressing human LCAX-1 exchanger0dead variants were generated by microinjecting of plasmid DNA into *lcax-1*$^{+/-}$ gonads to produce extrachromosomal arrays. The injected plasmid contained an LCAX-1 variant with the promoter region of *lcax-1* and the 3’ UTR of *unc-54*. Pharyngeal mCherry was used as an injection marker. The plasmid construction, worm injection, and verification by sequencing was performed by SunyBiotech (Fujian, China) using established protocols.

V.B.8: Survival assay in worms

The survival assay in worms was performed as previously described in **Section III.B.4**, but with worms expressing exchanger-dead LCAX-1 mutants.

V.B.9: Lysosome size assay in worms

The lysosome size assay in worms was performed as previously described in **Section III.B.5**, but with worms expressing exchanger-dead LCAX-1 mutants.

V.B.10: Lysosomal Ca^{2+} imaging in worms

Lysosomal Ca^{2+} imaging in worms was performed as previously described in **Section III.B.9**, but with worms expressing exchanger-dead LCAX-1 mutants.

V.B.11: Cytosolic Ca^{2+} dynamics

Cytosolic Ca^{2+} dynamics were evaluated as previously described in **Section III.B.11**, but with cells expressing E248A LCAX-1.

V.B.12: Whole-cell electrophysiology

Whole-cell electrophysiology was carried out as previously described in **Section III.B.12**, but with cells expressing E248A LCAX-1.

V.B.13: Image acquisition

Widefield microscopy was carried out on an IX83 inverted microscope (Olympus Corporation of the Americas, Center Valley, PA, USA) using a 60X, 1.4 numerical aperture (NA), differential interference contract (DIC) oil immersion objective (PLAPON) and Evolve Delta 512 EMCCD camera (Photometrics, USA), and controlled using MetaMorph Premier Ver 7.8.12.0 (Molecular Devices, LLC, USA).

For *CalipHluor2.0* imaging in worms, images were acquired as described in **Section III.B.13**. For cytosolic Ca^{2+} recording cells, Fura Red was recorded as described in **Section III.B.13**. To check expression of LCAX-1 in the relevant experiments, EGFP images were acquired as described in **Section III.B.13**. For yeast vacuole imaging, DsRed images were acquired using a 545/25 band-pass excitation filter, 595/50 band-pass emission filter, and an 89016 dichroic; FM4-64 images were acquired using a 545/25 band-pass excitation filter, 632/60 band-pass emission filter, and an 89016 dichroic.

Confocal images were captured with a Leica TCS SP5 II STED laser confocal microscope (Leica Microsystems, Buffalo Grove, IL, USA) equipped with a 63X, 1.4 NA, oil immersion objective.Alexa647 was excited using an He-Ne laser with wavelength of 633nm. All emissions were filtered using an acousto-optical beam splitter (AOBS) with settings suitable for each fluorophore and recorded using hybrid detector.

V.B.14: Image analysis

Images were analyzed using Fiji (NIH, USA). For lysosomal pH and Ca^{2+} measurements with *CalipHluor 2.0* and cytosolic Ca^{2+} measurements with Fura Red, images were analyzed as described in **Section III.B.14.**

V.B.15: Statistics

For statistical analysis between two samples, a two-sample two-tailed test assuming unequal variance was conducted. For comparison of multiple samples, one-way ANOVA with a post hoc Tukey test was conducted. All statistical analysis was performed in Origin.

V.C: Results and Discussion

V.C.1: Homology-based modelling of LCAX-1

As discussed in **Section V.A.2**, LCAX-1 lacks homology with CAX families or other CaCA transporters. However, it phenocopies the well-known *S. cerevisiae* CAX gene, VCX1, which restores homeostasis by extracting excess cytosolic Ca^{2+} and accumulating it in the vacuole in exchange for vacuolar H^+ (*46*, *52*). Despite a lack of global homology, we explored the key structural and topological features shared between LCAX-1 and VCX1. We generated a 3D model of LCAX-1 based off of VCX1 and other proteins homologous to segments of LCAX-1 (**Table 5.3**). LCAX-1 is much smaller than VCX1, with only 7 transmembrane segments (instead of 11), the first of which (MR) having regulatory role (**Fig. 5.4A,B**). The rest of the transmembrane helices show two-fold antiparallel symmetry, with the two halves of the protein (M1-M3 and M4-M6) highly homologous to each other (**Tables 5.1**). The two EΦGD(KR)(ST) motifs in LCAX-1 occur in the central part of transmembrane segments M1 and M4, and are located in close proximity along the central core of the protein (**Fig. 5.4A,C cyan**). This is reminiscent

of the two GNXXE motifs in VCX1 in the central part of transmembrane segments M2 and M7, which are spatially proximal and meet at a kink in the central hourglass pore (**Fig. 5.4B,D cyan)**. Interestingly, the 3D structure of the motifs in LCAX-1 looks more like the core is kinked outward, rather than inward. This will be discussed more in the concluding chapter, but is similar to the structure of CAX from *A. fulgidus* or could be another indication of dimerization. We also found that the 10-15 residues downstream of each EΦGD(KR)(ST) motif in LCAX-1 are highly conserved and have high homology to the residues downstream of the GNXXE motifs in VCX1 (**Fig. 5.4A-D yellow and purple**). This indicates that, in addition to the signature EΦGD(KR)(ST) motifs being potentially involved in Ca^{2+} binding, the surrounding region may be relevant for Ca^{2+}/H^{+} exchange activity.

LCAX-1 has a large cytosolic loop connecting the two symmetrical halves of the protein (between M3 and M4), similar to the cytosolic loop in VCX1 (which connects M5 and M6). The cytosolic loop of LCAX-1 contains a high density of acidic residues, especially in a portion that is highly conserved and homologous to the analogous region of VCX1 (**Fig. 5.4A-D, green**). Importantly, the cytosolic loop also forms an α-helix parallel to the membrane directly under the putative Ca^{2+} binding sites. Thus, this region may mop up Ca^{2+} in the cytosol, especially after cytosolic Ca^{2+} elevation, to bring it in close proximity to the central core. Finally, the putative lysosome-targeting motif of LCAX-1 appears in the same spatial localization as the analogous vacuole-targeting motif in VCX1 (**Fig. 5.4A-D, red**). Both appear on a small cytosolic loop, and as such are available for binding by relevant adaptor and transport proteins. Thus, LCAX-1 contains many of the same key transport and structural elements as VCX1, and exhibits them in a very similar 3D orientation. As such, we wondered whether mutating some of the key residues in these regions may reduce or eliminate LCAX-1 exchange activity.

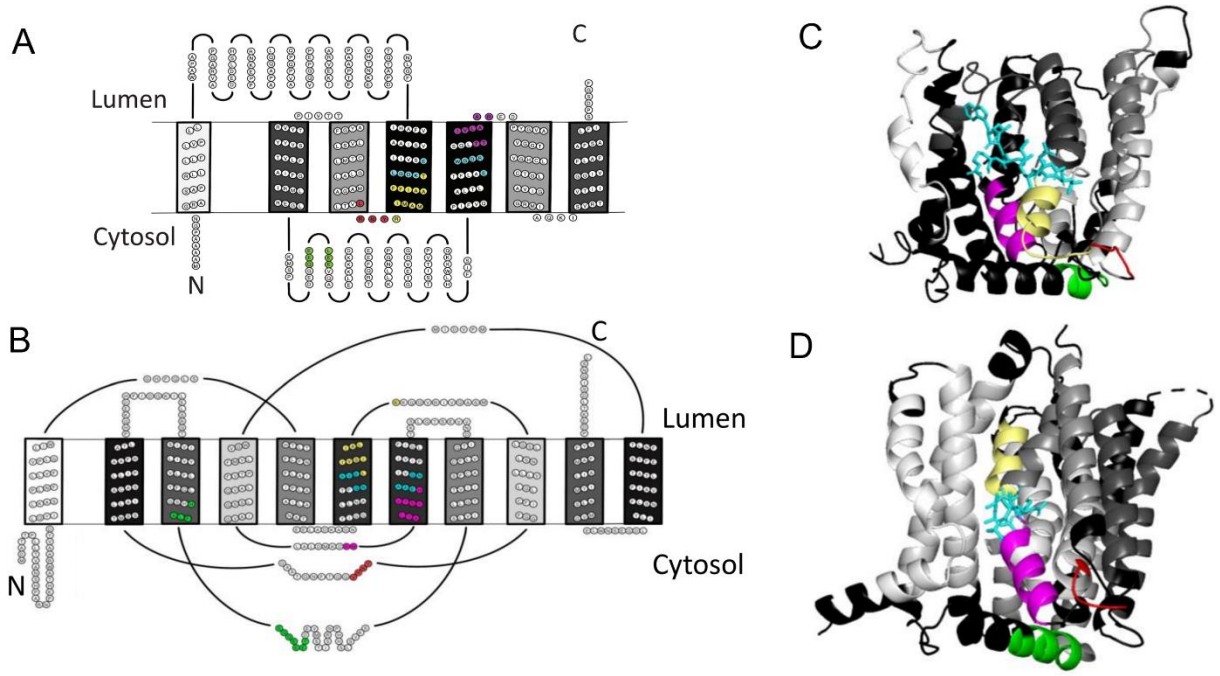

Figure 5.4: Topological and structural similarities between LCAX-1 and VCX1. (A,B) Topology of LCAX-1 (a) and VCX1 (b) created using TOPO2. Grayscale shows internal symmetry of transmembrane segments. Ca^{2+} binding regions (light blue), homologous regions adjoining the Ca^{2+} binding regions (yellow and purple), acidic helices (green), and lysosome/vacuole-targeting motifs (red) are highlighted. (C,D) Homology-based model of LCAX-1 (c) based on VCX1 (d).

V.C.2: Identification of exchanger-dead mutants

From these bioinformatic analyses, we identified three key glutamates that may be involved in Ca^{2+} binding. The first one is E108, which is the key glutamate in the highly conserved ELGDKT motif on M1 of LCAX-1 (**Fig. 5.5A-B, dark blue)**. The second one is E188, which is one of the conserved glutamates on the acidic cytosolic loop of LCAX-1 (**Fig. 5.5A-B, green)**. The third one is E248, which is the key glutamate in the highly conserved EWGDRS motif on M4 of LCAX-1 (**Fig. 5.5A-B, magenta)**. We hypothesize that single mutations of these glutamate residues to alanine will reduce the ability of LCAX-1 to bind Ca^{2+} and act as a Ca^{2+}/H^{+} exchanger. It is important to note here that these residues have already been speculated to be involved in cation recognition, and that a homozygous missense E108G

mutation in humans leads to CDG Type II (*53–55*). But our previous bioinformatic analyses strengthen these speculations on the basis of homology and spatial proximity.

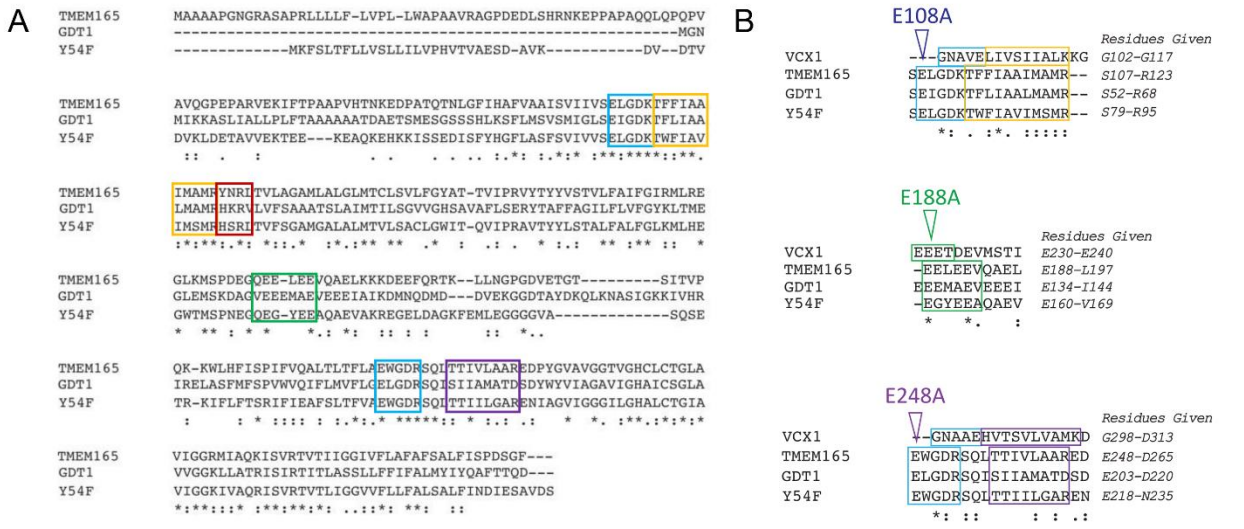

Figure 5.5: Key regions of LCAX-1 sequence. (A) Full sequence alignment of three proteins in the UPF0016 family: TMEM165/LCAX-1 (*H. sapiens*), *Y54F10AL.1*/*lcax-1* (*C. elegans*), and GDT1 (*S. cerevisiae*) using Clustal Omega. Calcium binding regions, homologous regions to VCX1, acidic helices, and lysosome/vacuole-targeting motifs are highlighted according to colors indicated in Figure 5.4. (B) Alignment of the Ca^{2+} binding sites (top and bottom) and acidic helix (middle) of VCX1 (*S. cerevisiae*), TMEM165/LCAX-1 (*H. sapiens*), *Y54F10AL.1*/*lcax-1* (*C. elegans*), and GDT1 (*S. cerevisiae*) using Clustal Omega. Asterisks, colons and periods indicate full, strong and weak conservation, respectively.

Before testing whether these mutants alter LCAX-1 transport activity, we wanted to see whether they affect expression levels and subcellular localization of LCAX-1. Indeed, overexpression of all mutants (E108A, E188A, and E248A) of LCAX-1 fused to EGFP in HeLa cells led to the same whole-cell EGFP intensity, indicating that these mutants do not affect the expression levels of LCAX-1 (**Fig. 5.6A,B**). In addition, the fractions of LCAX-1 localizing to lysosomes and Golgi are not significantly altered by these mutations (**Fig. 5.6A,C-E**). We see a slight change with E248A LCAX-1, which seems to slightly favor lysosomal localization over Golgi localization. However, we are not concerned about this observation for two reasons: (i) the detected change is likely not physiologically significant; and (ii) the increase in lysosome localization is functionally opposing the expected decrease in LCAX-1 activity. Thus, any detected changes in LCAX-1 activity are not due to changes in expression level or subcellular localization.

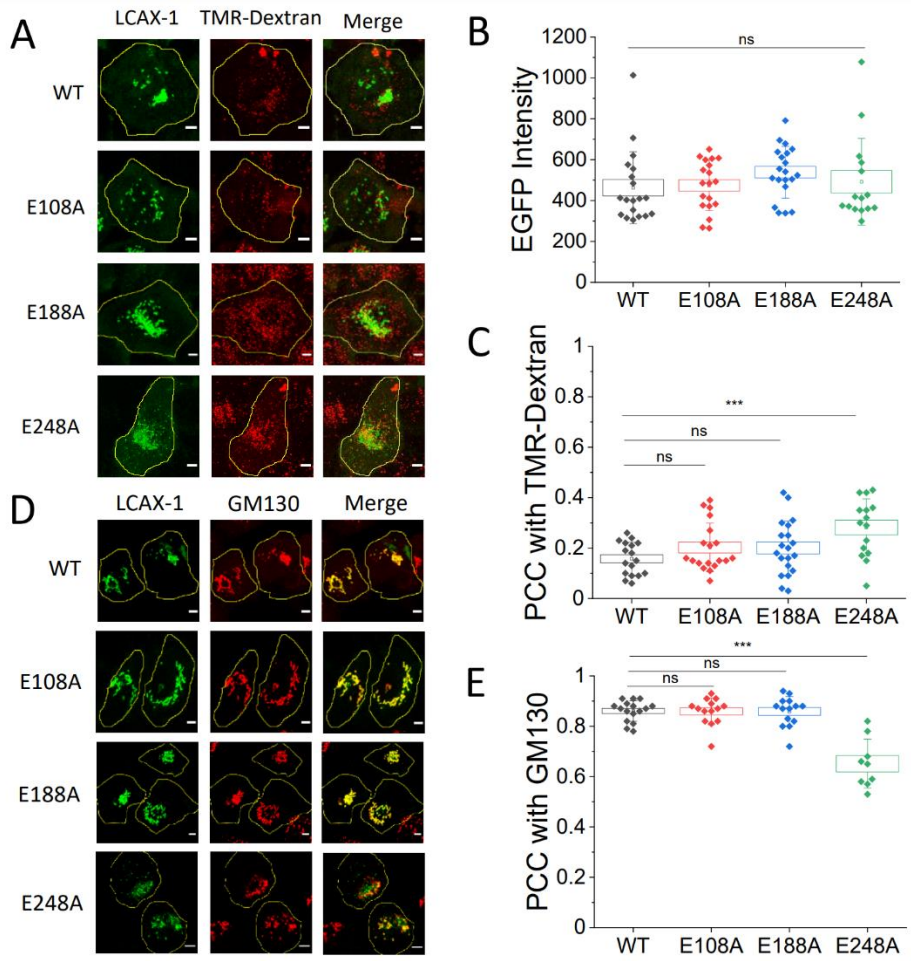

Figure 5.6. Expression and localization of LCAX-1 mutants. (A) Representative fluorescence images of HeLa cells transfected with the indicated LCAX-1-EGFP mutant (green) and labeled with 5 mg/mL TMR-dextran (red). (B) Whole-cell fluorescence intensity of LCAX-1-EGFP in cells transfected with the indicated mutant. (C) Pearson correlation coefficient (PCC) of LCAX-1-EGFP with TMR-dextran in cells transfected with the indicated mutant. (D) Representative immunofluorescence images of HeLa cells transfected with the indicated LCAX-1-EGFP mutant (green) and stained with an antibody to GM-130 (red). (E) PCC of LCAX-1-EGFP with GM130 in cells transfected with the indicated mutant. Scale bar 5µm. Boxes and bars represent s.e.m. and standard deviation, respectively. ns, not significant ($p>0.05$); *$p<0.05$; **$p<0.01$; ***$p<0.001$ (one-way ANOVA with Tukey post hoc test).

V.C.3: Worm phenotype assays with exchanger-dead mutants

Based on the observations and hypothesis discussed above, we proceeded to test whether LCAX-1 activity is affected by E108A, E188A, and E248A mutations. We first assayed the phenotypes of *lcax-1*$^{+/-}$ expressing extrachromosomal arrays of these human LCAX-1 mutants. As in previous chapters, we looked at overall worm survival, coelomocyte lysosome size, and lysosomal Ca^{2+} concentrations (**Fig. 5.7A**). Extrachromosomal expression of E108A or E248A variants, harboring mutations in the putative Ca^{2+}-binding sites on M1 and M4 of LCAX-1, failed to rescue the low survival of *lcax-1*$^{+/-}$ worms (**Fig. 5.7B**). This indicates that these glutamates are key for LCAX-1 activity, perhaps through Ca^{2+} binding. Furthermore, expression of these mutations also failed to rescue the large lysosome size of *lcax-1*$^{+/-}$

worms, confirming that the effect of these mutations occurs directly on lysosomes (**Fig. 5.7C**). A mutation in the acidic loop, E188A, led to only partial LCAX-1 activity in these assays (**Fig. 5.7B,C**). Thus, the acidic loop may be involved in augmenting Ca^{2+} current by LCAX-1, but not absolutely crucial for ion conductance.

Interestingly, expression of all mutants partially rescued lysosomal Ca^{2+} levels, measured with *CalipHluor 2.0* (**Fig. 5.7D**). However, these Ca^{2+} measurements were complicated by several factors. First, we again see varying percentages of lysosomes whose Ca^{2+} levels are below the quantifiable range of *CalipHluor 2.0*, making it difficult to precisely compare the average Ca^{2+} levels between the mutants (**Fig. 5.7E**). Second, the heterozygous knockout background of *lcax-1*$^{+/-}$ and the possible dimerization of LCAX-1 may permit heterodimers of WT and mutant LCAX-1 to form functional transporters on lysosomes. Thus, the Ca^{2+} measurement data here are difficult to interpret. One trend that does emerge from all plots of lysosomal Ca^{2+} here is that the E108A and E248A mutants behave very similarly to each other, and very differently from the E188A mutation. This makes sense given the hypothesized roles of these individual glutamates. However, better conclusions can be made from homozygous knockout systems, done in the next sections.

V.C.4: Yeast survival assay with exchanger-dead mutants

Next, we sought to test whether human LCAX-1 and putative exchanger-dead mutant versions of LCAX-1 affect Ca^{2+}-dependent survival of *S. cerevisiae*. In the strain K665, which lacks both its vacuolar Ca^{2+} importers (PMC1 and VCX1), high extracellular Ca^{2+} is toxic (**Fig. 5.8A**) (*56*). Exogenous expression of the CAX genes from *A. thaliana* reverses this phenotype. Indeed, we see that exogenous expression of WT human LCAX-1 in K665 reverse its Ca^{2+} sensitivity (**Fig. 5.8B**). We confirmed expression and vacuolar localization of overexpressed human LCAX-1 using RT-PCR and fluorescence imaging, respectively (**Fig. 5.8C,D**). Interestingly, we see that K665 colonies transformed with WT LCAX-1 exhibit a red pigmentation, while K665 colonies do not (**Fig. 5.8E**). This red pigmentation is lost when yeast is grown in high Ca^{2+} media. Strains of *S. cereivisiae* that have mutations in certain steps of the adenine biosynthetic pathway (such as the ade2-1 mutation in K665) (*57*) accumulate an adenine-

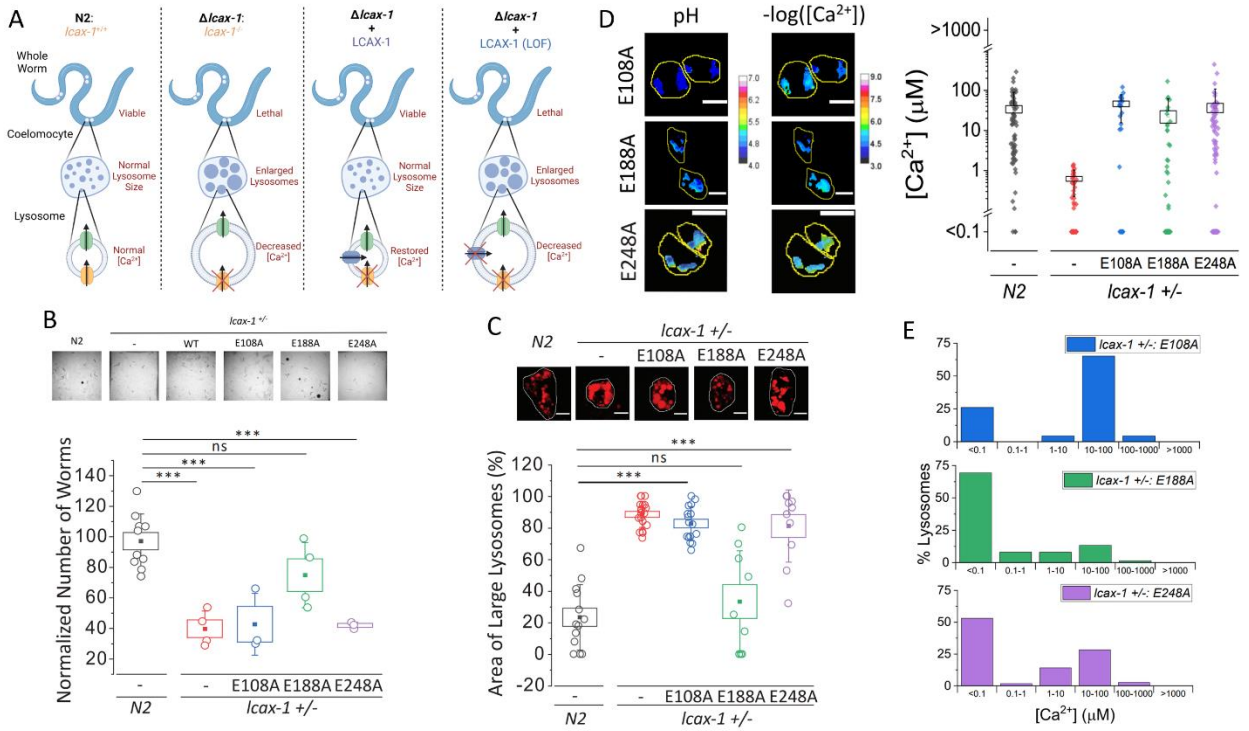

Figure 5.7: Worm phenotypes of LCAX-1 exchanger-dead mutants. (A) Principle underlying determination of mutant LCAX-1 function by rescue of *lcax-1*$^{+/-}$ worm phenotypes. (B) Top, representative images showing the number of progeny of N2 worms or *lcax-1*$^{+/-}$ worms with extrachromosomal expression of the indicated mutant of human LCAX-1. Bottom, number of progeny of of *lcax-1*$^{+/-}$ worms extrachromosomally expressing the indicated human LCAX-1 variant (n=3 replicates). (C) Top, representative fluorescence images of lysosomes in coelomocytes in worms of the indicated genetic background. Lysosomes are labelled with Alexa647 duplex DNA. Bottom, percentage of area occupied by enlarged lysosomes in the indicated genetic background. N>5 cells, >50 lysosomes. (D) Left, representative pH and –log([Ca^{2+}]) maps in *CalipHluor2.0*-labeled lysosomes in coelomocytes of *lcax-1*$^{+/-}$ worms extrachromosomally expressing the indicated human LCAX-1 variant. Right, distribution of lysosomal Ca^{2+} in the indicated genetic backgrounds. Lysosomes with Ca^{2+} levels below O/R_{min} or above O/R_{max} of *CalipHluor2.0* are plotted as <0.1μM and >1000μM, respectively. (E) Distribution of lysosomes with the indicated Ca^{2+} concentration measured using *CalipHluor2.0* in the indicated genetic backgrounds. Scale bar 5 μm. Boxes and bars represent the s.e.m. and standard deviation, respectively. ns, not significant (p>0.05); ***p<0.001 (one-way ANOVA with Tukey post hoc test).

intermediate-derived red pigment inside vacuoles (*58*). The intermediate phosphoribosylaminoimidazole (AIR) is transported glutathione-dependently into vacuoles where it is polymerized and modified to form the characteristic red pigment. The structure of this pigment has yet to be fully established. Importantly, development of red pigmentation in ade2 mutants requires normal vacuolar function (*59*). This concept has even been used to screen for chemicals that disrupt vacuolar function by loss of red pigmentation (*60*). Thus, human LCAX-1 rescues vacuolar dysfunction in K665 under normal osmotic conditions, but high Ca^{2+} causes vacuolar dysfunction even as LCAX-1 rescues lethality. While we cannot rule out the

effect of LCAX-1 on other aspects of the adenine-derived pigment biosynthetic pathway, its lysosomal roles in humans and nematodes established elsewhere in this manuscript support the hypothesis that the red pigment implies rescuing of vacuolar dysfunction. Combined, this indicates that human LCAX-1 can facilitate Ca^{2+} transport from the cytosol into the vacuole, phenocopying VCX1. On the other hand, E248A LCAX-1 failed to fully reverse this phenotype (**Fig. 5.8B**). Thus, E248 seems to be key for LCAX-1 to transport Ca^{2+} into the vacuole.

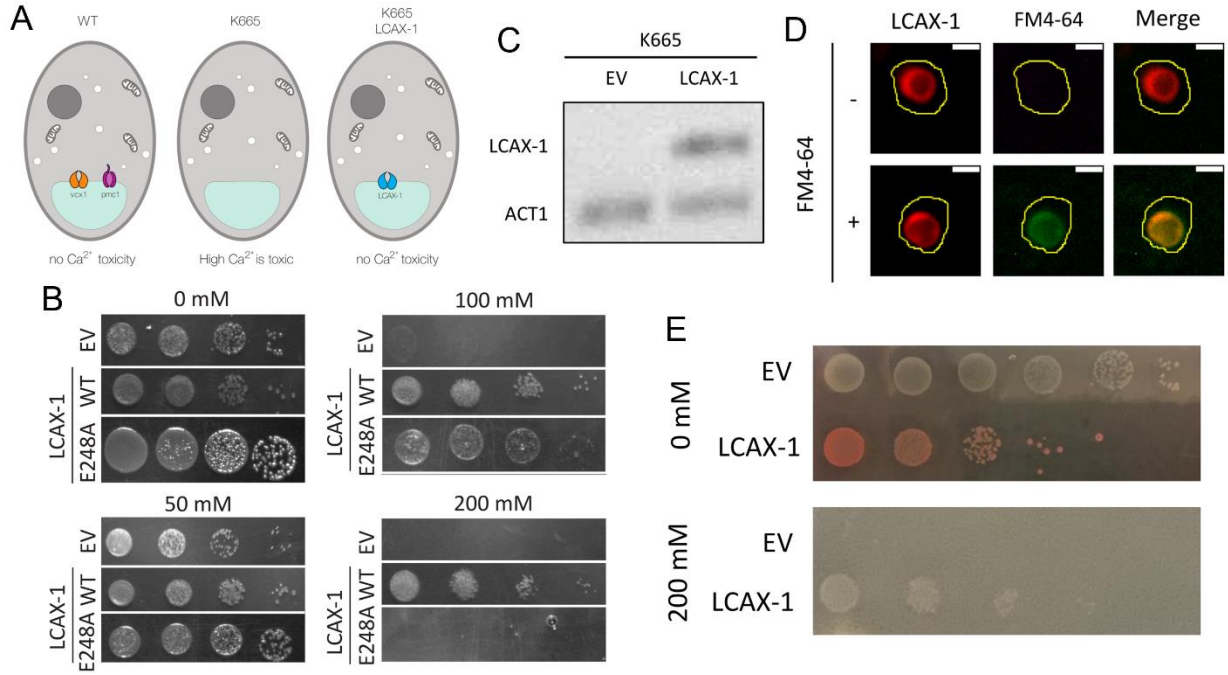

Figure 5.8: Yeast phenotypes of LCAX-1 WT and E248A mutant. (A) Rescue assay in *S. cerevisiae* strain K665, where the loss of VCX1 and PMC1 cause lethality in environmental Ca^{2+}. Expression of a vacuolar Ca^{2+} importer would rescue this lethality at high Ca^{2+} by restoring vacuolar function. (B) Growth of K665 transformants integrating either an empty vector (EV) or the indicated variant of human LCAX-1, after 2 days at 30°C on YPD plates supplemented with the indicated concentration of $CaCl_2$. Columns indicate 10-fold dilutions from left-to-right. (C) RT-PCR of LCAX-1 (*H. sapiens*) and ACT1 (*S. cerevisiae*) in the K665 strain transformed with empty vector (EV) or LCAX-1. (D) Representative fluorescence images of K665 transformed with LCAX-1-DsRed (red) and labelled with the vacuolar membrane marker FM4-64 (green), where indicated. (E) Color of K665 transformed to integrate an empty vector (EV) or human LCAX-1, after 2 days at 30°C on YPD plates supplemented with the indicated concentration of $CaCl_2$. Columns indicated 10-fold dilutions from left-to-right. Scale bar 2µm.

V.C.5: Ca^{2+} transport by exchanger-dead mutants

Finally, we tested whether the E248A mutation affects the ability of LCAX-1 to transport Ca^{2+} in mammalian cells. Indeed, expressing E248A LCAX-1 in LCAX-1 KO cells failed to restore low cytosolic

Ca^{2+} after a cytosolic spike (**Fig. 5.9A-C**). In addition, E248A LCAX-1 conducts far less pH-driven Ca^{2+} current than WT LCAX-1 (**Fig. 5.9D-E**). Combined, these results indicate that E248 is key for LCAX-1 to transport Ca^{2+} from the cytosol to lysosomes in mammalian cells. It further supports the conclusion that WT LCAX-1 directly conducts Ca^{2+}/H^{+} exchange, and is not merely an accessory unit or otherwise indirect facilitator of exchange.

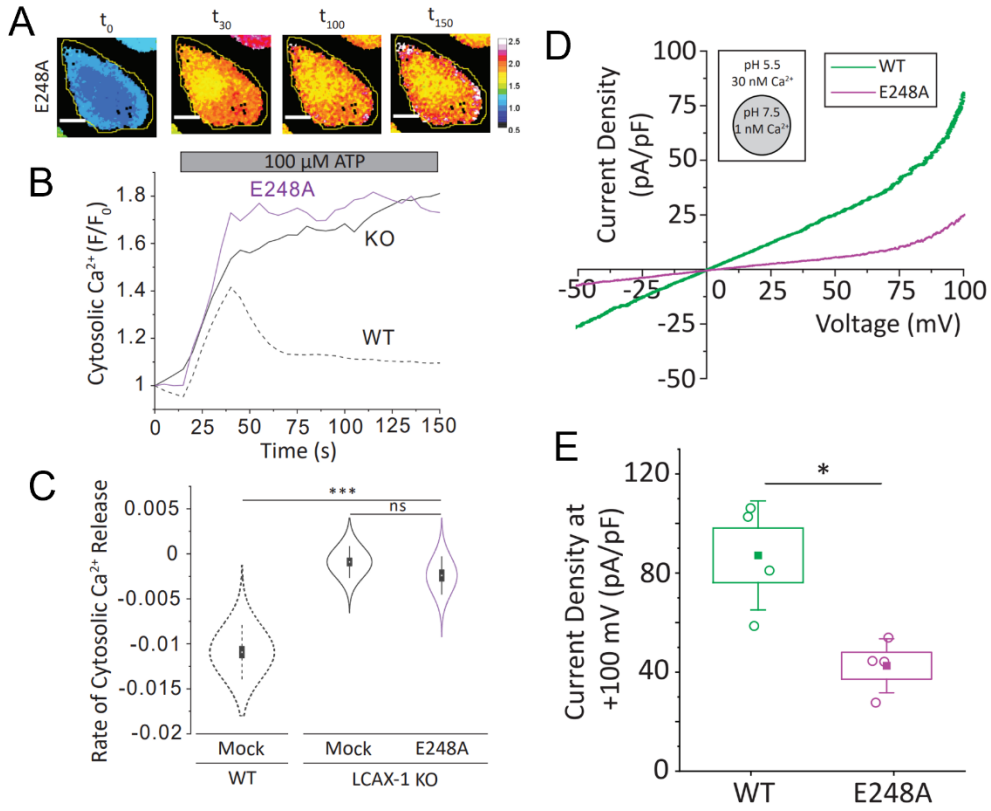

Figure 5.9: Ca^{2+} transport by E248A LCAX-1 in mammalian cells. (A) Representative 440/488 maps of Fura Red in LCAX-1 KO HeLa cells treated with 100 µM ATP after transfection with E248A LCAX-1-EGFP. Maps shown are at t=0s (prior to ATP treatment), t=30s, t=100s, and t=150s. (B) Representative cytosolic Ca^{2+} traces given by the 440/488 ratio of Fura Red in (b). Curves are normalized to the value at t=0. (C) Slope of the linear fit of the cytosolic Ca^{2+} decrease following maximum 440/488 of Fura Red. (D) Representative current density curves of HeLa cells expressing WT (green) or E248A (magenta) LCAX-1-EGFP, with experimental conditions indicated in the inset. (E) Current density at +100 mV across the plasma membrane of the indicated cell types from (d). Violin plots show normal distributions with the box showing standard error of the mean. Boxes and bars represent the s.e.m. and standard deviation, respectively. ns, not significant ($p>0.05$); *$p<0.05$; ***$p<0.001$ (one-way ANOVA with Tukey post hoc test).

V.D: Conclusion

Through bioinformatic analyses of LCAX-1 sequence and structure, we identified key residues in putative Ca^{2+} binding sites. Two of these (E108 and E248) were located in highly conserved

EΦGD(KR)(ST) motifs and came in close proximity to each other in the central core of the protein. The third (E188) was located on the large cytosolic loop that lays parallel to the membrane and confers Ca^{2+} specificity to the exchanger. The regions of LCAX-1 surrounding these residues are highly similar to the analogous regions of VCX1, implying they may also have a role in Ca^{2+}/H^{+} exchange. Interestingly, we see that E108A and E248A mutations render LCAX-1 non-functional, such that its expression does not rescue lysosomal/vacuolar Ca^{2+} dysregulation in worms, yeast, or mammalian cell models. On the other hand, the E188A mutation does not seem to have such a severe effect on ion exchange by LCAX-1. Thus, it seems like the acidic loop may not be absolutely critical for ion conductance, but that it augments currents, especially following a cytosolic Ca^{2+} spike. These results strengthen our conclusion that LCAX-1 directly transports Ca^{2+}, and is not just an accessory subunit or indirect facilitator of ion import. They also offer further insight into how this novel family of ion exchangers may function similar to CAX proteins but with a distinct structure. In addition, they prove that the physiological relevance of LCAX-1 in previous assays lies in its ability to transport Ca^{2+}. Finally, they further lead us to hypothesize that LCAX-1 acts as a dimer (or other multimer), as will be discussed in the concluding chapter.

V.E: References

1. R. Dutzler, E. B. Campbell, M. Cadene, B. T. Chait, R. MacKinnon, X-ray structure of a ClC chloride channel at 3.0 A reveals the molecular basis of anion selectivity. *Nature*. **415**, 287–294 (2002).

2. R. Dutzler, E. B. Campbell, R. MacKinnon, Gating the selectivity filter in ClC chloride channels. *Science*. **300**, 108–112 (2003).

3. A. Accardi, C. Miller, Secondary active transport mediated by a prokaryotic homologue of ClC Cl- channels. *Nature*. **427**, 803–807 (2004).

4. L. Leisle, Y. Xu, E. Fortea, S. Lee, J. D. Galpin, M. Vien, C. A. Ahern, A. Accardi, S. Bernèche, Divergent Cl- and H+ pathways underlie transport coupling and gating in CLC exchangers and channels. *eLife*. **9** (2020), doi:10.7554/eLife.51224.

5. K. Wang, S. S. Preisler, L. Zhang, Y. Cui, J. W. Missel, C. Grønberg, K. Gotfryd, E. Lindahl, M. Andersson, K. Calloe, P. F. Egea, D. A. Klaerke, M. Pusch, P. A. Pedersen, Z. H. Zhou, P. Gourdon, Structure of the human ClC-1 chloride channel. *PLoS Biol.* **17**, e3000218 (2019).

6. E. Park, R. MacKinnon, Structure of the CLC-1 chloride channel from Homo sapiens. *eLife*. **7** (2018), doi:10.7554/eLife.36629.

7. E. Park, E. B. Campbell, R. MacKinnon, Structure of a CLC chloride ion channel by cryo-electron microscopy. *Nature*. **541**, 500–505 (2017).

8. S. Weinert, N. Gimber, D. Deuschel, T. Stuhlmann, D. Puchkov, Z. Farsi, C. F. Ludwig, G. Novarino, K. I. López-Cayuqueo, R. Planells-Cases, T. J. Jentsch, Uncoupling endosomal CLC chloride/proton exchange causes severe neurodegeneration. *EMBO J.* **39**, e103358 (2020).

9. G. Novarino, S. Weinert, G. Rickheit, T. J. Jentsch, Endosomal chloride-proton exchange rather than chloride conductance is crucial for renal endocytosis. *Science*. **328**, 1398–1401 (2010).

10. S. Weinert, S. Jabs, C. Supanchart, M. Schweizer, N. Gimber, M. Richter, J. Rademann, T. Stauber, U. Kornak, T. J. Jentsch, Lysosomal pathology and osteopetrosis upon loss of H+-driven lysosomal Cl- accumulation. *Science*. **328**, 1401–1403 (2010).

11. T. Sekine, F. Komoda, K. Miura, J. Takita, M. Shimadzu, T. Matsuyama, A. Ashida, T. Igarashi, Japanese Dent disease has a wider clinical spectrum than Dent disease in Europe/USA: genetic and clinical studies of 86 unrelated patients with low-molecular-weight proteinuria. *Nephrol. Dial. Transplant.* **29**, 376–384 (2014).

12. Y. Bignon, A. Alekov, N. Frachon, O. Lahuna, C. Jean-Baptiste Doh-Egueli, G. Deschênes, R. Vargas-Poussou, S. Lourdel, A novel CLCN5 pathogenic mutation supports Dent disease with normal endosomal acidification. *Hum. Mutat.* **39**, 1139–1149 (2018).

13. P. M. Kekenes-Huskey, V. T. Metzger, B. J. Grant, J. Andrew McCammon, Calcium binding and allosteric signaling mechanisms for the sarcoplasmic reticulum Ca^2+ ATPase. *Protein Sci.* **21**, 1429–1443 (2012).

14. A. P. Einholm, B. Vilsen, J. P. Andersen, Importance of transmembrane segment M1 of the sarcoplasmic reticulum Ca2+-ATPase in Ca2+ occlusion and phosphoenzyme processing. *J. Biol. Chem.* **279**, 15888–15896 (2004).

15. G. Inesi, D. Lewis, C. Toyoshima, A. Hirata, L. de Meis, Conformational fluctuations of the Ca2+-ATPase in the native membrane environment. Effects of pH, temperature, catalytic substrates, and thapsigargin. *J. Biol. Chem.* **283**, 1189–1196 (2008).

16. Z. Zhang, D. Lewis, C. Sumbilla, G. Inesi, C. Toyoshima, The role of the M6-M7 loop (L67) in stabilization of the phosphorylation and Ca(2+) binding domains of the sarcoplasmic reticulum Ca(2+)-ATPase (SERCA). *J. Biol. Chem.* **276**, 15232–15239 (2001).

17. P. T. Ellinor, J. Yang, W. A. Sather, J. F. Zhang, R. W. Tsien, Ca2+ channel selectivity at a single locus for high-affinity Ca2+ interactions. *Neuron*. **15**, 1121–1132 (1995).

18. P. Hess, R. W. Tsien, Mechanism of ion permeation through calcium channels. *Nature*. **309**, 453–456 (1984).

19. J. Yang, P. T. Ellinor, W. A. Sather, J. F. Zhang, R. W. Tsien, Molecular determinants of Ca2+ selectivity and ion permeation in L-type Ca2+ channels. *Nature*. **366**, 158–161 (1993).

20. J. Wu, Z. Yan, Z. Li, X. Qian, S. Lu, M. Dong, Q. Zhou, N. Yan, Structure of the voltage-gated calcium channel Ca(v)1.1 at 3.6 Å resolution. *Nature*. **537**, 191–196 (2016).

21. J. O. Meyer, S. Dahimene, K. M. Page, L. Ferron, I. Kadurin, J. I. J. Ellaway, P. Zhao, T. Patel, S. W. Rothwell, P. Lin, W. S. Pratt, A. C. Dolphin, Disruption of the Key Ca2+ Binding Site in the Selectivity Filter of Neuronal Voltage-Gated Calcium Channels Inhibits Channel Trafficking. *Cell Rep.* **29**, 22-33.e5 (2019).

22. J. Liao, F. Marinelli, C. Lee, Y. Huang, J. D. Faraldo-Gómez, Y. Jiang, Mechanism of extracellular ion exchange and binding-site occlusion in a sodium/calcium exchanger. *Nat. Struct. Mol. Biol.* **23**, 590–599 (2016).

23. C. Cang, K. Aranda, Y. Seo, B. Gasnier, D. Ren, TMEM175 is an organelle K(+) channel regulating lysosomal function. *Cell*. **162**, 1101–1112 (2015).

24. X. Tao, R. K. Hite, R. MacKinnon, Cryo-EM structure of the open high-conductance Ca2+-activated K+ channel. *Nature*. **541**, 46–51 (2017).

25. D. A. Doyle, J. Morais Cabral, R. A. Pfuetzner, A. Kuo, J. M. Gulbis, S. L. Cohen, B. T. Chait, R. MacKinnon, The structure of the potassium channel: molecular basis of K^+ conduction and selectivity. *Science*. **280**, 69–77 (1998).

26. J. D. Brunner, R. P. Jakob, T. Schulze, Y. Neldner, A. Moroni, G. Thiel, T. Maier, S. Schenck, Structural basis for ion selectivity in TMEM175 K+ channels. *eLife*. **9** (2020), doi:10.7554/eLife.53683.

27. S. Oh, N. Paknejad, R. K. Hite, Gating and selectivity mechanisms for the lysosomal K+ channel TMEM175. *eLife*. **9** (2020), doi:10.7554/eLife.53430.

28. W. Wang, X. Zhang, Q. Gao, M. Lawas, L. Yu, X. Cheng, M. Gu, N. Sahoo, X. Li, P. Li, S. Ireland, A. Meredith, H. Xu, A voltage-dependent K+ channel in the lysosome is required for refilling lysosomal Ca2+ stores. *J. Cell Biol.* **216**, 1715–1730 (2017).

29. L. Bao, C. Kaldany, E. C. Holmstrand, D. H. Cox, Mapping the BKCa channel's "Ca2+ bowl": side-chains essential for Ca2+ sensing. *J. Gen. Physiol.* **123**, 475–489 (2004).

30. J. Wie, Z. Liu, H. Song, T. F. Tropea, L. Yang, H. Wang, Y. Liang, C. Cang, K. Aranda, J. Lohmann, J. Yang, B. Lu, A. S. Chen-Plotkin, K. C. Luk, D. Ren, A growth-factor-activated lysosomal K+ channel regulates Parkinson's pathology. *Nature*. **591**, 431–437 (2021).

31. S. Jinn, C. Blauwendraat, D. Toolan, C. A. Gretzula, R. E. Drolet, S. Smith, M. A. Nalls, J. Marcus, A. B. Singleton, D. J. Stone, Functionalization of the TMEM175 p.M393T variant as a risk factor for Parkinson disease. *Hum. Mol. Genet.* **28**, 3244–3254 (2019).

32. D. Demaegd, A.-S. Colinet, A. Deschamps, P. Morsomme, Molecular evolution of a novel family of putative calcium transporters. *PLoS ONE*. **9**, e100851 (2014).

33. J. S. Lolkema, A. Dobrowolski, D.-J. Slotboom, Evolution of antiparallel two-domain membrane proteins: tracing multiple gene duplication events in the DUF606 family. *J. Mol. Biol.* **378**, 596–606 (2008).

34. K. Murata, K. Mitsuoka, T. Hirai, T. Walz, P. Agre, J. B. Heymann, A. Engel, Y. Fujiyoshi, Structural determinants of water permeation through aquaporin-1. *Nature*. **407**, 599–605 (2000).

35. A. Yamashita, S. K. Singh, T. Kawate, Y. Jin, E. Gouaux, Crystal structure of a bacterial homologue of Na+/Cl--dependent neurotransmitter transporters. *Nature*. **437**, 215–223 (2005).

36. C. Hunte, E. Screpanti, M. Venturi, A. Rimon, E. Padan, H. Michel, Structure of a Na+/H+ antiporter and insights into mechanism of action and regulation by pH. *Nature*. **435**, 1197–1202 (2005).

37. Y.-J. Chen, O. Pornillos, S. Lieu, C. Ma, A. P. Chen, G. Chang, X-ray structure of EmrE supports dual topology model. *Proc Natl Acad Sci USA*. **104**, 18999–19004 (2007).

38. M. Rapp, E. Granseth, S. Seppälä, G. von Heijne, Identification and evolution of dual-topology membrane proteins. *Nat. Struct. Mol. Biol.* **13**, 112–116 (2006).

39. J. Liao, H. Li, W. Zeng, D. B. Sauer, R. Belmares, Y. Jiang, Structural insight into the ion-exchange mechanism of the sodium/calcium exchanger. *Science*. **335**, 686–690 (2012).

40. T. Iwamoto, T. Y. Nakamura, Y. Pan, A. Uehara, I. Imanaga, M. Shigekawa, Unique topology of the internal repeats in the cardiac Na+/Ca2+ exchanger. *FEBS Lett.* **446**, 264–268 (1999).

41. E. M. Schwarz, S. Benzer, Calx, a Na-Ca exchanger gene of Drosophila melanogaster. *Proc Natl Acad Sci USA*. **94**, 10249–10254 (1997).

42. X. Cai, J. Lytton, The cation/Ca(2+) exchanger superfamily: phylogenetic analysis and structural implications. *Mol. Biol. Evol.* **21**, 1692–1703 (2004).

43. T. Kamiya, M. Maeshima, Residues in internal repeats of the rice cation/H+ exchanger are involved in the transport and selection of cations. *J. Biol. Chem.* **279**, 812–819 (2004).

44. K.-J. Kang, T. G. Kinjo, R. T. Szerencsei, P. P. M. Schnetkamp, Residues contributing to the Ca2+ and K+ binding pocket of the NCKX2 Na+/Ca2+-K+ exchanger. *J. Biol. Chem.* **280**, 6823–6833 (2005).

45. R. J. Winkfein, R. T. Szerencsei, T. G. Kinjo, K. Kang, M. Perizzolo, L. Eisner, P. P. M. Schnetkamp, Scanning mutagenesis of the alpha repeats and of the transmembrane acidic residues of the human retinal cone Na/Ca-K exchanger. *Biochemistry*. **42**, 543–552 (2003).

46. A. B. Waight, B. P. Pedersen, A. Schlessinger, M. Bonomi, B. H. Chau, Z. Roe-Zurz, A. J. Risenmay, A. Sali, R. M. Stroud, Structural basis for alternating access of a eukaryotic calcium/proton exchanger. *Nature*. **499**, 107–110 (2013).

47. M. Wu, S. Tong, S. Waltersperger, K. Diederichs, M. Wang, L. Zheng, Crystal structure of Ca2+/H+ antiporter protein YfkE reveals the mechanisms of Ca2+ efflux and its pH regulation. *Proc Natl Acad Sci USA*. **110**, 11367–11372 (2013).

48. T. Nishizawa, S. Kita, A. D. Maturana, N. Furuya, K. Hirata, G. Kasuya, S. Ogasawara, N. Dohmae, T. Iwamoto, R. Ishitani, O. Nureki, Structural basis for the counter-transport mechanism of a H+/Ca2+ exchanger. *Science*. **341**, 168–172 (2013).

49. B. Suresh, A. Saminathan, K. Chakraborty, C. Cui, L. Becker, Y. Krishnan, Tubular lysosomes harbor active ion gradients and poise macrophages for phagocytosis. *BioRxiv* (2020), doi:10.1101/2020.12.05.413229.

50. S. Brenner, The genetics of Caenorhabditis elegans. *Genetics*. **77**, 71–94 (1974).

51. V. Au, E. Li-Leger, G. Raymant, S. Flibotte, G. Chen, K. Martin, L. Fernando, C. Doell, F. I. Rosell, S. Wang, M. L. Edgley, A. E. Rougvie, H. Hutter, D. G. Moerman, CRISPR/Cas9 Methodology for the Generation of Knockout Deletions in Caenorhabditis elegans. *G3 (Bethesda)*. **9**, 135–144 (2019).

52. A. Miseta, R. Kellermayer, D. P. Aiello, L. Fu, D. M. Bedwell, The vacuolar Ca^{2+} /H^{+} exchanger Vcx1p/Hum1p tightly controls cytosolic Ca^{2+} levels in *S. cerevisiae*. *FEBS Lett.* **451**, 132–136 (1999).

53. C. Rosnoblet, D. Legrand, D. Demaegd, H. Hacine-Gherbi, G. de Bettignies, R. Bammens, C. Borrego, S. Duvet, P. Morsomme, G. Matthijs, F. Foulquier, Impact of disease-causing mutations on TMEM165 subcellular localization, a recently identified protein involved in CDG-II. *Hum. Mol. Genet.* **22**, 2914–2928 (2013).

54. J. Stribny, L. Thines, A. Deschamps, P. Goffin, P. Morsomme, The human Golgi protein TMEM165 transports calcium and manganese in yeast and bacterial cells. *J. Biol. Chem.* **295**, 3865–3874 (2020).

55. S. Schulte Althoff, M. Grüneberg, J. Reunert, J. H. Park, S. Rust, C. Mühlhausen, Y. Wada, R. Santer, T. Marquardt, TMEM165 deficiency: postnatal changes in glycosylation. *JIMD Rep.* **26**, 21–29 (2016).

56. K. D. Hirschi, R. G. Zhen, K. W. Cunningham, P. A. Rea, G. R. Fink, CAX1, an H+/Ca2+ antiporter from Arabidopsis. *Proc Natl Acad Sci USA*. **93**, 8782–8786 (1996).

57. K. W. Cunningham, G. R. Fink, Calcineurin-dependent growth control in Saccharomyces cerevisiae mutants lacking PMC1, a homolog of plasma membrane Ca2+ ATPases. *J. Cell Biol.* **124**, 351–363 (1994).

58. K. G. Sharma, R. Kaur, A. K. Bachhawat, The glutathione-mediated detoxification pathway in yeast: an analysis using the red pigment that accumulates in certain adenine biosynthetic mutants of yeasts reveals the involvement of novel genes. *Arch. Microbiol.* **180**, 108–117 (2003).

59. T. R. Amen, E. V. Mikhailova, V. V. Alenin, A. V. Artyomov, P. A. Dementyev, M. A. Khodorkovskii, T. O. Artamonova, I. M. Kuznetsova, T. R. Soidla, O. V. Nevzglyadova, Structural and functional characteristics of various forms of red pigment of yeast Saccharomyces cerevisiae and its synthetic analog. *Cell and tissue biol.* **7**, 86–94 (2013).

60. H. Tournu, J. Carroll, B. Latimer, A.-M. Dragoi, S. Dykes, J. Cardelli, T. L. Peters, K. E. Eberle, G. E. Palmer, Identification of small molecules that disrupt vacuolar function in the pathogen Candida albicans. *PLoS ONE*. **12**, e0171145 (2017).

VI. Conclusion and Outlook

VI.A: Structure of LCAX-1

One of the more curious aspects of LCAX-1 (and other members of the UPF0016 family) is its structure. It has no notable overall homology to the CaCA superfamily of Ca^{2+}/cation exchangers, despite exhibiting similar functions (*1*). Because of this, the UPF0016 family may represent a distinct family of ancient and conserved Ca^{2+}/cation exchangers. As discussed in previous chapters, the UPF0016 family members have similar overall topologies and key elements as the CAX family of Ca^{2+}/H^{+} exchangers. Thus, the UPF0016 family seems to be evolutionarily related to the CAX family in some way, both in terms of function and sequence. However, this connection remains to be determined fully. Future work with LCAX-1 should look at determining its structure and transport cycle mechanism. This would provide the best insight into the similarities and differences between LCAX-1 and CAX proteins, in terms of transport dynamics and overall structure.

Structure determination of LCAX-1 will also help answer a key question that remains about LCAX-1 from this work. Several experiments discussed in previous chapters have indicated that LCAX-1 may act as a dimer. In these experiments, we used a heterozygous knockout worm, which we referred to as *lcax-1*$^{+/-}$. Coelomocyte lysosomes in this worm have significantly lower Ca^{2+} levels than coelomocyte lysosomes in N2 worms. Surprisingly, upon extrachromosomal expression of human LCAX-1 mutants that either localize exclusively to the Golgi (G304R) or are unable to transport Ca^{2+} (E248A), we see partial rescue of lysosomal Ca^{2+} (**Fig. 3.9D and 5.7D**). However, in other assays in worms or mammalian cells, these mutants completely failed to recover lysosomal Ca^{2+}/H^{+} exchange activity by LCAX-1. This leads us to suspect that LCAX-1 functions as a dimer, where a mutant monomer (from extrachromosomal expression) and WT monomer (from the remaining *lcax-1* copy in the heterozygous knockout background) can combine to form a partially functional LCAX-1 dimer. This WT-mutant heterodimer seems to have enough functionality to restore lysosomal Ca^{2+} levels partially, but not enough to rescue defects in lysosome size or worm survival (**Fig. 6.1A**).

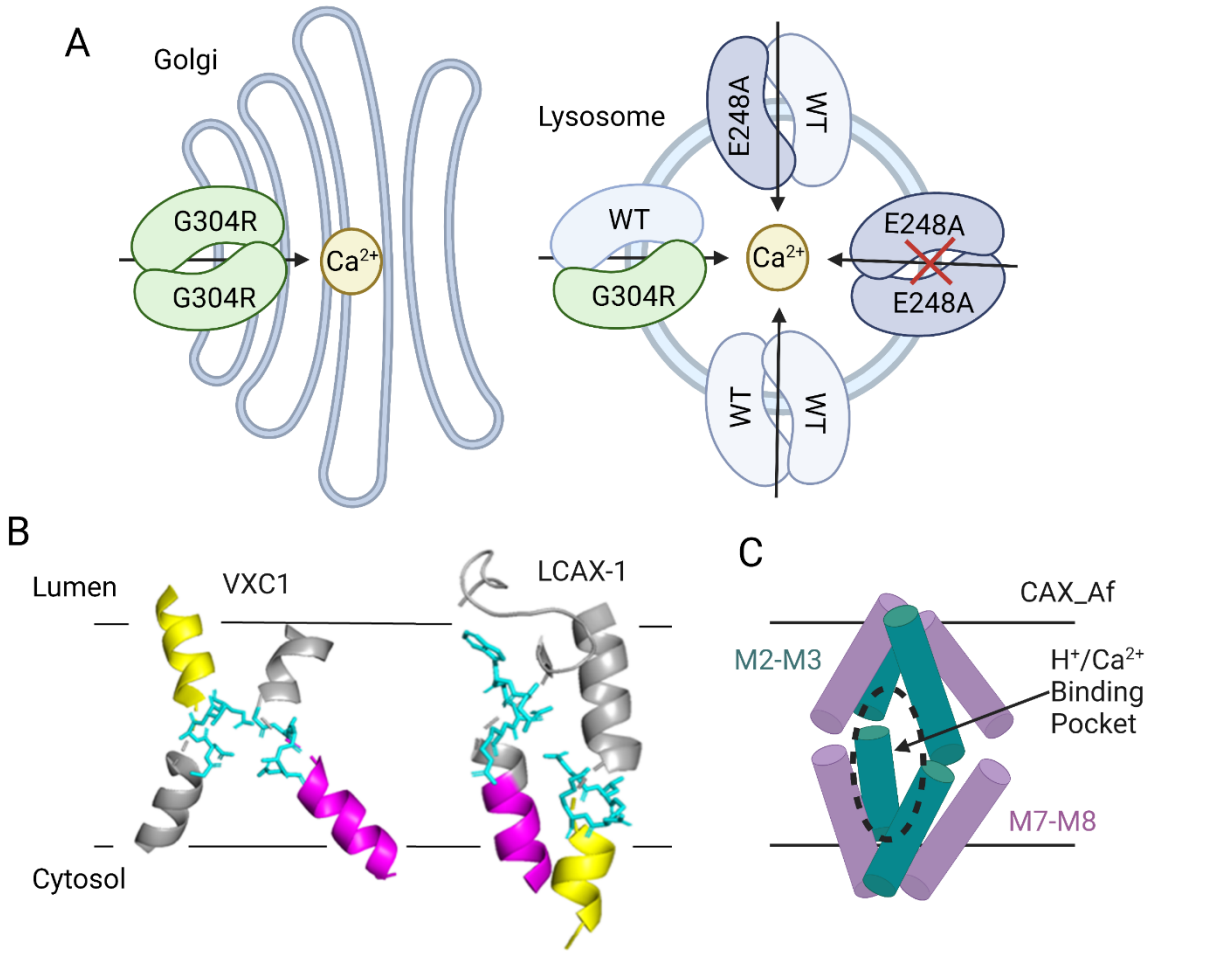

Figure 6.1: Dimerization of LCAX-1. (A) LCAX-1 dimerization hypothesis: Mutant-WT heterodimers may still import Ca^{2+} into lysosomes, while mutant-mutant homodimers do not. (B) Different kinking of core helices in VCX1 and LCAX-1. (C) Core helices of CAX from *A. fulgidus*, where M2, M3, M7, and M8 all kink outward to form a cation binding pocket.

Our hypothesis that LCAX-1 acts as a dimer is also based on several other observations of LCAX-1 and Ca^{2+}/H^{+} exchangers in general. First, LCAX-1 is smaller than almost all known cation exchangers and transporters. It has only 7 transmembrane domains and a mass of about 35 kDa. On the other hand, VCX1 and other CAX family proteins have 11 transmembrane domains and a mass of about 45 kDa (*2*). Most other cation exchangers are also much larger than LCAX-1. Whether the additional transmembrane domains are critical for LCAX-1 function is unknown. If so, it is likely that LCAX-1 dimerization provides the additional size and transmembrane segments for functionality. Interestingly, a pH-regulated lysosomal Ca^{2+} channel was recently identified that has 7 transmembrane segments and a mass of about 35 kDa. This channel is called "responsive to centrifugal force and shear stress 1" (RECS1)

or “transmembrane BAX inhibitor motif containing 1” (TMBIM1), and seems to be a facilitator of apoptosis triggered by lysosomal stress (*3*). TMBIM family members form functional dimers and higher-order multimers, although the monomers seem to be functional (*4*). Thus, it seems reasonable to suppose that LCAX-1 can form functional multimers to make up for its small size. Second, LCAX-1 is an example of a two-domain fusion protein, which contains two homologous domains with antiparallel membrane orientation (*1*). These types of proteins evolved from an ancestral gene encoding a dual-topology protein (*1*). This ancestral protein could then associate into an antiparallel homodimer. This type of evolution has been characterized for several other transmembrane proteins (*5*, *6*). The idea that a single LCAX-1 monomer may have evolved from a duplication event of its homologous halves makes it reasonable to suppose that the monomers could also associate. Indeed, the two homologous halves of LCAX-1 must have “dimerized” to form what is now a single LCAX-1 monomer. The exact same interactions would occur to form an association between LCAX-1 monomers into dimers. Third, many Ca^{2+}/cation exchangers in the CaCA family form functional multimers. The crystal structure of the Ca^{2+}/H^{+} exchanger YfkE showed that it exists as a trimer (*7*). Mammalian NCXs and NCKXs are predicted to form homodimers (*8, 9*). In these exchangers, multimerization seems to support Ca^{2+} transport by stabilizing the protein in cell membranes during large conformational changes. Other Ca^{2+} and cation channels also form functional dimers (*10–12*). Fourth, an interesting difference between LCAX-1 and VCX1 structure emerged from our homology-based modelling experiments. In VCX1, the central two transmembrane segments are kinked inward, where the Ca^{2+}-binding motifs on each segment come together, forming an hourglass-shaped core (**Fig. 6.1B**) (*2*). In LCAX-1, the two central transmembrane segments are kinked outward, separating the Ca^{2+}-binding motifs that occur at the kinks. This structure is interesting in that implies that a single monomer does not have a Ca^{2+}-binding pocket. But a dimer of two such outward kinks could assemble to generate a Ca^{2+}-binding pocket. Indeed, this is how CAX from *A. fulgidus* transports Ca^{2+}, although the association between two outwardly-kinked cores occurs within a single monomer (**Fig. 6.1C**) (*13*). Thus, it makes sense given the structure of the ion-binding core of LCAX-1 for it to require dimerization to function. Finally, LCAX-1 exists in numerous splice-transcript isoforms

that are shorter than the WT protein. Compared to the WT protein of 324 amino acids, short-form and long-form transcripts exist that lead to proteins of 129 and 259 amino acids (*14*). These proteins have different effects on protein glycosylation than the WT protein (*14*). Interestingly, the short-form LCAX-1 could form homodimers and id expressed at low levels across diverse human cells (*14*).

Because of all of these literature, bioinformatic, and experimental suggestions, we hypothesize that LCAX-1 functions as a dimer or higher-order multimer. Future directions for LCAX-1 should explore this via structural studies. Identifying key residues involved in the dimerization interface would enable further mutational studies to explore the relevance of LCAX-1 oligomerization to lysosomal Ca^{2+} dysregulation phenotypes.

VI.B: Stoichiometry of Exchange

Another outstanding question with regards to LCAX-1 functionality is whether its activity is capable of generating and maintain the observed 5000-fold gradient of Ca^{2+} across the lysosome membrane. Theoretical calculations of lumenal Ca^{2+} filling by a Ca^{2+}/H^+ exchanger can predict this based on three factors: membrane potential, pH gradient, and stoichiometry of ion exchange. Electroneutral transport (1 Ca^{2+}:2 H^+) would be unaffected by the membrane potential, and a lysosomal pH of 5.0 could theoretically generate a 25,000-fold Ca^{2+} gradient (*15*). But the same pH gradient and 1 Ca^{2+}:1 H^+ stoichiometry would only generate a 50-fold Ca^{2+} gradient, assuming a lumen-positive 30 mV membrane potential (*15*). Thus, endolysosome Ca^{2+}/H^+ exchange by LCAX-1 would require an exchange stoichiometry of at least 2-3 H^+ per Ca^{2+}, based on thermodynamic grounds alone.

We did not quantify the stoichiometry of ion exchange in the experiments in this thesis, but our electrophysiology data implies several aspects of the stoichiometry of LCAX-1. First, we see that LCAX-1 current is dependent on membrane potential, such that exchange cannot be electroneutral (1 Ca^{2+}:2 H^+) (**Fig. 3.13C**). Second, LCAX-1 currents on the plasma membrane with no pH gradient or membrane potential are outwardly rectifying (**Fig. 4.7B, black trace at 0mV**). In these experiments, the only ion gradient is an inward Ca^{2+} gradient. As such, Ca^{2+} must be moving inward in these conditions and >2H^+ ions must be moving outward to explain the net outward current. Once a steep pH gradient is applied, the

direction of exchange reverses to be inwardly rectifying (**Fig. 4.7B, green trace at 0mV**). Under these conditions, >2H^+ ions are moved inward down the pH gradient, per Ca^{2+} ion moved outward up its gradient. At resting lysosomal membrane potentials (highly lumen-positive) and resting lysosomal pH, we see highly inwardly rectifying current (positive current moving into the cytosol) (**Fig. 4.7B, green trace at -30mV**). This makes sense, as we would expect to see 1 Ca^{2+} imported from the cytosol for every >2 H^+ exported into the cytosol, to give net inwardly rectifying current. As discussed above, this stoichiometry of exchange by LCAX-1 would be enough to sustain the high lysosomal Ca^{2+} gradient.

Such stoichiometry of exchange (2-4 ions per Ca^{2+} ion) is common for other Ca^{2+}/cation exchangers, such as the ones in the CaCA superfamily. The human Na^+/Ca^{2+} exchanger NCX1 facilitates Ca^{2+} efflux from the cell in a 3-4 Na^+:1 Ca^{2+} ratio (*16–20*). An archaeal NCX homolog, NCX_Mj, also displays this ion-exchange stoichiometry (*21*, *22*). The human K^+-dependent Na^+/Ca^{2+} exchangers NCKX1 and NCKX2 facilitate Ca^{2+} efflux from certain cells in a 4 Na^+:1 Ca^{2+}, 1 K^+ ratio (*17*, *23–25*). The yeast Ca^{2+}/H^+ exchanger VCX1 loads vacuolar Ca^{2+} in a 2 H^+:1 Ca^{2+} ratio (*17*, *26*, *27*). The Arabidopsis Ca^{2+}/H^+ exchanger CAX1 loads vacuolar Ca^{2+} in a 3 H^+:1 Ca^{2+} ratio (*17*, *28*, *29*).

Thus, based on thermodynamic grounds, experimental suggestions, and CaCA stoichiometries, we hypothesize that LCAX-1 uses >2H^+ ions per Ca^{2+} ion imported into the lysosome. Future work on LCAX-1 should quantify this ratio with more certainty. This can be done using electrophysiological experiments to explore the effect of different ion gradients on the reversal potential (*30–33*). Using thermodynamic equations, the ratio of ion exchange can be calculated from this relationship.

VI.C: Relevance to Other Import Mechanisms

Another outstanding question concerning LCAX-1 activity is how its H^+-driven Ca^{2+} import fits in with other models of lysosomal Ca^{2+} import. As discussed in Chapter 1, there has been substantial evidence of pH gradient-dependent lysosomal Ca^{2+} import mechanisms. However, some experiments in certain cell types have indicated that the endoplasmic reticulum drives lysosomal Ca^{2+} refilling, not the pH gradient (*34*). Exactly how our model of LCAX-1 function fits in with these findings should be an aspect of future explorations.

One possible way to reconcile our findings with previous is to explore cell-to-cell differences in LCAX-1 expression and function. We already know from data presented in this thesis that cells from different tissue have different expression levels of LCAX-1. Specifically, COS7 cells express LCAX-1 at low levels, such that we see very little mopping up of cytosolic Ca^{2+} following a spike. On the other hand, HeLa cells express LCAX-1 at sufficient levels to mop up spiked Ca^{2+} from the cytosol. SK-BR-3 cells express LCAX-1 at an even higher level, potentially to handle large Ca^{2+} transport needed in breast tissue. Beyond expression levels, there may be cell-to-cell heterogeneity in terms of LCAX-1 subcellular localization. Our data seem to indicate that higher expression levels correlate with more significant lysosome populations. However, it could be that different cell types display distinct transport machinery that leads LCAX-1 to have slightly different intracellular distributions. The studies showing a lack of pH gradient-dependent Ca^{2+} lysosomal import used HEK cells (*34*). How HEK cells compare to HeLa and SK-BR-3 cells in terms of LCAX-1 expression and localization and unknown. Thus, it would be interesting to explore whether cells from different tissue have completely distinct lysosomal Ca^{2+} uptake mechanisms.

Another way to reconcile our results with previous seemingly contradictory findings is to explore the differences in triggers and probes used to visualize lysosomal Ca^{2+} import. In our experiments, we primarily used ATP to trigger a cytosolic Ca^{2+} spike, and then we follow the restoration of cytosolic Ca^{2+} with the small molecule Fura Red. Experiments that have shown a lack of pH gradient-dependent Ca^{2+} import used ML-SA1 to trigger a cytosolic Ca^{2+} spike, and then followed the restoration of the lysosome-releasable Ca^{2+} pool with the lysosome-targeted GECI GCaMP3-ML1 (*34*). Thus, there are key experimental differences that may explain our experimental findings. First, ATP primarily triggers Ca^{2+} release from IP3R receptors on the ER, while ML-SA1 primarily triggers Ca^{2+} release from TRPML1 channels on the lysosome. This could indicate that a pH gradient-dependent lysosomal Ca^{2+} uptake mechanism (such as LCAX-1 activity) is critical to mop up ER-derived cytosolic Ca^{2+}, but not to mop up lysosome-derived cytosolic Ca^{2+}. How molecules such as LCAX-1 could differentiate between such pools of cytosolic Ca^{2+} is difficult to explain, but could involve a complicated network of membrane contact

sites and feedback loops between ER and lysosome channels and transporters. Second, our readout for lysosomal Ca^{2+} import is the decrease in cytosolic Ca^{2+} (and we also look directly at the effect of LCAX-1 on resting lysosomal Ca^{2+} levels), while their readout for lysosomal Ca^{2+} import is the maintenance of a cytosolic Ca^{2+} spike in response to subsequent treatments with ML-SA1 (*34*). These are fundamentally different setups, which each are indirect methods of analyzing lysosomal Ca^{2+} refilling. It would be interesting to explore the effect of LCAX-1 overexpression or depletion in their experimental setup to visualize lysosomal Ca^{2+} import.

Finally, it is also possible that LCAX-1 is simultaneously the molecule responsible for ER-driven lysosomal Ca^{2+} import and pH gradient-driven lysosomal Ca^{2+} import. ER-lysosome contacts are mediated by a range of molecular tethers (*35*). For example, oxysterol binding protein (OSBP) on the lysosome anchor to the ER vesicle associated membrane protein (VAMP)-associated proteins (VAPs) (*36*). Disruption of these tethers leads to dysregulated ER-lysosome communication, especially in cholesterol transfer and subsequent activation of mTORC1. Loss of the lysosomal cholesterol transporter, Niemann-Pick C1 (NPC1), leads to OSBP-mediated cholesterol trafficking and constitutive mTORC1 activation, causing the lysosome storage disorder NPC (*36*). Interestingly, NPC1 has also been implicated in directly tethering the ER to endocytic organelles by interacting with the ER sterol transport proteins ORP5 and Gramd1b (*37*, *38*). A striking finding in our bioinformatic analyses is the high homology between the C-terminal transmembrane domain of LCAX-1 with a region of NPC1 (**Table 5.3**). This homology was so high that we used it as a template for our homology-based model of LCAX-1. Whether this region of NPC1 is critical for its interaction with ER-localized proteins is unknown. However, it is possible given this homology that LCAX-1 also directly interactions with ER proteins, such as ORP5, at membrane contact sites. Thus, LCAX-1 may mediate ER-derived lysosomal Ca^{2+} import in a manner that does not require a pH gradient (since it would be transporting Ca^{2+} down the steep ER-lysosome gradient) under certain circumstances, which is why previous experiments have not seen an effect of lysosome pH neutralization on Ca^{2+} import. Simultaneously, LCAX-1 may mediate cytosol-derived lysosomal Ca^{2+} import in a manner that requires a pH gradient to drive Ca^{2+} up the steep cytosol-lysosome gradient, under

other circumstances. A more detailed exploration of whether LCAX-1 is present at ER-lysosome membrane contact sites, and whether it affects import of Ca^{2+} from the ER, would help answer this question.

Thus, although our results seem to be at odds with some previous experiments, there are many possible ways to reconcile this difference. Further experiments should explore cell-to-cell differences in LCAX-1 function, the response of LCAX-1 to different sources of cytosolic Ca^{2+}, and the relevance of LCAX-1 to ER-lysosome contact and communication. Answering these questions would help further characterize the different ways lysosomes restore their Ca^{2+} store.

VI.D: Physiological Outlook

The final outstanding question concerning LCAX-1 that we will discuss is its role in human health and disease. As experiments in this work have shown, a complete homozygous loss of the LCAX-1 homolog is embryonic lethal to worms. On the other hand, heterozygous knockout of LCAX-1 leads to low brood size and lysosome storage phenotypes. Thus, we suspect that LCAX-1 maintaining the lysosomal Ca^{2+} store is critical for human health. The connection between LCAX-1 and human physiology and disease should be a focus of future studies on LCAX-1. We will conclude this thesis with a discussion of a few pathologies in which LCAX-1 may play a role, either as a player involved in the physiology or as a therapeutic target.

The first group of disorders where LCAX-1 function at the lysosomes may be critical is certain types of congenital disorders of glycosylation (CDG). The high abundance of LCAX-1 on the Golgi has led to exploration of its Golgi-related functionality and effects on protein glycosylation to describe the phenotypes seen in CDG (*39*). However, any potential relevance of its lysosomal function to CDG has thus far been overlooked. Interestingly, in a patient with heterozygous missense mutations (c.376C>T [p.R126C]) and (c.910G>A [p.G304R]), LCAX-1 is absent in lysosomes (*40*). Despite LCAX-1 presence on the Golgi, this patient manifested a less severe form of CDG Type II, presenting with characteristic deformities that are also observed in lysosomal storage disorders such as fucosidosis and Gaucher's disease. While LCAX-1 undoubtedly carries out important Golgi-related roles that lead to CDG

phenotypes, our data show that LCAX-1 carries out an additional function in that it regulates lysosomal Ca^{2+} import. Combined with the phenotypes of a patient lacking the lysosomal population of LCAX-1, we hypothesize that loss of its role on lysosomes contributes to the developmental defects and other phenotypes in patients with CDG.

Another interesting link to explore is between LCAX-1 and a potentially fatal congenital disorder called Hirschsprung's disease (HSCR). HSCR is defined by the absence of enteric neurons at the end of the bowel, which causes constitutive bowel constriction and functional obstruction (*41*). Children with HSCR have a range of gastrointestinal complications, as well as poor growth and developmental problems (*41*). Untreated disease is fatal because bloodstream bacterial infections occur along with bowel inflammation or bowel perforation (*41*). Many trophic factors, cell surface receptors, transcription factors, and signaling molecules are required for ENS precursor cells to colonize the fetal bowel (*41*). As such, a number of genetic risk factors have been implicated in the failure of ENS precursor colonization and the development of HSCR. A single nucleotide variant in LCAX-1 has been implicated in the pathology of HSCR (*42*). Interestingly, this leads to the mutation A261E, which is located in the region adjacent to a putative Ca^{2+} binding site in LCAX-1. This region is highly conserved in the UPF0016 family and is similar to the analogous region of LCAX-1 (**Fig. 5.5B**). Thus, we suspect that the A261E mutation may cause disruption of the stabilizing forces necessary for the Ca^{2+} binding sites to facilitate ion exchange, leading to the phenotypes of HSCR. The connection between lysosomal Ca^{2+} dysregulation and HSCR is completely unexplored, but several clues imply a role for lysosomes in the pathophysiology of HSCR. First, enteric neurons may be impaired secondarily by constitutive metabolic defects, such as lysosome storage disorders (*43*). Second, a patient with HSCR also had a rare lysosomal storage disorder called cystinosis (*44*). This association could either have been incidental or suggestive of a link between lysosome storage disorders and the development of HSCR. Future work on LCAX-1 should explore the effect of the A261E mutation on the ability of the protein to import Ca^{2+}, and should investigate the role this key residue plays in the structure and molecular dynamics of LCAX-1.

Finally, the links between LCAX-1 and lysosome storage disorders (LSDs) or neurodegenerative disorders should be explored. LSDs primarily result from deficiencies in lysosomal enzymes, but also from non-enzymatic membrane proteins, such as ion channels or small molecule transporters (*45*, *46*). Specifically, dysregulation of lysosomal Ca^{2+} is directly implicated in lysosome storage disorders (*47*). The best example is mucolipidosis IV (ML-IV), which is caused by mutations in the Ca^{2+} channel mucolipin-1 (MCOLN1 or TRPML1) (*48*). In addition, the lysosomal Ca^{2+} store is reduced in NPC, although the mechanisms and relevance are unknown (*49*, *50*). Furthermore, lysosomal Ca^{2+} dysregulation is also implicated in diverse neurological disorders. Mutations in CACNA1A, a voltage-dependent lysosomal Ca^{2+} release channel, causes spinocerebellar ataxia type 6 or episodic ataxia type 2 (*51*, *52*). Mutations in ATP13A2, a facilitator of lysosomal Ca^{2+} import, is a risk gene for a juvenile form of Parkinson's disease (*53–55*). A range of forms of neurodegeneration, such as Alzheimer's disease, amyotrophic lateral sclerosis, and Huntington's disease, have been linked to anomalies in cellular Ca^{2+} signaling (*56*). Thus, it is reasonable to assume that defects in lysosomal Ca^{2+} import by LCAX-1 could lead to lysosome storage and/or neurodegenerative phenotypes. On the other hand, LCAX-1 could be a therapeutic target to modulate lysosomal Ca^{2+} as a way to correct dysregulation. For example, inhibiting LCAX-1 could compensate for TRPML1 defects in ML-IV. Exploring these avenues could open up a wide array of physiologically relevant roles for LCAX-1 in maintaining human health.

VI.E: References

1. D. Demaegd, A.-S. Colinet, A. Deschamps, P. Morsomme, Molecular evolution of a novel family of putative calcium transporters. *PLoS ONE*. **9**, e100851 (2014).

2. A. B. Waight, B. P. Pedersen, A. Schlessinger, M. Bonomi, B. H. Chau, Z. Roe-Zurz, A. J. Risenmay, A. Sali, R. M. Stroud, Structural basis for alternating access of a eukaryotic calcium/proton exchanger. *Nature*. **499**, 107–110 (2013).

3. P. Pihán, F. Lisbona, J. Borgonovo, S. Edwards-Jorquera, P. Nunes-Hasler, K. Castillo, O. Kepp, H. Urra, S. Saarnio, H. Vihinen, A. Carreras-Sureda, S. Forveille, A. Sauvat, D. De Giorgis, A. Pupo, D. A. Rodríguez, G. Quarato, A. Sagredo, F. Lourido, A. Letai, C. Hetz, Control of lysosomal-mediated cell death by the pH-dependent calcium channel RECS1. *Sci. Adv.* **7**, eabe5469 (2021).

4. N. Saraiva, D. L. Prole, G. Carrara, C. Maluquer de Motes, B. F. Johnson, B. Byrne, C. W. Taylor, G. L. Smith, Human and viral Golgi anti-apoptotic proteins (GAAPs) oligomerize via different

mechanisms and monomeric GAAP inhibits apoptosis and modulates calcium. *J. Biol. Chem.* **288**, 13057–13067 (2013).

5. J. S. Lolkema, A. Dobrowolski, D.-J. Slotboom, Evolution of antiparallel two-domain membrane proteins: tracing multiple gene duplication events in the DUF606 family. *J. Mol. Biol.* **378**, 596–606 (2008).

6. M. Rapp, E. Granseth, S. Seppälä, G. von Heijne, Identification and evolution of dual-topology membrane proteins. *Nat. Struct. Mol. Biol.* **13**, 112–116 (2006).

7. M. Wu, S. Tong, S. Waltersperger, K. Diederichs, M. Wang, L. Zheng, Crystal structure of Ca2+/H+ antiporter protein YfkE reveals the mechanisms of Ca2+ efflux and its pH regulation. *Proc Natl Acad Sci USA.* **110**, 11367–11372 (2013).

8. A. Schwarzer, T. S. Kim, V. Hagen, R. S. Molday, P. J. Bauer, The Na/Ca-K exchanger of rod photoreceptor exists as dimer in the plasma membrane. *Biochemistry*. **36**, 13667–13676 (1997).

9. X. Ren, D. A. Nicoll, G. Galang, K. D. Philipson, Intermolecular cross-linking of Na+-Ca2+ exchanger proteins: evidence for dimer formation. *Biochemistry*. **47**, 6081–6087 (2008).

10. X. Cai, R. M. Nwokonko, N. A. Loktionova, R. Abdulqadir, J. H. Baraniak, Y. Wang, M. Trebak, Y. Zhou, D. L. Gill, Pore properties of Orai1 calcium channel dimers and their activation by the STIM1 ER calcium sensor. *J. Biol. Chem.* **293**, 12962–12974 (2018).

11. J. Clatot, M. Hoshi, X. Wan, H. Liu, A. Jain, K. Shinlapawittayatorn, C. Marionneau, E. Ficker, T. Ha, I. Deschênes, Voltage-gated sodium channels assemble and gate as dimers. *Nat. Commun.* **8**, 2077 (2017).

12. N. J. Marianayagam, M. Sunde, J. M. Matthews, The power of two: protein dimerization in biology. *Trends Biochem. Sci.* **29**, 618–625 (2004).

13. T. Nishizawa, S. Kita, A. D. Maturana, N. Furuya, K. Hirata, G. Kasuya, S. Ogasawara, N. Dohmae, T. Iwamoto, R. Ishitani, O. Nureki, Structural basis for the counter-transport mechanism of a H+/Ca2+ exchanger. *Science*. **341**, 168–172 (2013).

14. M.-A. Krzewinski-Recchi, S. Potelle, A.-M. Mir, D. Vicogne, E. Dulary, S. Duvet, W. Morelle, G. de Bettignies, F. Foulquier, Evidence for splice transcript variants of TMEM165, a gene involved in CDG. *Biochim. Biophys. Acta Gen. Subj.* **1861**, 737–748 (2017).

15. A. J. Morgan, F. M. Platt, E. Lloyd-Evans, A. Galione, Molecular mechanisms of endolysosomal Ca2+ signalling in health and disease. *Biochem. J.* **439**, 349–374 (2011).

16. M. P. Blaustein, W. J. Lederer, Sodium/calcium exchange: its physiological implications. *Physiol. Rev.* **79**, 763–854 (1999).

17. L. Emery, S. Whelan, K. D. Hirschi, J. K. Pittman, Protein Phylogenetic Analysis of Ca(2+)/cation Antiporters and Insights into their Evolution in Plants. *Front. Plant Sci.* **3**, 1 (2012).

18. D. M. Bers, K. S. Ginsburg, Na:Ca stoichiometry and cytosolic Ca-dependent activation of NCX in intact cardiomyocytes. *Ann. N. Y. Acad. Sci.* **1099**, 326–338 (2007).

19. H. Dong, J. Dunn, J. Lytton, Stoichiometry of the Cardiac Na+/Ca2+ exchanger NCX1.1 measured in transfected HEK cells. *Biophys. J.* **82**, 1943–1952 (2002).

20. Y. Fujioka, M. Komeda, S. Matsuoka, Stoichiometry of Na+-Ca2+ exchange in inside-out patches excised from guinea-pig ventricular myocytes. *J Physiol (Lond)*. **523 Pt 2**, 339–351 (2000).

21. I. Shlosman, F. Marinelli, J. D. Faraldo-Gómez, J. A. Mindell, The prokaryotic Na+/Ca2+ exchanger NCX_Mj transports Na+ and Ca2+ in a 3:1 stoichiometry. *J. Gen. Physiol.* **150**, 51–65 (2018).

22. F. Marinelli, L. Almagor, R. Hiller, M. Giladi, D. Khananshvili, J. D. Faraldo-Gómez, Sodium recognition by the Na+/Ca2+ exchanger in the outward-facing conformation. *Proc Natl Acad Sci USA*. **111**, E5354-62 (2014).

23. P. P. Schnetkamp, Calcium homeostasis in vertebrate retinal rod outer segments. *Cell Calcium*. **18**, 322–330 (1995).

24. H. Reiländer, A. Achilles, U. Friedel, G. Maul, F. Lottspeich, N. J. Cook, Primary structure and functional expression of the Na/Ca,K-exchanger from bovine rod photoreceptors. *EMBO J.* **11**, 1689–1695 (1992).

25. H. Dong, P. E. Light, R. J. French, J. Lytton, Electrophysiological characterization and ionic stoichiometry of the rat brain K(+)-dependent NA(+)/CA(2+) exchanger, NCKX2. *J. Biol. Chem.* **276**, 25919–25928 (2001).

26. V. Denis, M. S. Cyert, Internal Ca(2+) release in yeast is triggered by hypertonic shock and mediated by a TRP channel homologue. *J. Cell Biol.* **156**, 29–34 (2002).

27. K. W. Cunningham, G. R. Fink, Calcineurin-dependent growth control in Saccharomyces cerevisiae mutants lacking PMC1, a homolog of plasma membrane Ca2+ ATPases. *J. Cell Biol.* **124**, 351–363 (1994).

28. K. D. Hirschi, R. G. Zhen, K. W. Cunningham, P. A. Rea, G. R. Fink, CAX1, an H+/Ca2+ antiporter from Arabidopsis. *Proc Natl Acad Sci USA*. **93**, 8782–8786 (1996).

29. S. Blackford, P. A. Rea, D. Sanders, Voltage sensitivity of H+/Ca2+ antiport in higher plant tonoplast suggests a role in vacuolar calcium accumulation. *J. Biol. Chem.* **265**, 9617–9620 (1990).

30. X. Z. Chen, M. J. Coady, F. Jackson, A. Berteloot, J. Y. Lapointe, Thermodynamic determination of the Na+: glucose coupling ratio for the human SGLT1 cotransporter. *Biophys. J.* **69**, 2405–2414 (1995).

31. N. Zerangue, M. P. Kavanaugh, Flux coupling in a neuronal glutamate transporter. *Nature*. **383**, 634–637 (1996).

32. G. A. Fitzgerald, C. Mulligan, J. A. Mindell, A general method for determining secondary active transporter substrate stoichiometry. *eLife*. **6** (2017), doi:10.7554/eLife.21016.

33. L. Leisle, C. F. Ludwig, F. A. Wagner, T. J. Jentsch, T. Stauber, ClC-7 is a slowly voltage-gated 2Cl(-)/1H(+)-exchanger and requires Ostm1 for transport activity. *EMBO J.* **30**, 2140–2152 (2011).

34. A. G. Garrity, W. Wang, C. M. Collier, S. A. Levey, Q. Gao, H. Xu, The endoplasmic reticulum, not the pH gradient, drives calcium refilling of lysosomes. *eLife*. **5** (2016), doi:10.7554/eLife.15887.

35. W. M. Henne, Discovery and Roles of ER-Endolysosomal Contact Sites in Disease. *Adv. Exp. Med. Biol.* **997**, 135–147 (2017).

36. C.-Y. Lim, O. B. Davis, H. R. Shin, J. Zhang, C. A. Berdan, X. Jiang, J. L. Counihan, D. S. Ory, D. K. Nomura, R. Zoncu, ER-lysosome contacts enable cholesterol sensing by mTORC1 and drive aberrant growth signalling in Niemann-Pick type C. *Nat. Cell Biol.* **21**, 1206–1218 (2019).

37. D. Höglinger, T. Burgoyne, E. Sanchez-Heras, P. Hartwig, A. Colaco, J. Newton, C. E. Futter, S. Spiegel, F. M. Platt, E. R. Eden, NPC1 regulates ER contacts with endocytic organelles to mediate cholesterol egress. *Nat. Commun.* **10**, 4276 (2019).

38. X. Du, J. Kumar, C. Ferguson, T. A. Schulz, Y. S. Ong, W. Hong, W. A. Prinz, R. G. Parton, A. J. Brown, H. Yang, A role for oxysterol-binding protein-related protein 5 in endosomal cholesterol trafficking. *J. Cell Biol.* **192**, 121–135 (2011).

39. F. Foulquier, M. Amyere, J. Jaeken, R. Zeevaert, E. Schollen, V. Race, R. Bammens, W. Morelle, C. Rosnoblet, D. Legrand, D. Demaegd, N. Buist, D. Cheillan, N. Guffon, P. Morsomme, W. Annaert, H. H. Freeze, E. Van Schaftingen, M. Vikkula, G. Matthijs, TMEM165 deficiency causes a congenital disorder of glycosylation. *Am. J. Hum. Genet.* **91**, 15–26 (2012).

40. C. Rosnoblet, D. Legrand, D. Demaegd, H. Hacine-Gherbi, G. de Bettignies, R. Bammens, C. Borrego, S. Duvet, P. Morsomme, G. Matthijs, F. Foulquier, Impact of disease-causing mutations on TMEM165 subcellular localization, a recently identified protein involved in CDG-II. *Hum. Mol. Genet.* **22**, 2914–2928 (2013).

41. R. O. Heuckeroth, Hirschsprung disease - integrating basic science and clinical medicine to improve outcomes. *Nat. Rev. Gastroenterol. Hepatol.* **15**, 152–167 (2018).

42. VCV000691394.2 - ClinVar - NCBI, (available at https://www.ncbi.nlm.nih.gov/clinvar/variation/691394/?oq=%22Clinical+Genetics,+Erasmus+University+Medical+Center%22[submitter]+AND+%22TMEM165%22[gene]&m=NM_018475.5(TMEM165):c.782C%3EA%20(p.Ala261Glu)).

43. R. P. Kapur, Developmental disorders of the enteric nervous system. *Gut*. **47 Suppl 4**, iv81-3; discussion iv87 (2000).

44. D. Mittal, A. Bagga, R. Tandon, M. C. Sharma, V. Bhatnagar, Hirschsprung's disease with infantile nephropathic cystinosis. *J. Indian Assoc. Pediatr. Surg.* **20**, 153–154 (2015).

45. F. M. Platt, B. Boland, A. C. van der Spoel, The cell biology of disease: lysosomal storage disorders: the cellular impact of lysosomal dysfunction. *J. Cell Biol.* **199**, 723–734 (2012).

46. A. H. Futerman, G. van Meer, The cell biology of lysosomal storage disorders. *Nat. Rev. Mol. Cell Biol.* **5**, 554–565 (2004).

47. K. Kiselyov, S. Yamaguchi, C. W. Lyons, S. Muallem, Aberrant Ca2+ handling in lysosomal storage disorders. *Cell Calcium*. **47**, 103–111 (2010).

48. R. Bargal, N. Avidan, E. Ben-Asher, Z. Olender, M. Zeigler, A. Frumkin, A. Raas-Rothschild, G. Glusman, D. Lancet, G. Bach, Identification of the gene causing mucolipidosis type IV. *Nat. Genet.* **26**, 118–123 (2000).

49. E. Lloyd-Evans, A. J. Morgan, X. He, D. A. Smith, E. Elliot-Smith, D. J. Sillence, G. C. Churchill, E. H. Schuchman, A. Galione, F. M. Platt, Niemann-Pick disease type C1 is a sphingosine storage disease that causes deregulation of lysosomal calcium. *Nat. Med.* **14**, 1247–1255 (2008).

50. E. Lloyd-Evans, H. Waller-Evans, Lysosomal ca2+ homeostasis and signaling in health and disease. *Cold Spring Harb. Perspect. Biol.* **12** (2020), doi:10.1101/cshperspect.a035311.

51. O. Zhuchenko, J. Bailey, P. Bonnen, T. Ashizawa, D. W. Stockton, C. Amos, W. B. Dobyns, S. H. Subramony, H. Y. Zoghbi, C. C. Lee, Autosomal dominant cerebellar ataxia (SCA6) associated with small polyglutamine expansions in the alpha 1A-voltage-dependent calcium channel. *Nat. Genet.* **15**, 62–69 (1997).

52. C. Denier, A. Ducros, A. Durr, B. Eymard, B. Chassande, E. Tournier-Lasserve, Missense CACNA1A mutation causing episodic ataxia type 2. *Arch. Neurol.* **58**, 292–295 (2001).

53. B. Dehay, A. Ramirez, M. Martinez-Vicente, C. Perier, M.-H. Canron, E. Doudnikoff, A. Vital, M. Vila, C. Klein, E. Bezard, Loss of P-type ATPase ATP13A2/PARK9 function induces general lysosomal deficiency and leads to Parkinson disease neurodegeneration. *Proc Natl Acad Sci USA.* **109**, 9611–9616 (2012).

54. A. Ramirez, A. Heimbach, J. Gründemann, B. Stiller, D. Hampshire, L. P. Cid, I. Goebel, A. F. Mubaidin, A.-L. Wriekat, J. Roeper, A. Al-Din, A. M. Hillmer, M. Karsak, B. Liss, C. G. Woods, M. I. Behrens, C. Kubisch, Hereditary parkinsonism with dementia is caused by mutations in ATP13A2, encoding a lysosomal type 5 P-type ATPase. *Nat. Genet.* **38**, 1184–1191 (2006).

55. N. Narayanaswamy, K. Chakraborty, A. Saminathan, E. Zeichner, K. Leung, J. Devany, Y. Krishnan, A pH-correctable, DNA-based fluorescent reporter for organellar calcium. *Nat. Methods*. **16**, 95–102 (2019).

56. I. Bezprozvanny, Calcium signaling and neurodegenerative diseases. *Trends Mol. Med.* **15**, 89–100 (2009).